

**University of Alberta**

Effect of Liquid Viscosity, Surface Tension and Nozzle Size on Atomization in  
Two-Phase Nozzles

by

Chidirim Enoch Ejim



A thesis submitted to the Faculty of Graduate Studies and Research  
in partial fulfillment of the requirements for the degree of

Doctor of Philosophy

Department of Mechanical Engineering

Edmonton, Alberta

Spring 2008



Library and  
Archives Canada

Published Heritage  
Branch

395 Wellington Street  
Ottawa ON K1A 0N4  
Canada

Bibliothèque et  
Archives Canada

Direction du  
Patrimoine de l'édition

395, rue Wellington  
Ottawa ON K1A 0N4  
Canada

*Your file    Votre référence*  
*ISBN: 978-0-494-45419-0*  
*Our file    Notre référence*  
*ISBN: 978-0-494-45419-0*

**NOTICE:**

The author has granted a non-exclusive license allowing Library and Archives Canada to reproduce, publish, archive, preserve, conserve, communicate to the public by telecommunication or on the Internet, loan, distribute and sell theses worldwide, for commercial or non-commercial purposes, in microform, paper, electronic and/or any other formats.

The author retains copyright ownership and moral rights in this thesis. Neither the thesis nor substantial extracts from it may be printed or otherwise reproduced without the author's permission.

**AVIS:**

L'auteur a accordé une licence non exclusive permettant à la Bibliothèque et Archives Canada de reproduire, publier, archiver, sauvegarder, conserver, transmettre au public par télécommunication ou par l'Internet, prêter, distribuer et vendre des thèses partout dans le monde, à des fins commerciales ou autres, sur support microforme, papier, électronique et/ou autres formats.

L'auteur conserve la propriété du droit d'auteur et des droits moraux qui protègent cette thèse. Ni la thèse ni des extraits substantiels de celle-ci ne doivent être imprimés ou autrement reproduits sans son autorisation.

---

In compliance with the Canadian Privacy Act some supporting forms may have been removed from this thesis.

Conformément à la loi canadienne sur la protection de la vie privée, quelques formulaires secondaires ont été enlevés de cette thèse.

While these forms may be included in the document page count, their removal does not represent any loss of content from the thesis.

Bien que ces formulaires aient inclus dans la pagination, il n'y aura aucun contenu manquant.

  
**Canada**

## ABSTRACT

The main objectives of this study were to compare global Sauter Mean Diameter ( $SMD_{gb}$ ) produced from sprays of different viscosities, surface tension and sizes of small-scale fluid coker (FC) nozzles. The final objective was to establish a  $SMD_{gb}$  correlation as a function of nozzle size, viscosity, surface tension and flow conditions. This study was performed as first step in understanding the atomization behaviour of FC nozzles in situ.

Compressed air was used as the gas phase, the liquids were water, canola oil and glycerine solution. Liquid viscosities were varied from 1 mPa-s to 67 mPa-s, and surface tensions were varied from 25 mN/m to 70 mN/m. All fluid properties were at 21°C. The liquid flow rates were varied from 95g/s to 195 g/s, and the Gas-to-Liquid-Ratio ( $GLR$ ), by mass, was fixed at 1%, similar to the commercial FC nozzles. Operating conditions with 2%  $GLR$  were also studied. Fluid mixing pressures in the test were between 516 kPa to 998 kPa. The nozzles used were a one-quarter and one third scale nozzle, which were geometrically similar to a commercial FC nozzle. Dimensional analysis was used to determine the flow conditions required to operate the nozzles at similar flow conditions. The  $SMD$  within the spray was measured using a Dantec 2-D Particle Dynamics Analyzer (PDA). Measurements were performed at axial distances of 100, 202 and 405 mm from the nozzle exit and within spray widths of -50 mm to 50 mm in the horizontal plane.

The results showed that drop size increases significantly between 34 to 64% with liquid viscosity. Surface tension effects on drop size can be negligible at 1%  $GLR$  and axial position within  $32D$  of the nozzle exit. The other results showed an increase (between 15

and 25%) in drop size with a decrease in surface tension. The  $SMD_{gb}$  increased by up to 31% with the bigger nozzle. Finally, the  $SMD_{gb}$  correlation estimated drop size within 17% maximum deviation. Results from this study provide a comprehensive means of improving the design of two-phase fluid coker nozzles.

## **DEDICATION**

This thesis is specially dedicated to my dear wife Ibiroke Charlie Ejim, my son Esomchi Oluwanifise Jachin Ejim, and my daughter Ebubechi Oluwakanyinsola Micaiah Ejim. I will also like to dedicate this thesis to my parents, Mr. H.C and Mrs. P.N. Ejim, and my wonderful in-laws, Mr. Steve and Mrs. Jean Akinbolade.

## ACKNOWLEDGEMENTS

I thank my saviour and Lord Jesus Christ for sustaining me physically and mentally throughout the duration of my thesis.

I would like to express my gratitude to my supervisors, Professors Alidad Amirfazli and Brian Fleck for giving me the opportunity to work in this research area. I learned a great deal during the period of time we worked together. Their advice, support and guidance were invaluable and highly appreciated.

The expertise of the machine shop staff, Greg, Berny, Roger, Rick and Liana, was of great help in the laboratory. I appreciate all the time they took out of their busy schedules to assist me.

To my colleagues Tony, Fashid, Aziz, and Javed, thanks for the fun times and the memorable moments. You all definitely had an impact on me.

I would like to thank my parents and my in-laws for always supporting me morally and spiritually. To my siblings - Ihechiluru, Chiimela, Uzochi, Kelechi -, and siblings in-law – Vincent, Dayo, Taye, Kehinde -, thanks for all the encouragements. I love you all.

Finally, I sincerely thank my lovely wife Ibronke, my son Esomchi and my daughter Ebubechi for their moral support and prayers. Their assistance and encouragement in putting a smile on my face during the rigours of this thesis, made these years bearable.

# TABLE OF CONTENTS

<b>CHAPTER 1 INTRODUCTION</b> .....	1
1.1 The Fluid Coker .....	1
1.2 Original Contribution in Atomization Study.....	5
1.3 Thesis Scope and Objectives.....	7
<b>CHAPTER 2 LITERATURE - ATOMIZERS AND ATOMIZATION PRINCIPLES</b> ..	9
2.1 Classification of common atomizers.....	9
2.1.1 Single-phase atomizers (Plain orifice pressure atomizers) .....	10
2.1.2 Twin-fluid atomizers .....	11
2.1.3 Effervescent atomizers .....	13
2.2 The fluid coker atomizer/nozzle.....	15
2.3 Liquid atomization and related parameters .....	15
2.3.1 Variables affecting liquid atomization .....	17
2.3.2 Forces and mechanisms in liquid atomization .....	19
2.4 Summary of atomizer drop size correlations .....	24
2.4.1 Single-phase atomizers – Plain orifice pressure atomizers .....	24
2.4.2 Twin-fluid atomizers.....	27
2.4.3 Effervescent atomizers .....	29
2.4.3.1 Viscosity Effects .....	30
2.4.3.2 Surface Tension Effects .....	31
2.4.3.3 Geometry Effects .....	34
2.5 Literature summary and relation to FC nozzles .....	36

<b>CHAPTER 3 EQUIPMENT SPECIFICATION AND CALIBRATION</b> .....	38
3.1 Nozzle Assembly .....	38
3.2 Test Liquids.....	42
3.3 Test Equipment .....	43
3.4 Measurement of Liquid Physical Properties .....	60
3.5 Equipment Calibration .....	63
<b>CHAPTER 4 NOZZLE SCALE-UP AND MIST EXTRACTION DESIGN</b> .....	67
4.1 Maximum feasible test nozzle size .....	67
4.1.1 Design using the Taitel and Dukler flow map .....	68
4.1.2 Design using the Baker-Scott flow map.....	72
4.1.3 Design using existing test data from commercial scale nozzles .....	75
4.2 Effective mist extraction design for nozzle sprays .....	79
4.2.1 Maximum possible entrained gas from nozzle.....	81
4.2.1.1 Single-phase gas jet entrainment equation.....	81
4.2.1.2 Effervescent spray entrainment equation.....	82
4.2.2 Duct layout design for minimum system pressure loss.....	83
<b>CHAPTER 5 EXPERIMENTAL PROCEDURE AND DATA ANALYSIS</b> .....	87
5.1 Equipment layout and flow loop .....	87
5.2 Determining experimental flow conditions.....	89
5.3 Data Processing.....	92
5.3.1 Velocity-Drop size correlation coefficient .....	92



5.3.2 Determining important jet parameters and characteristics .....	93
5.3.3 Estimating liquid volume/mass balance in the spray .....	96
5.3.4 Summation of measured <i>SMD</i> profiles .....	98
5.3.5 <i>SMD<sub>gb</sub></i> Correlation.....	101
5.3.6 Error/Uncertainty Analysis .....	102
<b>CHAPTER 6 RESULTS AND DISCUSSION – VELOCITY DATA.....</b>	<b>104</b>
6.1 Velocity-Drop size correlation .....	104
6.2 Number-weighted and mass-weighted velocity profiles .....	110
6.3 Axial variation of jet-half-width and centreline velocity .....	113
6.4 Self-similarity in velocity profiles .....	117
6.4.1 Different liquid viscosities .....	122
6.4.2 Different liquid surface tension .....	126
6.4.3 Different nozzle sizes .....	131
<b>CHAPTER 7 RESULTS AND DISCUSSION – DROP SIZE DATA .....</b>	<b>135</b>
7.1 Liquid volume flux .....	135
7.1.1 Air-water systems .....	135
7.1.2 Air-glycerine solutions and air-canola oil systems .....	138
7.2 Effect of Liquid Viscosity on drop size at 1% <i>GLR</i> .....	140
7.3 Effect of Liquid Viscosity on drop size at 2% <i>GLR</i> .....	144
7.4 Effect of surface tension on drop size at 1% <i>GLR</i> .....	147
7.5 Effect of surface tension on drop size at 2% <i>GLR</i> .....	151

7.6 Effect of Nozzle size geometry .....	153
7.6.1 Geometric effects at 1% <i>GLR</i> using air and glycerine-water mixture .....	153
7.6.2 Geometric effects at 1% <i>GLR</i> using air and water .....	155
7.4 Correlation for <i>SMD</i> .....	158
<b>CHAPTER 8 SUMMARY AND CONCLUSIONS</b> .....	162
<b>BIBLIOGRAPHY</b> .....	165
<b>APPENDICES</b> .....	172

## LIST OF TABLES

Table 2.1 Literature summary of <i>SMD</i> variation with liquid viscosity, surface tension and exit orifice diameter .....	37
Table 3.1 Typical flow conditions and steam-bitumen properties of the commercial coker nozzle .....	42
Table 3.2 Optical settings of the PDA unit used in the study .....	54
Table 3.3 Properties of the test liquids at 21°C. Data with superscripts ‘*’ were adopted from White [39] .....	63
Table 3.4 Summary of PDA calibration results using borosilicate particles .....	66
Table 4.1 Nozzle scaling design using the Taitel and Dukler flow regime parameters. Design data are for $9.5 \times 10^{-5} \text{ m}^3/\text{s}$ (1.5 USGPM) and 1% <i>GLR</i> in the SS-1.0 .....	71
Table 4.2 Nozzle scaling design using the Baker-Scott flow regime parameters. Design data are for $9.5 \times 10^{-5} \text{ m}^3/\text{s}$ (1.5 USGPM) and 1% <i>GLR</i> in the SS-1.0..	74
Table 4.3 Comparison of absolute mixing and exit pressures at constant gas and liquid mass flow rates in the FS-1.0 and FS-1.5 nozzles .....	75

Table 6.1 Summary of slopes from log-log plots of centreline velocity vs effective axial distance for all two-phase spray systems in this study.....	116
Table 6.2 Summary of curve-fit coefficients of $(r/r_{1/2})^2$ (Eqn. 5.4 (c)) for all two-phase spray systems in this study.....	121
Table 6.3 Test conditions at 1% <i>GLR</i> to study the effect of liquid viscosity on atomization using the SS-1.0 nozzle.....	122
Table 6.4 Test conditions at 2% <i>GLR</i> to study the effect of liquid viscosity on atomization using the SS-1.0 nozzle.....	125
Table 6.5 Test conditions at 1% <i>GLR</i> to study the effect of surface tension on atomization using the SS-1.0 nozzle.....	127
Table 6.6 Test conditions at 2% <i>GLR</i> to study the effect of surface tension on atomization using the SS-1.0 nozzle.....	129
Table 6.7 Test conditions at 1% <i>GLR</i> using air and glycerine solution to study the effect of nozzle size on atomization for SS-1.0 ( $D = 3.1$ mm) and SS-1.3 ( $D = 4.1$ mm) nozzles.....	131

Table 6.8 Test conditions at 1% *GLR* using air and water to study the effect of nozzle size on atomization for SS-1.0 ( $D = 3.1$  mm) and SS-1.3 ( $D = 4.1$  mm) nozzles.....131

Table 7.1 Test data used in curve-fit for  $SMD_{gb}$  correlation. Data is for  $x = 100$  mm...159

## LIST OF FIGURES

Figure 1.1 Schematic of processes in a Fluid Coker (FC) .....	2
Figure 1.2 Schematic of the jet-bed interaction in a Fluid Coker (FC).....	3
Figure 2.1 A typical configuration of atomization process in a plain orifice atomizer...	11
Figure 2.2 Schematic of a typical air-assist atomizer .....	12
Figure 2.3 Schematic showing layout of air-blast (plain-jet) atomizer .....	12
Figure 2.4 Schematic showing the cross-section of a typical effervescent atomizer.....	14
Figure 2.5 Schematic of gas and liquid mixing in a typical fluid coker nozzle. (Cross section shown).....	15
Figure 3.1 Photograph of the quarter-scale nozzle assembly (SS-1.0) .....	38
Figure 3.2 Drawing showing nozzle geometry and nominal nozzle dimensions of the SS-1.0. (Dimensions are in millimetres) .....	39
Figure 3.3 Schematic showing layout of test equipment in the experimental set-up .....	44

Figure 3.4 Photograph of the positive displacement pump used in the experiment .....	45
Figure 3.5 Photograph of the liquid flow meter used in the experiment .....	46
Figure 3.6 Photograph of the compressor showing external components .....	48
Figure 3.7 Photograph of the air mass flow meter used in the experiment .....	49
Figure 3.8 Photographs of a pressure gauge and transducer unit used in the experiments .....	51
Figure 3.9 Photographs showing sections of the liquid reservoir/collector .....	53
Figure 3.10 Schematic showing top view and optical path for set-up of the PDA unit .....	55
Figure 3.11 Photographs showing sections of the liquid reservoir/collector .....	55
Figure 3.12 Photograph of the Refractometer used in the study.....	58
Figure 3.13 Photograph showing parts of the 3-D traverse system .....	60

Figure 4.1 A photograph showing the SS-1.3 and SS-1.0 nozzles for size comparison. Labelled sections of the SS-1.0 have been shown in Figure 3.1 .....	78
Figure 4.2 Photograph showing test equipment and final set-up for effective mist extraction from the sprays .....	85
Figure 5.1 Schematic of flow loop in the experimental set-up .....	87
Figure 5.2 Schematic of spray cross-section (top) and typical <i>SMD</i> and liquid volume flux, $q_L$ , profiles (bottom) seen in a spray from a line scan across the spray axis .....	100
Figure 6.1 Profiles of <i>CC</i> across the spray and at axial positions 100, 202, and 405 mm for the SS-1.0 nozzle ( $D = 3.1\text{mm}$ ). Data is for water at $95 \times 10^{-6} \text{ m}^3/\text{s}$ and 1.0% <i>GLR</i> . The error bars show the 95% confidence limits for the <i>CC</i> values.....	105
Figure 6.2 Profiles of <i>CC</i> across the spray and at axial positions, $x = 100, 202,$ and 405 mm for the SS-1.0 nozzle ( $D = 3.1\text{mm}$ ). Data is for air-water spray ( $\mu_L = 1 \text{ mPa}\cdot\text{s}, \gamma = 70 \text{ mN/m}$ ) with liquid flow rate of $95 \times 10^{-6} \text{ m}^3/\text{s}$ and 2.0% <i>GLR</i> . The error bars show the 95% confidence limits for the <i>CC</i> values ...	105



Figure 6.3 Profiles of  $CC$  across the spray and at axial positions,  $x = 100, 202,$  and  $405$  mm for the SS-1.0 nozzle ( $D = 3.1$ mm). Data is for air-glycerine solution spray ( $\mu_L = 67$  mPa-s,  $\gamma = 61$  mN/m) with liquid flow rate of  $114 \times 10^{-6}$  m<sup>3</sup>/s and 1.0%  $GLR$ . The error bars show the 95% confidence limits for the  $CC$  values..... 107

Figure 6.4 Profiles of  $CC$  across the spray and at axial positions,  $x = 100$  and  $202$  mm for the SS-1.0 nozzle ( $D = 3.1$ mm). Data is for air-glycerine solution spray ( $\mu_L = 67$  mPa-s,  $\gamma = 61$  mN/m) with liquid flow rate of  $105 \times 10^{-6}$  m<sup>3</sup>/s and 2.0%  $GLR$ . The error bars show the 95% confidence limits for the  $CC$  values ..... 108

Figure 6.5 Profiles of  $CC$  across the spray and at axial positions,  $x = 100, 202,$  and  $405$  mm for the SS-1.0 nozzle ( $D = 3.1$ mm). Data is for air-canola oil spray ( $\mu_L = 66$  mPa-s,  $\gamma = 25$  mN/m) with liquid flow rate of  $105 \times 10^{-6}$  m<sup>3</sup>/s and 1.0%  $GLR$ . The error bars show the 95% confidence limits for the  $CC$  values..... 109

Figure 6.6 Profiles of  $CC$  across the spray and at axial positions,  $x = 100, 202,$  and  $405$  mm for the SS-1.0 nozzle ( $D = 3.1$ mm). Data is for air-canola oil spray ( $\mu_L = 66$  mPa-s,  $\gamma = 25$  mN/m) with liquid flow rate of  $105 \times 10^{-6}$  m<sup>3</sup>/s and 2.0%  $GLR$ . The error bars show the 95% confidence limits for the  $CC$  values..... 110

Figure 6.7 Number and mass-weighted velocity profiles at axial positions (a) 100 mm, (b) 202 mm, and (c) 405 mm for SS-1.0. Data is for water at  $95 \times 10^{-6} \text{ m}^3/\text{s}$  and 1.0% *GLR*. The error bars show the 95% confidence limits for the velocity measurements. Lines are to guide the eyes ..... 112

Figure 6.8 Variation of jet-half-width (from number and mass-weighted velocity profiles) at axial positions 100, 202, and 405 mm for SS-1.0. Data is for water at  $95 \times 10^{-6} \text{ m}^3/\text{s}$  and 1.0% *GLR*..... 113

Figure 6.9 Variation of centreline velocity at axial positions 100, 202, and 405 mm using (a) mass-weighted data, (b) number-weighted data. Data is for water at  $95 \times 10^{-6} \text{ m}^3/\text{s}$  and 1.0% *GLR*. using SS-1.0 ..... 115

Figure 6.10 Comparison of normalized mass-weighted and number-weighted velocity profiles for self similarity at axial positions (a) 100 mm, (b) 202 mm, and (c) 405 mm. Data is for water at  $95 \times 10^{-6} \text{ m}^3/\text{s}$  and 1.0% *GLR* using SS-1.0 nozzle ..... 118

Figure 6.11 Comparison of self similarity at different axial positions for the normalized (a) mass-weighted and (b) number-weighted velocity profiles. Data is for water at  $95 \times 10^{-6} \text{ m}^3/\text{s}$  and 1.0% *GLR* using SS-1.0 nozzle..... 120

Figure 6.12 Comparison of normalized velocity profiles at axial distances (a) 100 mm, (b) 202 mm, and (c) 405 mm, for different liquid viscosities at  $GLR = 1\%$  using SS-1.0 nozzle. Note that MW and NW denote mass-weighted and number-weighted velocity data ..... 124

Figure 6.13 Comparison of normalized velocity profiles at axial distances (a) 100 mm, and (b) 202 mm, for different liquid viscosities at  $GLR = 2\%$ . Note that MW and NW denote mass-weighted and number-weighted velocity data ..... 126

Figure 6.14 Comparison of normalized velocity profiles at axial positions (a) 100 mm, (b) 202 mm, and (c) 405 mm, for different liquid surface tensions at  $GLR = 1\%$  using SS-1.0 nozzle. Note that MW and NW denote mass-weighted and number-weighted velocity data ..... 129

Figure 6.15 Comparison of normalized velocity profiles at axial positions (a) 100 mm, and (b) 202 mm, for different liquid surface tensions at  $GLR = 2\%$ . Note that MW and NW denote mass-weighted and number-weighted velocity data. 130

Figure 6.16 Comparison of normalized velocity profiles for SS-1.0 and SS-1.3 nozzles at axial distances (a) 100 mm, and (b) 202 mm, for air and glycerine solution at  $GLR = 1\%$ . Note that MW and NW denote mass-weighted and number-weighted velocity data ..... 132

Figure 6.17 Comparison of normalized velocity profiles for SS-1.0 and SS-1.3 nozzles at axial distances (a) 100 mm, and (b) 202 mm, for air and water at  $GLR = 1\%$ .

Note that MW and NW denote mass-weighted and number-weighted velocity data ..... 133

Figure 7.1 Plots of volume flux across the spray at 3 axial distances using SS-1.0 nozzle.

Data is for an air-water system with liquid flow rate of  $95 \times 10^{-6} \text{ m}^3/\text{s}$  and 1%  $GLR$  ..... 136

Figure 7.2 Plots of volume per unit time per unit radius at 3 axial distances within a spray

using SS-1.0 nozzle. Data is for an air-water system with liquid flow rate of  $95 \times 10^{-6} \text{ m}^3/\text{s}$  and 2%  $GLR$  ..... 137

Figure 7.3 Radial plots of liquid volume flux within a spray at 3 axial distances using SS-

1.0. Data is for an air-glycerine solution system with liquid flow rate of  $114 \times 10^{-6} \text{ m}^3/\text{s}$  and 1%  $GLR$ ..... 139

Figure 7.4 Radial plots of liquid volume flux within a spray at 3 axial distances using SS-

1.0. Data is for an air-canola oil system with liquid flow rate of  $105 \times 10^{-6} \text{ m}^3/\text{s}$  and 1%  $GLR$  ..... 140

Figure 7.5 <i>SMD</i> profiles for comparison of liquid viscosity at $x = 100$ mm ( $GLR = 1\%$ ) using SS-1.0. Error bars denote a 95% confidence interval. Sampling time is 360 seconds .....	141
Figure 7.6 <i>SMD</i> profiles for comparison of liquid viscosity at $x = 202$ mm ( $GLR = 1\%$ ) using SS-1.0 nozzle. Error bars denote a 95% confidence interval. Sampling time is 360 seconds .....	142
Figure 7.7 <i>SMD</i> profiles for comparison of liquid viscosity at $x = 405$ mm ( $GLR = 1\%$ ) using the SS-1.0 nozzle. Error bars denote a 95% confidence interval. Sampling time is 360 seconds .....	143
Figure 7.8 <i>SMD</i> profiles for comparison of liquid viscosity at $x = 100$ mm ( $GLR = 2\%$ ) using SS-1.0 nozzle. Error bars denote a 95% confidence interval. Sampling time is 360 seconds .....	145
Figure 7.9 <i>SMD</i> profiles for comparison of liquid viscosity at $x = 202$ mm ( $GLR = 2\%$ ) using SS-1.0 nozzle. Error bars denote a 95% confidence interval. Sampling time is 360 seconds .....	146
Figure 7.10 <i>SMD</i> profiles for comparison of surface tension at $x = 100$ mm ( $GLR = 1\%$ ) using SS-1.0 nozzle. Error bars denote a 95% confidence interval. Sampling time is 360 seconds .....	148

Figure 7.11 *SMD* profiles for comparison of liquid viscosity at  $x = 202$  mm ( $GLR = 1\%$ ) using SS-1.0 nozzle. Error bars denote a 95% confidence interval. Sampling time is 360 seconds ..... 149

Figure 7.12 *SMD* profiles for comparison of surface tension at  $x = 405$  mm ( $GLR = 1\%$ ) using SS-1.0 nozzle. Error bars denote a 95% confidence interval. Sampling time is 360 seconds. .... 150

Figure 7.13 *SMD* profiles for comparison of surface tension at  $x = 100$  mm ( $GLR = 2\%$ ) using SS-1.0 nozzle. Error bars denote a 95% confidence interval. Sampling time is 360 seconds ..... 151

Figure 7.14 *SMD* profiles for comparison of surface tension at  $x = 202$  mm ( $GLR = 2\%$ ) using SS-1.0 nozzle. Error bars denote a 95% confidence interval. Sampling time is 360 seconds ..... 152

Figure 7.15 *SMD* profiles for comparison of nozzle size effects at  $x = 100$  mm ( $GLR = 1\%$ ) using SS-1.0 ( $D = 3.1$  mm) and SS-1.3 ( $D = 4.1$  mm). Data was produced using air and glycerine-water mixture. Sampling time is 360 seconds ..... 154

Figure 7.16 *SMD* profiles for comparison of nozzle size effects at  $x = 202$  mm  
(*GLR* = 1%) using SS-1.0 ( $D = 3.1$  mm) and SS-1.3 ( $D = 4.1$  mm). Data was  
produced using air and glycerine-water mixture. Sampling time is 360  
seconds ..... 155

Figure 7.17 *SMD* profiles for comparison of nozzle size effects at  $x = 100$ mm  
(*GLR* = 1%) using SS-1.0 ( $D = 3.1$  mm) and SS-1.3 ( $D = 4.1$  mm). Data was  
produced using air and water. Sampling time is 360 seconds..... 156

Figure 7.18 *SMD* profiles for comparison of nozzle size effects at  $x = 202$ mm  
(*GLR* = 1%) using SS-1.0 ( $D = 3.1$  mm) and SS-1.3 ( $D = 4.1$  mm).Data was  
produced using air and water. Sampling time is 360 seconds..... 157

Figure 7.19 Comparison of correlation and measured  $SMD_{gb}$  ..... 161

## LIST OF SYMBOLS

### Latin Letters

a, b, c, d, e – Indices (or Exponents) from regression for correlation equation

$A_p$  - Probe area of the measurement volume ( $m^2$ )

C (or Constant) – The constant term from regression for a correlation

d – Drop diameter ( $\mu m$ )

$d_G$  - Bubble diameter ( $\mu m$ )

$d_{lig}$  – Ligament diameter ( $\mu m$ )

$d_L$  - Thickness of liquid annulus surrounding a bubble at the nozzle exit ( $\mu m$ )

$d_i$  - Diameter of illuminated area of the probe volume (m)

$dP/dx$  - Pressure drop per unit length ( $N/m^3$ )

D - Atomizer exit orifice diameter (m)

$D_i$  - Diameter of the  $i$ th drop ( $\mu m$ )

$D_p$  – Diameter of liquid prefilmer (m)

$D_t$  – Internal diameter of the tube (or conduit) section of the nozzle (m)

E - Entrainment number

g - Acceleration due to gravity ( $m/s^2$ )

$G_G$  - Mass flux of the gas through a conduit cross-section ( $kg/m^2s$ )

$G_L$  - Mass flux of the liquid through a conduit cross-section ( $kg/m^2s$ )

L - Atomizer exit orifice length (m)

$L_c$  - Characteristic nozzle dimension (m)

$L_s$  - Slit width of the receiver (m)

$L_t$  – Length of the tube (or conduit) section of the nozzle (m)



$m$  – Mass flow rate (kg/s)

$m_e$  - Mass flow rate of entrained fluid (kg/s)

$m_G$  - Mass flow rate of gas (kg/s)

$m_L$  - Mass flow rate of liquid (kg/s)

$M$  – Molecular weight (g/mole)

$N$  - Total number of drops

$P$  – Absolute pressure of fluid mixture at point of interest (Pa)

$P_{atm}$  – Local atmospheric (or barometric) pressure (Pa)

$P_G$  – Atomizing gas supply (or injection) pressure (Pa)

$q_L$  – Volume of liquid per unit area per unit time (m/s)

$Q_G$  – Gas volume flow rate (m<sup>3</sup>/s)

$Q_L$  – Liquid volume flow rate (m<sup>3</sup>/s)

$Q_{G_0}$  – Gas volume flow rate at nozzle exit (m<sup>3</sup>/s)

$r$  – Radial measurement distance from the center of the spray (m)

$r_{1/2}$  – Jet half-width (or jet radius,  $r_{jet}$ ) (m)

$R$  – Maximum radial measurement distance from the center of the spray (m)

$R_G$  - Characteristic gas constant (J/kg-K)

$R_U$  - Universal Gas Constant (J/mol-K)

$R^2$ -value - Square of the Pearson product moment correlation coefficient of data points

$S$  – Sample standard deviation

$S_1$  - Slope of the plot of jet half-width against axial distance

$S_R$  – Saturation Ratio

$t$  – Student's t distribution sampling coefficient

$T_{abs}$  - Absolute temperature of fluid mixture at point of interest (K)

T – Taitel and Dukler flow regime parameter

$T_i$  - Total sampling time (s)

$U_c$  - Characteristic fluid velocity in the nozzle (m/s)

$U_d$  - Drop velocity (m/s)

$U_g$  - Absolute gas velocity in the ambient (m/s)

$U_{gL}$  - Relative velocity between liquid and ambient gas (m/s)

$U_{nw}$  – Number-weighted drop velocity (m/s)

$U_{max}$  (or  $U_{CL}$ ) - Mean velocity at the center of the spray (m/s)

$U_{mw}$  – Mass-weighted drop velocity (m/s)

$U_{y_i}$  - Uncertainty in parameter  $y_i$

$U_A$  – Air velocity (m/s)

$U_G$  – Gas velocity (m/s)

$U_L$  - Liquid velocity (m/s)

$U_{mean}$  – Mean value of a parameter or physical quantity

$U_R$  - Relative velocity between liquid and atomizing gas in the nozzle (m/s)

$U_X$  - Overall uncertainty in a parameter  $X$

$x$  – Axial distance from nozzle exit (m)

$x_{eff}$  - Effective axial distance from the virtual origin

$y$  – Lateral or horizontal distance from the central axis of the nozzle or spray (m)

X – Taitel and Dukler flow regime parameter

## Greek Letters

$\alpha$  - Void fraction

$\beta$  - Coefficient in the model for a self-similar mean velocity profile

$\delta$  - Jet (or spray) half-width (m)

$\Delta P_L$  - Liquid injection pressure differential across the nozzle (Pa)

$\phi$  - Scattering (or off-axis) angle ( $^\circ$ )

$\gamma$  - Liquid surface tension (mN/m)

$\lambda$  - Baker-Scott flow regime parameter

$\mu_G$  - Gas absolute (or dynamic) viscosity (Pa-s)

$\mu_L$  - Liquid absolute (or dynamic) viscosity (Pa-s)

$\nu_L$  - Liquid kinematic viscosity ( $m^2/s$ )

$\psi$  - Baker-Scott flow regime parameter

$\rho_e$  - Density of entrained fluid ( $kg/m^3$ )

$\rho_d$  - Drop density ( $kg/m^3$ )

$\rho_g$  - Ambient gas density ( $kg/m^3$ )

$\rho_A$  - Atomizing air density ( $kg/m^3$ )

$\rho_G$  - Atomizing gas density ( $kg/m^3$ )

$\rho_L$  - Liquid density ( $kg/m^3$ )

$\tau_d$  - Drop (or particle) time scale (s)

$\tau_f$  - Fluid time scale (s)

## LIST OF ABBREVIATIONS

ALR - Air-to-liquid ratio (by mass)

ADSA-P - Axi-symmetric Drop Shape Analysis-Profile

ASHRAE - American Society of Heating, Refrigeration and Air-conditioning Engineers

CC – Correlation Coefficient

DR –Density Ratio between atomizing gas and liquid

FC – Fluid Coker

Fr – Froude Number

FS-1.0 – Full-Scale nozzle currently used in the fluid coker

FS-1.5 - Full-Scale nozzle with 1.5 times the dimensions of FS-1.0

GLR - Gas-to-liquid ratio (by mass)

HVAC - Heating, Ventilation and Air-conditioning

MW – Mass-weighted

NW – Number-weighted

Oh - Ohnesorge Number

PCA - Principle Component Analysis

PD – Positive Displacement

PDA - Particle Dynamics Analyzer

Re – Reynolds Number

RPM – Revolutions per Minute

SCFM – Standard Cubic Feet per Minute

SMD (or  $D_{32}$ ) Sauter Mean Diameter ( $\mu\text{m}$ )

$SMD_{gb}$  – Global SMD ( $\mu\text{m}$ )

SMD<sub>i</sub> – SMD at ith measurement point (μm)

SNO - Solvent Neutral Oil

SR – Slip Ratio

SS-1.0 - Small-Scale nozzle used for tests

SS-1.25 - Small-Scale nozzle with 1.25 times the dimensions of SS-1.0

SS-1.3 - Small-Scale nozzle used for tests with 1.3 times the dimensions of SS-1.0

SS-1.35 - Small-Scale nozzle with 1.35 times the dimensions of SS-1.0

St - Stokes number

T & D - Taitel and Dukler

USGPM – U.S. Gallons per minute

We – Weber Number

2D – Two dimensional

3D – Three dimensional

# CHAPTER 1

## INTRODUCTION

Processes involving the application of gas-liquid sprays can be found in aircraft, marine and industrial gas turbine combustors, incinerators, industrial furnaces and boilers, and internal combustion (IC) engines. These applications require breakup (or atomization) of the bulk liquid (i.e. fuel) with assistance from the gas, to produce small drops with high surface area-to-volume ratio in the combustion zone. This increases fluid mixing and evaporation resulting in more complete fuel combustion with reduction in soot and unburnt fuel emission. Understanding of atomization for such nozzles is also important for other chemical reactions, such as cracking of heavy oil.

### 1.1 The Fluid Coker

In the petroleum industry one application of two-phase (gas-liquid) sprays is in a fluid coker (FC), shown in Figure 1.1, used in upgrading bitumen to synthetic crude oil. In the FC, steam and bitumen at 350°C are premixed to form a two-phase mixture, and fed through sets of nozzles, with typical throughput of 47 USGPM ( $3 \times 10^{-3} \text{ m}^3/\text{s}$ ) of bitumen, steam-to-bitumen ratio by mass  $\sim 1\%$ , and mixing pressure of 240 psig (1756 kPa) [1<sup>a</sup>, b]. The nozzles atomize the bitumen into fine drops, which are injected into the FC reactor, where they come in contact with steam-fluidized bed of coke at 540°C and nominal size of 170  $\mu\text{m}$  [2]. A desired bitumen drop size in contact with a given coke particle is one with the same nominal diameter as the coke particle. This ensures that the coke is adequately and sufficiently coated with a thin layer of bitumen. The presence of the

higher temperature coke particles results in thermal cracking (or breakdown) of the high molecular weight bitumen droplets into lighter refineable hydrocarbon by-products. The by-products such as naphtha, kerosene distillates and gas oils rise to the top of the FC reactor, where they are separated from other by-products of the coking reaction and coke particles.

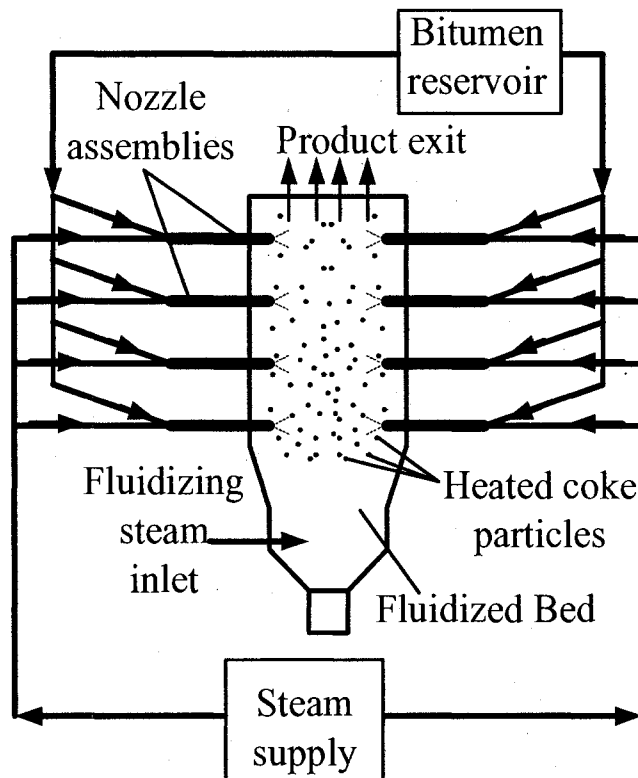


Figure 1.1 - Schematic of processes in a Fluid Coker (FC)

Typical ambient pressure in the fluid coker is 30 psig with fluidizing steam velocity of 1.8 m/s [1°]. Suspended coke particles initially travel vertically upwards with a velocity of ~ 0.6 m/s [1°] at the centre of the coker to the top of the fluid bed, and fall under gravity at the coker walls. This continuous recirculatory motion results in a region with

the lowest void fraction (i.e. gas volume fraction) in the coker is  $\sim 45\%$ , which occurs within 914 mm [1<sup>d</sup>] of the coker wall. This region is termed the annulus and is characterized by coke particles falling under gravity. The distance beyond the annulus up to the centre of the coker is termed the core and can have a void fraction up to  $\sim 89\%$  [1<sup>e</sup>]. The nozzle protrusion into the coker is about 762 mm [1<sup>e</sup>]. Therefore, the steam-bitumen jet penetrates a dense layer of coke about 152 mm thick in the annulus region before reaching the coke particles travelling vertically upwards in the less densely packed core region. A schematic of the jet-bed interaction is presented in Figure 1.2.

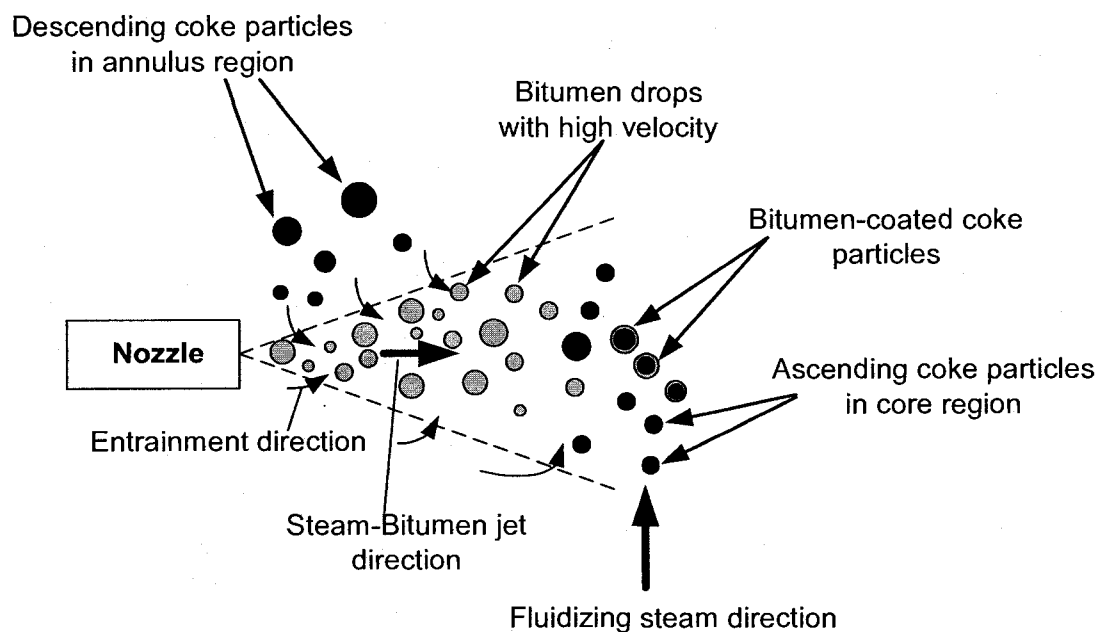


Figure 1.2 - Schematic of the jet-bed interaction in a Fluid Coker (FC)

The smaller descending coke particles are entrained by the steam-bitumen jet and can be coated by the bitumen drops before they are reintroduced into the core region by the high velocity jet. The larger descending coke particles are deflected from their original



trajectory but continue to fall to the lower sections of the coker. The bitumen drops that reach the core region also coat the ascending coke particles to produce the lighter molecular weight hydrocarbon vapours.

Increased product yield is achieved from effective thermal cracking, which in turn depends on spray penetration and spread, as well as the size of the bitumen drops among other factors. For a spray penetration and spread from a given nozzle, the liquid (i.e. bitumen) drop size is influenced by its physical properties such as surface tension and viscosity [3<sup>a</sup>] at the operating temperature and flow conditions. Due to inability of measurement instruments to access the interior of the FC because of high reactor temperatures and densely packed coke environment, in general, it is not possible to determine the influence of bitumen surface tension and viscosity on the mean drop size in the field. Furthermore, it is not cost-effective to carry out drop size measurements using a full-scale nozzle at commercial operating conditions. Hence the atomization behaviour of the nozzles in the FC for various feed bitumen properties is currently unknown, leading to inability to ascertain effective spraying of the bitumen feed for optimization of the product yield or design of next generation of nozzles for forthcoming plants.

Small-scale laboratory tests provide inexpensive and easily accessible methods of obtaining drop size information. Data from these laboratory tests can be used to study atomization behaviour of various controlled process conditions. Jermy et al. [4] have demonstrated the use of small-scale test rigs to study full-scale gas-liquid injector spray behaviour. In their study an attempt was made to conserve important dimensionless

parameters such as drop *Reynolds number*, *Weber number* and *Stokes number* relevant to the gas-liquid spray. Since it was not possible to conserve these dimensionless parameters Jermy et al. [4] developed an error function method that represented a suitable compromise between the dimensionless quantities in the small and full-scale processes. Heskestad [5] has performed small-scale spray studies for fire protection required for prior final selection and performance evaluation of nozzle and sprays in a full-scale process. In their work, the water flow rates required for the extinction of heat released from methane gas at a given distance of the nozzle from the heat source was investigated. This was performed by maintaining a 10:1 geometric ratio between the three nozzles tested and conserving drop size scaling from sprays produced by the test nozzles. Hence from references [4] and [5], results from small-scale atomization tests can be used to understand and implement methods for understanding full-scale process conditions, and nozzle designs. In the current study the small-scale tests will aid to ensure effective spraying that could lead to increase in product yield, in future.

## **1.2 Original Contributions in Atomization Study**

Several atomization studies have been performed in literature to determine the influence of liquid viscosity, surface tension and nozzle exit diameter on mean drop size. These studies have aided in developing semi-empirical correlations or models for the classes of nozzles tested. For example, Elkotb [6] and Yamane et al. [7] have studied the atomization behaviour of single-phase atomizers specific to diesel injectors and developed corresponding drop size correlations with fluid properties and atomizer geometry. For two-phase atomizers, e.g. twin-fluid atomizers, Elkotb [8], Rizkalla and

Lefebvre [9], Lefebvre [10], El Shanawany and Lefebvre [11] have also presented mean drop size correlations, which distinctly highlight the importance of fluid properties, flow conditions and nozzle geometry. The latter studies pertain to nozzles used in gas turbines. In more recent years Buckner and Sojka [12], Lund et al. [13] and Santangelo and Sojka [14] have performed studies on other two-phase nozzles such as effervescent atomizers. In all the studies, the goal was to determine the influence of fluid properties on atomization. From the above references it is evident that the atomization study for different nozzle designs and classes is a very important subject.

Although different classes of nozzles for gas-liquid flows exist such as twin-fluid nozzles and effervescent nozzles, the typical nozzles currently used in FCs for bitumen upgrading do not belong specifically to any of the nozzle classes mentioned. From the cited literature above it is evident that atomization studies are required for each particular class or design of nozzles. As such, the atomization characteristics of FC nozzles using various liquid properties are likely to behave differently from the other classes of gas-liquid nozzles. To the best of the author's knowledge there has been no study on the effects of liquid properties and nozzle size on the atomization behaviour of FC nozzles. This is the main motivation of the current work. This thesis utilized two-phase dynamic similarity to establish the operating flow conditions from the full-scale to small-scale nozzle, and the maximum geometrically similar nozzle scale-up size used during testing. This thesis is the first for two-phase nozzles that has examined the profile of the spray to establish a concept of a representative (or global) drop size characteristic of a spray based on area and liquid volume flux. This is in contrast to the use of centerline drop size to

characterize sprays, which is common in literature related to this type of study. Finally, the concept of a representative (or global) drop size within the spray was also introduced to make drop size comparisons in the different sprays, and to develop a drop size correlation for the two-phase nozzles used in this study.

### **1.3 Thesis Scope and Objectives**

The first and second objectives of this study are to determine the effects of viscosity and surface tension, respectively, on mean drop size in sprays produced from a typical one-quarter scale FC nozzle at room temperature. The third objective is to verify the effects of nozzle size on mean drop size. These three objectives will be based on comparing the differences in drop sizes due to the physical properties mentioned. The final objective is to establish an empirical relationship for the mean drop size in the spray as a function of nozzle size, viscosity, surface tension and flow conditions. To achieve the above objectives, a suitable experimental set-up was designed and implemented. The spray was discharged into still ambient air with 100% void fraction. The ambient laboratory void fraction was not identical to that in the fluid coker since no solid particles were present to interact with the spray. However, laboratory conditions near the nozzle were most comparable to jet behaviour prior to contact between drops and solids in the fluid coker, in high void fraction regions (89%), which is of the order of 100%. The ambient temperature of the laboratory was also not the same as in the fluid coker. However, the temperature dependent properties of the fluids, for example liquid viscosity density were within range of those in the fluid coker. This was done to achieve a level of transferability of results from laboratory conditions to those in the fluid coker. In addition

to the above objectives, the drop size measurements were performed across the entire spray cross-section instead of the central spray axis, which is common in previous studies in literature ([12], [13], [14]). The flow conditions studied have a gas-to-liquid ratio by mass (*GLR*) of 1%, which corresponds to the *GLR* for the steam-bitumen system in the FC. It is intended that the results from this small-scale nozzle study could be applied to the full-scale FC nozzles to better understand their operating performance.

The remainder of this thesis is divided as follows: Chapter 2 briefly discusses the common atomizers in literature and their atomization characteristics in order to allow for comparison with results from this study. Chapter 3 presents the equipment used in this study and their calibration results. Chapter 4 presents the design of a feasible larger nozzle to be used for studying the effects of nozzle size on mean drop size. The design methodology for effective removal of mists produced from nozzle sprays is also presented in Chapter 4. The experimental procedure and data analysis techniques are presented in Chapter 5. The test results are presented in two Chapters. The velocity data is Chapter 6, whereas the drop size data are discussed in Chapter 7. Finally, the conclusions and recommendations for continued work on these nozzles are mentioned in Chapter 8.

## CHAPTER 2

### LITERATURE - ATOMIZERS AND ATOMIZATION PRINCIPLES

Atomization is the disintegration of bulk liquid into drops [3<sup>b</sup>], which is accomplished using an atomizer (or nozzle). From Nasr et al. [15<sup>a</sup>], the Sauter Mean Diameter (*SMD* or  $D_{32}$ ) is the characteristic drop size used in atomization studies, and is defined as the ratio of the total volume of drops to the total surface area of drops in the spray. The *SMD* is defined mathematically in Eqn. (2.1).

$$SMD \text{ (or } D_{32}) = \frac{\sum_{i=1}^N D_i^3}{\sum_{i=1}^N D_i^2} \quad (2.1)$$

In Eqn. (2.1),  $D_i$  and  $N$  denote the diameter of the  $i$ th drop and total number of drops, respectively, at a point in the spray. Liu [16<sup>a</sup>] stated that the *SMD* is used as characteristic atomization diameter because in combustion processes, where fuel atomization is important, the *SMD* properly indicates the fineness or atomization quality of a spray.

It may be ascertained if the *SMD* is the representative diameter for atomized bitumen drops required in coating coke particles in the FC. From Chan et al. [1<sup>f</sup>], the energy required to form bitumen drops is equal to the surface energy ( $\gamma \sum_{i=1}^N \pi D_i^2$ ), where  $\gamma$  denotes the surface tension of the liquid. From Liu [16<sup>b</sup>], the surface energy per unit mass of liquid is a measure of the energy requirement for atomizing the liquid. In any given unit

time, mass of atomized liquid is given by  $\rho_L \frac{\pi}{6} \sum_{i=1}^N \pi D_i^3$ , where  $\rho_L$  denotes the liquid density. Hence the ratio of the surface energy to mass of liquid atomized per unit time can be written as given by  $(6\gamma/\rho_L)^* \left\{ \frac{\sum_{i=1}^N D_i^2}{\sum_{i=1}^N D_i^3} \right\}$ . Notice that the term in the curly brackets is the inverse of the expression for the *SMD* presented in Eqn. (2.1). Hence, it is considered that the *SMD* is the representative diameter for the atomized bitumen drops used in coating the solid coke particles in the FC. As such, the *SMD* will be used as the main measure of drop size in this study.

## 2.1 Classification of common atomizers

To better understand the operating features of the test nozzles in this study, it is best to highlight the characteristics of the atomizers (nozzles) presented in literature. A brief overview of typical conventional atomizer classifications is mentioned below.

### 2.1.1 Single-phase atomizers (Plain orifice pressure atomizers)

Plain orifice pressure atomizers are mainly single-phase atomizers in which the liquid is fed through a small orifice  $\sim 0.3$  mm at high pressures. Typical pressures are of the order  $10^2$  and  $10^5$  kPa for spray coating and combustion processes, respectively [15<sup>b</sup>]. The pressure imparted to the liquid is converted to kinetic energy, resulting in a high liquid velocity relative to the stagnant or slow-moving ambient gas environment. This high liquid relative velocity aids in the disintegration of the bulk liquid after exiting the orifice resulting in drop formation. A typical application of this type of atomizer is in fuel

injectors used in diesel engines, which are capable of producing drops of  $SMD \sim 20 \mu\text{m}$  [16<sup>c</sup>]. A sketch of this type of atomizer is shown in Figure 2.1.

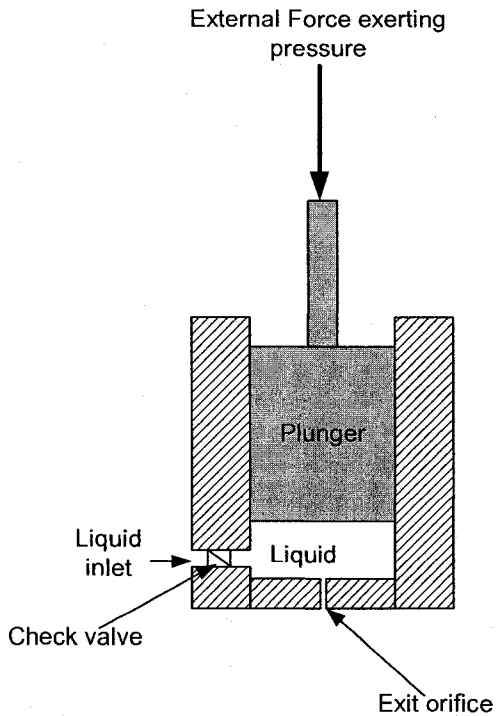


Figure 2.1: A typical configuration of atomization process in a plain orifice atomizer.

### 2.1.2 Twin-fluid atomizers

Twin-fluid atomizers are gas-liquid atomizers that utilize the kinetic energy of the gas stream to atomize the liquid. They are classified into air-assist and air-blast atomizers, and in either atomizer type fluid mixing may be done internally or externally with respect to the location of the exit orifice. Typical sketches of each atomizer are presented in Figures 2.2 and 2.3.



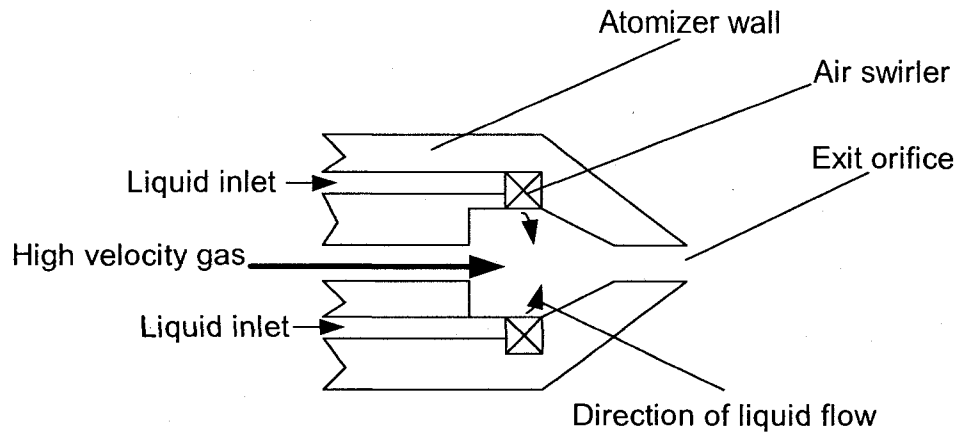


Figure 2.2: Schematic of a typical air-assist atomizer

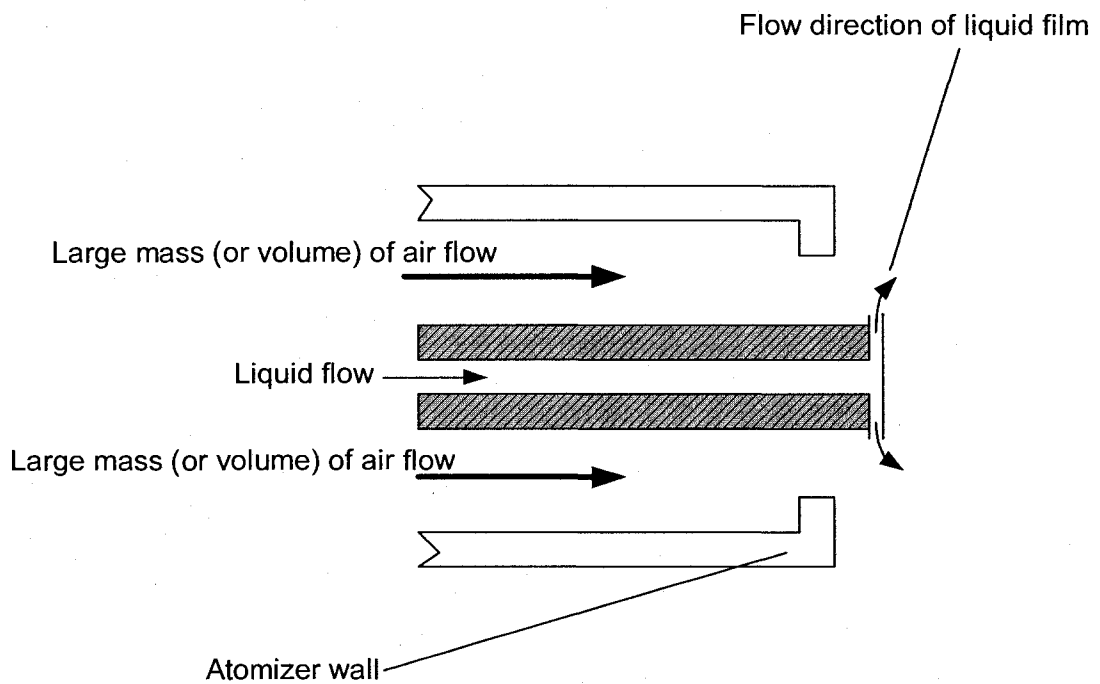


Figure 2.3: Schematic showing layout of air-blast (plain-jet) atomizer.

The main difference between the air-assist and the air-blast atomizers is in the magnitude of gas to liquid mass ratio and operating gas pressure/velocity [15<sup>o</sup>]. In air-assist atomizers, the liquid is atomized using a low gas-to-liquid ratio (by mass), *GLR* (less

than 100%), and high gas pressures (greater than 200 kPa). The associated high gas velocity (usually sonic) has sufficient kinetic energy to atomize the liquid with relatively low velocity. On the other hand, liquid atomization using air-blast atomizers is characterized by high *GLR* (greater than 100%) and low gas pressures (less than 200 kPa). Although the corresponding gas velocity is low (less than 150 m/s) in these atomizers, the large quantity of air utilized possesses the required kinetic energy to atomize the liquid stream.

One of the main advantages of twin-fluid atomizers over pressure (single-phase) atomizers is that the former yields similar drop sizes at much lower pressures of the liquid than the latter. Note that lower operating pressures translate to smaller equipment and operating costs relative to the pressure atomizers. However, a major drawback of air-assist atomizers is the need to provide and install an external supply line for the high-pressure gas in the component utilized, whereas in air-blast atomizers atomization is poor at low gas velocities [3<sup>c</sup>].

### **2.1.3 Effervescent atomizers**

Sovani et al. [17] have stated that effervescent atomizers are a type of gas-liquid atomizers that have been commonly employed in recent years. A typical layout of this atomizer is shown in Figure 2.4.

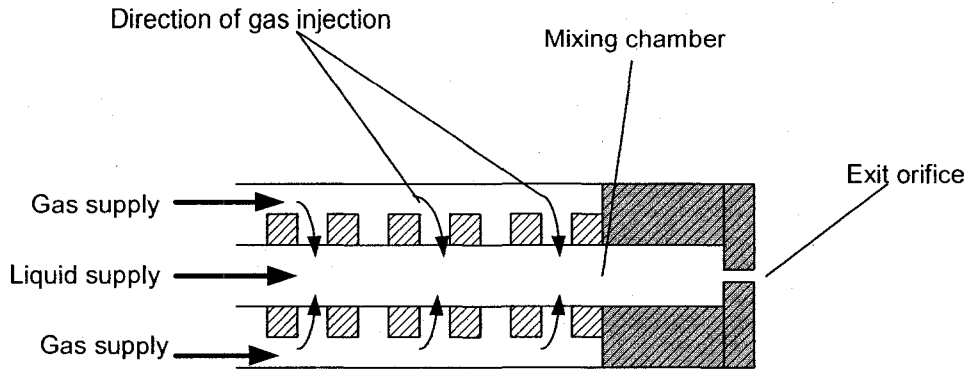


Figure 2.4: Schematic showing the cross-section of a typical effervescent atomizer.

From Figure 2.4, the bulk liquid in effervescent atomizers is supplied through the central tube section to flow to the atomizer exit. At the same time, gas supply pressure,  $P_G$ , at a slightly higher pressure than the liquid, is injected through pores surrounding the central tube section containing the bulk liquid. This section of the atomizer, where the two fluids come in contact is known as the mixing chamber, and precedes the atomizer exit orifice. The gas injected into the liquid stream forms bubbles resulting in a bubbly two-phase mixture, which flows towards the atomizer exit. At the exit, the gas bubbles expand rapidly resulting in disintegration of the liquid stream into drops. The advantages of effervescent nozzles over conventional pressure and twin-fluid atomizers, as stated by Sovani et al. [17], are good atomization even at low gas injection pressures and low gas flow rates. Good atomization can also be achieved at lower liquid injection pressures than those typically used in single-phase pressure atomization. Furthermore, effervescent atomizers can produce smaller drops at any given gas injection pressure than those produced by conventional twin-fluid atomization methods. Finally, effervescent atomizers are inexpensive and are easier to maintain compared to conventional pressure atomizers and twin-fluid atomizers. One of the main limitations of effervescent

atomizers, just as in any gas-liquid twin-fluid atomizers, is the need to have a separate gas supply at about the same pressure as the liquid. This requirement can be easily met since the gas flow rate required is small [17].

## 2.2 The fluid coker atomizer/nozzle

The typical layout showing fluid inlet and exit in the fluid coker (FC) nozzle whose atomization performance is to be studied is presented in Figure 2.5.

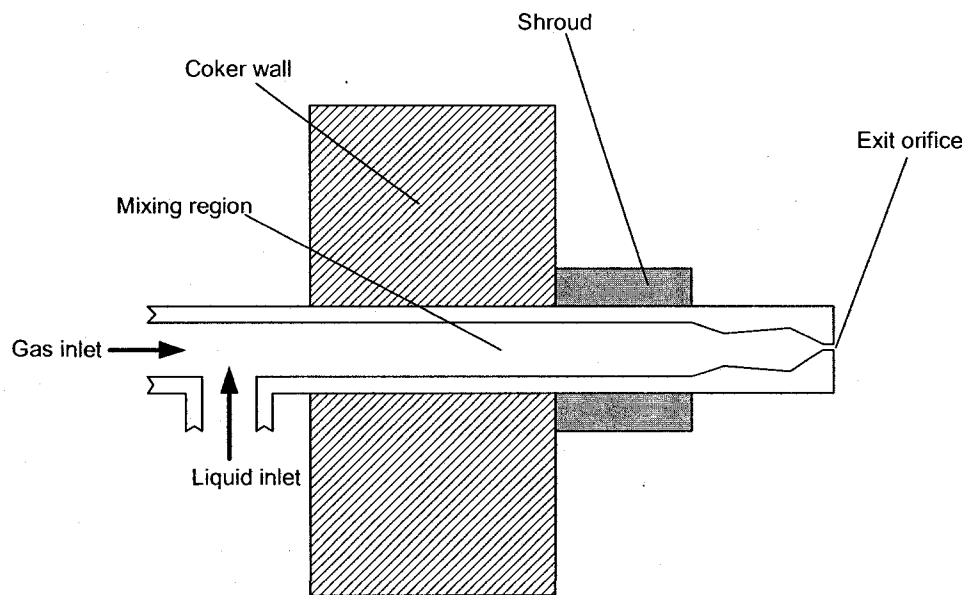


Figure 2.5: Schematic of gas and liquid mixing in a typical fluid coker nozzle. (Cross section shown).

In the FC nozzles, the gas and liquid supply come from separate lines with approximately equal internal diameter. The fluids are mixed at a junction, which could be a Tee or Wye fitting. The FC nozzles operate typically at a  $GLR \sim 1\%$  and mixing pressure  $\sim 1756$  kPa [1<sup>a</sup>, b] to form a two-phase mixture. The gas pressure, which is sufficient to prevent liquid

flow into the air-line, ensures fluid flow into the conduit or tube. The gas expands as the mixture flows through the tube, due to pressure losses, and undergoes further expansion through sections of the nozzle with variable cross-section. At the nozzle exit, the gas is often under-expanded, so it expands rapidly and disintegrates the bulk liquid into ligaments and droplets.

In the FC nozzles, the location at which the gas and liquid are mixed is far from the exit orifice due to a physical restriction inherent in the coker design. As shown in Figure 2.5 the mixing point is determined by the coker wall thickness and length of the shroud, which provides structural rigidity/stability to the nozzle assembly in the coker. The combined coker wall thickness and shroud length is approximately equal to the length of the conduit or tube through which the two-phase mixture flows. Secondly, due to strict maintenance requirements, it is generally not feasible to have the steam line near the exit orifice as in effervescent nozzles/atomizers.

From the description of FC nozzle operation above, it is evident they do not belong exclusively to any of the classes of gas-liquid nozzles mentioned in the previous sections. However, they have operating characteristics closely related to air-assist and effervescent atomizers. Air-assist atomizers typically operate using a small amount of gas mixed with the liquid (*GLR* less than 100%), gas pressure greater 200 kPa, and high gas velocity. Nozzles in the FC typically operate at *GLR* ~ 1% and fluid pressures ~ 1756 kPa, which is within the range in air-assist atomizers, but with gas velocity in the mixture approximately equal to the liquid velocity. Effervescent atomizers are characterized by

gas and liquid mixing through pores at some point upstream of the exit orifice, with the gas velocity almost equal to the liquid velocity. The same applies to FC nozzles except that the gas and liquid mixing is done using tees or wyes with equal internal diameters but much further upstream from the exit. Note that due to the longer conduit length in the FC nozzle system, flow conditions within the conduit can affect nozzle performance in comparison with effervescent atomizers.

Having described the operation of different classes of atomizers, it is imperative to outline the atomization characteristics of gas-liquid nozzles from literature. This is to aid in the plausible explanation of the atomization behaviour of FC nozzles from test results.

## **2.3 Liquid atomization and related parameters**

### **2.3.1 Variables affecting liquid atomization**

Studies on sprays produced by single-phase atomizers (e.g. plain orifice pressure atomizers) have shown that drop size and distribution within a spray depend on the following [3<sup>a</sup>]:

- Liquid surface tension ( $\gamma$ ), viscosity ( $\mu_L$ ) and density ( $\rho_L$ )
- Atomizer dimensions such as exit orifice length ( $L$ ) and diameter ( $D$ )
- Atomizer operating conditions such as liquid injection pressure differential ( $\Delta P_L$ ) across the nozzle (i.e. the pressure difference between the injection line pressure and gas pressure in the ambient that the jet is discharged)
- Liquid velocity,  $U_L$  ( $\sim (\Delta P_L / \rho_L)^{0.5}$ ) exiting the nozzle

- The ambient gas density  $\rho_g$ , absolute gas velocity in the ambient ( $U_g$ ) and relative velocity between the liquid and ambient gas ( $U_{gL}$ )
- Turbulence in the liquid flow

In twin-fluid atomizers, liquid atomization also depends on the liquid properties, atomizer dimension and ambient gas properties mentioned above. However, in addition, the atomizing gas density ( $\rho_G$ ), gas-to-liquid mass ratio ( $GLR$ ), turbulence in the mixture and relative velocity ( $U_{GL}$ ) between the atomizing gas and liquid at the nozzle exit also affect droplet formation [3<sup>c</sup>, 3<sup>d</sup>]. In effervescent atomizers, the atomizing gas injection pressure ( $P_G$ ),  $GLR$ , ambient gas density, design of atomizer internal geometry, liquid viscosity and surface tension affect the liquid atomization [17].

For the current type of nozzle used in the FC, studies by Kirpalani and McCracken [18] have examined nozzle performance of the horizontally-mounted, full-size (or commercial) nozzle using air and water. Their observations indicate that the  $SMD$  depends on flow characteristics within the nozzle, liquid mass flow rate and  $GLR$ . Tafreshi et al. [19] also studied the atomization quality of the nozzle used in [18] using air and water. They discovered that flow conditions/regimes in the pipe section of the nozzle affects the atomization quality. In [18, 19]  $SMD$  measurements were performed at a single point, which was at the edge or periphery of the spray. Copan et al. [20] performed quantitative atomization studies by testing a small-size nozzle, similar to the one in this study, using air and liquid nitrogen. Radial profiles of  $SMD$  were measured within the spray for the nozzles, which were oriented vertically downwards. Their results

showed that the *GLR* influences the magnitude of the *SMD*. Similar observations were made by Ariyapadi et al. [21] who also tested the same small-scale FC nozzle using air and water. The nozzle orientation was also vertically downwards, as in Copan et al. [20], and radial profiles of *SMD* were also presented. They [21] further observed that the *SMD* is also affected by the orientation/angle at which the gas and liquid enter the mixing point of the nozzle assembly.

The similarity between the studies in [20, 21] and this work is that radial profiles of *SMD* within the spray were presented. Note from the studies [18 – 21], the nozzles were tested using the same gas and liquid. Hence, it was not possible to study the effect of different liquid properties, such as viscosity or surface tension, on atomization for these types of FC nozzles. This is the main difference between the above study and this work, which is part of the objectives of the current study.

### **2.3.2 Forces and mechanisms in liquid atomization**

Greater understanding of the forces responsible for atomization is required to gain knowledge of the relevant dimensionless quantities associated with mean drop sizes produced from nozzle flows. Based on the variables affecting atomization, the corresponding relevant forces for drop formation can be established. The main forces responsible for liquid atomization are: hydrodynamic (or inertial), aerodynamic, viscous and surface tension forces [15<sup>c</sup>]. The surface tension forces tend to act on the liquid surface to exhibit a minimum surface energy, whereas the liquid viscous forces tend to oppose a change in liquid geometry. Hence these forces are consolidating or cohesive.



The hydrodynamic forces arise from turbulence in the issuing jet, whereas the aerodynamic forces are contributed by either the gas used to atomize the liquid or the ambient gas or both. These latter forces are disruptive forces, since they tend to act opposite to the consolidating or cohesive forces. The ratio of hydrodynamic (or inertial) forces to viscous forces is defined as the *Reynolds number* ( $Re = \rho_L U_c L_c / \mu_L$ ), whereas the ratio of aerodynamic forces to surface tension forces is defined as the *Weber number* ( $We = \rho_g U_c^2 L_c / \gamma$ ). The notations  $U_c$  and  $L_c$  denote characteristic fluid velocity and dimension in the nozzle, respectively. The subscripts “g” and “L” refer to the gas and liquid phases, respectively, in the expressions for the *Weber* and *Reynolds number*.

From basic atomization theory [16<sup>d</sup>] for single-phase nozzles, when a liquid jet is discharged from a nozzle into a gaseous ambient surrounding, there is interaction at the gas-liquid interface between the disruptive and cohesive forces mentioned above. At the liquid surface, the cohesive surface tension forces pull the liquid surface inwards towards the direction of the central axis of the bulk liquid, the hydrodynamic forces cause undulations/perturbations due to turbulence and the aerodynamic forces exert a drag/shearing effect, which is more pronounced due to the jet turbulence as presented by Shavit and Chigier [22]. These effects result in the creation of oscillations on the liquid surface. When the oscillations increase to a point such that disruptive forces exceed the consolidating forces, the bulk liquid disintegrates into drops. This first stage of drop formation is known as *primary atomization*. Hence this stage of atomization is mainly due to the action of internal forces e.g. turbulence, inertial effects, change in velocity profile (velocity profile relaxation or bursting effect) and/or surface tension as suggested

by McCarthy and Molloy [23] i.e. high  $Re$  is a major factor in atomization. Note that velocity profile relaxation is the change in the velocity profile of the jet downstream of the nozzle exit as a result of momentum transfer between transverse layers within the jet [23].

Atomization studies by Pilch and Erdman [24] on gas-liquid systems have shown that large drops formed during *primary atomization*, are unstable if they exceed a critical drop size. These large drops undergo further atomization to form more stable drop sizes, which are below the critical drop size. This stage of drop formation is known as *secondary atomization*. From [24], the susceptibility of a drop to undergo secondary atomization depends on two force ratios acting on the drop. First, the magnitude of the aerodynamic drag force, which for a given gas density, results from greater relative velocity induced at the liquid/air interface, compared to the opposing surface tension forces. Recall that the ratio of these two forces represents the *Weber number*. Secondly, the ratio of liquid internal viscous force to surface tension force on the drop, denoted by the *Ohnesorge number*,  $Oh (= \mu_L / \sqrt{\rho_L \gamma d})$ . The symbol,  $d$ , denotes the drop size. Studies by Hsiang and Faeth [25] and documented atomization review by Rissio [26] have shown that for low viscous drops or drops with small *Ohnesorge numbers*, i.e.  $Oh < 0.1$ , the onset of secondary atomization occurs at a minimum  $We \sim 12$ . Hence, drops with a *Weber number* above this critical value, for  $Oh < 0.1$ , will undergo further breakup to attain more stable drop sizes. For more viscous drops ( $Oh > 0.1$ ), secondary atomization becomes more difficult, because viscous forces inhibit drop deformation and breakup. Larger values of Weber number are required to initiate drop breakup and are therefore characterized by

longer total breakup times. [25, 26]. Brodkey [27] has provided a useful empirical correlation for the critical *Weber number* as a function of the *Ohnesorge number* given by:  $We = 12(1+1.077Oh^{1.6})$ . The correlation is for gas-liquid systems, valid for  $Oh < 5$  and  $We < 60$ , and has an accuracy of  $\pm 20\%$ .

Pioneer atomization studies by Lefebvre et al. [28], and Roesler and Lefebvre [29] have shown that another possible mechanism for liquid atomization exists when effervescent atomizers are utilized. Lefebvre et al. [28] postulated that the mechanism stems from ‘bubble explosion’ as the small bubbles contained/surrounded by the liquid exists the atomizer. As *GLR* increases, the number and/or size of the bubbles also increases. The numerous bubbles contained within the liquid coalesce at the nozzle exit to form a central gas core surrounded by a thin annular liquid sheath. Liquid atomization is enhanced because the gas ‘squeezes’ the liquid into ligaments at the nozzle exit, and then disintegrates the ligaments by ‘explosion’ downstream of the nozzle exit [28]. Roesler and Lefebvre [29] quantified this atomization mechanism in effervescent atomizers in terms of ‘bubble energy’. They [29] stated that jet break up occurs when the bubbles within the bulk liquid possess enough energy to overcome the surface tension forces that hold the liquid jet together. When the *GLR* and liquid injection pressure increase, the bubbles have enough energy to atomize the liquid through bubble explosion. However, the effect of bubble explosion is reduced when the *GLR* and liquid injection pressure are decreased. For such situations, the bubbles improve atomization by squeezing the liquid into thin shreds and ligaments at the nozzle exit [29].

From the studies in [28] and [29], it is evident that the liquid atomization mechanism in effervescent nozzles depends on the two-phase flow regime at the nozzle exit. Sovani et al. [17] have shown that the two-phase flow regimes at the nozzle exit may be bubbly, slug, or annular. Whalley [30] defines bubbly flow regime as when the gas exist as bubbles of approximately uniform sizes in the continuous liquid phase. Slug flow regime occurs when the bubbles coalesce and form large bullet-shaped bubbles, with small gas bubbles distributed throughout the liquid. In annular flow regime, the gas occupies the core and the liquid flows as a thin film along the duct walls. Effervescent atomizer studies by Chin and Lefebvre [31] have shown that the flow regime at the nozzle exit for vertically mounted atomizers is bubbly for  $GLR$  less than or equal to 2.5%, annular for  $GLR$  between 2.5% and 40%, and ‘dispersed’ for  $GLR$  greater than 40%. For horizontally-mounted nozzles, the flow regime is bubbly at  $GLR$  less than 2%, whereas at  $GLR$  greater than 2%, it is ‘dispersed’ prior to discharge into the ambient. Note that for both nozzle orientations, the dispersed flow regime implies that the liquid phase is discharged from nozzle exit as drops in air i.e. primary atomization occurs upstream of the nozzle exit [31].

The FC nozzles in this study are mounted horizontally (as shown in Figure 2.5) and operate at a  $GLR$  of 1%. From the literature in this section, *primary atomization* should occur when the jet is discharged into the ambient since the liquid is disintegrated by the rapid expansion of the gas as the two-phase mixture enters ambient conditions. Drop size measurements performed in this study are done in the regions of the spray where *secondary atomization* is ongoing or complete.

## 2.4 Summary of atomizer drop size correlations

This section presents a summary of drop size correlations derived from dimensional analysis (using the atomization forces mentioned above) and experiments for the common atomizer classifications mentioned in section 2.1. The main objective is to highlight the relationship between atomization variables and *SMD* for the atomizers presented.

### 2.4.1 Single-phase atomizers – Plain orifice pressure atomizers

There are many studies in which drop size correlations for plain orifice pressure atomizers have been presented based on experimental studies. Each correlation was derived from a separate experimental study because of differences in nozzle design and flow conditions. Only the more recent studies will be presented here, and subsequently a summary of the relationship between atomization variables and *SMD*.

Elkotb [6] used dimensionless analysis and experimental data to show the relationship between *SMD*, liquid properties, process variables and nozzle orifice diameters. For sprays produced by pintle type Direct Injection diesel injectors and discharged into ambient surroundings of temperature 20°C, the ensuing *SMD* correlation is:

$$SMD = 3.08 v_L^{0.385} \gamma^{0.737} \rho_L^{0.737} \rho_g^{0.06} \Delta P_L^{-0.54} \quad (2.2)$$

In Eqn. (2.2), the symbols have the same meaning as defined earlier in section 2.3.1. The units of  $\rho_g$ , and  $\Delta P_L$  are  $\text{kg/m}^3$  and Pa, respectively, whereas *SMD*,  $v_L$ ,  $\rho_L$  and  $\gamma$ , have

units of  $\mu\text{m}$ ,  $\text{m}^2/\text{s}$ ,  $\text{kg}/\text{m}^3$  and  $\text{N}/\text{m}$ , respectively. Equation (2.2) is valid within the ranges:  $0.81 \times 10^{-6} \leq \nu_L \leq 8.6 \times 10^{-6} \text{ m}^2/\text{s}$ ,  $20.4 \times 10^{-3} \leq \gamma \leq 27.5 \times 10^{-3} \text{ N}/\text{m}$ ,  $732 \leq \rho_L \leq 847 \text{ kg}/\text{m}^3$ ,  $1.20 \leq \rho_g \leq 8.20 \text{ kg}/\text{m}^3$ , and  $78 \times 10^5 \leq \Delta P_L \leq 200 \times 10^5 \text{ Pa}$ . Note that Elkotb [6] studied sprays produced from nozzle orifice diameters between 0.5 - 1.2 mm. However, an insignificant dependence of *SMD* on the nozzle orifice diameters was observed hence the resulting *SMD* correlation did not include a nozzle orifice parameter.

Yamane et al. [7] also used dimensionless analysis and experimental data to show the relationship between *SMD*, liquid properties, process variables and nozzle orifice diameters for non-evaporating unsteady dense sprays.

$$SMD = 47D \text{Re}_L^{-0.5} \left( \frac{\rho_g}{\rho_L} \right)^{0.26} \quad (2.3)$$

The units of  $\rho_g$ , and  $\Delta P_L$  are  $\text{kg}/\text{m}^3$  and  $\text{Pa}$ , respectively, whereas *SMD*,  $\nu_L$ ,  $\rho_L$  and  $\gamma$  have units of  $\mu\text{m}$ ,  $\text{m}^2/\text{s}$ ,  $\text{kg}/\text{m}^3$  and  $\text{N}/\text{m}$ , respectively. The range of validity of Equation (2.3) is  $\nu_L = 2.2 \times 10^{-6} \text{ m}^2/\text{s}$ ,  $\gamma = 27 \times 10^{-3} \text{ N}/\text{m}$ ,  $L/D = 4$ ,  $0.15 \leq D \leq 0.2 \text{ mm}$ ,  $9.84 \times 10^{-3} \leq \rho_g/\rho_L \leq 50.9 \times 10^{-3}$ , and  $2.6 \times 10^4 \leq \text{Re}_L \leq 4 \times 10^4$ .

From Eqns. (2.2) and (2.3), it is evident that the *SMD* is related to the atomization variables as follows:

- Increases with liquid kinematic viscosity ( $\nu_L$ ). This is because viscosity inhibits the change in liquid geometry and delays atomization.

- Increases with surface tension ( $\gamma$ ) because this variable prevents the formation of a new liquid surface.
- Decreases with increasing liquid injection pressure differential ( $\Delta P_L$ ), since the latter is the source of kinetic energy that increases the turbulence level in the jet and promotes jet break up.
- Increases with liquid density ( $\rho_L$ ), since an increase in liquid density results in a lower jet velocity (i.e.  $U_L \sim (\Delta P_L / \rho_L)^{0.5}$ ), which is responsible for creating the turbulence to enhance atomization.
- Increases with ambient gas density  $\rho_g$ . In [24] it is shown that an increase in  $\rho_g$ , should increase the aerodynamic drag force on the drops, thereby augmenting secondary atomization, and lead to a reduction in the maximum drop size. However, the increase in *SMD* with increase in  $\rho_g$  observed in [6] and [7] was attributed to a reduction in relative velocity between the ambient gas and drops, which resulted from the increased drag.
- May increase with exit orifice diameter up to  $\sim D^{0.5}$ . Knowledge of atomization theory from the previous Section indicates that increasing the diameter increases the thickness of the liquid jet, which has to undergo primary atomization. This results in larger ligaments produced from the atomization process resulting in bigger drop sizes, compared to a nozzle with smaller exit diameter. Note that Eqn. (2.2) (from [6]) did not contain a diameter term as in Eqn. (2.3) (from [7]). Although the drop sizes observed in [6] increased with nozzle diameter, there was no significant difference between the drop sizes. Hence,  $D$  was not included in Eqn. (2.2). These

variations in  $SMD$  with  $D$  highlight the effect of differences in nozzle design and flow conditions, which is applicable to plain orifice pressure atomizers.

#### 2.4.2 Twin-fluid atomizers

Drop size correlations in twin-fluid atomizers such as air-assist atomizers have been studied by Elkotb et al. [8]. In their work, air and kerosene were the gas and liquid phases, respectively, and the correlation obtained using dimensionless analysis is as follows:

$$SMD = 51D Re^{-0.39} We^{-0.18} GLR^{-0.29} \quad (2.4)$$

In Eqn (2.4),  $Re$  and  $We$  are based on the relative velocity between the gas and liquid streams,  $U_R (= U_G - U_L)$ . Substituting the expressions of  $Re$  and  $We$  into Eqn. (2.4) yields that the  $SMD$  is directly proportional to exit orifice diameter ( $D^{0.4}$ ), absolute viscosity of the liquid ( $\mu_L^{0.4}$ ) and surface tension ( $\gamma^{0.2}$ ). The reason for the relationship between these three variables and the  $SMD$  is the same as explained in the previous section for plain orifice pressure atomizers. Note the comparison between the indices (or exponents) of  $D$ , in Eqns. (2.3) and (2.4). Also compare the indices of  $\mu_L$ , and  $\gamma$  in Eqn. (2.4) with those in Eqns. (2.2) and (2.3). It shows that the exponents for  $\mu_L$  and  $D$  are  $\sim 0.5$  and  $\sim 0.5$ , respectively. However, the exponent for  $\gamma$  are  $\sim 0.2$  and  $\sim 0.7$  for the air-assist atomizer and plain orifice pressure atomizers, respectively. This latter relation suggests lesser dependence of the  $SMD$  on surface tension in sprays produced by air-assist atomizer compared to plain orifice pressure atomizers. The other result from substitution into



Eqn. (2.4) indicates that the *SMD* is inversely proportional to the relative velocity ( $U_R$ ) and *GLR*. Note that *SMD* is inversely proportional to  $U_R$  and *GLR* since increase in the latter variables results in higher gas kinetic energy. Recall that higher gas kinetic energy is required to attain favourable atomization (small drops) in twin-fluid atomizers.

The use of dimensionless analysis to obtain drop size correlations for air-blast atomizers such as prefilming air-blast atomizers have been presented by Rizkalla and Lefebvre [9], Lefebvre [10], El Shanawany and Lefebvre [11]. In the latter work, the atomizing gas was air, whereas the liquids were water, kerosene and specially prepared liquids of high viscosity. The spray data from these fluids were studied using three geometrically similar nozzles. The general form of *SMD* correlation was presented as:

$$\frac{SMD}{L_c} = \left[ A \left( \frac{\gamma}{\rho_A U_A^2 D_p} \right)^{0.6} \left( \frac{\rho_L}{\rho_A} \right)^{0.1} + B \left( \frac{\mu_L^2}{\gamma \rho_L D_p} \right)^{0.5} \right] \left( 1 + \frac{1}{ALR} \right) \quad (2.5)$$

In Eqn. (2.5), subscript ‘A’ denotes air, which is the gas phase, whereas  $D_p$  represents the diameter of the liquid prefilmer (section of an air-blast atomizer, which reduces the bulk liquid into thin films prior to contact and atomization by the gas phase). The characteristic length,  $L_c$  is typically the hydraulic mean diameter of the air duct at the atomizer exit plane. The constants  $A$  and  $B$  depend on atomizer design and evaluated from experimental data as 0.33 and 0.068, respectively [11]. Semaio et al. [32] also obtained satisfactory results using Eqn. (2.5) when compared to experimental results from similar prefilming airblast atomizers.

Similar to Eqn. (2.4) for air-assist atomizers, Eqn. (2.5) shows that the *SMD* increases with a characteristic diameter, surface tension ( $\gamma$ ) and absolute liquid viscosity ( $\mu_L$ ), but inversely proportional to *GLR* and air properties such as density and velocity. Note that these trends are also similar in air-assist atomizers for the same reasons outlined above.

Studies by El Shanawany and Lefebvre [11], which lead to the formulation of Eqn. (2.5) summarized their findings that for liquids with relatively low viscosities such as water and kerosene, the main parameters affecting *SMD* are surface tension, air velocity and air density. For liquids of high viscosity, the *SMD* depends more on the liquid properties, especially viscosity, and is less sensitive to variations in air properties. Similar observations were made Rizkalla and Lefebvre [9] and Lefebvre [10].

### **2.4.3 Effervescent atomizers**

Effervescent atomizers involve complex two-phase phenomena that are difficult to model. Hence, general models for these types of atomizers are rare [17]. Note that this further emphasizes the need to establish a relevant correlation for a specific nozzle type, design and flow conditions, which is characteristic of FC nozzles. The sections below provide the results from different relevant experimental studies on the effects of viscosity, surface tension and nozzle exit diameter on *SMD* in effervescent atomizers.

#### 2.4.3.1 Viscosity effects

Buckner and Sojka [12], Lund et al. [13], and Santangelo and Sojka [14] have reported the effect of liquid viscosity on *SMD* for measurements obtained along the central axis of the spray. In the study by Buckner and Sojka [12] the liquids used were mixtures of glycerine and water ( $400 < \mu_L < 968$  mPa-s and  $\gamma = 67$  mN/m,) with liquid mass flow rates between  $11$  and  $26 \times 10^{-3}$  kg/s. Typical liquid injection pressures varied between  $1,000$  and  $2,400$  kPa for  $5\% < GLR < 35\%$ . Buckner and Sojka [12] observed a maximum 6% difference in *SMD* at a given *GLR* and liquid injection pressure for the viscosity range studied. They [12] concluded that *SMD* was relatively independent of liquid viscosity. However, no clear discussion was presented to explain the observed variation of *SMD* with liquid viscosity.

Lund et al. [13] studied the effects of viscosity on *SMD* using glycerine-water mixtures and Solvent Neutral Oil (SNO)-100 and Benzoin Universal Calibration fluid in the range  $20 < \mu_L < 80$  mPa-s and  $\gamma = 30$  and  $67$  mN/m. In their work the typical flow conditions were  $1\% < GLR < 7\%$ , mixing chamber pressure between  $239$  and  $515$  kPa and mass flow rates below  $1.5 \times 10^{-3}$  kg/s. The maximum difference in *SMD* was 12% for the viscosity range studied. The final observation from this work was that *SMD* increased slightly with viscosity based on drop size data obtained at the centreline of the spray. They quoted similar observations as in Buckner and Sojka [12], but did not present any discussion to explain their findings. The slight dependence of *SMD* on viscosity observed in [12] and [13] is very different from the behaviour of single-phase and two-phase atomizers. As mentioned in previous sections, in the latter nozzles the *SMD* increases

with liquid viscosity (to a power from 0.4 to 1.0), since viscosity inhibits the change in geometry of the bulk liquid.

Santangelo and Sojka [14] used corn syrup, SNO-320 oil and corn/water mixtures to study the effects of viscosity on *SMD* for the fluid property range:  $112 < \mu_L < 820$  mPa-s and  $\gamma = 29$  and  $74$  mN/m. The liquid mass flow rate was maintained at  $5 \times 10^{-3}$  kg/s, with liquid pressure between 102 and 1088 kPa and  $2\% < GLR < 10\%$ . They observed that *SMD* increased by about 115% at the lowest *GLR*, whereas at the highest *GLR*, the *SMD* increased by 75%. The conclusion from this study was that *SMD* increased significantly with liquid viscosity. Note that this trend is similar to single-phase and twin-fluid atomizers mentioned in previous sections. The explanation for this trend between *SMD* and liquid viscosity was explained using bubble expansion. At the nozzle exit, the higher viscosity liquid (820 mPa-s) contains mainly single bubbles in the liquid core, whereas the lower viscosity liquids (112 and 412 mPa-s) contain multiple bubbles. The latter set of bubbles produce smaller drops compared to the former resulting in larger *SMDs* with increasing liquid viscosity.

#### **2.4.3.2 Surface Tension Effects**

Lund et al. [13] and Santangelo and Sojka [14] also studied the effect of surface tension on *SMD* at the spray axis for effervescent atomizers discharging into ambient air. Lund et al. [13] observed that *SMD* decreased significantly (between 14 and 23%) when surface tension increased from 30 to 67 mN/m. The decrease in *SMD* was found to increase with *GLR*. The decrease in *SMD* with increasing surface tension is contrary to general results

observed in sprays issuing from single-phase and twin-fluid atomizers mentioned in previous sections. From their observations, Lund et al. [13] postulated an *SMD* model shown in Eqn. (2.6a), which is based on *primary atomization* with negligible *secondary atomization*.

$$SMD = \left[ \frac{3\pi}{\sqrt{2}} d_{lig}^3 \left( 1 + \frac{3\mu_L}{\sqrt{\rho_L} d_{lig}} \right)^{\frac{1}{2}} \right]^{\frac{1}{3}} \quad (2.6a)$$

$$\frac{4(d_L^2 + d_L d_G)}{d_G^2} = \frac{SR}{GLR} \left( \frac{\rho_G}{\rho_L} \right) \quad (2.6b)$$

$$SR = \left( \frac{(\sqrt{\alpha})}{1 + 75(1 - \alpha)} \right)^{0.5} \sqrt{\left( \frac{\rho_L}{\rho_G} \right)} \quad (2.6c)$$

$$\alpha = \frac{1}{1 + \frac{SR}{GLR} \left( \frac{\rho_G}{\rho_L} \right)} \quad (2.6d)$$

In Eqn. (2.6a)  $d_{lig}$  is the ligament diameter. Lund et al. [13] derived Eqn. (2.6b) from gas and liquid continuity equation to relate the ligament diameter to  $d_L$ , the thickness of the liquid annulus that surrounds a bubble (with diameter  $d_G$ ) at the exit orifice. The notations  $SR$  and  $\alpha$  denote the slip ratio and void fraction, respectively. The slip ratio is defined as the ratio of gas to liquid velocity, whereas the void fraction is the ratio of cross-sectional area occupied by the gas to that of orifice area [30]. Note that Lund et al. [13] estimated  $\alpha$  iteratively using Eqns. (2.6c) and (2.6d).

The effervescent nozzle tested by Lund et al. [13] was mounted vertically. Thus the *SMD* model in Eqn. (2.6) is restricted to annular flow regimes at the nozzle exit, where the atomizing gas occupies a large portion of the core and is surrounded by a liquid annulus/sheath [30]. Recall from Section 2.3.2 that annular flow regime occurs at the nozzle exit for typical vertically mounted effervescent atomizers for *GLR* between 2.5 and 40% [31]. Lund et al. [13] used *GLR* between 1% and 7%, which mostly falls within range of annular flow at the atomizer exit stated in [31].

Comparison of Eqn. (2.6) with experimental data at *GLR* < 2% overestimated *SMD* by about 25%, whereas for *GLR* > 4% it predicted *SMD* within 5% of the experimental data. The increase in *SMD* with decreasing surface tension in the effervescent atomizer study above is different from observations in single-phase and twin-fluid atomizers discussed in previous sections. In the latter atomizers, increase in surface tension results in bigger drop sizes, since surface tension forces tend to oppose deformation forces responsible for atomization.

Santangelo and Sojka [14] observed a maximum of 12% decrease in *SMD* (occurred at *GLR* = 2%) when the surface tension was increased from 29 to 74 mN/m. The conclusion was *SMD* increased slightly with a decrease in surface tension. The disparity between their [14] observations and the significant variation of *SMD* with surface tension observed by Lund et al. [13] was attributed to differences in breakup mechanisms. The first step in drop formation in effervescent atomizers is the breakup of a liquid sheet or sheath into ligaments by single-bubble expansion. The *SMD* formed in this step is known

to be directly proportional to surface tension as stated by Squire [33]. The second step is the further breakup of the ligaments formed into drops due to the action of aerodynamically induced shear and disturbances. The *SMD* produced from this mechanism is inversely proportional to the surface tension, which is predicted from the Weber theory [34]. Santangelo and Sojka [14] concluded that the first step of drop formation was more prevalent in their work since there was less dependence of *SMD* on surface tension. Note that this trend in *SMD* variation with surface tension is also different from single-phase and twin fluid atomizers for the same reason stated in the previous paragraph.

#### **2.4.3.3 Geometry Effects**

Lefebvre et al. [28], and Roesler and Lefebvre [29] have studied the effect of exit orifice diameter on *SMD* in effervescent atomizers discharging into ambient air. Lefebvre et al. [28] used water and nitrogen as the liquid and gas phases, respectively. Tests were performed for liquid injection pressures 34.5 kPa, 138 kPa and 345 kPa, liquid flow rates up to  $\sim 1.5 \times 10^{-3}$  kg/s, and gas-to-liquid ratios,  $0.2\% \leq GLR \leq 22\%$ . The nozzle exit orifice diameter was varied by inserting three different screw caps of diameters 0.8, 1.6 and 2.4 mm, and drop size measurements were taken at the spray centreline. Lefebvre et al. [28] observed that for  $GLR \leq 1\%$ , the smallest nozzle exit diameter produced the smallest drop sizes, but drop sizes were about the same at higher *GLR*. Analysis of their data (for  $GLR \leq 1\%$ ) showed that the maximum difference in *SMD* between the smallest and largest exit orifice diameters was about 90% at 138 kPa and *GLR* of 0.2%. No specific explanation for this trend in *SMD* was provided in [28]. However, from our

knowledge of atomizers in previous sections, operating an effervescent atomizer at very low  $GLR \sim 0.2\%$  increases its atomization characteristics towards that of a single-phase atomizer. This results in the effervescent atomizer producing bigger  $SMD$  for larger nozzle exit diameters, which is similar to the atomization characteristics of a typical single-phase atomizer. Lefebvre et al. [28] concluded that except for the lowest  $GLR$ , where the smallest nozzle exit diameter yields the smallest drop sizes, the  $SMD$  was largely insensitive to the exit orifice diameter, when operating at the same  $GLR$ . Note that analysis of data for  $GLR > 1\%$  in [28], indicated there was a 12% maximum difference in  $SMD$  between the largest and smallest exit orifice diameter at a given  $GLR$  and liquid injection pressure.

Roesler and Lefebvre [29] studied the influence of nozzle exit diameter on  $SMD$  using air and water at  $0.1\% \leq GLR \leq 5\%$ . The liquid injection pressures were between 173 kPa and 690 kPa, and the nozzle exit orifice diameters were also replaceable, with diameters of 1.0, 1.5 and 2.0 mm. They [29] observed that an increase in nozzle exit diameter had little effect on  $SMD$ . Analysis of their data showed an 11% maximum difference in  $SMD$  between the nozzle exit diameters tested, at a given  $GLR$  and liquid injection pressure.

From the studies in [28] and [29], and the comprehensive effervescent atomization review by Sovani et al. [17], the general conclusion is that  $SMD$  is largely independent of exit orifice diameter, for a given effervescent flow condition. The independence of  $SMD$  on nozzle exit diameter in typical effervescent atomizers differs from observations in single-phase and twin-fluid atomizers, which were discussed in previous sections. Recall



that the atomization mechanism in atomizers operating in the effervescent mode stems from bubble explosion just after the nozzle exit or bubble expansion at the nozzle exit, which squeezes the liquid into thin shreds and ligaments. The inherent energy in bubble explosion or expansion is typically a strong function of flow conditions such as *GLR*, liquid injection pressure, and ambient pressure downstream of the atomizer exit [29]. For the same liquid injection pressure and *GLR* in nozzles with different exit orifices, the bubbles still possess sufficient energy to atomize the bulk liquid. Since this atomization energy does not depend on nozzle exit size, the variation of *SMD* with nozzle exit diameter is insignificant.

## **2.5 Literature summary and relation to FC nozzles**

A summary of the variation of *SMD* with liquid viscosity, surface tension and nozzle exit diameter from literature discussed above can be presented in Table 2.1. As mentioned in previous sections, the FC nozzle has common characteristics with the twin-fluid air-assist atomizer and the effervescent atomizer. Table 2.1 shows that for these two types of atomizers, there is no distinguished and universally accepted trend of the effects of viscosity, surface tension and exit diameter on *SMD*. This observation indicates this branch of science is dependent on atomizer design and flow conditions. Since the FC nozzles in this work have a unique geometric and hydraulic design, it is therefore imperative to ascertain specifically the effects of these fluid properties and nozzle parameters on their atomization performance for effective process optimization and plant performance.

Table 2.1: Literature summary of *SMD* variation with liquid viscosity, surface tension and exit orifice diameter

<b>Atomizer</b>	<b>Liquid viscosity, <math>\mu_L</math></b>	<b>Surface tension, <math>\gamma</math></b>	<b>Exit diameter, <math>D</math></b>
<b>Single-Phase</b>	<i>SMD</i> increases with $\mu_L$ (varies $\sim \mu_L^{0.4 \text{ to } 0.5}$ )	<i>SMD</i> increases with $\gamma$ (varies $\sim \gamma^{0.7}$ )	<i>SMD</i> increases with $D$ (varies $\sim D^{0.5}$ )
<b>Twin-fluid</b>	<i>SMD</i> increases with $\mu_L$ (varies $\sim \mu_L^{0.4 \text{ to } 1.0}$ )	<i>SMD</i> increases with $\gamma$ (varies $\sim \gamma^{0.2}$ )	<i>SMD</i> increases with $D$ (varies $\sim D^{0.5}$ )
<b>Effervescent</b>	<i>SMD</i> may increase by only 6 to 12%, or up to 115% with increase $\mu_L$ (i.e. varies $\sim \mu_L^{0.1 \text{ to } 0.4}$ )	<i>SMD</i> may decrease by 13 to 23% with increase in $\gamma$ (varies $\sim \gamma^{-0.1 \text{ to } -0.3}$ )	<i>SMD</i> increased by only 11 to 12% with increase in $D$ (i.e. varies $\sim D^{0.1 \text{ to } 0.2}$ )

# CHAPTER 3

## EQUIPMENT SPECIFICATION AND CALIBRATION

This Chapter briefly describes the nozzle, equipment selection process and specifications. Calibration was performed on the equipment to ascertain proper operation. The calibration results are presented in Appendix A1.

### 3.1 Nozzle Assembly

One of the small-scale nozzle assemblies used in this study is shown in Figure 3.1. For naming convenience, this small scale nozzle will be denoted SS-1.0, where SS implies 'Small-Scale'. The internal geometry of the nozzle head and nominal nozzle dimensions of SS-1.0 is shown in Figure 3.2.

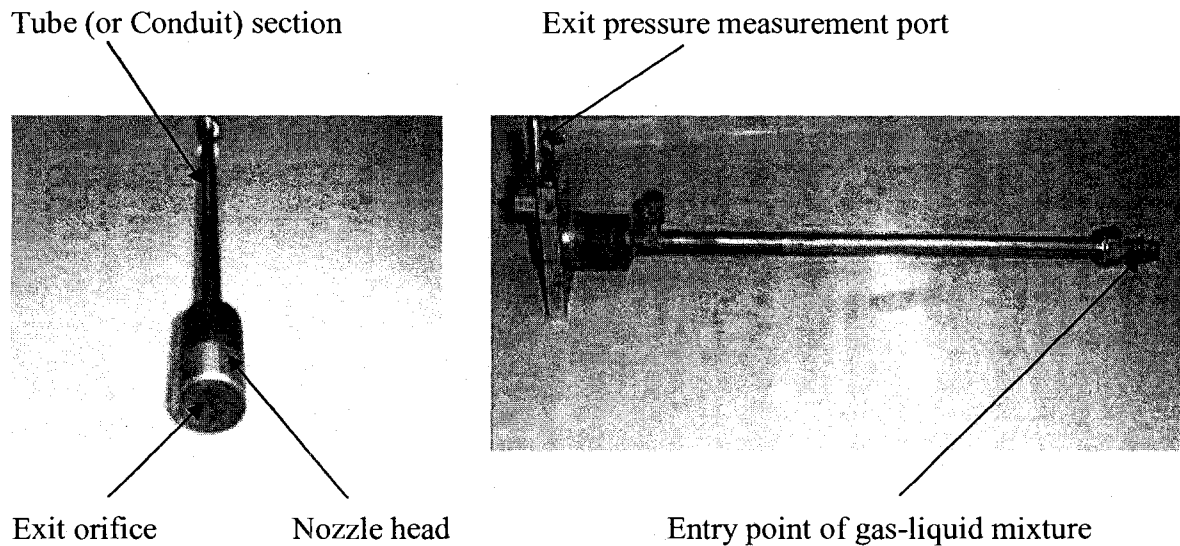


Figure 3.1 – Photograph of the quarter-scale nozzle assembly (SS-1.0).

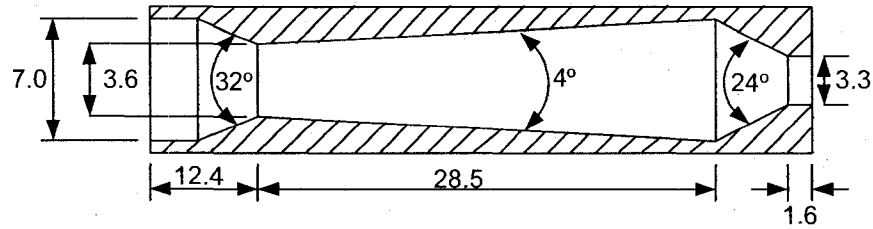


Figure 3.2 – Drawing showing nozzle geometry and nominal nozzle dimensions of the SS-1.0. (Dimensions are in millimetres)

The measured exit orifice diameter ( $D$ ) of the SS-1.0 is  $3.1 \times 10^{-3}$  m, whereas the corresponding tube (or conduit) length ( $L_i$ ) and internal diameter ( $D_i$ ) is  $368 \times 10^{-3}$  and  $5.2 \times 10^{-3}$  m, respectively. The nozzle is geometrically one-quarter scale of a patented full-scale design (US Patent # 6003789) employed in a fluid coker (FC) for bitumen/heavy oil upgrading. The nominal operating flow rates of the SS-1.0, using air and water, is  $9.5 \times 10^{-5}$  m<sup>3</sup>/s (1.5 USGPM), and 1% *GLR* at a 15°C (288 K) [1]. This nominal operating flow rate is obtained using dimensional analysis as illustrated in the next paragraph. The other nozzle used in this study had a geometry scale of 1.3 times the size of the SS-1.0. This nozzle was designed to study the effect of nozzle geometry size on atomization. The design procedures are discussed in Chapter 4.

To establish the nominal flow conditions in the SS-1.0 nozzle that corresponds to the full-scale nozzle, dynamic similarity was employed. Dynamic similarity in two-phase (gas-liquid) flow, as presented by Chesters [35], has been demonstrated experimentally by Geraets [36] in estimating pressure drop along two-phase (gas-liquid) horizontal flows with an uncertainty of  $\pm 5\%$ . Hurlbert et al. [37] also applied similar gas-liquid dynamic

similarity in predicting pressure drops along horizontal tubes. The requirements include geometrical similarity and the conservation of the following dimensionless groups:

$$\frac{\rho_G}{\rho_L} \quad \frac{Q_G}{Q_L} \quad \frac{\mu_G}{\mu_L} \quad \frac{\rho_L U_c L_c}{\mu_L} \quad \frac{U_c^2}{gL_c} \quad \frac{\rho_L U_c^2 L_c}{\gamma} \quad \frac{P_G}{\rho_L U_c^2} \quad (3.1)$$

All variables in the expression above have their usual meaning as already defined. The notations  $Q_G$  and  $Q_L$  represent the gas and liquid volume flow rates, respectively. The symbols  $g$ ,  $U_c$  and  $L_c$  denote the acceleration due to gravity, characteristic velocity and length, respectively. Geraets [36] chose the liquid superficial velocity (liquid flow rate divided by cross-sectional area) as  $U_c$  and tube diameter as  $L_c$ . Using the ideal gas equation and combining  $(Q_G/Q_L)$ , and  $(\rho_G/\rho_L)$ , Equation (3.1) can be finally re-written as:

$$\frac{P_G}{R_G T_{abs} \rho_L}, \frac{m_G}{m_L}, \frac{\mu_G}{\mu_L}, Re, Fr, We, Eu \quad (3.2)$$

In Eqn. (3.2), the first term is the density ratio, where  $P_G$  is the absolute pressure of the gas phase at the region of interest, which is the mixing point at the inlet to the nozzle assembly. The symbols  $R_G$  and  $T_{abs}$  denote the characteristic gas constant and absolute temperature of the gas, respectively. Note that the second and third terms are the *GLR* and viscosity ratios, respectively. The last four terms are the superficial liquid *Reynolds number* (*Re*), *Froude number* (*Fr*), *Weber number* (*We*), and *Euler Number* (*Eu*), respectively. Note from Geraets [36] that in most cases matching the required terms in the conduit may not be practically feasible. Hence, similar to standard dimensional

analysis, restriction on some of the quantities may be relaxed depending on knowledge of the dominant forces in the system as stated by Douglas et al. [38]. The viscosity ratio is negligible since for most fluids  $\mu_G \ll \mu_L$ . The *Euler Number* is negligible in horizontal gas-liquid flows and for constant  $(Q_G/Q_L)$ , *Fr* and density ratio are the most important parameters that can affect gas-liquid flow regimes at the region of interest [36]. This implies that the *GLR* is an important parameter that must be matched for dynamic similarity in gas-liquid flows. Finally, since *Fr* is an important parameter to match in the conduit, the *Re* and *We* restrictions can be relaxed.

To apply the above dimensional analysis criteria, the operating condition of the commercial coker nozzle presented in Table 3.1 are used. For air and water at 15°C in the SS-1.0, the *GLR* must be the same as that of the full-scale steam-bitumen system (i.e. 1%), as required by dimensional analysis. Since the SS-1.0 is geometrically one-quarter scale of the full-scale nozzle, for equal superficial liquid *Froude Number* as in the full-scale nozzle, the corresponding liquid flow rate in the SS-1.0 is 1.5 USGPM ( $9.5 \times 10^{-5}$  m<sup>3</sup>/s). Note that for equal density ratios in both systems, the mixing pressure at the inlet to the SS-1.0 should correspond to 576 kPa (70 psig). However, the measured fluid mixing pressure is ~ 507 kPa (60 psig), which is fairly close to the value from dimensional analysis. The superficial liquid *Reynolds Numbers* are  $2.9 \times 10^4$  and  $2.0 \times 10^4$  for the full-scale and SS-1.0 nozzle, respectively. The corresponding superficial liquid *Weber Number* is  $7.2 \times 10^4$  and  $9 \times 10^2$ , for the full-scale and SS-1.0 nozzle, respectively.

Table 3.1 – Typical flow conditions and steam-bitumen properties of the commercial coker nozzle [1].

Liquid volume flow rate, $Q_L$ (USGPM)	47 ( $3 \times 10^{-3} \text{ m}^3/\text{s}$ )
$GLR$ (%)	1.0
Steam-Bitumen Mixing Pressure, $P_{mix}$ (psig)	240 (1756 kPa)
Temperature ( $^{\circ}\text{C}$ )	350 (623 K)
Characteristic Gas Constant of Steam, $R_{gas}$ (J/kgK)	461.4
Steam density, $\rho_G$ ( $\text{kg}/\text{m}^3$ )	6.08
Bitumen density $\rho_L$ ( $\text{kg}/\text{m}^3$ )	868
Steam absolute viscosity, $\mu_G$ ( $\times 10^{-5} \text{ kg}/\text{ms}$ )	2.227
Bitumen absolute viscosity, $\mu_L$ (kg/ms)	~ 0.001
Bitumen surface tension, $\gamma$ (N/m)	0.012

### 3.2 Test Liquids

From Chapter 2, liquid viscosity ( $\mu_L$ ) and surface tension ( $\gamma$ ) are physical properties that significantly affect liquid atomization. To achieve the goal of understanding the effect of  $\mu_L$  on  $SMD$ , it was imperative to use two liquids with significantly different  $\mu_L$ , but with far less variation in  $\gamma$ . Similarly, to study the effect of  $\gamma$  on  $SMD$ , one can use two liquids with significantly different  $\gamma$ , but with smaller variation in  $\mu_L$ . Water and canola oil were

the pure liquids chosen in this study because they have significantly different values of surface tension and viscosity. Furthermore, they were easily available and from safety considerations they are not easily flammable (Canola oil).

Pure liquids have a constant viscosity and surface tension at a given temperature. For flexibility in matching either physical property of water and canola oil, it was imperative to mix two liquids. Note that this method of varying liquid properties is common practice in atomization studies, e.g. in Buckner and Sojka [12] and Lund et al. [13]. It was decided to mix pure glycerine and water, since the surface tension of both liquids is close to one another. From White [39] the surface tension of pure glycerine and water is about 62 mN/m and 72 mN/m, respectively, at 20°C. From Przybylski [40] the viscosity of canola is about 71 mPa-s at 20°C. It is possible to obtain this viscosity by mixing the glycerine and water at a given mass ratio, since the viscosity of pure water and glycerine is 1mPa-s and 1000 mPa-s [39], respectively, at 20°C. The correct mass ratio was determined experimentally by measuring the physical properties of different glycerine-water mixtures.

### **3.3 Test Equipment**

Prior to purchasing the equipment to be used in the experiment, it was carefully considered that each had the capacity to, at least, supply  $9.5 \times 10^{-5} \text{ m}^3/\text{s}$  (1.5 USGPM) of water, at a 1% *GLR*. Secondly, it was required that the equipment be able to deliver more gas and liquid at higher pressures, in the event that such flow conditions are desired later



in the experiment. The set-up of the entire test rig is presented in Figure 3.3, whereas the equipment specifications are discussed in subsequent sections.

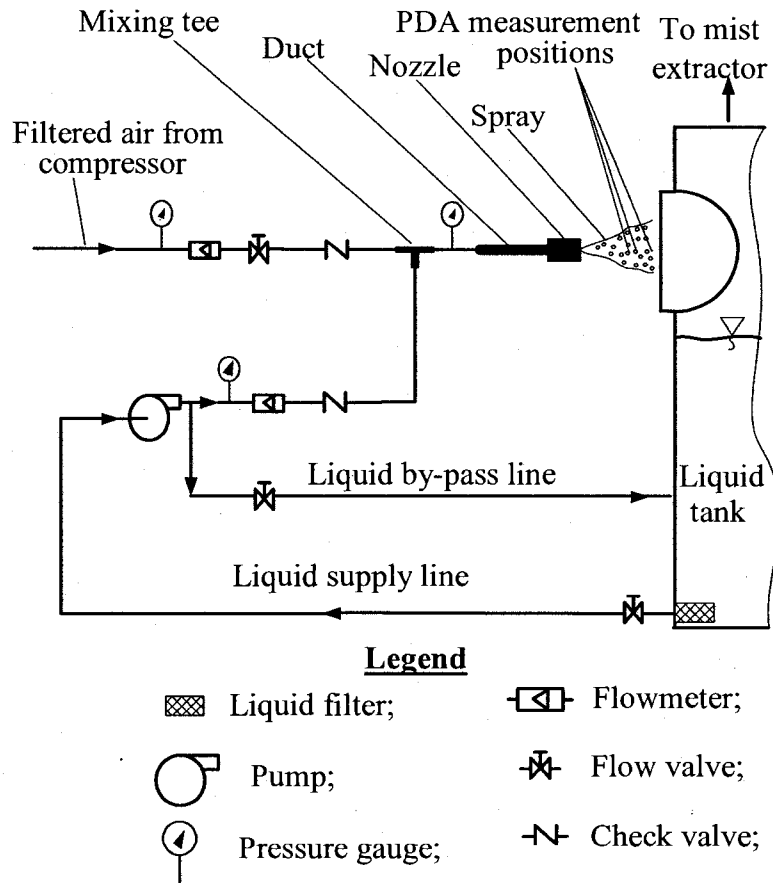


Figure 3.3 – Schematic showing layout of test equipment in the experimental set-up.

### Pump

The pump used in this study was a model 2539A (series 4) vane-type positive displacement (PD) pump from PROCON pumps. The pump was coupled to a 3-phase, 1.12kW (1.5 horsepower) NEMA motor, which provided the rotary motion required to drive the pump. The pump/motor speed was varied using a series 15J Inverter control

from BALDOR. Since viscous liquids were to be pumped, the motor power stated above was specified to ensure that the pump had sufficient power to transport these liquids. The photograph of the pump is shown in Figure 3.4.

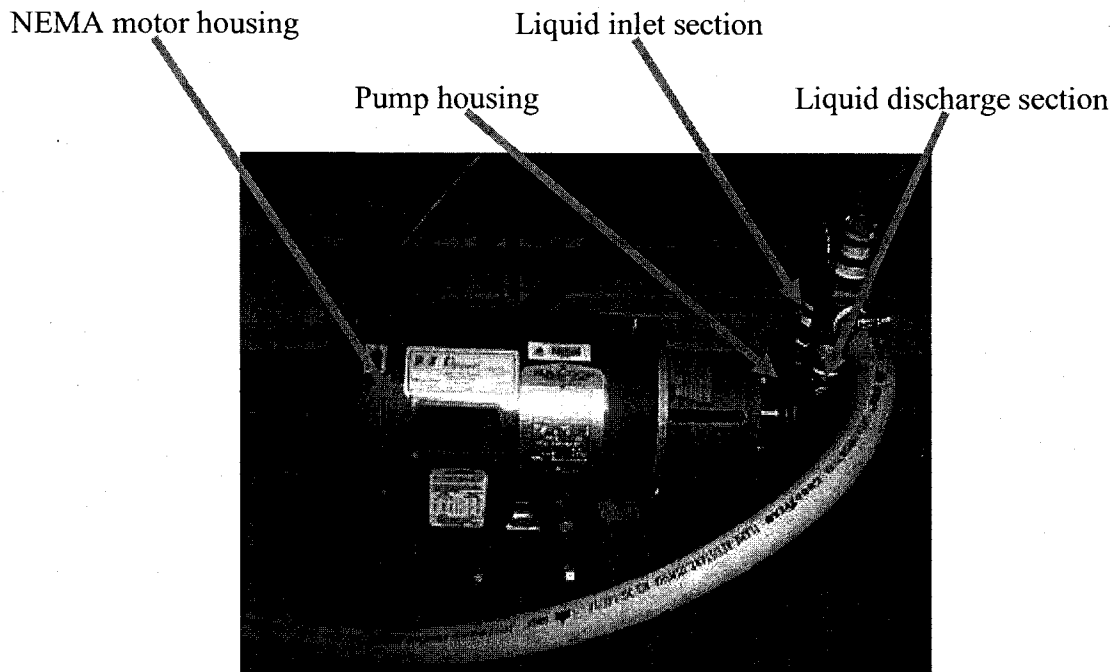


Figure 3.4 – Photograph of the positive displacement pump used in the experiment.

A PD pump was chosen over a centrifugal pump because the PD pump is able to operate at a higher efficiency when handling highly viscous liquids than a centrifugal pump, as presented by Parker [41]. Furthermore, fluids of large gas fractions or slurries can be transported without equipment degradation using PD pumps compared to centrifugal pumps [41]. This second reason enables use of the pump if transportation of slurries is required in future experiments. The PD pump has the capacity to deliver up to  $3.5 \times 10^{-4}$  m<sup>3</sup>/s (5.5 USGPM) of water at a discharge pressure of up to 1825 kPa (250 psig) at 20°C.

The maximum pump/motor speed is 1725 RPM (revolutions per minute), and the maximum operating temperature recommended by the manufacturer is 65°C.

### Liquid flow meter

The liquid volume flow rate was measured using a model HLIT205PL inline liquid flow meter manufactured by HEDLAND. The meter can allow a maximum water flow rate of  $3.2 \times 10^{-4} \text{ m}^3/\text{s}$  (5 USGPM), and has an accuracy of  $\pm 2\%$  of Full Scale. The flow meter can operate effectively up to a pressure of 24 MPa (3500 psig) and temperature of 115°C. The photograph of the flow meter is presented in Figure 3.5.

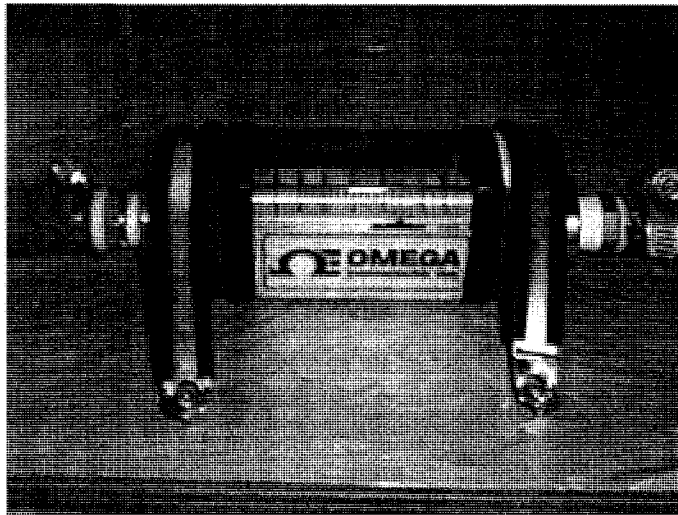


Figure 3.5 – Photograph of the liquid flow meter used in the experiment.

This flow meter was chosen over regular inline rotameters for two main reasons. First, it offers the flexibility of operating effectively when viscous fluids are flowing through it, compared to regular inline rotameters. Although the meter scales were calibrated using water by the manufacturer, it can also be calibrated using other liquids. Secondly, they

can withstand pressures higher than the maximum pressure from the pump specified above (1825 kPa or 250 psig). This is unlike regular rotameters, which have a maximum operating pressure up to about 1128 kPa or (150 psig) [42].

The flow meter in Figure 3.5 is a variable area instrument made up of a piston-assembly. Within the piston assembly, a precision-machined, sharp-edge orifice forms an annular opening with a contoured metering cone. The piston assembly carries a cylindrical ceramic magnet that is magnetically coupled to an external indicating magnet, which moves in direct response to the piston movement. A spring in the piston assembly opposes flow in the forward direction and also decreases viscosity sensitivity in the flow meter. This allows the meter to be used in any position, including inverted. The flow meter was mounted horizontally throughout the experiment.

### Compressor

The air compressor was a GX4-150FF oil-injected rotary screw compressor manufactured by ATLAS COPCO. The compressor is air cooled, and belt driven by a 3.73 kW (5hp), 3-phase electric motor. The photograph of the compressor is shown in Figure 3.6. Ambient air drawn into the unit is first passed through a two-stage 3 micron filter before the air undergoes compression. The compressed air and oil flow into an oil separator/tank, where most of the oil is removed. The compressed air flows through the oil separator and is discharged/stored in a 0.2 m<sup>3</sup> (200-litre) air receiver. The wet compressed air enters the dryer section, where the air is cooled and the moisture is drained as condensate. The dry air is then forced out of the dryer section towards the compressed air outlet.

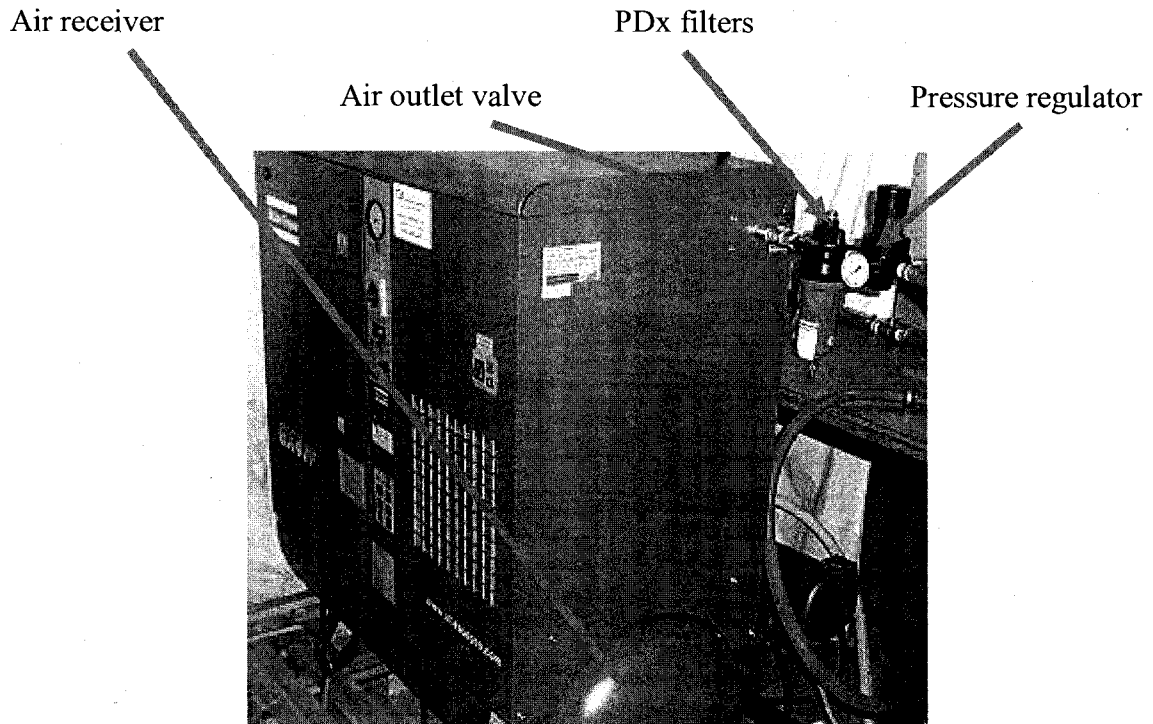


Figure 3.6 – Photograph of the compressor showing external components.

To further ensure that no compressor oil drops or particles are mixed with air, an ATLAS COPCO PDx filter was installed at the compressor air outlet. The PDx filters are high efficiency air filters, which trap solid particles down to  $0.01\mu\text{m}$ . A pressure regulator is coupled downstream of the PDx filter to be able convenient variation of the compressed air pressure. The maximum pressure and flow capacity of the compressor is 1480 kPa (200 psig) and 0.1 kg/s (179.5 SCFM) of free air, respectively. Note that the temperature of air leaving the compressor's air receiver does not exceed  $33^{\circ}\text{C}$ . For effective compressor operation, the range of ambient air temperature at the compressor inlet is between 0 and  $40^{\circ}\text{C}$ .

### *Air Mass FlowMeter*

The instrument used to measure air flow rate was a model GFM67 thermal mass flow meter manufactured by AALBORG Instruments and Controls Inc. The maximum air flow rate through the meter is  $5 \times 10^{-3} \text{ m}^3/\text{s}$  (10.6 SCFM) and has an accuracy (or uncertainty) of  $\pm 3\%$  of Full Scale for gas temperatures between 0 and 50°C. The flow meter can withstand pressures up to 3540 kPa (500 psig). Figure 3.7 shows a photograph of the flow meter.

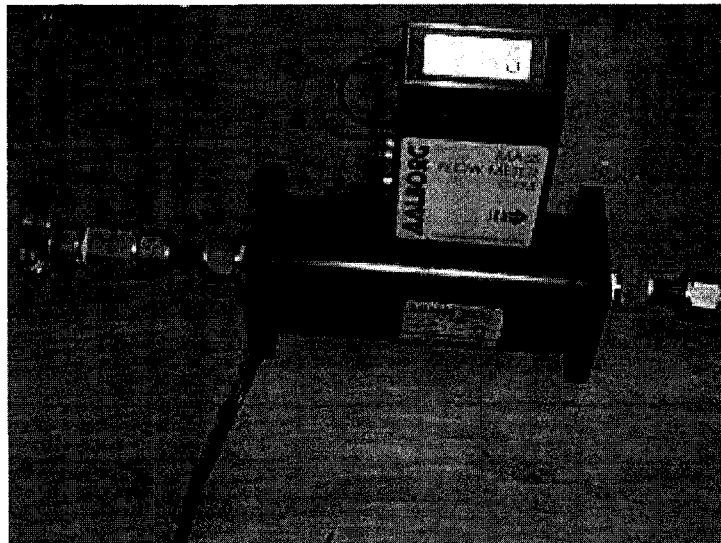


Figure 3.7 – Photograph of the air mass flow meter used in the experiment.

During operation, a gas stream enters the flow meter and is split in two paths – a small portion through a capillary stainless steel sensor tube and the other through the primary flow conduit. The geometries of both paths in the meter are factory-designed to ensure laminar flow, which makes the ratio of their respective flow rates constant. Therefore, the flow rate measured in the sensor tube is directly proportional to the total flow through the meter.

To measure the flow rate through the sensor tube, first two sections of the sensor tube are heated by precision wound heater-sensor coils. When flow takes place, heat is transferred through the thin wall of the sensor tube to the gas. The gas carries the heat from the upstream to the downstream coil windings. The resultant temperature differential is proportional to the change in resistance of the sensor winding, which is detected by an electronic circuit. This temperature-dependent resistant gradient at the sensor windings is in turn linearly proportional to the instantaneous rate of gas flow through the sensor tube. This measured gas flow through the sensor winding, combined with its ratio to the flow rate in the primary path/conduit, gives the total flow rate through the meter.

### **Pressure Gauges and Transducers**

Fluid static pressures were measured using Type 316 glycerine-filled stainless steel pressure gauges, manufactured by Ametek U.S Gauge. The glycerine-filled gauge was preferred to dampen any possible flutter of the gauge needle and enable accurate reading of the pressure. The gauges have a 0.1 m (4") dial face and are mounted inline with the flow. The maximum pressure that can be measured with the gauges is 2160 kPa (300 psig) with an accuracy of 1% full scale. The pressure measurement devices are shown in Figure 3.8.

A pressure transducer was used to measure the nozzle exit pressure, since the ordinary pressure gauges were too big to be mounted at this section. The transducer was connected to the exit pressure port (see Figure 3.1) via thin flexible tubes.

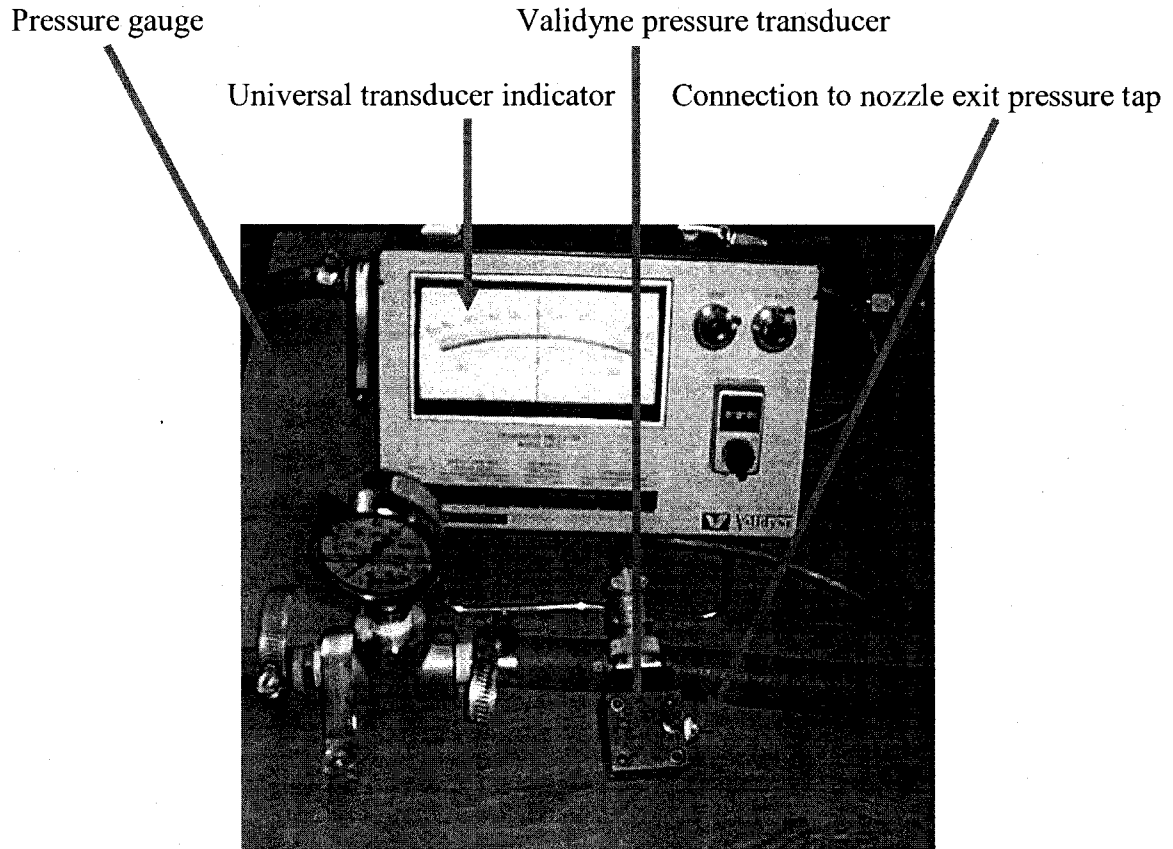


Figure 3.8 – Photographs of a pressure gauge and transducer unit used in the experiments.

The pressure transducer was manufactured by VALIDYNE with an integrated deflector plate able to handle a maximum of 1817 kPa (250 psig). Fluid pressure, which comes in contact with the Validyne plate causes it to deflect (or strain). The amount of the deflection is proportional to the magnitude of the fluid pressure on the plate. The plate deflection is converted into a voltage by the transducer, and the output is amplified and displayed on a CD12 VALIDYNE universal transducer indicator.



### *Liquid Reservoir/Collector*

The liquid reservoir was a model OTC250T heavy duty, polyethylene, cylindrical tank (open at the top) and manufactured by Zeebest Plastics. This tank material was preferred over a metallic one because it had excellent rust and corrosion resistance, and is easier to cut out sections for tank modification. The tank is 1.85 m (73") high with a diameter of 0.91 m (36"), and capable of holding 1.14 m<sup>3</sup> of liquid. Only the bottom 0.91 m (36") was used as a liquid reservoir, since a 0.61 m (24") diameter hole was cut at the tank centre. Another polyethylene cylinder 0.61 m (24") diameter and 0.91 m (36") was bolted across the face of the 0.61 m (24") diameter hole. This protruding section guides the spray into the tank to prevent liquid spillage on the laboratory floor. Figure 3.9 shows a photograph of both sections of the liquid reservoir/collector.

Since liquid from the tank first flows into the pump, a high capacity nylon suction strainer (or filter) was installed at the liquid outlet section at the bottom of the plastic tank. This strainer, which was supplied by McMaster Carr, is suitable for different hydraulic fluids and has a high surface area for greater dirt retention in high-flow applications. The screen is made of Type 304 stainless steel for corrosion and oxidation resistance and can be used up to a maximum temperature of 135°C. From pump specification sheets, particles or debris greater than 125 microns in the liquid flowing through the pump will result in catastrophic pump failure. The liquid flow meter specification sheet states that at least a 74 micron filter is required to prevent damage to the operation of the flow meter. Hence, the strainer installed in the tank was sized for 74 micron.

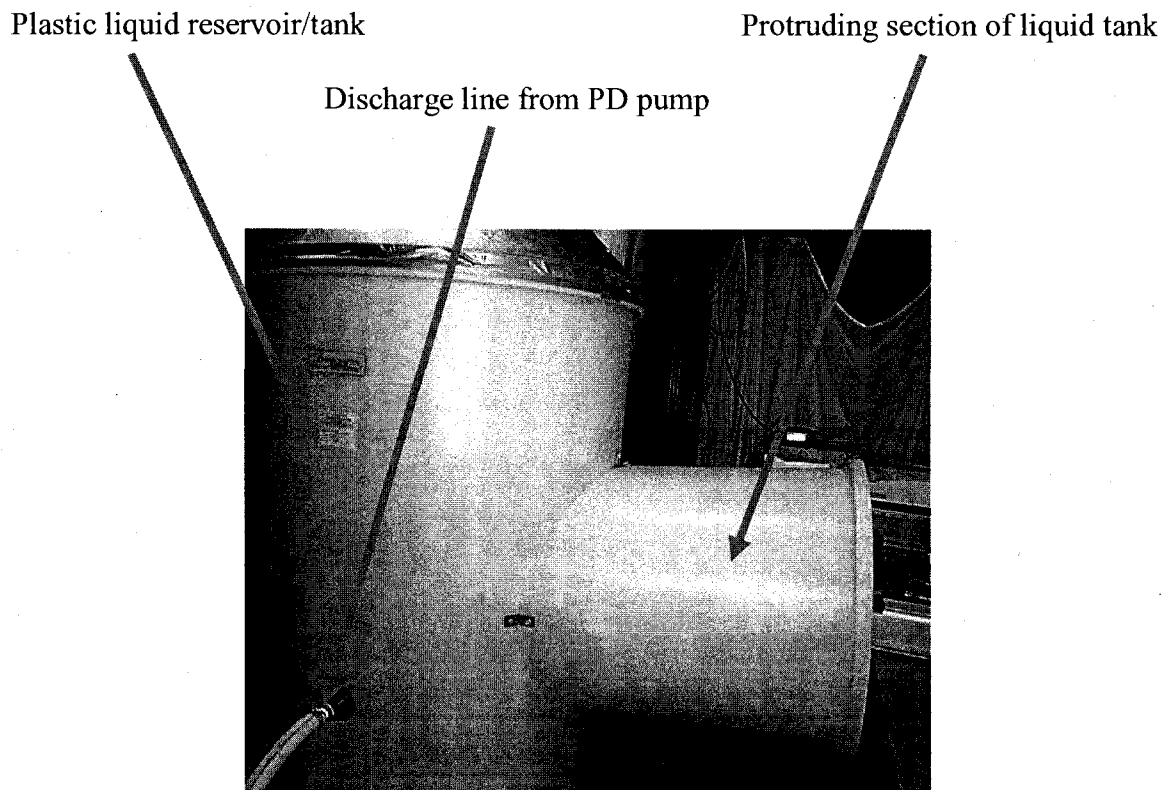


Figure 3.9 – Photographs showing sections of the liquid reservoir/collector.

Note that smaller sized filters were considered to remove finer particles that may be mixed with liquid. However, since viscous fluids were to be pumped, these finer filters were not used to prevent excessive pressure drop across the filter. This can result in the reduction of liquid flow through the pump (i.e. pump starvation), which is undesirable and can lead to eventual pump failure.

### The 2D-Particle Dynamics Analyzer (PDA)

The Particle Dynamics Analyzer (PDA) is a well-established non-intrusive laser measurement equipment used to simultaneously measure particle size of known refractive index and velocity [43]. A Model 57x50 2D-Fiber PDA manufactured by Dantec Dynamics was used to measure the drop size and velocity ( $U_d$ ) within the spray. The acronym '2D' implies the instrument can measure drop velocity in two orthogonal axis. The optical settings of the PDA unit are presented in Table 3.2. A schematic and photograph of the PDA unit set-up is shown in Figure 3.10 and Figure 3.11, respectively.

Table 3.2 – Optical settings of the PDA unit used in the study

Nd-YAG laser wavelength (nm)	532
He-Ne laser wavelength (nm)	632.8
Transmitter focal length (mm)	400
Receiver focal length (mm)	310
Beam diameter (mm)	1.35
Beam expansion ratio	1.0
Beam spacing (mm)	38.0
Receiver slit width or aperture (mm)	0.1
Scattering (or off-axis angle), $\phi$	30°

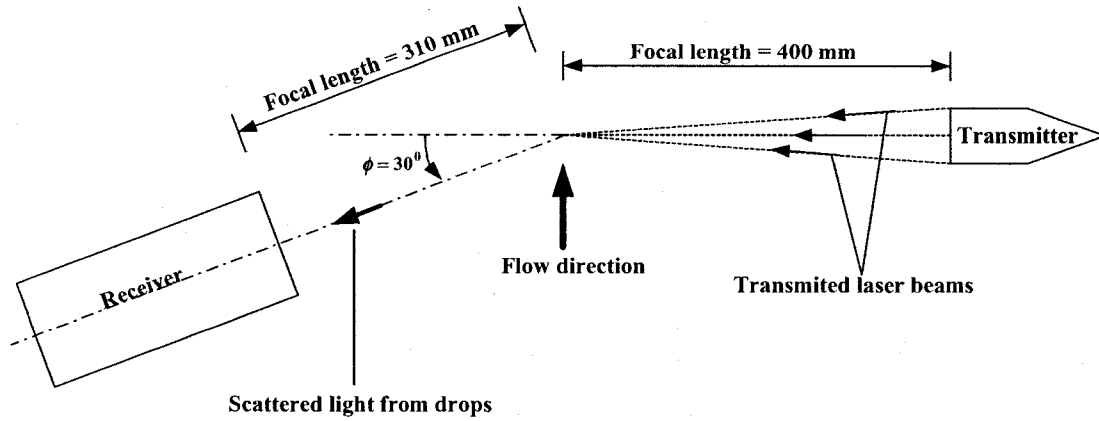


Figure 3.10: Schematic showing top view and optical path for set-up of the PDA unit.

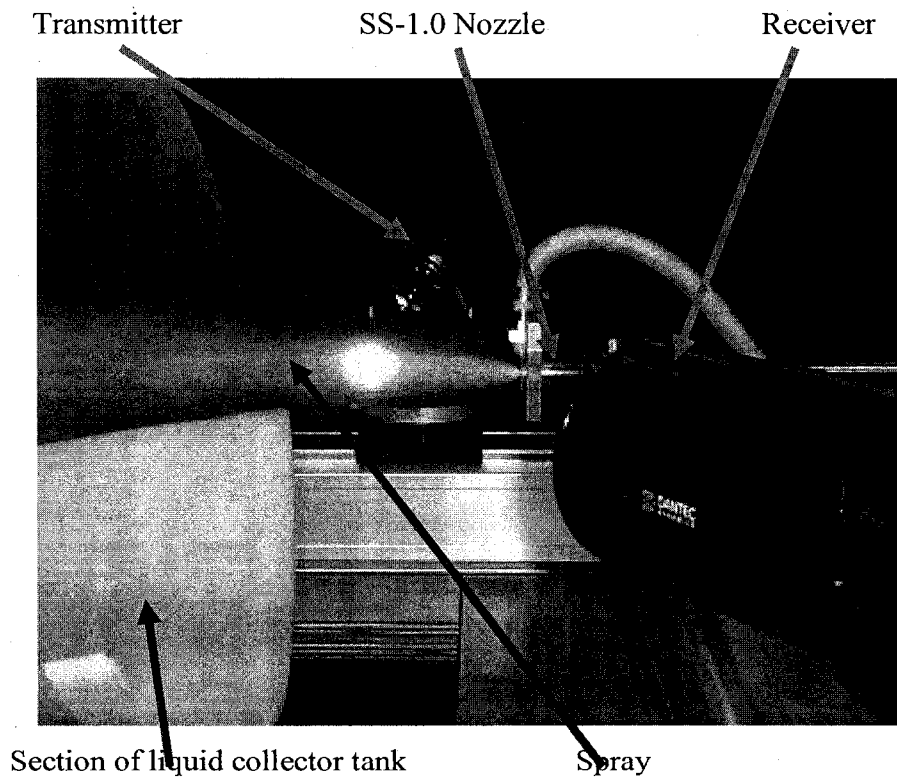


Figure 3.11: Photograph showing side view set-up of the PDA unit.

A green Nd-YAG and red He-Ne laser with wavelengths of 532 and 632.8 nm, respectively, are produced in the PDA unit and each split in two by the unit's Bragg cell. The laser powers for the Nd-YAG and He-Ne were 200 mW and 20 mW, respectively. The resulting pairs of beams, which are in a plane 90° apart, pass through the transmitter and converge at the focal length of the transmitter lens to form a control volume. The PDA receiver was focused by adjusting the iris of the receiver to coincide with the position of the control volume. For velocity measurements within a spray, drops passing through the control volume transmit Doppler frequencies or signals that are directly proportional to their velocity, which are detected by the receiver. For drop size measurements, the size of a drop through the control volume is directly proportional to the phase shift of scattered light from the drop incident on the receiver detectors. The phase shift is detected by the receiver, which is used to determine the drop size. Further detailed information on the laser systems are provided in the Dantec User Manual [43].

One of the uncertainties associated with the PDA measurement technique is due to the Gaussian beam effect or trajectory effect, as presented by Durst et al. [44]. Each laser beam used in the PDA has a Gaussian intensity profile. When small drops pass through the centre of the control volume, they are illuminated uniformly and scatter light, which is easily detected by the receiver detectors. However, when large drops pass through the control volume, a situation may arise where the incident light can be refracted and reflected on different surfaces of the drop. This non-uniform illumination of the drop can result in refracted and reflected rays with about the same intensity on the receiver detectors. This phenomenon is known as the Gaussian beam effect and results in errors in

the size measurements of the PDA. For data collection, the PDA was operated in forward-scatter and refraction mode, and the receiver was set to a scattering (or off-axis) angle ( $\phi$ ) of  $30^\circ$  for the air-water tests. Forward scattering is chosen in this study since from laser theory scattered light from particles in this mode is about  $10^2$  orders of magnitude higher compared to the backward scattering mode [43]. Furthermore, first order refraction is the most dominant scattering mode at  $\phi = 30^\circ$  for water drops in air [43]. However, a specific scattering angle was not stated for canola oil drops or drops from the glycerine-water mixture. For consistency and also based on the high confidence level in drop size measurement at this scattering angle [43], the scattering angle was also set to  $30^\circ$  for these tests.

Another uncertainty of the PDA associated with the Gaussian intensity profile is the accurate determination of the probe volume and area used to measure the liquid volume flux and number density as mentioned in Widmann et al. [45] and Dullenkopf et al. [46]. Small drops have to pass through the centre of the probe volume to scatter light that can be detected by the receiver detectors. This implies that the small drops, which do not pass through the centre of the probe volume may not be detected. This can result in poor drop counting and inaccurate number density measurements. Large drops that pass at the edge of the Gaussian intensity profile can scatter sufficient light which can be easily detected by the receiver detectors. However, the scattered light signal does not give the correct size of the large drop and the probe area, which can lead to inaccurate measurement of the liquid volume flux.

During measurements using the PDA, safety considerations were implemented. The equipment was operated in an enclosed section of the laboratory with proper safety signs and warnings to prevent unauthorized individuals from entering this restricted area. Secondly, the operator had to wear laser safety goggles at all times to prevent accidental eye exposure to the laser beams. The laser safety goggles used during the tests were MODEL NO G.1-1126 from Trinity Technologies. These laser safety goggles had an optical density of 6+ at 190-540 nm, and 2+ @ 633 nm, which were sufficient to prevent exposure to wavelengths for the Nd-YAG (532 nm) and He-Ne (632.8 nm).

### The Refractometer

The Refractometer was used to measure test liquid refractive indices, which are required input parameters to the PDA. Figure 3.12 shows the Fisher Refractometer Model 13-947 used in this study.

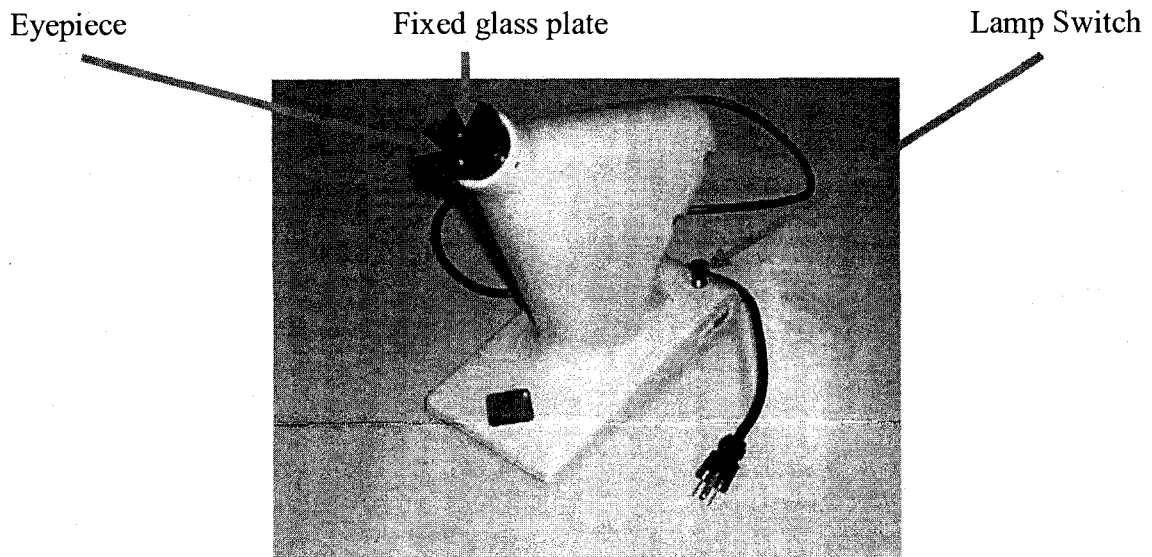


Figure 3.12: Photograph of the Refractometer used in the study.

The refractometer had an illuminated scale for direct reading of refractive indices between 1.30 and 1.90 with an accuracy of  $\pm 0.002$  units. A second scale can be used to directly read percent sucrose from 0 to 80% with an accuracy of  $\pm 1\%$ . The Refractometer eyepiece consists of a 2 mm aperture and a fixed glass plate with parallel plane faces. The unit also consists of a small glass prism with bevelled edge, which can be attached onto the fixed glass plate to form a v-shaped sample well between the bevelled edge and fixed glass plate. To measure the refractive index of a liquid, a drop of the liquid is placed in the sample well. The drop covers the aperture and when the lamp switch is depressed a clear image of the scale can be seen through the aperture. A virtual image or secondary is also seen, which is due to refraction of light travelling through the sample and prism. The refractive index of the liquid corresponds to the reading where the virtual image falls on the illuminated scale.

### **The 3-D Traverse System**

To enable measurement of drop size and velocity at different sections of the spray, the nozzle assembly was mounted on a traverse mechanism. The traverse mechanism is a model 41T33 manufactured by Dantec, and is capable of three dimensional (3-D) motion using a model 41T52 traverse controller. The maximum travel of the traverse mechanism along any 3D axis is  $610 \times 10^{-3}$  m and accuracy within 0.1 mm. The motion of the traverse mechanism can be controlled remotely from a data acquisition computer, which is connected to the traverse controller. A photograph of the traverse system is shown in Figure 3.13.



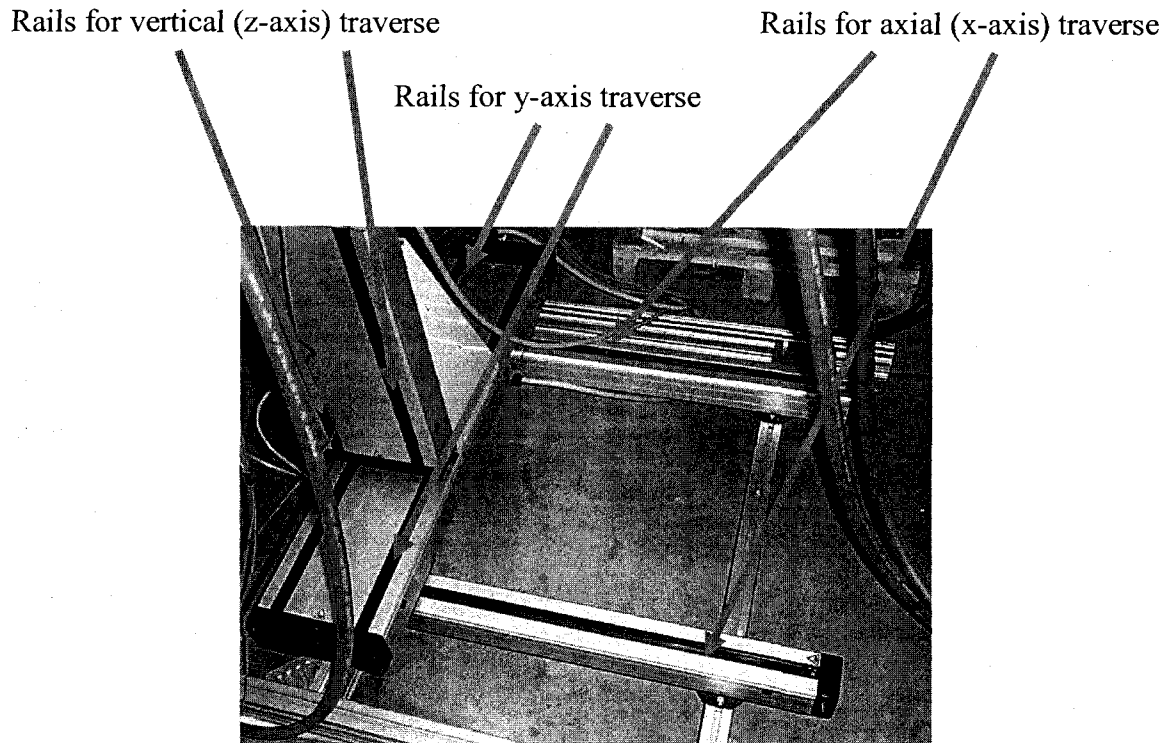


Figure 3.13: Photograph showing parts of the 3-D traverse system.

### 3.4 Measurement of Liquid Physical Properties

To measure liquid density,  $\rho_L$ , a known volume of the liquid was first measured using a graduated measuring cylinder with maximum error of 1ml. Subsequently the cylinder containing the known volume of liquid was weighed using a Type PE 3000 electronic mass balance manufactured by Mettler instruments with accuracy within 0.1 g. The mass of the liquid was computed by subtracting the mass of the empty measuring cylinder. The density was determined from the quotient of the computed liquid mass and known volume. The liquid temperature was measured with using a Type J thermocouple from All Temp Sensors. This thermocouple can measure temperatures between 0 – 760°C,

with an accuracy of 0.75% full scale. The entire procedure was repeated at least 5 times to obtain the average density of the liquid.

To measure the liquid viscosity,  $\mu_L$ , the liquid kinematic viscosity,  $\nu_L$  had to be measured first. Liquid kinematic viscosity,  $\nu_L$  was measured using models 200D979 and 300J695 Cannon-Fenske Routine viscometers with typical precisions within 0.2%. The measurement procedure first required recording the time taken for a sample of the liquid to drain between two fixed level points in the viscometers. Next, this time was multiplied by the corresponding viscometer constant to obtain the liquid kinematic viscosity. The above procedure was repeated at least 5 times and the average kinematic viscosity determined. The corresponding absolute viscosity,  $\mu_L$ , of the liquid was determined by obtaining the product of the average liquid density and kinematic viscosity.

Liquid surface tension,  $\gamma$ , was measured using the pendant-drop technique in conjunction with the computer code ADSA-P (Axisymmetric Drop Shape Analysis-Profile). In this procedure, a drop is suspended from the tip of a syringe and its photograph taken. The image of the drop is loaded onto the ADSA-P software and its density specified. From the drop curvature, the software computes the liquid surface tension. This procedure was repeated 6 times to obtain the average liquid surface tension.

Recall from Section 3.2 that the specified liquids chosen for this study were water, canola oil and a mixture of water and glycerine. Filtered tap water from the main supply was used but its density and viscosity were not measured. It was assumed that the density and

viscosity of the tap water were about the same as those specified in White [39], because the water was filtered. Since it was possible that unfiltered mineral contamination may be present in the tap water, its surface tension had to be measured using the pendant-drop method.

For the canola oil, the density, viscosity and surface tension were measured using the measurement procedures already stated above. To determine the correct mass ratio of water and glycerine required to obtain the same viscosity as canola oil, different mass ratios were tested. The glycerine-water mass ratios tested were 80%-20%, 81%-19% and 82%-18%. It was observed that the 82%-18% ratio had the closest liquid viscosity to canola oil.

The corresponding refractive indices of all three test liquids were also measured using the Fischer Refractometer. The average of 5 readings was taken for each liquid. The summary of all the liquid physical properties is presented in Table 3.3. From the Table, the glycerine-water mixture has surface tension close to that of water but with 67 times the viscosity of water. Similarly, the viscosity of the glycerine-water mixture is the same as that of canola oil, but has a surface tension of 2.5 times that of canola oil. The significant difference in the respective viscosities and surface tensions of the liquids shown above is deemed sufficient to study the effects of these properties on *SMD*.

Table 3.3 – Properties of the test liquids at 21°C. Data with superscripts ‘\*’ were adopted from White [39].

Test Liquid	Density, $\rho_L$ (kg/m <sup>3</sup> )	Absolute viscosity, $\mu_L$ (mPa-s)	Surface tension, $\gamma$ (mN/m)	Refractive Index ( $\pm 0.002$ )
Water	998*	1*	70 $\pm$ 2	1.333
Glycerine-water mixture (82%-18%)	1200 $\pm$ 30	67 $\pm$ 3	61 $\pm$ 4	1.445
Canola oil	905 $\pm$ 1	66 $\pm$ 1	25 $\pm$ 3	1.471

### 3.5 Equipment Calibration

#### Air Mass flow meter

The mass flow meter was calibrated using a model G828 Bell-Prover with a precision of 0.05% and manufactured by American Meter Company. The Bell-Prover consists of a large cylindrical copper tank, which floats (and can also be almost submerged) in water contained in a slightly larger steel container. The top of the cylindrical tank is bell-shaped, and the tank diameter and volume are about 0.61 m (24") and  $3.9 \times 10^{-3} \text{ m}^3$  (5.5ft<sup>3</sup>), respectively. The top part of the larger steel tank (just above the highest liquid level) has an air inlet and outlet section. When the outlet section is closed, all the incoming air is channelled into the steel tank causing the submerged cylindrical tank to rise. The air inlet section was connected in series with the air mass flow meter, a needle valve (for accurate flow metering) and building air supply. The cylindrical tank was first

submerged and a given flow rate was set to flow through the air mass flow meter. The outlet section was closed and the time taken to displace  $2.8 \times 10^{-3} \text{ m}^3$  ( $4 \text{ ft}^3$ ) of the bell was recorded. The flow rate was computed from the quotient of the displaced volume ( $2.8 \times 10^{-3} \text{ m}^3$ ) and the recorded time. This procedure was repeated 3 times to obtain the average flow rate, which was compared to the reading from the air mass flow meter. The calibration plot is presented in Figure A1-1. The error bars show that the repeatability falls within 1.5% of full scale reading.

### **Liquid flow meter**

The flow meter scale was factory-calibrated for water, as mentioned in section 3.3. However, it had to be calibrated using water in the laboratory to ensure effective operation, and also for correct measurement of canola oil and the glycerine-water flow rates. The liquid flow meter was calibrated by connecting it in series to the PD pump, liquid collector tank, and a needle valve. The needle valve was used for precise flow metering. To collect the liquid, a 20 litre bucket was mounted on a Type PE 16 electronic mass balance manufactured by Mettler instruments with accuracy within 0.1 g. The flow meter was set to a given liquid flow rate and the time taken to almost fill a 20 litre bucket was recorded using a stop watch. The mass of liquid collected was recorded, and divided by its known density (from Table 3.3) and the time taken to collect the liquid. This procedure was repeated 3 times. Each measured liquid flow rate was compared to the corresponding flow meter reading. The resulting plots for water, canola oil and the glycerine-water mixture are shown in Figures A1-2, A1-3, and A1-4, respectively. The corresponding maximum repeatability in Figures A1-2, A1-3, and A1-4, are 2.1%, 3.3%,

and 0.8% at full scale. The repeatability of the flow meter from the calibration test using water (2.1%) is very close to that specified by the manufacturer (2%). Note in Figures A1-3 and A1-4, the mismatch between the measured data and best-fit line is greater at the lower flow rates. This may be attributed to slight viscosity effects at this range of flow rates.

### **Pressure Gauges and Transducers**

The pressure gauges and Validyne pressure transducer were mounted onto a model DPI603 electronic pressure calibrator with a precision of 0.05% manufactured by Druck. The electronic pressure calibrator can detect a maximum pressure of 2162 kPa (300 psig). The piston of the calibrator was pumped to increase the static pressure in the unit and the gauges/transducer. The corresponding pressure readings from the gauges/transducer and electronic calibrator were recorded. The calibration plot showing the mean readings from the both pressure gauges is shown in Figure A1-5. Based on a 95% confidence, the repeatability is about 128 kPa (5 psig), which corresponds to 1.7% full scale. Figure A1-6 presents the calibration plot for the Validyne transducer. The error bars indicate a repeatability of 100 kPa (1 psig) for a 95% confidence.

### **The 2-D PDA**

To test the accuracy of the PDA unit for drop size measurements, small samples of borosilicate particles (Duke Scientific) of nominal diameter  $4.9 \pm 0.5 \mu\text{m}$  and standard deviation of  $0.6 \mu\text{m}$  were passed through the control volume of the laser unit. A summary of the results from 4 runs is presented in Table 3.4.

Table 3.4 – Summary of PDA calibration results using borosilicate particles

Test Run #	Sample Size	Arithmetic Mean Diameter, D10 ( $\mu\text{m}$ )
1	2000	4.4
2	930	4.1
3	1553	4.2
4	796	4.0

The average arithmetic mean diameter and standard deviation were  $4.2\mu\text{m}$  and  $0.2\mu\text{m}$ , respectively. For a 95% confidence, using the nominal mean diameter and standard deviation of the borosilicate particles gives a mean diameter range of  $3.7\mu\text{m} - 6.1\mu\text{m}$ . The mean value of  $4.2\mu\text{m}$  obtained from the calibration lies within this range. Therefore, the PDA unit gives accurate drop size measurements within a 95% confidence interval.

# CHAPTER 4

## NOZZLE SCALE-UP AND MIST EXTRACTION DESIGN

This Chapter describes the design process employed in obtaining the maximum possible nozzle size, which given the set-up described in the previous Chapter can be used to study the effect of nozzle exit orifice on *SMD*. Furthermore, sprays generate a fine mist, which if not effectively removed can result in a back-wash of the mist into the PDA control volume leading to erroneous results. Secondly, mists float mid-air within the laboratory space leading to air pollution problems, or can settle on expensive laboratory equipment, and cause damage (especially when spraying oil or water-glycerine mixture). Neither of these is desirable, hence the design process for effective mist removal is also presented in this Chapter.

### 4.1. Maximum feasible test nozzle size

One of the objectives of this thesis is to determine the effect of nozzle size on *SMD*. To study this effect and make conclusions that may be applied to the atomization characteristics of full-size (or commercial) nozzles in the FC, it was imperative to produce geometrically similar nozzles. Note that satisfaction of geometrical similarity is one of the criteria required in dimensionless analysis in fluid mechanics, as suggested by White [39]. Recall from Section 3.1 that the nozzle initially available for tests was the SS-1.0, which is geometrically one-quarter scale of a typical FC nozzle. The SS-1.0 has nominal operating flow rates of  $9.5 \times 10^{-5} \text{ m}^3/\text{s}$  (1.5 USGPM) and 1% *GLR*, using air and water at a 15°C (288 K) [1]. From prior hydraulic tests performed on the current SS-1.0 with laboratory facilities, the equipment limitation on water volume flow rate at 1% *GLR*



is only close to  $\sim 17.3 \times 10^{-5} \text{ m}^3/\text{s}$  (2.75 USGPM). Hence, prior to studying the effects of nozzle size on *SMD*, it was necessary to determine and manufacture the maximum possible nozzle size that the laboratory equipment can handle. This section presents the design procedures employed. Flow similarity corresponds to  $9.5 \times 10^{-5} \text{ m}^3/\text{s}$  (1.5 USGPM) and 1% *GLR*, which are nominal flow conditions for air and water flowing in the SS-1.0.

Three different approaches to the nozzle design are discussed in the subsequent sections. Two of the design methods are based on flow regime maps found in literature, whereas the third method is based on actual experimental data from similar designs of FC nozzles. The main reason for choosing these 3 approaches was to determine the variability of the different possible nozzle sizes that can be obtained from the 3 design methods. From these results a conservative nozzle size can be chosen.

#### **4.1.1 Design using the Taitel and Dukler flow map**

The Taitel and Dukler (T & D) [47] flow regime map is a theoretically based map that can be used in estimating flow regimes of horizontal two-phase mixtures. The flow regimes in this map are classified as: dispersed bubble, annular dispersed liquid, intermittent, stratified wavy, and stratified smooth. The T & D map is versatile and widely used and has been employed to effectively estimate flow regimes of two-phase mixtures at pressures and temperatures up to  $6.8 \times 10^3 \text{ kPa}$  (68 atm) and  $38^\circ\text{C}$ , respectively, for different fluid densities, viscosities and pipe diameters [47].

From the T & D map, the flow conditions of  $9.5 \times 10^{-5} \text{ m}^3/\text{s}$  (1.5 USGPM) and 1% *GLR* corresponds to a dispersed bubbly flow. The T & D flow coefficients that define dispersed bubbly flow are X and T, which are defined in [47] as:

$$X = \left[ \frac{\left| (dP/dx)_L^S \right|}{\left| (dP/dx)_G^S \right|} \right]^{\frac{1}{2}} \quad (4.1)$$

$$T = \left[ \frac{\left| (dP/dx)_L^S \right|}{(\rho_L - \rho_G)g} \right]^{\frac{1}{2}} \quad (4.2)$$

In Eqns. (4.1) and (4.2),  $(dP/dx)$  denotes pressure drop per unit length, superscript *S* denotes superficial conditions (i.e. conditions observed if only one phase flows through the pipe), and subscripts *L* and *G* denote properties of the liquid and gas phases, respectively. The fluid density is denoted by  $\rho$  and *g* is acceleration due to gravity.

Note that for similar flow regime points in the dispersed bubbly regime, the flow conditions at a given point for all nozzles must have equal corresponding values of X and T. Therefore, matching corresponding expressions for X and T can be used in the nozzle scale-up design process.

From section 3.1, the SS-1.0 has a conduit and exit orifice diameter of  $5.2 \times 10^{-3} \text{ m}$  and  $3.1 \times 10^{-3} \text{ m}$ , respectively. Based on the nominal flow of  $9.5 \times 10^{-5} \text{ m}^3/\text{s}$  (1.5 USGPM) and 1% *GLR* in the nozzle, using air and water at  $15^\circ\text{C}$  (288 K), the superficial air and water

Reynolds numbers are  $1.2 \times 10^4$  and  $2.1 \times 10^4$ , respectively. The corresponding values at the nozzle exit are  $2.2 \times 10^4$  and  $3.9 \times 10^4$ , respectively. Therefore, the superficial flow conditions yield a turbulent flow in the SS-1.0, since the superficial Reynolds numbers are greater than 2,300 (the transitional Reynolds number in single-phase pipe flows) [39]. Using  $dP/dx$  equation stated in [47] for turbulent flow through pipes and after manipulation and simplification, yields Eqn. (4.3):

$$dP/dx = \frac{0.142 \mu^{0.2} \rho^{0.8} Q^{1.8}}{D^{4.8}} \quad (4.3)$$

In Eqn. (4.3),  $\mu$ ,  $Q$  and  $D$  denote viscosity, volume flow rate and pipe diameter, respectively. Equation (4.3) can be substituted into Eqns. (4.1) and (4.2). The equations for mass ( $m$ ) conservation ( $\rho Q = \text{constant}$ ) and equation of state for the gas ( $P = \rho RT$ ) can also be substituted into the resulting expressions for further data manipulation. The above substitutions can also be combined with the previous statement that similar flow regimes at a specific location in all nozzles must have equal corresponding values of  $X$  and  $T$ . The final simplified expression for Eqn (4.1) reduces to:

$$\left[ P \left( \frac{Q_L}{m_G} \right)^{1.8} \right]_{\text{current nozzle}} = \left[ P \left( \frac{Q_L}{m_G} \right)^{1.8} \right]_{\text{new nozzle}} \quad (4.4)$$

Eqn (4.2) reduces to:

$$\left[ \frac{D^{4.8} (\rho_L R_G T_{abs} - P)}{Q_L^{1.8}} \right]_{\text{current nozzle}} = \left[ \frac{D^{4.8} (\rho_L R_G T_{abs} - P)}{Q_L^{1.8}} \right]_{\text{new nozzle}} \quad (4.5)$$

In Eqns. (4.4) and (4.5),  $R_G$  is the characteristic gas constant,  $m_G$  is the mass flow rate of gas,  $T_{abs}$  and  $P$  are absolute mixture temperature and pressure at the point of interest. Equations (4.4) and (4.5) can be applied to the fluid mixing point in the nozzle assembly conduit and nozzle exit. For the SS-1.0, Table 4.1 presents the corresponding parameters at the fluid mixing point and nozzle exit for  $9.5 \times 10^{-5} \text{ m}^3/\text{s}$  (1.5 USGPM) and 1%  $GLR$  at a mixture temperature of  $15^\circ\text{C}$  (288 K).

Table 4.1 – Nozzle scaling design using the Taitel and Dukler flow regime parameters. Design data are for  $9.5 \times 10^{-5} \text{ m}^3/\text{s}$  (1.5 USGPM) and 1%  $GLR$  in the SS-1.0.

Location	$D$ (mm)	$P$ (kPa)	X	T
<b>Fluid mixing point</b>	5.73	519	8111	24884
<b>Nozzle exit</b>	3.10	276	4318	1308

The values in the last two columns of Table 4.1 for each nozzle section can be substituted into their respective equations (Eqns. ((4.4) and (4.5))). Further substitution of the resulting Eqn. (4.4) into Eqn. (4.5) for equal  $GLR$  and same gas-liquid system in the SS-1.0 and new nozzles yields the much simplified expression:

$$\frac{D_{\text{new nozzle}}}{D_{\text{current nozzle}}} = \left[ \frac{Q_{L\_new\ nozzle}}{Q_{L\_current\ nozzle}} \right]^{\frac{3}{8}} \quad (4.6)$$

The water volume flow rate for the SS-1.0 is known to be  $9.5 \times 10^{-5} \text{ m}^3/\text{s}$  (1.5 USGPM) at 1% *GLR*. Recall that the maximum water volume flow rate through the SS-1.0 at 1% *GLR* is  $\sim 17.3 \times 10^{-5} \text{ m}^3/\text{s}$  (2.75 USGPM). Substituting these liquid volume flow rates into Eqn. (4.6) gives a maximum geometric ratio that can be tested in the laboratory as 1.25 times the SS-1.0. This nozzle will henceforth be denoted SS-1.25, for convenience. From Eqn. (4.4), for a water volume flow rate of  $17.3 \times 10^{-5} \text{ m}^3/\text{s}$  (2.75 USGPM) through the SS-1.25, the corresponding absolute pressures at the mixing point and exit is about 510 kPa and 270 kPa, respectively. Note that for the same flow conditions through the SS-1.0, the corresponding mixing and exit pressures are 1177 and 600 kPa, respectively. The high pressures are of course due to the smaller diameters associated with the SS-1.0 compared to the SS-1.25. This is because transporting the same quantity of fluid through a smaller cross-sectional area requires higher pump power due to the higher frictional losses associated with smaller diameters. The higher pump power corresponds to higher static pressures in the SS-1.0 than in the SS-1.25.

#### 4.1.2 Design using the Baker-Scott flow map

Baker [48] developed a flow regime map for horizontal two-phase flow, which was subsequently modified by Scott [49]. The Baker-Scott flow regime map is widely used in the field of two-phase flow. The vertical and horizontal axes of the map are labelled  $G_G/\lambda$  and  $G_L\psi\lambda/G_G$ . From [48],  $G_G$  and  $G_L$  denote the mass flux of the gas and liquid, respectively, and the parameters  $\lambda$  and  $\psi$  are defined as:

$$\lambda = \left( \frac{\rho_G}{\rho_{air}} \frac{\rho_L}{\rho_{water}} \right)^{\frac{1}{2}} \quad (4.7)$$

$$\psi = \frac{\gamma_{water}}{\gamma} \left( \frac{\mu_L}{\mu_{water}} \right)^{\frac{1}{3}} \left( \frac{\rho_{water}}{\rho_L} \right)^{\frac{2}{3}} \quad (4.8)$$

In Eqn. (4.8),  $\gamma$  denotes liquid surface tension. The properties of air and water in Eqns. (4.7) and (4.8) are based on a temperature of 15°C and atmospheric conditions as defined in Baker [48]. The corresponding values are as follows:  $\rho_{air} = 1.23 \text{ kg/m}^3$ ;  $\rho_{water} = 1000 \text{ kg/m}^3$ ;  $\mu_{water} = 10^{-3} \text{ kg/ms}$ ; and  $\gamma_{water} = 0.072 \text{ N/m}$ .

To achieve 'similar' flow conditions using the Baker-Scott map,  $G_G/\lambda$  and  $G_L\psi\lambda/G_G$  for both nozzles must be equal. For air and water as test liquids, equating  $G_G/\lambda$  and also using the equation of state for the gas yields:

$$\left[ \frac{m_G}{D^2} \left( \frac{R_G T_{abs}}{P} \right)^{\frac{1}{2}} \right]_{current\ nozzle} = \left[ \frac{m_G}{D^2} \left( \frac{R_G T_{abs}}{P} \right)^{\frac{1}{2}} \right]_{new\ nozzle} \quad (4.9)$$

Also equating  $G_L\psi\lambda/G_G$  yields:

$$\left[ \frac{\rho_L Q_L}{m_G} \left( \frac{P}{R_G T_{abs}} \right)^{\frac{1}{2}} \right]_{current\ nozzle} = \left[ \frac{\rho_L Q_L}{m_G} \left( \frac{P}{R_G T_{abs}} \right)^{\frac{1}{2}} \right]_{new\ nozzle} \quad (4.10)$$

The corresponding values for the parameters in Eqns. (4.9) and (4.10) are presented in Table 4.2.

Table 4.2 – Nozzle scaling design using the Baker-Scott flow regime parameters. Design data are for  $9.5 \times 10^{-5} \text{ m}^3/\text{s}$  (1.5 USGPM) and 1% *GLR* in the SS-1.0.

Location	$D$ (mm)	$P$ (kPa)	$G_G/\lambda$ ( $\text{kg}/\text{m}^2\text{s}$ )	$G_L \psi \lambda / G_G$
<b>Fluid mixing point</b>	5.73	519	17	222
<b>Nozzle exit</b>	3.10	276	76	164

For equal *GLR* and same gas-liquid system in both nozzles, Eqn. (4.9) and Eqn. (4.10) can be combined to give the final reduced expression:

$$\frac{D_{\text{new nozzle}}}{D_{\text{current nozzle}}} = \left[ \frac{Q_{L_{\text{new nozzle}}}}{Q_{L_{\text{current nozzle}}}} \right]^{\frac{1}{2}} \quad (4.11)$$

As in the previous section for 1% *GLR*, we can substitute into Eqn. (4.11)  $9.5 \times 10^{-5} \text{ m}^3/\text{s}$  (1.5 USGPM) for the water volume flow rate through the SS-1.0, and  $17.3 \times 10^{-5} \text{ m}^3/\text{s}$  (2.75 USGPM) as the maximum possible water flow rate. The result gives a maximum geometric ratio of 1.35 times the SS-1.0. This nozzle will henceforth be denoted SS-1.35. From Eqn. (4.10), for 1% *GLR* in an air-water system operating at  $15^\circ\text{C}$  (288 K), the corresponding absolute pressures at the mixing point and exit is about 410 kPa and 220 kPa, respectively.

#### 4.1.3 Design using existing test data from commercial scale nozzles

The final design procedure employed in the nozzle scale-up process was using a combination of air-water flow data from the SS-1.0 and full-scale (or commercial) nozzles. The full-scale flow data was obtained from Maldonado [50], from tests performed at the Syncrude Canada Research Centre. For convenience, the full-scale nozzles have been denoted names beginning with 'FS', which implies 'Full-Scale'. The corresponding operating flow conditions using air and water for the FS-1.0 (nozzle currently used in FC operations) and FS-1.5 (with nozzle size 1.5 times the FS-1.0) are presented in Table 4.3.

Table 4.3 – Comparison of absolute mixing and exit pressures at constant gas and liquid mass flow rates in the FS-1.0 and FS-1.5 nozzles

Q <sub>L</sub> (×10 <sup>-5</sup> m <sup>3</sup> /s)	m <sub>G</sub> (×10 <sup>-3</sup> kg/s)	FS-1.5		FS-1.0		$\frac{P_{mix\_FS-1.5}}{P_{mix\_FS-1.0}}$	$\frac{P_{exit\_FS-1.5}}{P_{exit\_FS-1.0}}$
		P <sub>mix</sub> (kPa)	P <sub>exit</sub> (kPa)	P <sub>mix</sub> (kPa)	P <sub>exit</sub> (kPa)		
250	88	1072	429	1809	814	0.59	0.53
284	33	771	271	1317	505	0.59	0.54
348	33	929	307	1574	585	0.59	0.52
388	33	1016	325	1731	634	0.59	0.51
408	33	1060	333	1808	658	0.59	0.51
450	18	920	245	1483	487	0.62	0.50
316	88	1299	498	2225	977	0.58	0.51
215	65	800	319	1384	605	0.58	0.53
230	78	942	377	1595	712	0.59	0.53
225	77	909	365	1549	691	0.59	0.53
204	85	876	360	1489	683	0.59	0.53



The FS-1.5 data is deemed sufficient to indicate the trend in flow condition changes associated with using bigger nozzles, which can be applied to the SS-1.0 scale-up design process.

Table 4.3 indicates that for the same gas and liquid flow rates through both nozzles, the mixing pressure in the FS-1.5 is ~59% the value in the FS-1.0. The corresponding exit pressure in the FS-1.5 is ~52% the value in FS-1.0. Therefore, to maintain a given pressure between nozzles of different sizes, the larger nozzle requires higher gas and/or liquid flow rates. This is similar to the observations in Sections 4.1.1 and 4.1.2.

To determine the maximum possible scale-up nozzle in laboratory, one can concentrate on the pressure at the nozzle exit. This is because it is the smallest section (or throat) of the nozzle and therefore governs the pressure inside the nozzles. For geometrically similar FC nozzles using identical gas and liquid (e.g. air and water in this case), the absolute pressure,  $P$  (kPa), at the nozzle exit depends on gas mass flow rate,  $m_G$  (kg/s), liquid volume flow rate,  $Q_L$  (m<sup>3</sup>/s) and nozzle exit diameter,  $D$  (m). Using dimensional analysis, the four parameters form a dimensionless group with the functional form in Eqn. (4.12), where  $P_{atm}$  denotes the local atmospheric pressure of 93 kPa, which was measured from a barometer in the laboratory building.

$$\frac{(P - P_{atm})^a D^b}{m_G^c Q_L^d} = \text{constant} \quad (4.12)$$

The air-water operating conditions for SS-1.0, FS-1.0 and FS-1.5 nozzles were fitted to Eqn. (4.12), by using the MAPLE software (see Appendix A2, Section A2-1 for output file). The best-fit line is presented in Figure A2-1, and has an  $R^2$ -value of 0.8986. The corresponding indices in Eqn (4.12) were:  $a = 1.00$ ,  $b = 2.15$ ,  $c = 0.60$  and  $d = 0.49$ , whereas the constant was 4.70. If we assume that Eqn. (4.12) holds for the geometrically similar FC nozzles, then it is possible to estimate the maximum nozzle scale-up size that can be tested in the laboratory at constant exit pressure. Re-writing Eqn. (4.12) yields:

$$\left[ \frac{P D^{2.15}}{m_G^{0.60} Q_L^{0.49}} \right]_{current\ nozzle} = \left[ \frac{P D^{2.15}}{m_G^{0.60} Q_L^{0.49}} \right]_{new\ nozzle} \quad (4.13)$$

Water volume flow rate of  $9.5 \times 10^{-5} \text{ m}^3/\text{s}$  (1.5USGPM) and 1% *GLR* (i.e.  $m_G = 0.95 \times 10^{-3} \text{ kg/s}$ ) in the SS-1.0, can be substituted into Eqn. (4.13) as well as the maximum possible water flow rate of  $17.3 \times 10^{-5} \text{ m}^3/\text{s}$  (2.75 USGPM). The resulting maximum scale-up nozzle size, which can produce the same *GLR* and exit pressure as the SS-1.0, is 1.35 times the size of SS-1.0. This is similar to the result in section 4.1.2, hence this nozzle can also be denoted SS-1.35.

In summary, from sections 4.1.1, 4.1.2 and 4.1.3, the maximum possible scale-up size lies between 1.25 and 1.35 times the size of SS-1.0. A conservative size to manufacture can be the average of the ratios (or scales). Hence in the laboratory, the maximum feasible scale-up size that can yield similar pressure and *GLR* as 1.5 USGPM and 1% *GLR* in the SS-1.0, should be geometrically 1.3 times the size of SS-1.0. This nozzle may be denoted

SS-1.3. A photograph of the SS-1.3, which was manufactured based on the design considerations in this section, is presented in Figure 4.1.

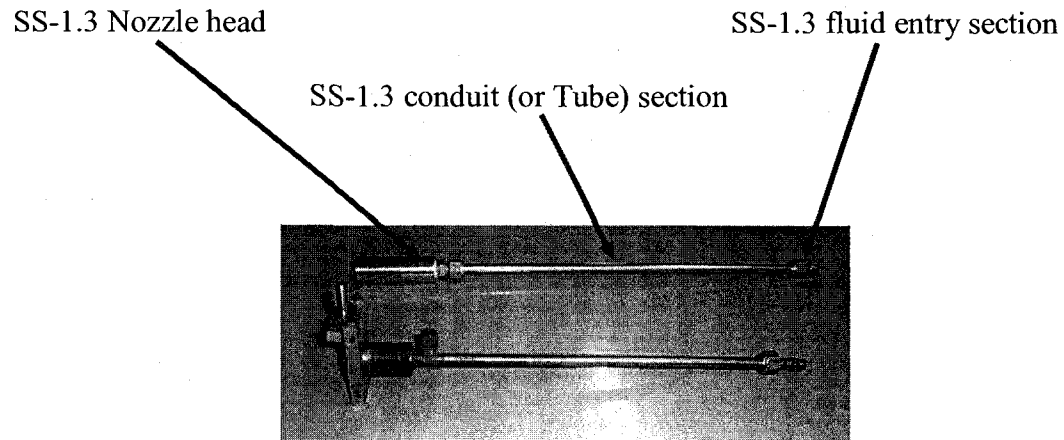


Figure 4.1– A photograph showing the SS-1.3 and SS-1.0 nozzles for size comparison. Labelled sections of the SS-1.0 have been shown in Figure 3.1.

To validate the design, the SS-1.3 was tested to ascertain the air-water flow conditions required to attain the same exit pressure (276 kPa) and *GLR* (1%) in the SS-1.0. Using air and water, the result showed that for 1% *GLR*,  $19 \times 10^{-5} \text{ m}^3/\text{s}$  (3.0USGPM) of water is required to give an exit pressure of 276 kPa. Note that the water flow rate of  $19 \times 10^{-5} \text{ m}^3/\text{s}$  (3.0USGPM) is only about 9% higher than the design water flow rate of  $17.3 \times 10^{-5} \text{ m}^3/\text{s}$  (2.75 USGPM). Hence, it can be said that the nozzle scale-up design process should satisfactorily replicate actual flow conditions. Note also that the flow rate of  $19 \times 10^{-5} \text{ m}^3/\text{s}$  obtained in the SS-1.3 has about the same superficial  $Fr_L$  as the SS-1.0 with a flow rate of  $9.5 \times 10^{-5} \text{ m}^3/\text{s}$ . Hence, the design is still within the accuracy for dimensional analysis used

in Section 3.1, which also establishes dynamic similarity between SS-1.3 and the full-scale commercial nozzle.

#### 4.2 Effective mist extraction design for nozzle sprays

Prior hydraulic tests on the SS-1.0 nozzle using water and canola oil, with air as the gas, showed that one of the major problems encountered in the laboratory was the production of mist from the sprays. The mist extractor initially present in the laboratory was a fume hood, which was connected directly above to the liquid collector tank. It was observed that the fume hood was not effectively removing the mist in the air-water system. Furthermore, the mist was more pronounced in the air-canola oil tests compared to air-water tests. This may indicate issues relating to evaporation, since increased mist production can be attributed to a lower rate of liquid evaporation. This can be explained comparing evaporation properties of the test fluids. From Baron and Willeke [51], evaporation of a liquid occurs when the saturation vapour pressure of the liquid is greater than the ambient partial pressure of the vapour. An important parameter in aerosol evaporation process is the ratio of partial pressure of vapour to the saturation vapour pressure. This parameter is called the Saturation Ratio,  $S_R (= \exp\{4\gamma M/\rho_L R_U T d\})$  [Baron and Willeke]. The symbols  $M$ ,  $R_U$  and  $d$  denote the liquid molecular weight, Universal Gas Constant (8.3144 J/mol-K), and drop size, respectively. The evaporation ability of the different test liquids can be compared for a given temperature and drop size, by comparing the term in curly “{}” brackets above. Liquids with smaller values of this term have a greater ability to evaporate and produce less mist. The values of liquid density and surface tension have already been presented in Table 3.3. The molecular weight of water

and glycerine are 18 and 92 g/mole [39], respectively. Based on the 82% glycerine and 18% mass fraction for the glycerine-water mixture, its molecular weight is  $\sim 79$  g/mol. The molecular weight for canola oil can be in the range of 700 – 900 g/mol, based on the constituents of canola oil presented by Shahidi [52]. Using a conservative molecular weight (700 g/mol) for the canola oil, the term  $\{4\gamma M/\rho_L R_U T_d\}$  for canola oil, glycerine-water and water, is in the ratio 15:3:1, respectively. This suggests that for the same drop size and temperature, water will evaporate faster (producing the least mist), whereas the canola oil evaporates slower (hence producing more mist).

Lastly, in general, the mist increased with  $GLR$  and as the nozzle assembly is traversed away from the PDA probe volume for axial measurements within the spray. In the latter instance, the nozzle exit is further away from the inlet of the liquid tank, and results in enhanced entrainment of the ambient gas as the spray enters the liquid tank. The ventilation system was not designed to handle the test flow conditions for the SS-1.0 nozzle. The layout consisted of a 0.2 m (8") diameter duct and from measured duct velocity ( $\sim 6$  m/s) an average flow rate through the fume-hood blower was estimated to be 0.184 standard  $m^3/s$  (390 SCFM). It was evident the flow rate required to eliminate (or reduce the mist to a minimum) must be much higher than the blower flow rate. A new centrifugal blower was available for installation that could yield much higher flow rates (up to 0.641 standard  $m^3/s$  (1360 SCFM)) at corresponding static pressures of the installed blower. The objective was to design a duct layout based on the performance curves of the new blower that is sufficient to eliminate the mist produced from the SS-1.0 flow conditions in the laboratory. The steps employed are presented below.

#### 4.2.1 Maximum possible entrained gas from nozzle

The first task was to determine the maximum possible total gas flow rate produced from the laboratory facility. Since most of the gas through the transparent duct and blower is due to ambient gas entrainment, single-phase gas and effervescent spray entrainment equations were considered to determine the total gas volume flow rate through the blower.

##### 4.2.1.1 Single-phase gas jet entrainment equation

Perry and Green [53] have stated that for a round, turbulent free-jet (where the jet and entrained fluid are air), the total jet flow rate,  $Q_G$ , is given by:

$$\frac{Q_G}{Q_{G_0}} = 0.32 \left( \frac{x}{D} \right) \quad (4.14)$$

Eqn. (4.14) is obtained from the original work of Ricou and Spalding [54] for single-phase turbulent free jets. In Eqn. (4.14),  $Q_{G_0}$ ,  $D$  and  $x$  denote initial jet flow rate, exit orifice diameter and axial distance from jet discharge, respectively. Note that Eqn. (4.14) is valid for  $7 < \frac{x}{D} < 100$ , and a jet is considered free if its cross-sectional area is less than one-fifth of the area through which it is flowing [53].

In the spray laboratory, if the fluid was gas only, the maximum possible flow at the nozzle exit,  $Q_{G_0}$ , is  $5 \times 10^{-3} \text{ m}^3/\text{s}$  (10.6 SCFM), which is the capacity of the mass flow meter. The maximum distance of the nozzle exit from the inlet of the liquid tank's

protruding section is about 0.61 m (24"). This distance is equivalent to  $x/D = 197$ , based on the exit orifice diameter of the SS-1.0. Note that it is assumed that no entrainment occurs as the flow enters the protruding section of the collector tank shown in Figure 3.9, since the flow is enclosed beyond this point and is not a free jet. If Eqn. (4.14) is also applicable up to  $x/D = 197$ , then  $Q_G = 0.314 \text{ m}^3/\text{s}$  (667 SCFM). When this flow rate is multiplied by a safety factor of 1.5, it yields  $0.471 \text{ m}^3/\text{s}$  (1001 SCFM). This is the minimum flow rate required from the blower when it is connected to the duct system, using the single-phase entrainment equation.

#### 4.2.1.2 Effervescent spray entrainment equation

To obtain a comparatively more exact total volume flow rate at the duct entrance for the two-phase mixture, an entrainment correlation for effervescent atomizers presented by Bush and Sojka [55] was employed. Again, the original equation is as stated in [54] for momentum driven jets, except it was modified for a two-phase flow. The relationship is given by:

$$\frac{m_e}{m_L} = E \sqrt{\frac{4}{\pi} \left( \frac{x}{D} \right)} \sqrt{\frac{\rho_e (GLR \rho_L + SR \rho_G)}{\rho_L \rho_G} \left( \frac{1}{SR} + GLR \right)} \quad (4.15)$$

In Eqn. (4.15), subscript 'e' denotes entrained parameters, whereas  $E$  is the Entrainment number. Although Eqn. (4.15) was developed for vertical two-phase spray, it can also be applied to the horizontal two-phase sprays from the SS-1.0 nozzle. This is because entrainment is a momentum driven phenomenon, and thus independent of nozzle orientation. From Eqn. (4.15), the highest entrainment occurs for the flow condition with

the highest rate of momentum change and for homogeneous conditions (i.e.  $SR = 1$ ). From [54], the average value of  $E$  for low-viscosity (viscosity,  $\mu_L < 100$  mPa-s) liquids is 0.15. During the nozzle hydraulic tests using air-water and air-canola oil, the maximum rate of momentum change occurred for  $10.5 \times 10^{-5} \text{ m}^3/\text{s}$  (1.66 UGPM) and 4%  $GLR$  in the air-canola oil tests. The viscosity of canola was 66 mPa-s. Substituting this data into relevant test data (see Appendix A2, Section A2-2) for this flow condition into Eqn. (4.15) yields a flow rate of  $0.257 \text{ m}^3/\text{s}$  (545 SCFM). Multiplying this flow rate by a safety factor of 1.5 yields a flow rate of  $(0.285) \text{ m}^3/\text{s}$  823 SCFM through the blower.

Based on results from Eqns. (4.14) and (4.15), a conservative flow rate requirement from the blower is  $0.471 \text{ m}^3/\text{s}$  (1001 SCFM). From the blower performance curve/specification sheets, the corresponding static pressure loss at  $0.471 \text{ m}^3/\text{s}$  (1001 SCFM) is 0.015 m (0.6") of water gauge.

#### **4.2.2 Duct layout design for minimum system pressure loss**

The second step in the effective mist removal process required designing a duct system such that the system pressure loss is less than or equal to 0.015 m (0.6") of water gauge i.e. flow rate is greater than or equal to  $0.471 \text{ m}^3/\text{s}$  (1001 SCFM). Lower system pressure losses increase flow rate through the blower and system, thereby reducing/eliminating the mist formed by the spray. System static pressure loss reduction requires minimizing the sum of frictional and separation losses in the system. The duct diameters considered were, 0.254m (10"), 0.305m (12") 0.356m 12", 14" and 0.406m (16"). The duct and system design process was in accordance to the 'American Society of Heating,



Refrigeration and Air-conditioning Engineers (ASHRAE) handbook and Heating, Ventilation and Air-conditioning (HVAC) design book by McQuiston, et al. [56]. Based on space availability in our test facility, possible noise level in the duct, lowest total system pressure loss and other design decisions using the ASHRAE and HVAC handbooks, the 0.406m (16") duct size was chosen. An Excel spreadsheet of the design parameters for the 0.406m (16") diameter duct and relevant design equations are presented in Appendix A2, Section A2-3. The estimated blower-system operating point occurred at 0.518 m<sup>3</sup>/s (1100 SCFM) and 0.014m (0.54") of water gauge and is presented in Figure A2-2. This flow rate satisfies the condition stated earlier for effective mist extraction i.e. the system pressure loss must be less than or equal to 0.015 m (0.6") of water gauge with a flow rate at least greater than 0.471 m<sup>3</sup>/s (1001 SCFM). A sketch showing only the duct layout for the spray system is presented in Figure A2-3.

The mist extraction system in Figure A2-3 was not installed due to prolonged installation delays. It was decided to purchase and install a stand alone mist extraction system, which was independent of the building HVAC system. The duct system was redesigned to suit this new set-up. The final layout is shown in Figure 4.2.

The mist removal system was manufactured by Machine Master and comprised of a 4-stage filtration system consisting of aluminium chevron-type mist eliminator, aluminium mesh pre-filter, a 95% ASHRAE V-Bag filter and a 99.97% HEPA filter cell.

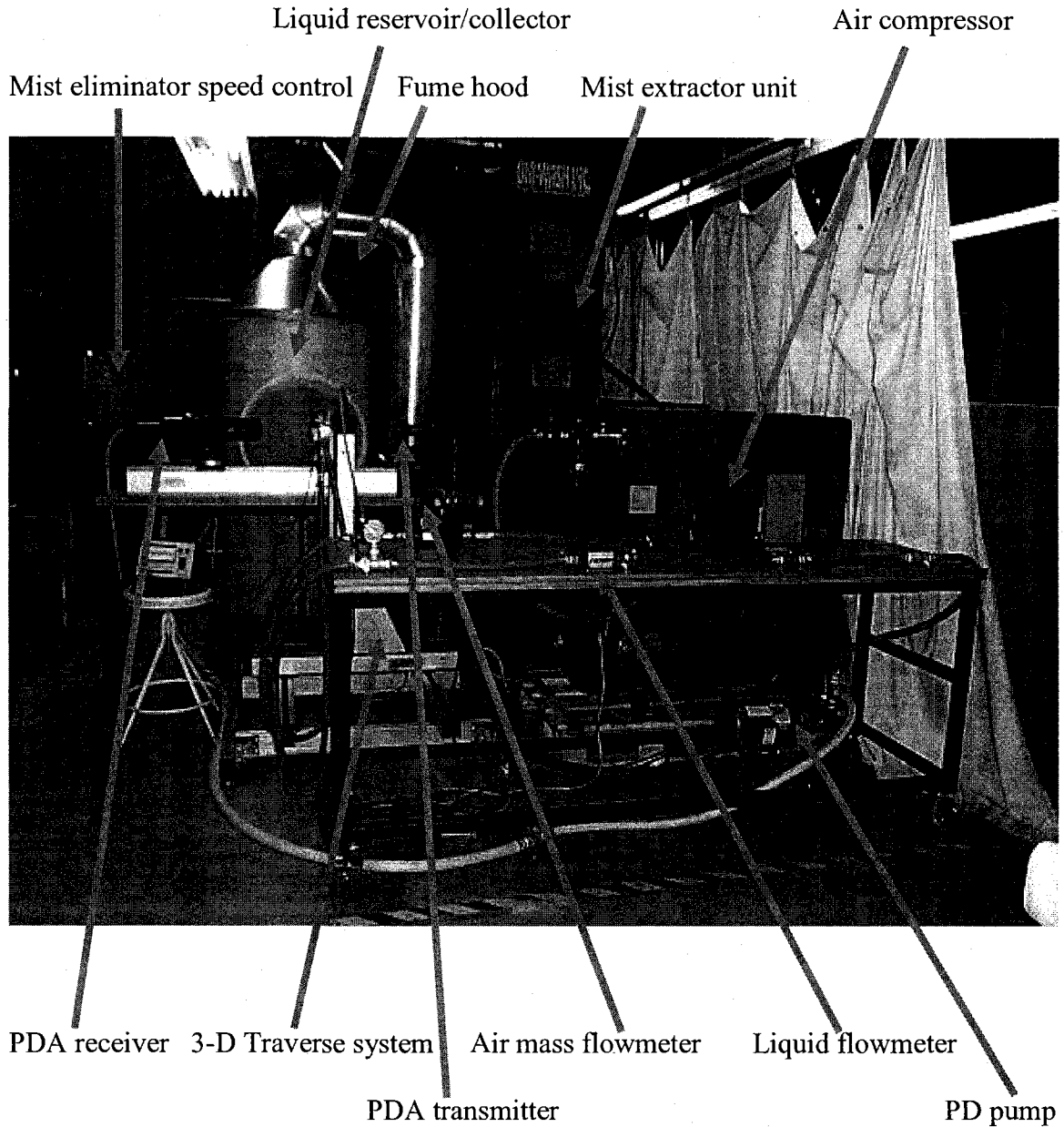


Figure 4.2 – Photograph showing test equipment and final set-up for effective mist extraction from the sprays.

The blower and motor assembly is a MM-2000 2.2 kW (3 horsepower) model with the capacity to extract about 56.6 m<sup>3</sup>/min (2000 CFM) of free air at a static pressure of 0.14 m (5.5”) water column. A drawing showing the different sections of the mist extractor

system is presented in Figure A2-4, whereas the performance curve for the centrifugal blower is presented in Figure A2-5. The motor speed was varied by a Reliance MD 60 AC Drive with speed regulation within 2% of motor base speed of 3450 RPM.

Recall that the design requirement is to extract  $0.471 \text{ m}^3/\text{s}$  (1001 SCFM) of air from the spray. Based on the redesigned ducting system and blower performance curve/specification sheets, it was evident that the current mist extraction system was more than sufficient to remove a much greater amount of mist from the sprays.

# CHAPTER 5

## EXPERIMENTAL PROCEDURE AND DATA ANALYSIS

This chapter briefly describes the procedure used in acquiring data within the spray. The technique used to determine the required air and liquid flow conditions to study the viscosity, surface tension and nozzle size effects on *SMD* are also presented. Finally, data analysis techniques are briefly mentioned.

### 5.1 Equipment layout and flow loop

A schematic showing only experimental set-up and flow loop is presented in Figure 5.1, which is similar to Figure 3.3. Note that Figure 5.1 has been presented here for easy understanding of the subsequent description of the flow loop.

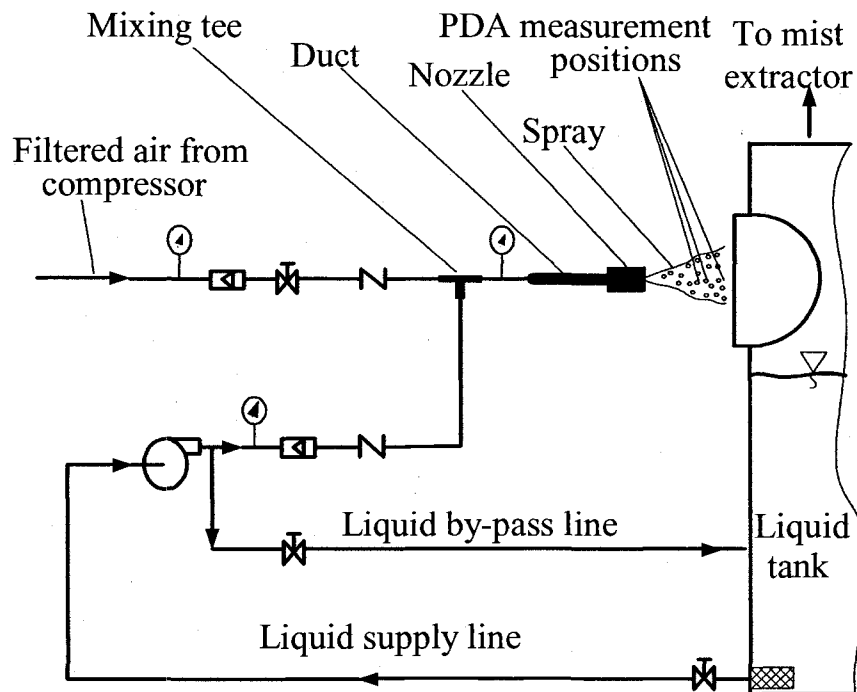


Figure 5.1 – Schematic of flow loop in the experimental set-up.

Compressed and filtered dry air from the compressor was pressure-regulated and supplied to the nozzle. Check valves were installed to prevent back flow of the fluid in both air and liquid lines. The mist extraction unit was switched on at low motor speed to encourage ventilation. The liquid in the collector tank was supplied to the nozzle via the positive displacement pump. A liquid by-pass line was installed to ensure sufficient flow rate through the pump and prevent pump shutdown due to excessive back pressure from transferring liquid through the small nozzle exit diameter. The desired air flow rate was controlled by adjusting the valve on the air line, whereas the required liquid flow rates was controlled using the speed control unit of the pump. The compressed air and liquid are supplied to the nozzle via a tee fitting. The tee fitting was used, since the gas and liquid mixing was specified [1] to be at 90° to each other, for these types of small-scale FC nozzles. Downstream of the gas and liquid mixing point the resulting spray was discharged into liquid collector tank/reservoir, with the liquid re-circulated back to the nozzle.

The air flow rate, liquid flow rate and nozzle exit pressures were monitored using the mass flow meter, liquid volume flow meter and Validyne transducer unit, respectively. Other line pressures were measured using the pressure gauges. The room, liquid, mixture and exit temperatures in the nozzle assembly were measured using J-type thermocouples. When the desired air and liquid flow conditions were attained, the flow rate through the mist removal system was adjusted by varying the speed of its motor. The adjustments were stopped when it was observed that no mists came out of the liquid collector tank. A precaution was taken to prevent/minimize interaction of the air flow at the inlet to the

protruding section of the liquid reservoir with the measurements within the PDA control volume. This was achieved by ensuring that the axial distance between of the control volume from the reservoir inlet was 12" (305 mm).

Data collection using the PDA unit was obtained by traversing the nozzle in 3-D so enable positioning of the PDA probe volume at different locations in the spray. To decrease experimental time, but yet have sufficient data, 2 to 3 runs were performed. The typical sample size and sampling time during data collection were set to 12000 or 360 seconds, respectively. This sample size and time were sufficient to ensure data was collected for steady state conditions, and independent of velocity samples [43]. Profiles of *SMD* (and corresponding mean axial velocities) were obtained within radial positions,  $-25.8 \leq y/D \leq 25.8$  about the spray axis, and axial positions,  $x = 100, 202$  and  $405$  mm downstream of the nozzle exit. Data at  $x = 100$ mm was the main focus of study since this is the region of interest downstream of the full-scale (or commercial) nozzle in the fluid coker. Note that for a given ambient condition and liquid used in spray studies, evaporation effects can be present with increasing axial distance from the nozzle exit [17]. This is because evaporation increases with spray surface area, and the latter increases with axial distance from the nozzle exit. However, data at  $x = 202$  and  $405$  mm were included to observe the variation of atomization properties with distance.

## **5.2 Determining experimental flow conditions**

To test for the effect of either surface tension, viscosity or nozzle geometry on *SMD* it is imperative to specify/decide on the process flow conditions required for the study at the

region of interest. A similar technique used by Chesters [35], Geraets [36], and Hurlbert et al. [37], and mentioned in Section 3.1 will be employed, but developed for *SMD* as the dependent variable instead of pressure drop. Note that the above technique is applicable to isothermal gas-liquid flows without mass transfer. The isothermal condition is applicable to the gas-liquid system in this study since the liquid-phase has larger specific heat value than that of the gas-phase, implying an approximately constant fluid temperature. This was substantiated by measuring the temperatures of the mixture at the mixing and exit points of the nozzle, which was observed to be constant. The mass transfer condition was satisfied in our system, since there was no phase change for either fluid.

In the scaled FC nozzle being studied, the exit orifice diameter is the smallest and last in contact with the two-phase mixture prior to being discharged into ambient surroundings. Hence the exit orifice is paramount in the atomization process since it controls the nozzle flow conditions. As such, similar to twin-fluid atomizers, the characteristic length in our dimensionless analysis is the exit orifice diameter. Hence in this analysis the flow conditions are based on the exit section of the nozzle since it is our region of interest. For a nozzle spraying into ambient surroundings of given temperature and pressure, the following can suffice:

$$SMD = f(D, L, \rho_G, \rho_L, Q_G, Q_L, \mu_G, \mu_L, \gamma, g) \quad (5.1)$$

In Eqn. (5.1)  $L$  represents nozzle, and using  $\rho_L$ ,  $Q_L$  and  $D$  as the repeating variables in the dimensional analysis yields Eqn. (5.2), which is a finally reduced form similar to those in Section 3.1:

$$\frac{SMD}{D} = f\left(\frac{L}{D}, \frac{\mu_G}{\mu_L}, \frac{m_G}{m_L}, \frac{P_G}{R_G T_{abs} \rho_L}, \frac{\rho_L Q_L}{\mu_L D}, \frac{Q_L^2}{g D^5}, \frac{\rho_L Q_L^2}{\gamma D^3}\right) \quad (5.2)$$

The term  $L/D$  in Eqn. (5.2) denotes conservation of geometric similarity of the nozzles, which has already been achieved in the nozzle design. The other terms have the same meaning as mentioned in Section 3.1, except that the region of interest in this case is the nozzle exit.

To study the effect of surface tension on  $SMD$ , all terms within the brackets in Eqn. (5.2) must be matched for different process flows except for the  $We$  term. Similarly, to study liquid viscosity effects on  $SMD$ , all terms within the brackets in Eqn. (5.2) must be matched in different flows except for the  $Re$  term. Note as mentioned in Section 3.1, perfect matching of all the terms on the right-hand side of Eqn. (5.2) is not always feasible [36]. Therefore restrictions on some of the terms can be relaxed based on knowledge of the dominant forces (in this case forces affecting atomization) in the system [38].

As mentioned in Section 3.1, for all fluids used in this study  $\mu_G \ll \mu_L$ , hence the second condition is also satisfied. The  $GLR$  (third term in the brackets) is an important



atomization parameter in gas-liquid flows (as established in Chapter 2), hence it was kept constant ( $GLR = 1$  and  $2\%$ ) when comparing two different sprays our analysis. Note that  $GLR$  is fixed at  $1\%$  because it is the flow condition in the commercial FC. From effervescent atomization literature the mixture pressure is an important parameter in the atomization of a given liquid density. Hence the density ratio (fourth term in the brackets in Eqn. (5.2)) was conserved in this study. Consider for instance, when investigating the influence of viscosity on  $SMD$ . During this study, for equal values of  $GLR$  and  $DR$ , the corresponding ratios of  $Re_L$ ,  $Fr_L$  and  $We_L$  in the water and glycerine-water liquid systems were 46, 0.7, and 0.5, respectively. The large  $Re_L$  ratio (46) between the respective liquids, compared to the other dimensionless quantities, suggests that viscosity effects should be most dominant for the flow conditions considered. The details are presented and discussed in Chapters 6 and 7.

### **5.3 Data Processing**

#### **5.3.1 Velocity-Drop size correlation coefficient**

It is important to estimate the magnitude of interdependence or relationship between the drop size and mean velocity within the spray, to understand the fluid mechanics within the spray. Knowledge of the fluid mechanics aids in also understanding the atomization behaviour of the spray. The correlation coefficient ( $CC$ ), is a statistical parameter used to determine if there is an association between two parameters, and also the strength of the association. The fundamental expressions are defined in the statistical text by Scheaffer and McClave [57]. In this study, the  $CC$  between the drop velocity and size was obtained from experimental data using the analogous definition in [57]. This is given by:

$$CC = \frac{\sum_{i=1}^N [(U_{d,i} - \bar{U}_d)(d_i - \bar{d})]}{\sqrt{\sum_{i=1}^N [(U_{d,i} - \bar{U}_d)^2 (d_i - \bar{d})^2]}} \quad (5.3)$$

In Eqn. (5.3),  $U_{d,i}$  and  $d_i$  denote the velocity and size of the  $i$ th drop, respectively, whereas the symbols with bars represent the arithmetic mean values. The symbol  $N$  denotes the total number of samples (or sample size). The values which are calculated from Eqn. (5.3) fall within the range  $-1 \leq CC \leq 1$ . Values of  $CC$  close to 1 indicate large drops have higher velocities or small drops have smaller velocities. On the other hand, values of  $CC$  close to -1 indicate that small drop sizes have higher velocities, or large drops have smaller velocities.

### 5.3.2 Determining important jet parameters and characteristics

In this section, the characteristics and parameters of single phase jets are defined. These parameters were evaluated for the two-phase jets in the current study. The single-phase jet characteristics were used to understand the behaviour of the two-phase jets, since literature on single-phase jet behaviour is well documented. Similar techniques are common in two-phase spray studies (e.g. [20], [21]) to compare the characteristics single-phase and two-phase sprays.

#### **Jet half-width**

From Pope [58<sup>a</sup>], one of the important characteristics of a round turbulent jet is the jet half-width,  $r_{1/2}$  (or jet radius,  $r_{jet}$ ). At a given axial location downstream of the nozzle exit,

the jet radius is defined as the radius from the spray axis, where the centerline (or maximum) velocity,  $U_{CL}$ , has reduced to half its value. From jet theory [58<sup>b</sup>], the jet half-width increases linearly with axial distance. Based on the maximum velocity from the velocity profiles obtained from the PDA measurements at the spray centreline, the different values of  $r_{jet}$  were determined.

### **Virtual origin**

For a linear increase of  $r_{1/2}$  with axial distance, a virtual origin of the jet can be defined as the axial distance, where the jet half-width is zero [58<sup>b</sup>]. Using experimental data, values of the evaluated jet half-widths were plotted against their corresponding axial locations. The virtual origin was determined from the linear plot by extrapolation to where the jet half-width was zero.

### **Self-similarity and velocity profile-fit**

Self-similarity in single-phase jets occurs beyond the developing region of the jet, i.e.  $x/D > 30$  [58<sup>c</sup>]. Self-similarity is characterised by the collapse onto a single curve for profiles of  $U/U_{CL}$  against  $r/r_{1/2}$ , (or  $r/x_{eff}$ ) at different axial distances within the developed regions of the jet. The symbol,  $x_{eff}$ , denotes the effective axial distance from the virtual origin, whereas  $r$  is a radial distance from the centre of the spray.

The momentum flow rate of a jet issuing into quiescent surroundings is conserved and is independent of axial position downstream of the nozzle exit [58<sup>d</sup>]. As a result of self-similarity and momentum conservation in the jet, the product of jet half-width and

centerline velocity is also independent of axial distance [58<sup>e</sup>]. Therefore, since the jet half-width increases linearly with axial distance, it implies the mean centreline velocity is inversely proportional to axial distance from the nozzle exit. Based on this relationship, for a turbulent round jet, the slope of the graph of mean velocity against axial distance (from the virtual origin) is  $\sim -1$ , on a log-log plot.

The velocity field in the self-similar region of a jet can be described using a velocity model. A typical model for a single-phase turbulent round jet presented in Pope [58<sup>f</sup>] is of the form:

$$\frac{\bar{U}(x, r)}{\bar{U}_{cl}(x)} = \frac{1}{\left[ 1 + \beta \left( \frac{r}{x_{eff}} \right)^2 \right]^2}, \quad (5.4a)$$

where,

$$\beta = \frac{(\sqrt{2} - 1)}{S_1^2} \quad (5.4b)$$

In Eqn. (5.4a),  $\beta$  is a coefficient, which depends on the rate at which the jet expands (or grows) downstream of the nozzle exit, whereas  $S_1$  denotes the slope of the plot of jet half-width against axial distance. Noting that  $r/x_{eff} = S_1 r/r_{1/2}$ , [58<sup>f</sup>], and combining with Eqns. (5.4a and 5.4b) yields the velocity model for a single-phase, turbulent, and self-similar jet to be:

$$\frac{\bar{U}(x, r)}{\bar{U}_{cl}(x)} = \frac{1}{\left[ 1 + 0.4142 \left( \frac{r}{r_{1/2}} \right)^2 \right]^2} \quad (5.4c)$$

For the different sprays in this study, values for the constant in Eqn. (5.4c) were evaluated by applying least square regression method on the experimental velocity data. Note that the velocities utilized in the velocity model analysis were the arithmetic mean drop velocity, and the mass-weighted mean velocity,  $U_{mw}$ . The mass-weighted velocity is defined as:

$$U_{mw} = \frac{\sum_{i=1}^N u_i d_i^3}{\sum_{i=1}^N d_i^3} \quad (5.4d)$$

### 5.3.3 Estimating liquid volume/mass balance in the spray

The amount of liquid present within the measurement region of the spray may be estimated from continuity. This was calculated by evaluating the volume of liquid through unit area of the PDA measurement volume, per unit time (also called liquid volume flux and denoted  $q_L$ ), which is expressed as:

$$q_L = \frac{\left( \sum_{i=1}^N \frac{\pi}{6} D_i^3 \right)}{A_p T_i} \quad (5.5)$$

In Eqn. (5.5),  $D_i$ ,  $T_i$  and  $N$  denote drop size, the total sampling time and total sample size, respectively. From the Dantec manual [43], the area,  $A_p$ , of the probe measurement volume is given as:

$$A_p = \frac{d_t L_s}{\sin \phi} \quad (5.6)$$

In Eqn. (5.6),  $d_t$  is the diameter of the illuminated volume,  $L_s$  is the slit width for the receiver, and  $\phi$  is the scattering angle. For the PDA system,  $d_t = 210 \times 10^{-6}$  m,  $\phi = 30^\circ$ , and  $L_s = 100 \times 10^{-6}$  m. These values give  $A_p = 42 \times 10^{-9}$  m<sup>2</sup>. The MATLAB program used in computing  $q_L$  from the text data is presented in Appendix A3.

An area averaging of the  $q_L$  across the spray gives the liquid volume flow rate within the measurement region of the spray. This area averaging is presented in Eqn. (5.7), where  $R$  is the largest measurement distance in the spray.

$$Q_L = \int q_L dA = \int q_L 2\pi r dr = 2\pi \int_0^R q_L r dr \quad (5.7)$$

The final integration of Eqn. (5.7) was evaluated using Simpson's rule. The corresponding estimated value of liquid volume flow rate was divided by the actual liquid flow rate injected into the nozzle to obtain the fraction (or percentage) of liquid within the measurement section in the spray.

Note, from Liu [16], the accuracy of Eqn. (5.7) is very dependent on accurate measurement of large drops in the drop distribution. It is therefore important to collect a sufficiently large number of samples to ensure that the large drops are statistically represented. However, Dullenkopf et al. [46] have observed that the method of

determining the mass balance in Eqn. (5.7) using the PDA can have large errors, especially in dense sprays. This is mainly due to the simultaneous presence of two or more drops in the PDA probe volume. Although, the sprays in this study are dense, the mass/volume balance method specified here was utilized to have an approximate estimate of the mass balance within the measurement section in the spray.

Note that Iso-kinetic sampling [19] is another method of obtaining liquid flux in a spray. In this method a 'L-shaped' tube, with internal diameter  $\sim 9$  mm, is placed parallel to the plane of the spray, with the orifice towards the spray. The amount of liquid entering the probe over a fixed sampling time is collected and measured. The procedure is repeated at various radial positions across the spray to obtain a liquid volume flux profile. The liquid profile is integrated to determine the amount of liquid in the spray. Iso-kinetic sampling was not used in this study because the viscous liquids (canola oil and glycerine solution) cannot flow freely through the measurement probe. This would have prevented more liquid from entering the probe within the sampling duration, resulting in inaccurate results compared to the less viscous liquid (water). Furthermore, viscous liquid through the probe would have taken a much longer time to drain than the less viscous liquids, and also be susceptible to residual liquid within the probe. This would have resulted in longer experimental and also inaccurate results for these types of liquids.

#### **5.3.4 Summation of measured *SMD* profiles**

In studying the effects of surface tension, viscosity or geometry, corresponding *SMD* profiles for similar process flow conditions can be compared using a single representative

*SMD* evaluated. This single representative *SMD* produced by the spray, at a given axial distance and process condition, is also necessary input parameter for drop correlation or modelling purposes. To date, in most studies using two-phase nozzles, a single *SMD* value obtained at the central axis of the spray is used as a representative diameter for the spray. This may not be a comprehensive representative drop diameter for the spray. For this reason, we introduce the concept of global *SMD* ( $SMD_{gb}$ ) in this study, as shown below.

A typical cross-section of a spray boundary (with flow either into or out of the plane of the page) is shown in Figure 5.2a. In most cases *SMD* and  $q_L$  profiles are symmetrical (or near-symmetrical) about the spray center or axis (i.e.  $r=0$ ), as shown in Figure 5.2b.

The *SMD* and liquid volume flux profiles have different magnitudes,  $SMD_i$  and  $(q_L)_i$ , respectively, at distance  $r$  from the spray centre up to the edge of the spray,  $R$ . Here,  $R$  can be taken as the furthest radial measurement location from the spray axis at a given axial downstream distance, or the radial distance from the spray centre where there is no significant change in drop velocity ( $U_d$ ) with radial distance. To ensure that the *SMDs* in dense and sparse region of the spray are represented without bias, each *SMD* is weighted with its corresponding liquid volume flux and integrated over the spray cross-section. This is mathematically representation of the averaging process in the  $r$  direction yields:



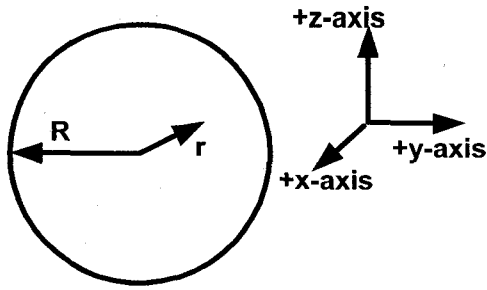


Figure 5.2 (a)

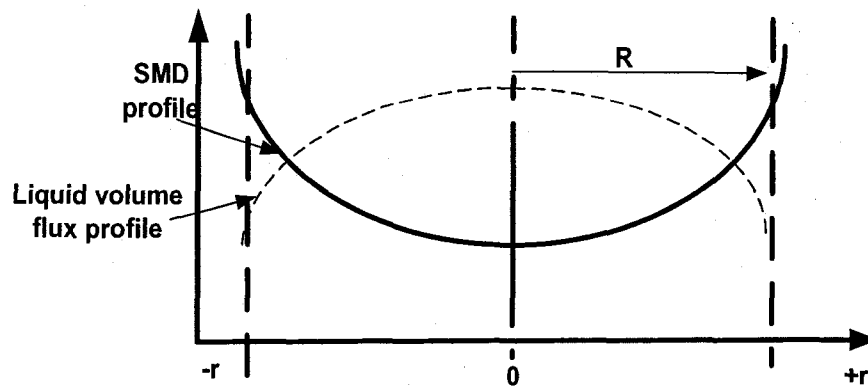


Figure 5.2 (b)

Figure 5.2: Schematic of spray cross-section (top) and typical  $SMD$  and liquid volume flux,  $q_L$  profiles (bottom) seen in a spray from a line scan across the spray through the spray axis.

$$SMD_{gb} \int_0^R (q_L)_i 2\pi r dr = \int_0^R SMD_i (q_L)_i 2\pi r dr \quad (5.8)$$

Simplifying gives:

$$SMD_{gb} = \frac{\int_0^R SMD_i (q_L)_i r dr}{\int_0^R (q_L)_i r dr} \quad (5.9)$$

Hence in a general case where the *SMD* profile ranges from  $-R \leq y \leq +R$  (as in this study), the global *SMD* can be evaluated from:

$$SMD_{gb} = \frac{\int_{-R}^{+R} SMD_i(q_L)_i r dr}{\int_{-R}^{+R} (q_L)_i r dr} \quad (5.10)$$

The terms within the integral signs were evaluated using Simpson's Rule.

### 5.3.5 *SMD<sub>gb</sub>* Correlation

Obtaining a correlation for the global *SMD* with respect to dimensionless process conditions is a necessary final step in studying the combined effect of surface tension, viscosity and geometry on drop size. Such correlations provide valuable information for nozzle design or process control to achieve a target magnitude of drop size within the specified limits of nozzle and process parameters. In this study, numerous *SMD* data were collected for the two nozzle sizes at various gas and liquid conditions. However, throughout the study the conserved dimensionless groups were  $L/D$  and  $\mu_G/\mu_L$ . One method of expressing *SMD* correlations is using a power-law relationship as presented and discussed in Chapter 2. Hence for the remaining groups in Eqn. (5.2), one can obtain a power-law relationship for the global *SMD* as follows:

$$\frac{SMD_{gb}}{D} = C(GLR)^a (DR)^b (Re)^c (Fr)^d (We)^e \quad (5.11)$$

In Eqn. (5.11),  $DR$  denotes density ratio, whereas  $C$ , and indices  $a$ ,  $b$ ,  $c$ ,  $d$  and  $e$  are constants obtained from regression curve-fit using experimental data. In the curve-fit procedure, Eqn. (5.11) is linearized to the form:

$$\begin{aligned} \text{LOG}_{10}\left(\frac{SMD_{gb}}{D}\right) = & C + a\text{LOG}_{10}(GLR) + b\text{LOG}_{10}(DR) + c\text{LOG}_{10}(Re) + d\text{LOG}_{10}(Fr) \\ & + e\text{LOG}_{10}(We) \end{aligned} \quad (5.12)$$

The constants in Eqn. (5.12) can be obtained from a least-squares method using a standard mathematical software. The Maple software was used in this study.

### 5.3.6 Error/Uncertainty Analysis

Uncertainty or error analysis is necessary to establish the bounds on the accuracy of measured experimental quantities. The random errors in the measured parameters were estimated using statistical techniques. From Coleman and Steele [59], a sample size,  $N (< 31)$ , with standard deviation,  $S$ , follows a  $t$  distribution with  $N - 1$  degrees of freedom. For this sample distribution, the corresponding random error (or uncertainty) in the measured mean is given by:

$$U_{mean} = t \frac{S}{\sqrt{N}} \quad (5.13)$$

In Eqn. (5.13),  $t$  is a value obtained from a  $t$  distribution table at a given confidence interval and  $N - 1$  degrees of freedom. The above equation was used in all the

measurements in this study. Note that to obtain the overall uncertainty  $U_X$  in a parameter  $X$  that is dependent on parameters,  $y_i$ , we have:

$$\frac{U_X}{X} = \left[ \sum_{i=1}^n \left( \frac{1}{X} \frac{\partial X}{\partial y_i} U_{y_i} \right)^2 \right]^{\frac{1}{2}} \quad (5.14)$$

In Eqn. (5.14),  $U_{y_i}$  is the uncertainty in parameter  $y_i$ .

The next Chapter presents the results of the measurement procedure and analysis presented above.

# CHAPTER 6

## RESULTS AND DISCUSSION – VELOCITY DATA

This Chapter presents results of the velocity profile within the measurement region in the spray. The first profiles presented here are mainly those of air-water. This was because a major proportion of the profiles had similar trends to the canola and glycerine-water sprays, and repetition was avoided. The remainder of the plots not shown in this section is presented in Appendix A4. It is imperative to observe the trends in the spray velocity profiles in order to aid in the explanation of the corresponding drop-size profiles, which are presented in Chapter 7.

### 6.1 Velocity-Drop size correlation

It was stated in Section 5.3.1 that the velocity-drop size correlation coefficient,  $CC$ , gives an indication of the relationship between the velocity and drop size within the spray. Figures 6.1 and 6.2 show the variation of  $CC$  across the spray, for water at  $95 \times 10^{-6} \text{ m}^3/\text{s}$  and 1% and 2%  $GLR$ , respectively. In Figure 6.1, the  $CC$  is negative ( $\sim -0.1$ ) at the spray centreline ( $r = 0$ ) for  $x = 100 \text{ mm}$ . This suggests that the small drops have higher velocities, whereas the bigger drops have lower velocities. This indicates that the small and large drops are undergoing acceleration and deceleration, respectively, which is due to the exchange of momentum between the gas (air) and drops. This physical process is typical of sprays in the near-field region as stated by Liu [16<sup>c</sup>], which is evident in Figure 6.1, but not significantly observed in Figure 6.2.

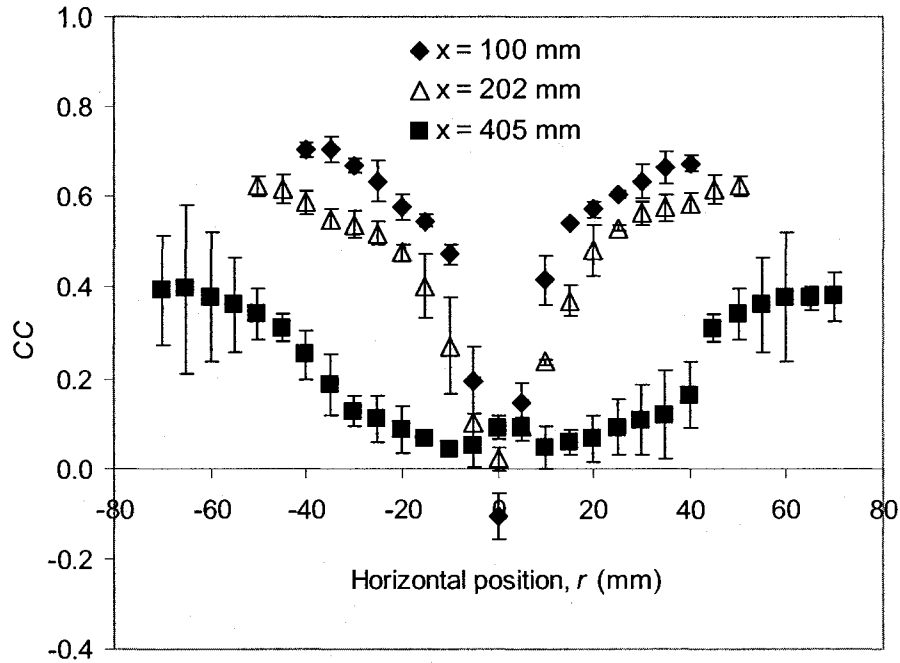


Figure 6.1 – Profiles of  $CC$  across the spray and at axial positions 100, 202, and 405 mm for the SS-1.0 nozzle ( $D = 3.1$ mm). Data is for water at  $95 \times 10^{-6} \text{ m}^3/\text{s}$  and 1.0%  $GLR$ . The error bars show the 95% confidence limits for the  $CC$  values.

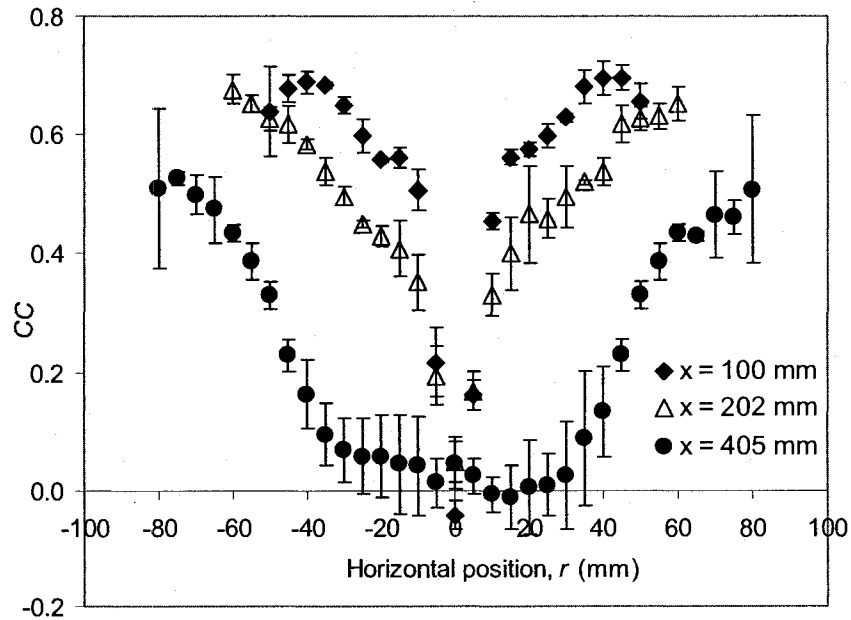


Figure 6.2 - Profiles of  $CC$  across the spray and at axial positions,  $x = 100, 202,$  and 405 mm for the SS-1.0 nozzle ( $D = 3.1$ mm). Data is for air-water spray ( $\mu_L = 1 \text{ mPa}\cdot\text{s}$ ,  $\gamma = 70 \text{ mN/m}$ ) with liquid flow rate of  $95 \times 10^{-6} \text{ m}^3/\text{s}$  and 2.0%  $GLR$ . The error bars show the 95% confidence limits for the  $CC$  values.

The trend in the graphs for each axial location shows that the  $CC$  values increase positively with increasing radial distance. The increasing trend in  $CC$  with radial distance first indicates a stronger linear relationship exists between the drop velocity and sizes, as one traverses outwards from the spray centreline. Secondly, it implies that the smaller drops have lower velocities, whereas the bigger drops have higher velocities. Thirdly, it can be deduced that the bigger drops are concentrated at the outer regions of the spray, whereas the smaller drops occupy regions closer to the centre of the spray. Based on these observations, it implies that the larger drops possess a higher momentum, which enables them occupy the outer regions of the spray. These findings are in agreement with the observations by Ariyapadi et al. [21] for sprays produced using a small-scale coker nozzle similar to the one being tested, and for effervescent and twin-fluid sprays as documented by Sovani et al. [17].

The shapes of the  $CC$  profiles vary with increasing axial distance from the nozzle exit. The profiles are 'V-shaped' at  $x = 100$  and  $202$  mm and tend to flatten more significantly at  $x = 405$  mm. As a result, from Figure 6.1, the maximum positive correlation at the outer regions of the spray are 0.4, 0.6 and 0.7 at  $x = 100$ , 202, and 405 mm, respectively, whereas at the spray centre the  $CC$  values (for the same axial positions) are -0.1, 0.0 and 0.1, respectively. This tendency towards flattening of the  $CC$  profile across the spray as axial distance increases indicates the attainment of velocity equilibrium between the drops and the carrier gas. This characteristic is also shown for the 2%  $GLR$  condition in Figure 6.2. According to Liu [16<sup>e</sup>], this trend is also a characteristic of two-phase sprays,

and occurs as the gas turbulence decays and the momentum exchanges between the gas and drops ceases.

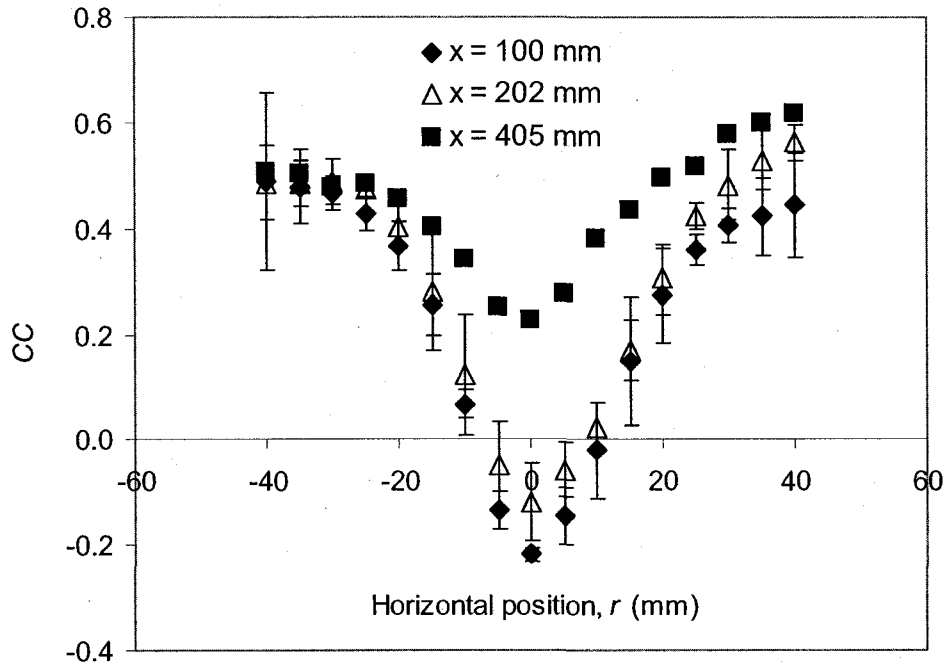


Figure 6.3 - Profiles of  $CC$  across the spray and at axial positions,  $x = 100, 202,$  and  $405$  mm for the SS-1.0 nozzle ( $D = 3.1$ mm). Data is for air-glycerine solution spray ( $\mu_L = 67$  mPa-s,  $\gamma = 61$  mN/m) with liquid flow rate of  $114 \times 10^{-6}$  m<sup>3</sup>/s and 1.0%  $GLR$ . The error bars show the 95% confidence limits for the  $CC$  values.

The  $CC$  profiles for glycerine solution at  $114 \times 10^{-6}$  m<sup>3</sup>/s and 1%  $GLR$  are shown in Figure 6.3. Figure 6.4 shows  $CC$  profiles for glycerine solution at  $105 \times 10^{-6}$  m<sup>3</sup>/s and 2%  $GLR$ . The 'V-shaped' profiles observed in Figures 6.1 and 6.2 are also present in Figures 6.3 and 6.4. However, Figures 6.3 and 6.4 show  $CC$  values  $\sim -0.2$  at  $x = 100$  mm, and  $-0.1$  at  $x = 202$  mm close to the spray centre ( $r = 0$ ). These  $CC$  values are higher than those observed for the water sprays in Figures 6.1 and 6.2. The higher  $CC$  values in the glycerine-solution spray may be attributed to the higher jet inertia compared to those of



the water sprays. The higher jet inertia results in a longer region where small drops following the gas phase have to decelerate compared to the water sprays. The  $CC$  profile at  $x = 405$  mm in Figure 6.3 shows a much shorter “V” shape than the other two. This implies the tendency for the profiles to flatten with increasing axial distance. Note that no  $CC$  plots at  $x = 405$  mm are present in Figure 6.4. No data was collected for the corresponding flow conditions at  $x = 405$  mm because the PDA receiver was susceptible to deposits of a thin liquid film affecting measurements.

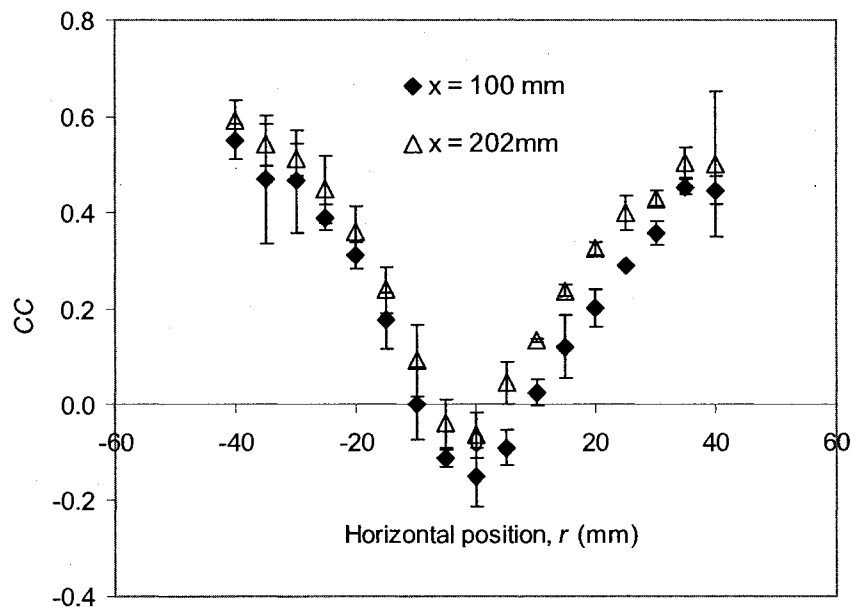


Figure 6.4 - Profiles of  $CC$  across the spray and at axial positions,  $x = 100$  and  $202$  mm for the SS-1.0 nozzle ( $D = 3.1$  mm). Data is for air-glycerine solution spray ( $\mu_L = 67$  mPa-s,  $\gamma = 61$  mN/m) with liquid flow rate of  $105 \times 10^{-6}$  m<sup>3</sup>/s and 2.0%  $GLR$ . The error bars show the 95% confidence limits for the  $CC$  values.

The corresponding  $CC$  profiles using canola oil at  $105 \times 10^{-6}$  m<sup>3</sup>/s are presented in Figures 6.5 and 6.6 for 1% and 2% flow conditions, respectively. The same ‘V’-shaped trends at  $x = 100$  and  $202$  mm are observed as in Figures 6.1 to 6.4 with a decreasing correlation at

the outer edges of the spray. The  $CC$  profiles at  $x = 405$  mm also tends to flatten just as in the other Figures. Note that there is no significantly observed negative correlation at  $x = 100$  mm and near the spray centre ( $r = 0$ ) in Figures 6.5 and 6.6., which is similar to the observation in the water spray at 2%  $GLR$  (Figure 6.2). Based on the trends in the  $CC$  profiles at  $x = 100$  mm and  $r = 0$ , in Figures 6.1 to 6.6 it can be concluded that the higher jet inertia, is associated with the glycerine solutions. This results in a longer region where small drops following the gas phase have to decelerate compared to the water and canola oil sprays.

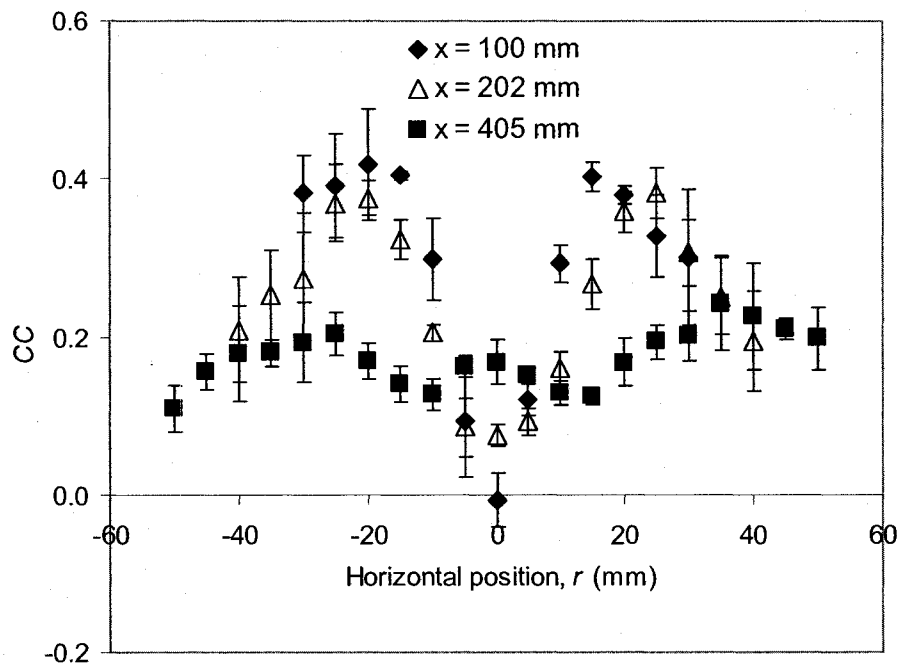


Figure 6.5 - Profiles of  $CC$  across the spray and at axial positions,  $x = 100$ , 202, and 405 mm for the SS-1.0 nozzle ( $D = 3.1$ mm). Data is for air-canola oil spray ( $\mu_L = 66$  mPa-s,  $\gamma = 25$  mN/m) with liquid flow rate of  $105 \times 10^{-6}$  m<sup>3</sup>/s and 1.0%  $GLR$ . The error bars show the 95% confidence limits for the  $CC$  values.

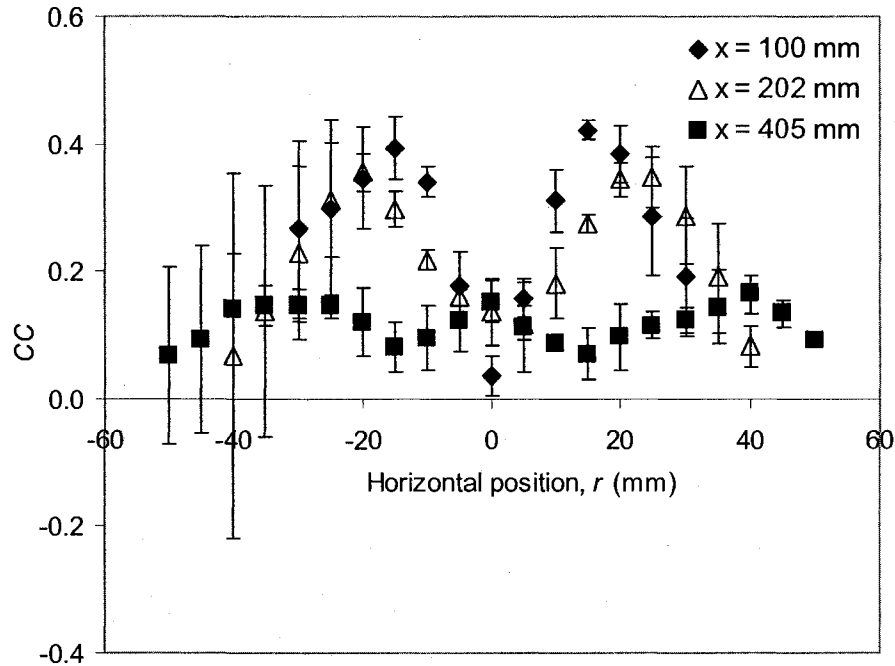


Figure 6.6 - Profiles of  $CC$  across the spray and at axial positions,  $x = 100, 202,$  and  $405$  mm for the SS-1.0 nozzle ( $D = 3.1$ mm). Data is for air-canola oil spray ( $\mu_L = 66$  mPa-s,  $\gamma = 25$  mN/m) with liquid flow rate of  $105 \times 10^{-6}$  m<sup>3</sup>/s and 2.0%  $GLR$ . The error bars show the 95% confidence limits for the  $CC$  values.

## 6.2 Number-weighted and mass-weighted velocity profiles

Figure 6.7 presents the number and mass-weighted velocity profiles across the spray for water at  $95 \times 10^{-6}$  m<sup>3</sup>/s and 1.0%  $GLR$ . Figure 6.7 shows that all the velocity profiles are bell-shaped for all axial positions. The highest velocity occurs at the centre of the spray ( $r = 0$ mm) and decreases with increasing radial distance from the centre of the spray. Similar results in Figure 6.7 have been observed in number-weighted velocity profiles in sprays produced by pressure, twin-fluid and effervescent atomizers as stated by Sovani [17]. The same observations were made by Copan et al. [20] and Ariyapadi et al. [21] for these types of FC nozzles. This study goes further to show the mass-weighted velocity

profiles to enable comparison with the number-weighted velocity profiles, which are commonly presented in literature.

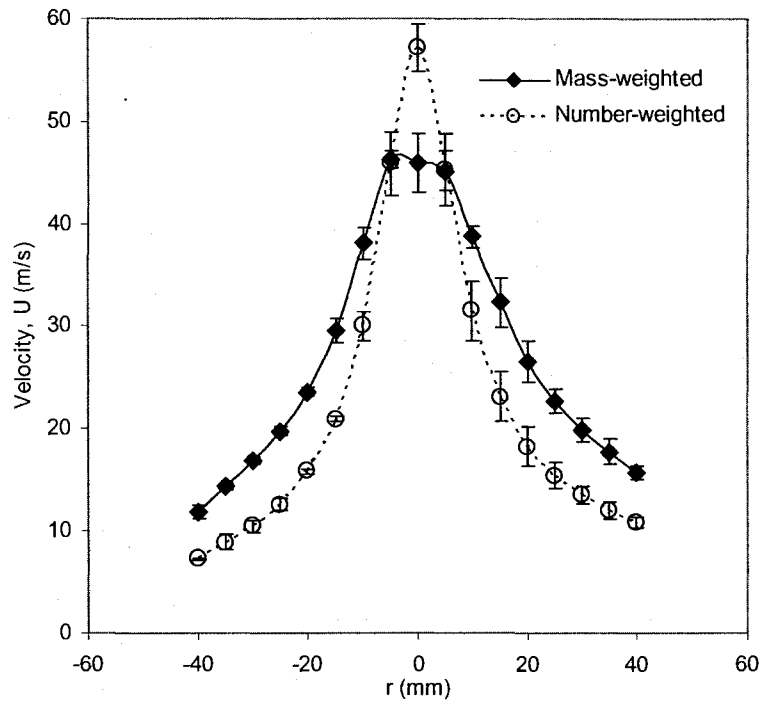


Figure 6.7 (a):  $x = 100$  mm

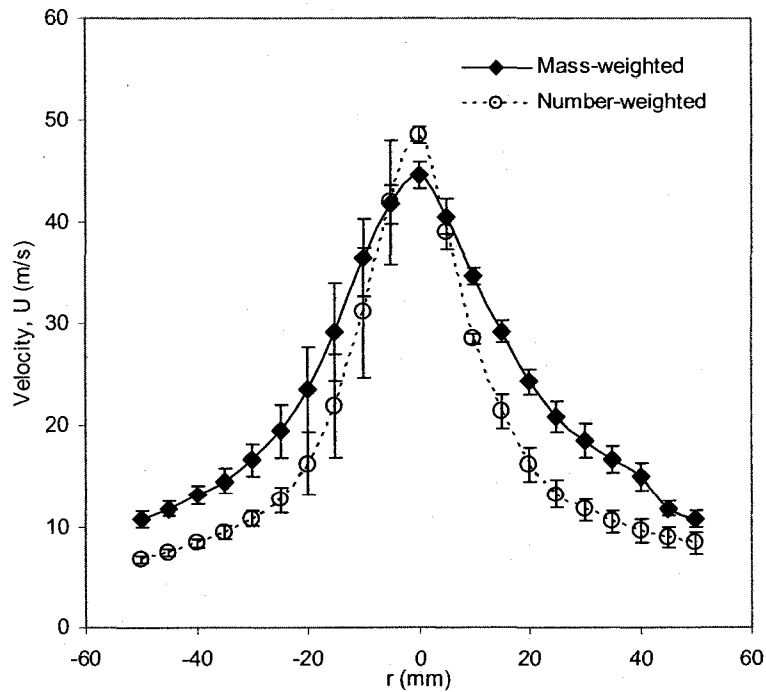


Figure 6.7 (b):  $x = 202$  mm

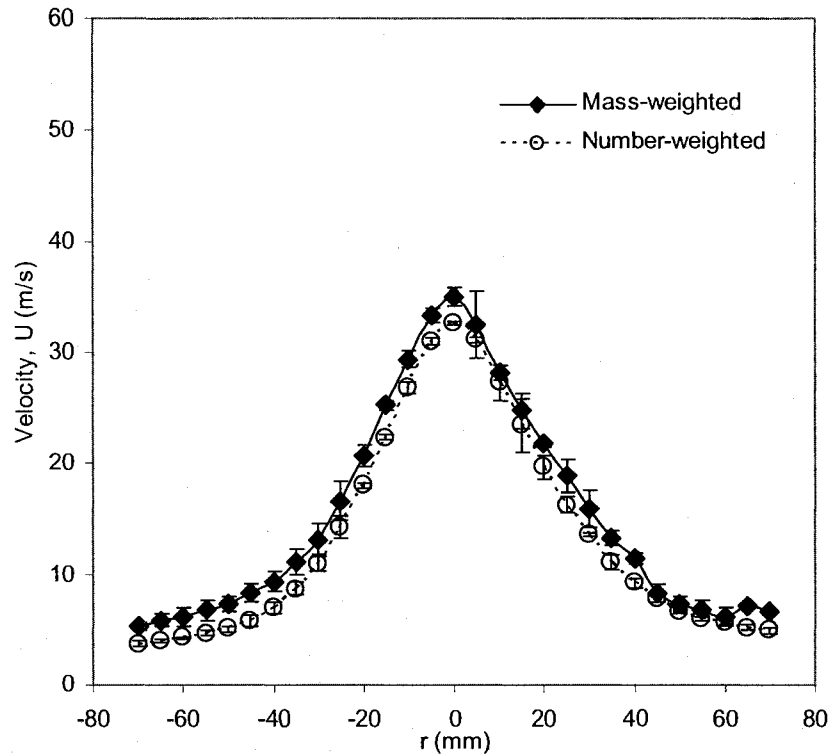


Figure 6.7 (c):  $x = 405$  mm

Figure 6.7 – Number and mass-weighted velocity profiles at axial positions (a) 100 mm, (b) 202 mm, and (c) 405 mm for SS-1.0. Data is for water at  $95 \times 10^{-6} \text{ m}^3/\text{s}$  and 1.0% GLR. The error bars show the 95% confidence limits for the velocity measurements. Lines are to guide the eyes.

Figure 6.7 also shows that at  $x = 100$  and 202 mm, the mass-weighted velocity,  $U_{mw}$  in most cases is greater (within limits of experimental error) than the number-weighted velocity,  $U_{nw}$ . The only exceptions are regions close to the spray center i.e.  $-10 < r < 10$  mm, where  $U_{mw} < U_{nw}$ . The  $U_{mw}$  depicts the momentum per unit volume of a drop in the spray. As mentioned in Section 6.1, a strong positive correlation exists between drop velocity and size for increasing radial positions away from the central regions of the spray. This strong correlation contributes more significantly to  $U_{mw}$  than  $U_{nw}$ , and can suggest that  $U_{mw}$  is a more significant parameter for spray penetration just

on entry into a fluid coker, compared to  $U_{nw}$ . With increasing axial distance ( $x = 405\text{mm}$ ) the differences in magnitude between both velocity profiles begin to decrease. At this point, the spray begins to tend towards attaining equilibrium conditions, which means the drop velocities are equal to the gas velocity. The axial distances where this occurs varies with drop sizes [16<sup>e</sup>].

### 6.3 Axial variation of jet-half-width and centreline velocity

The velocity data in Figure 6.7 were used to determine the jet half-width,  $r_{1/2}$  as defined in Section 5.3.2. The variation of  $r_{1/2}$  with axial distance is presented in Figure 6.8.

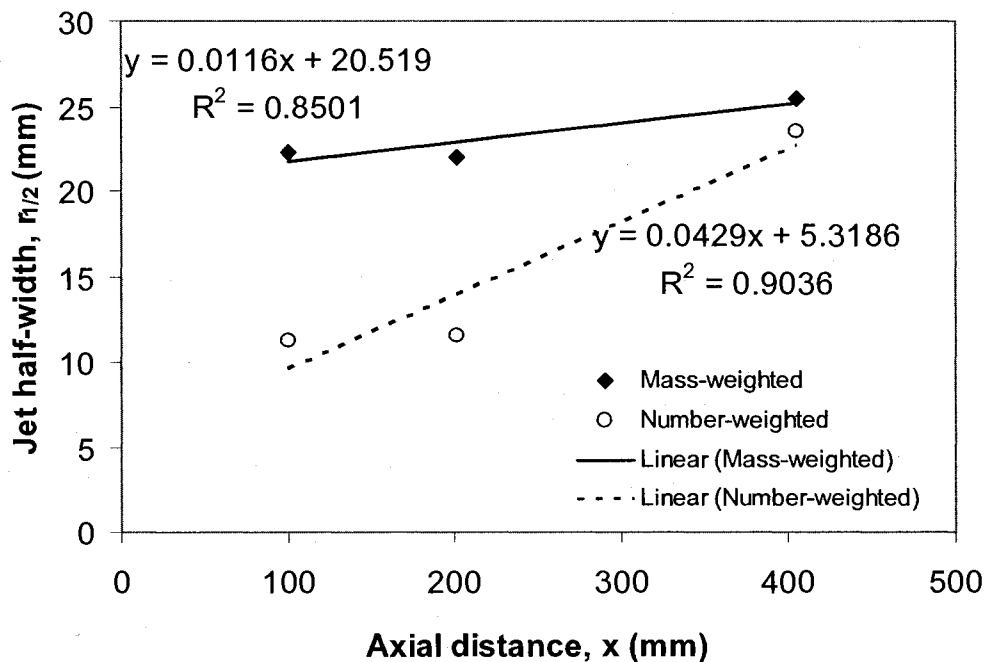


Figure 6.8 – Variation of jet-half-width (from number and mass-weighted velocity profiles) at axial positions 100, 202, and 405 mm for SS-1.0. Data is for water at  $95 \times 10^{-6} \text{ m}^3/\text{s}$  and 1.0% GLR.

Figure 6.8 shows that the jet-half-width based on the number-weighted velocity data varies almost linearly with axial distance, according to jet theory [58<sup>b</sup>]. Ariyapadi et al.

[21] also observed a similar trend in their studies using only number-weighted velocity data. However, comparison of the plots in Figure 6.8 also depicts that the rate of spread or expansion of the spray based on the mass-weighted velocity profile is slower than that obtained from the number-weighted velocity profile. This is a direct consequence from Figure 6.7, where there is lesser change in the width of the  $U_{mw}$  profiles compared to the  $U_{nw}$  profiles. Note that the strong linear correlation of jet half-width with axial distance presented here is as observed in majority of the sprays studied. Weak correlations are mainly evident when there is reduced jet expansion associated with the measurement region in the spray.

The values of the virtual origin,  $x_0$  were evaluated from the linear plots in Figure 6.8. The values were 1769 mm and 124 mm, for the number and mass weighted velocity data, respectively. The physical meaning implies that the spray behaves as if its origin is behind the nozzle at an axial position corresponding to the above values for both the mass-weighted and number-weighted velocity profile data. These values for the virtual origin were used to plot a log-log variation of centreline velocity with the effective axial distance from the virtual origin,  $x_{eff}$  ( $= x + x_0$ ), as shown in Figure 6.9. Similar to the previous paragraph, note that the strong linear correlation of decreasing jet centreline velocity with axial distance presented here is as observed in majority of the sprays studied. Weak correlations are mainly evident when there is reduced jet expansion associated with the measurement region in the spray.

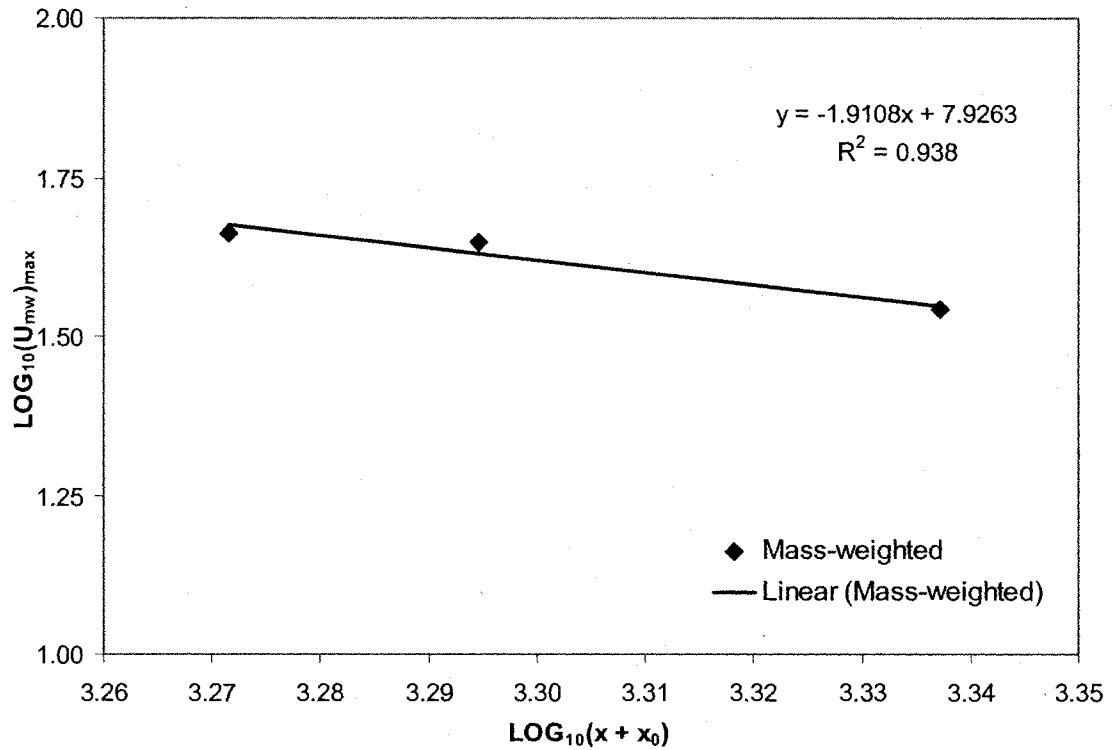


Figure 6.9 (a): Mass-weighted data

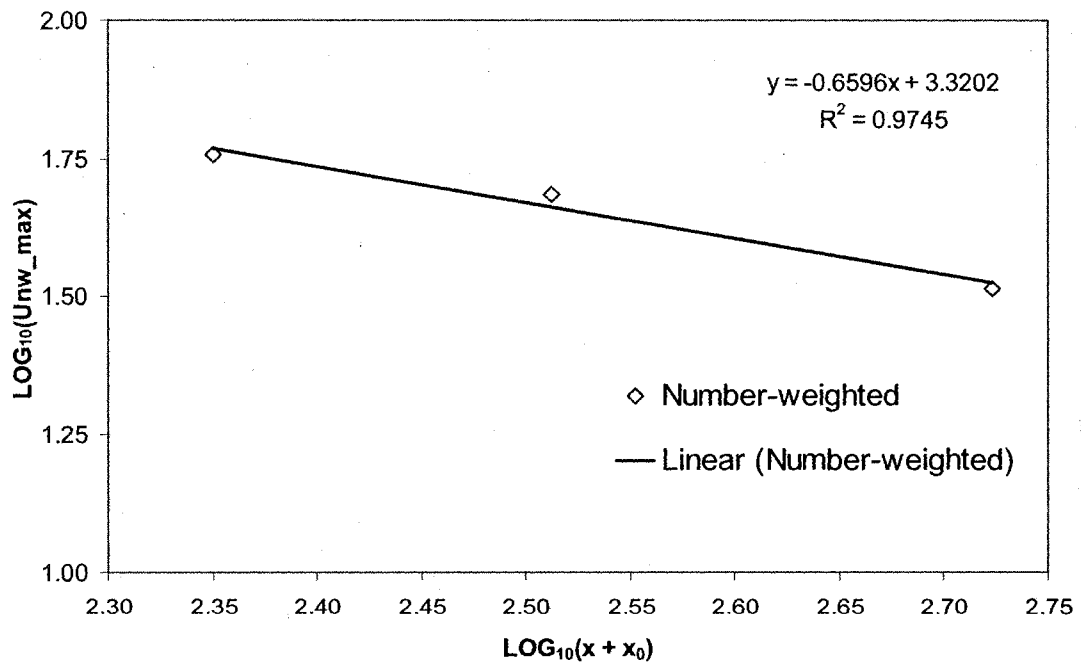


Figure 6.9 (b): Number-weighted data

Figure 6.9 – Variation of centreline velocity at axial positions 100, 202, and 405 mm using (a) mass-weighted data, (b) number-weighted data. Data is for water at  $95 \times 10^{-6} \text{ m}^3/\text{s}$  and 1.0% GLR. using SS-1.0.



The plots in Figure 6.9 show a decrease in centerline velocity with increasing axial distance. This trend combined with the increase in the jet half-width with increasing axial distance shows that momentum conservation within the spray is responsible for this characteristic. Figure 6.9 shows that the centreline velocity for the mass-weighted data decays with a slope of  $\sim -2$ , whereas that of the number-weighted velocity data decays with a  $\sim -0.7$  for the. Note from jet theory that the velocity for a single-phase turbulent round jet decays with a slope of  $\sim -1$  [58<sup>c</sup>]. The values of -0.7 and -2.0 obtained here are within the vicinity of -1.0, since they were obtained from a two-phase spray as against for a single-phase jet as derived from theory. Table 6.1 shows a summary of the values of the slopes for all the experiments. The average slopes from the number-weighted and mass-weighted data are -0.9 and -1.1, respectively. These values are within 10% of the theoretical value of -1.0 mentioned above, and suggest that the centreline velocity decay with axial distance in all the different gas-liquid systems is similar to those of single-phase turbulent round jets.

Table 6.1 – Summary of slopes from log-log plots of centreline velocity vs effective axial distance for all two-phase spray systems in this study.

Fluid System	Nozzle Name	Liquid volume flow rate, $Q_L$ ( $\times 10^{-6} \text{ m}^3/\text{s}$ )	GLR (%)	Slope from number-weighted data	Slope from mass-weighted data
Air-Water	SS-1.0	95	1	-0.7	-2.0
Air-Glycerine Solution	SS-1.0	114	1	-1.6	-0.5
Air-Canola Oil	SS-1.0	105	1	-0.7	-0.8
Air-Water	SS-1.0	95	2	-0.7	-13.8(outlier)
Air-Glycerine Solution	SS-1.0	105	2	-1.1	-0.2
Air-Canola Oil	SS-1.0	105	2	-0.7	-1.1
Air-Glycerine Solution	SS-1.0	79	1	-0.8	-0.5
Air-Glycerine Solution	SS-1.3	163	1	-0.5	-0.3
Air-Water	SS-1.3	190	1	-0.4	-0.3

#### 6.4 Self-similarity in velocity profiles

To determine if the velocity profiles within the spray attained self similarity, normalized velocity and normalized radial positions were plotted at different axial positions. Figure 6.10 shows the normalized profiles for the mass and number-weighted velocity profiles at  $x = 100, 202, \text{ and } 405 \text{ mm}$ .

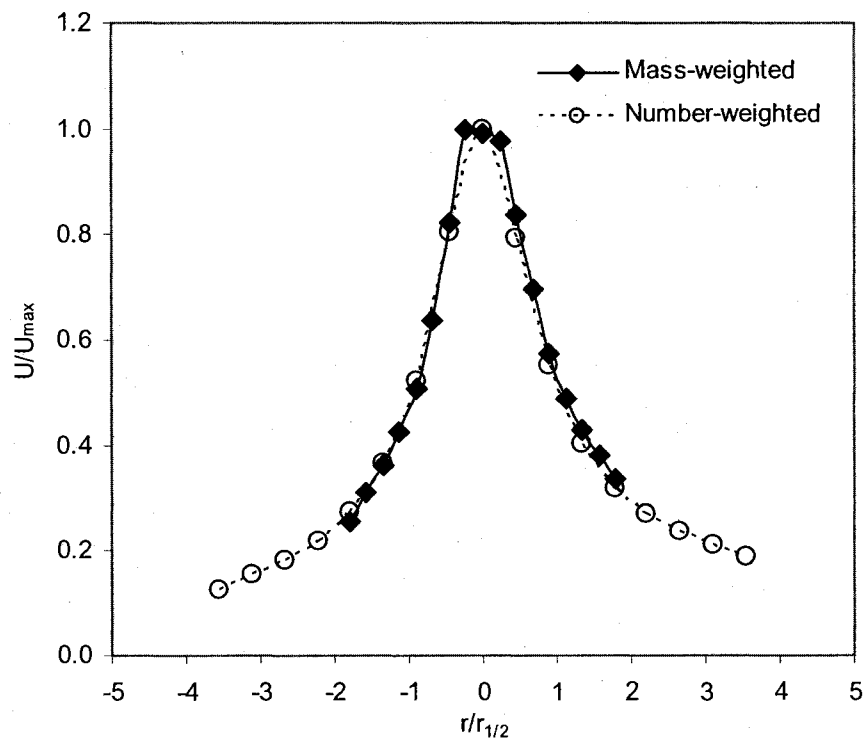


Figure 6.10 (a):  $x = 100 \text{ mm}$

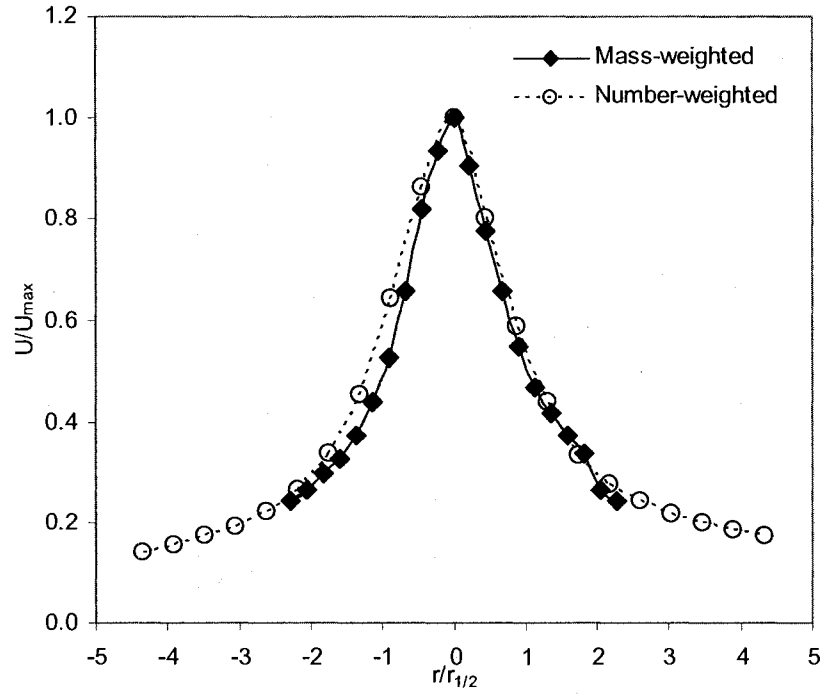


Figure 6.10 (b):  $x = 202$  mm

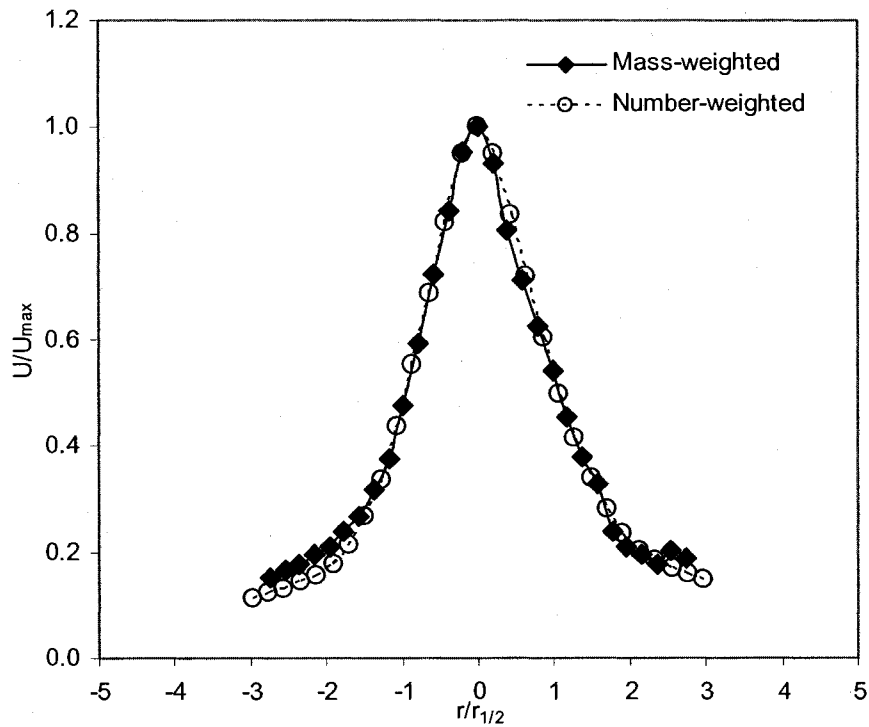


Figure 6.10 (c):  $x = 405$  mm

Figure 6.10 – Comparison of normalized mass-weighted and number-weighted velocity profiles for self similarity at axial positions (a) 100 mm, (b) 202 mm, and (c) 405 mm. Data is for water at  $95 \times 10^{-6} \text{ m}^3/\text{s}$  and 1.0% GLR using SS-1.0 nozzle.

The plots from Figure 6.10 show that the mass-weighted and number weighted velocity profiles collapse on each other at the axial distances of interest. This implies that both velocity profiles are self similar, which is a typical characteristic of turbulent sprays. The physical meaning being that the both profiles may be modeled with a single profile at the different axial distances (Eqn. 5.4 (c)). For all the other systems, the behaviour was similar to the plot of Figure 6.10. To determine the self similarity behaviour for each velocity profile with axial distances, Figure 6.11 was plotted.

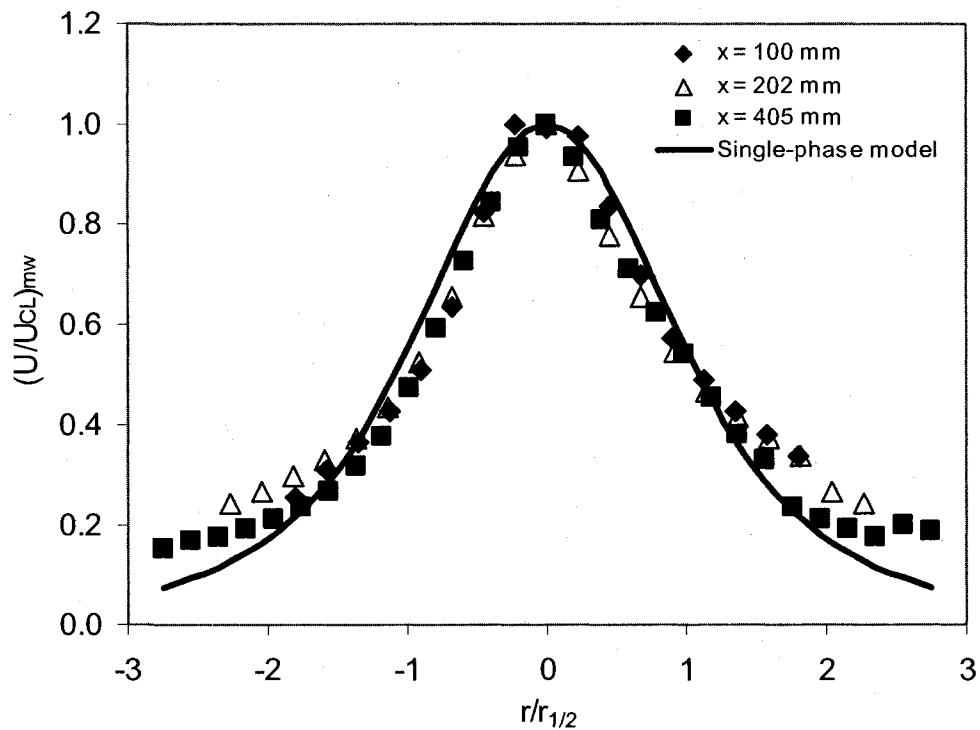


Figure 6.11 (a): Mass-weighted data

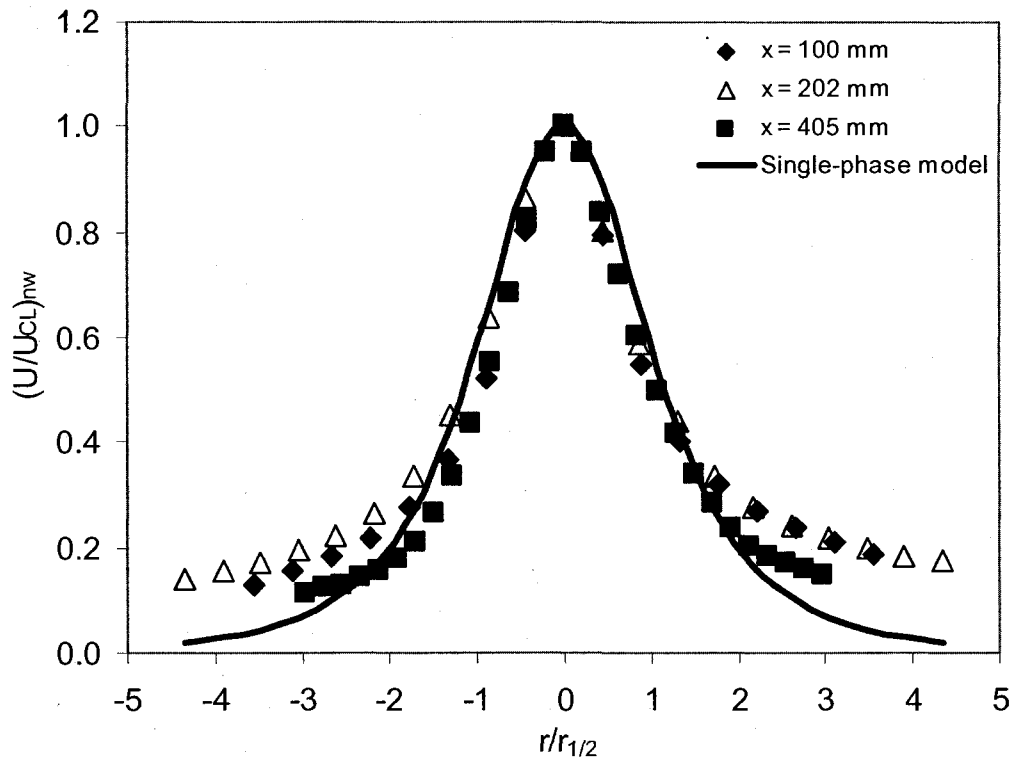


Figure 6.11 (b): Number-weighted data

Figure 6.11 – Comparison of self similarity at different axial positions for the normalized (a) mass-weighted and (b) number-weighted velocity profiles. Data is for water at  $95 \times 10^{-6} \text{ m}^3/\text{s}$  and 1.0% *GLR* using SS-1.0 nozzle.

Each plot in Figure 6.11 shows that there is a collapse of a majority of the data in the velocity profiles on one another. This confirms that both velocity profiles exhibit self similarity within the range of axial distances in this test. For comparison with a single-phase spray, the single-phase velocity model (Eqn. 5.4 (c)) has been superimposed on each plot. Using least-squares regression procedure, the coefficients of  $(r/r_{1/2})^2$  were evaluated to be 0.3510 and 0.3088 for the mass-weighted and number-weighted velocity profiles, respectively. The corresponding values of the coefficients of  $(r/r_{1/2})^2$  for all other systems are presented in Table 6.2. Note that the average values based on the number and

mass-weighted data are 0.3623 and 0.4073, respectively. The experimental values are within 13% and 2% compared to the theoretical value of 0.4142 (in Eqn. 5.4 (c)).

Table 6.2 – Summary of curve-fit coefficients of  $(r/r_{1/2})^2$  (Eqn. 5.4 (c)) for all two-phase spray systems in this study.

Fluid System	Nozzle Name	Liquid volume flow rate, $Q_L$ ( $\times 10^{-6}$ m <sup>3</sup> /s)	GLR (%)	Coefficient from number-weighted data	Coefficient from mass-weighted data
Air-Water	SS-1.0	95	1	0.3088	0.3510
Air-Glycerine Solution	SS-1.0	114	1	0.4342	0.5204
Air-Canola Oil	SS-1.0	105	1	0.3485	0.3783
Air-Water	SS-1.0	95	2	0.3256	0.3251
Air-Glycerine Solution	SS-1.0	105	2	0.4205	0.4920
Air-Canola Oil	SS-1.0	105	2	0.3364	0.3698
Air-Glycerine Solution	SS-1.0	79	1	0.3844	0.4560
Air-Glycerine Solution	SS-1.3	163	1	0.3650	0.4237
Air-Water	SS-1.3	190	1	0.3375	0.3491

Note that for all gas-liquid systems, there is lesser deviation between the single-phase model and the experimental data within the range  $-0.75 < (r/r_{1/2}) < 0.75$ . The large difference at the spray periphery suggests that the drop velocities do not decrease as fast that suggested by the single-phase. This can be attributed to the higher inertia of the drops compared to those of gas jets, which is what is the single-phase model in based on. A similar trend in the two-phase velocity profile in Figure 6.11, was also observed by Ariyapadi et al. [21]. To determine if self-similarity also exists for different liquid viscosities, surface tension and nozzle sizes, the corresponding normalized velocity profiles were plotted, using the same procedure for the air-water system.

#### 6.4.1 Different liquid viscosities

To investigate the effect of liquid viscosity on drop size using the SS-1.0 nozzle, the independent dimensionless quantities presented on the right-hand side of Eqn. 5.11 were computed. The most important dimensionless quantities to conserve were the  $GLR$  and density ratio ( $\rho_G/\rho_L$ ) since these quantities affect drop sizes in atomizers as established from atomization literature [3, 11, 13, 17]. The dimensionless quantity to vary considerably is the Liquid Reynolds number  $Re_L$ , since it compares drop viscosity to drop momentum/inertia.

The flow condition corresponding to  $GLR = 1\%$  using the SS-1.0 nozzle is presented in Table 6.3. Note that  $Re_L$  for the water system is about 46 times that of the glycerine-water system. It is presumed that this difference in  $Re_L$  is sufficient to investigate the effect of liquid viscosity on liquid atomization. The corresponding velocity profiles at  $x = 100, 202$  and 405 mm are presented in Figure 6.12.

Table 6.3 – Test conditions at 1%  $GLR$  to study the effect of liquid viscosity on atomization using the SS-1.0 nozzle.

Fluid System	Liquid volume flow rate, $Q_L$ ( $\times 10^{-6}$ m <sup>3</sup> /s)	$GLR$ , $\left(\frac{m_G}{m_L}\right)$ (%)	$DR$ , $\left(\frac{\rho_G}{\rho_L}\right)$	$Re_L$ , $\left(\frac{4\rho_L Q_L}{\pi\mu_L D}\right)$	$Fr_L$ , $\left(\frac{16Q_L^2}{\pi^2 g D^5}\right)$	$We_L$ , $\left(\frac{16\rho_L Q_L^2}{\pi^2 \gamma D^3}\right)$
Air-Water	95	1.0	0.0034	38791	5169	6948
Air-Glycerine Solution	114	1.0	0.0032	840	7527	13959
Ratio (Water-to-glycerine solution data)	0.8	1.0	1.1	46	0.7	0.5

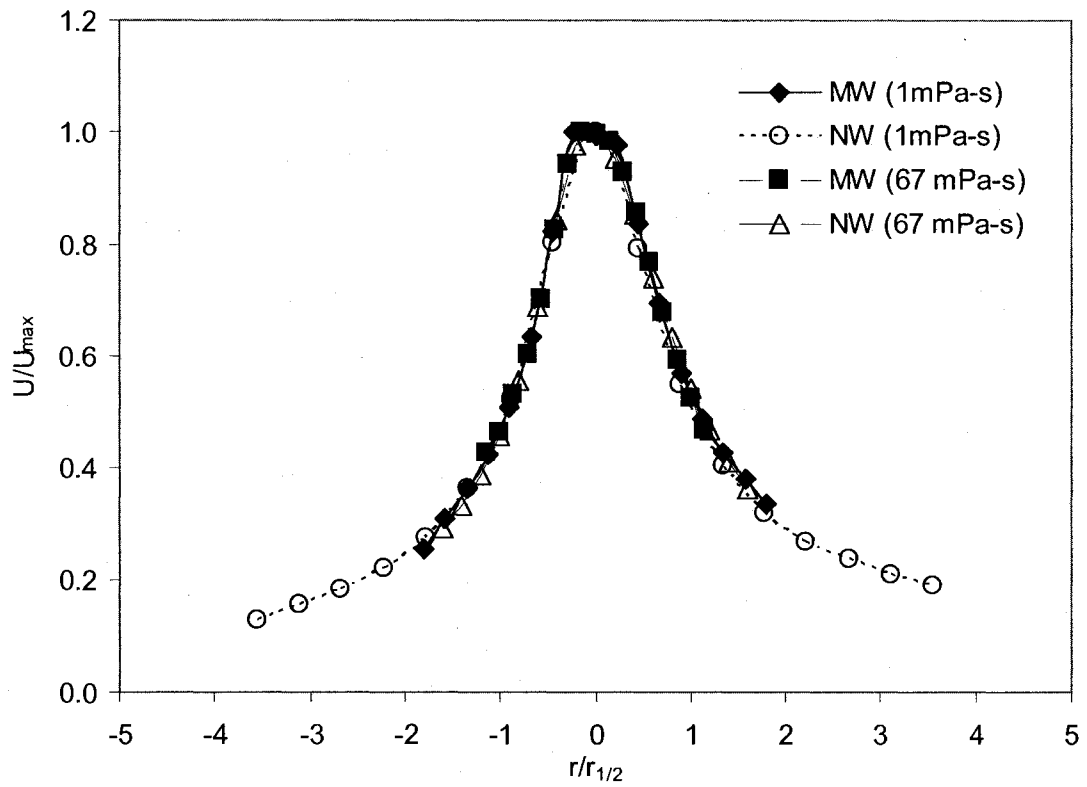


Figure 6.12 (a):  $x = 100$  mm

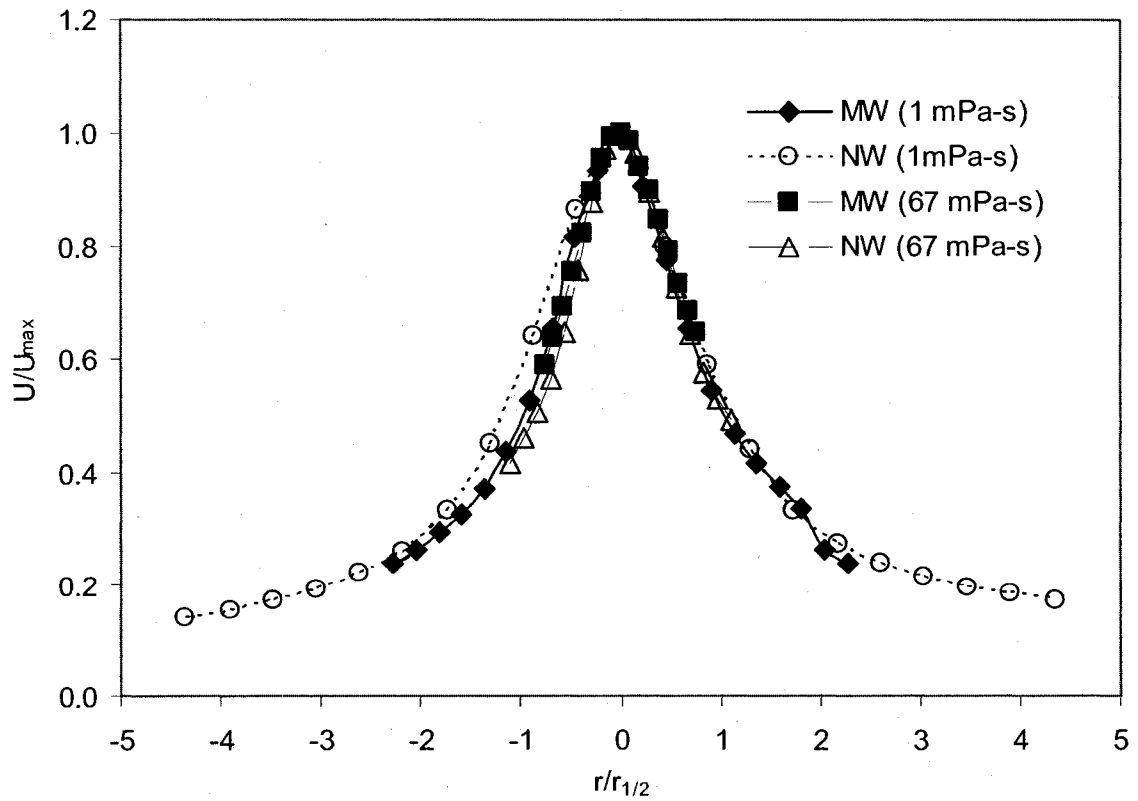


Figure 6.12 (b):  $x = 202$  mm



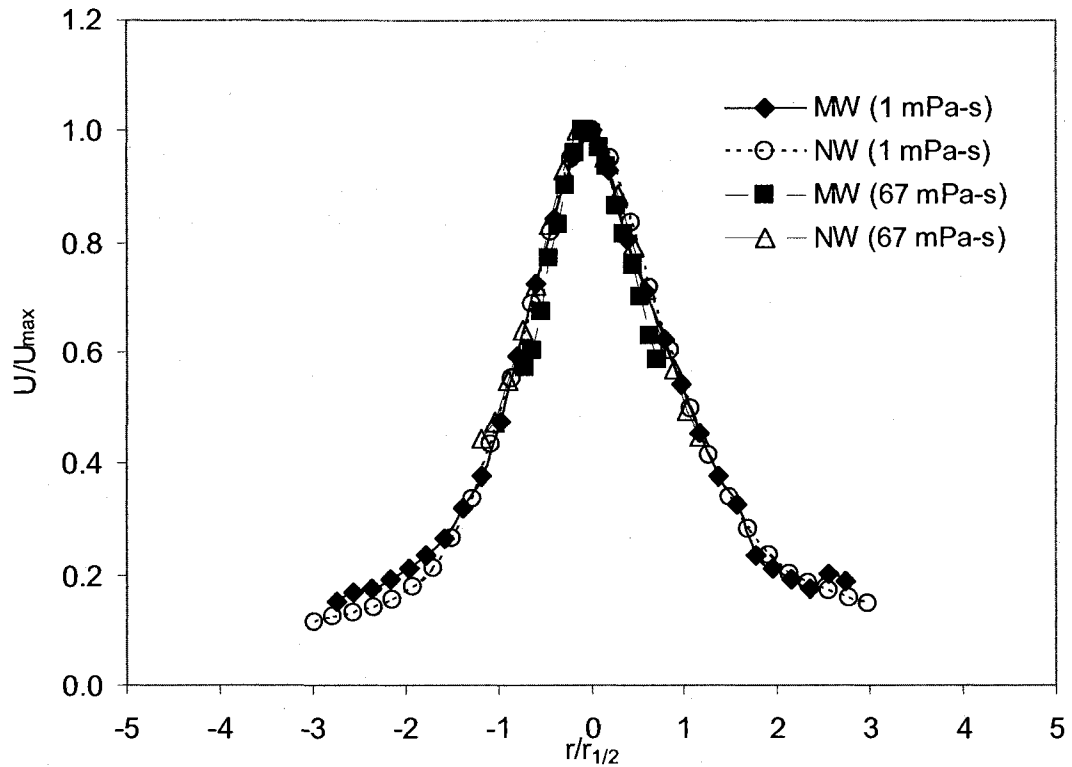


Figure 6.12 (c):  $x = 405\text{mm}$

Figure 6.12 – Comparison of normalized velocity profiles at axial distances (a) 100 mm, (b) 202 mm, and (c) 405 mm, for different liquid viscosities at  $GLR = 1\%$  using SS-1.0 nozzle. Note that MW and NW denote mass-weighted and number-weighted velocity data.

Figure 6.12 confirms two characteristics. The first is that self-similarity exists at all axial positions for both mass weighted and number-weighted velocity profiles for the 67 mPa-s liquid. Secondly, the normalized velocity profiles from the spray of the higher viscosity liquid also collapses on the profiles for the air-water system ( $\mu_L = 1 \text{ mPa-s}$ ). A similar observation for self-similarity for different liquid viscosities was also noticed at 2%  $GLR$ . The test conditions are presented in Table 6.4 and the corresponding plots are shown in Figure 6.13 for axial positions 100 and 202 mm. Note that no comparison was made at  $x = 405 \text{ mm}$ , since no data was collected for the glycerine solution. This was because of the susceptibility of liquid drops on the PDA receiver lens due to the large spray width at

this axial location. This would have resulted in measurement errors from the PDA system.

Table 6.4 – Test conditions at 2% GLR to study the effect of liquid viscosity on atomization using the SS-1.0 nozzle.

Fluid System	Liquid volume flow rate, $Q_L$ ( $\times 10^{-6}$ m <sup>3</sup> /s)	GLR, $\left(\frac{m_G}{m_L}\right)$ (%)	DR, $\left(\frac{\rho_G}{\rho_L}\right)$	$Re_L$ , $\left(\frac{4\rho_L Q_L}{\pi\mu_L D}\right)$	$Fr_L$ , $\left(\frac{16Q_L^2}{\pi^2 g D^5}\right)$	$We_L$ , $\left(\frac{16\rho_L Q_L^2}{\pi^2 \gamma D^3}\right)$
Air-Water	95	2.0	0.0046	38791	5169	6948
Air-Glycerine Solution	105	2.0	0.0042	770	6331	11742
Ratio (Water-to-glycerine solution data)	0.9	1.0	1.1	50	0.8	0.6

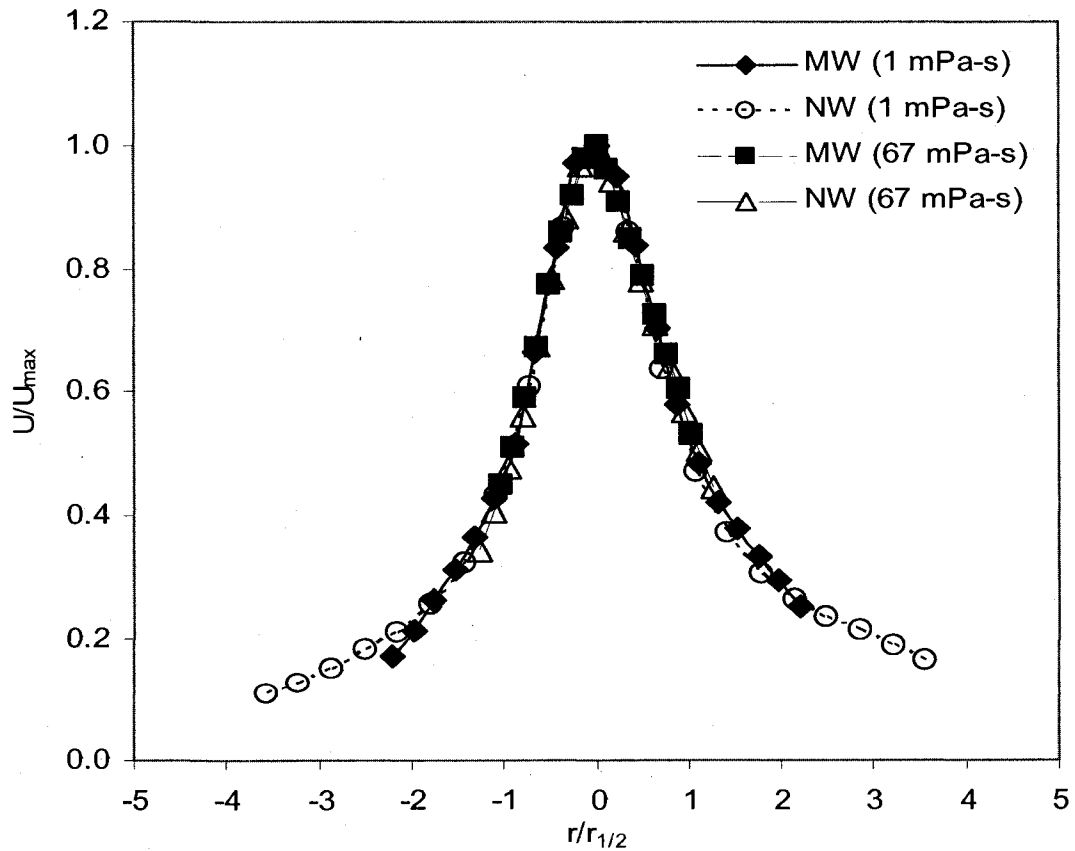


Figure 6.13 (a):  $x = 100$  mm

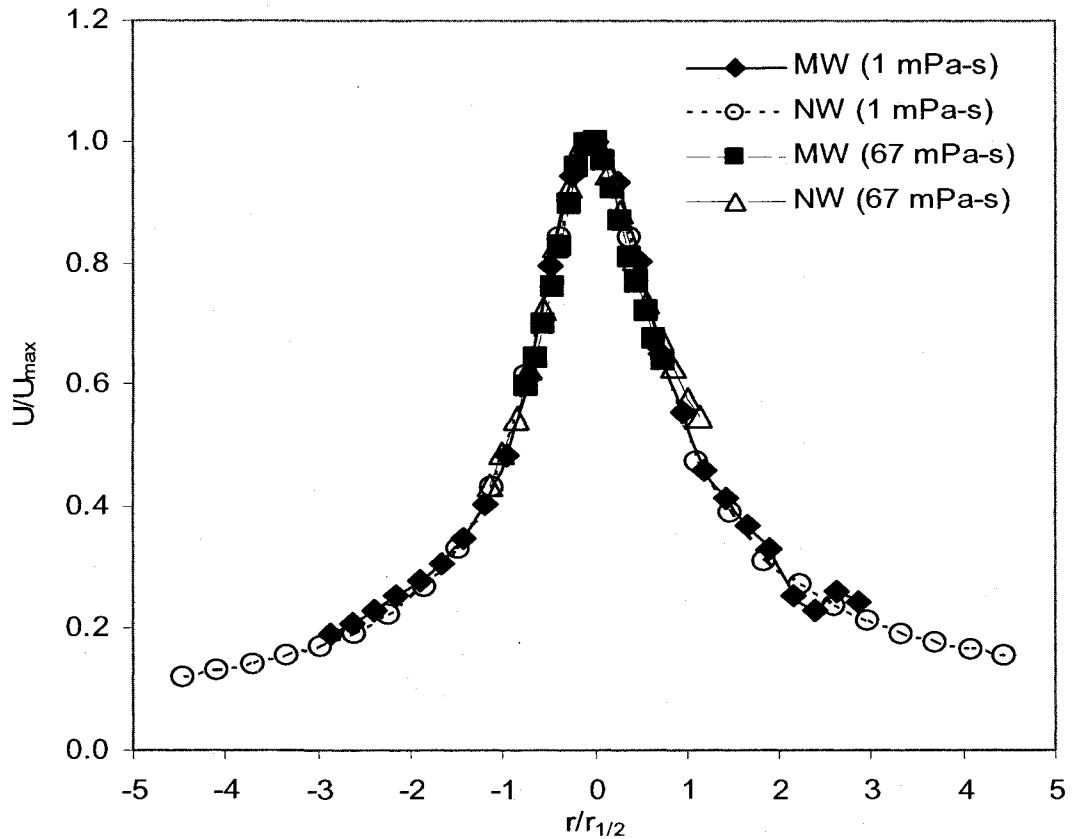


Figure 6.13 (b):  $x = 202$  mm

Figure 6.13 – Comparison of normalized velocity profiles at axial distances (a) 100 mm, and (b) 202 mm, for different liquid viscosities at  $GLR = 2\%$ . Note that MW and NW denote mass-weighted and number-weighted velocity data.

#### 6.4.2 Different liquid surface tension

To investigate the effect of surface tension on  $SMD$  the  $GLR$  and density ratio ( $\rho_G/\rho_L$ ) were kept constant, similar to the procedure in the last Section. However, the liquid *Weber Number*  $We_L$  was varied substantially since it compares surface tension and inertia forces. Table 6.5 show the flow conditions for  $GLR = 1\%$ .

Table 6.5 – Test conditions at 1% *GLR* to study the effect of surface tension on atomization using the SS-1.0 nozzle.

Fluid System	Liquid volume flow rate, $Q_L$ ( $\times 10^{-6}$ m <sup>3</sup> /s)	$GLR$ , $\left(\frac{m_G}{m_L}\right)$ (%)	$DR$ , $\left(\frac{\rho_G}{\rho_L}\right)$	$Re_L$ , $\left(\frac{4\rho_L Q_L}{\pi\mu_L D}\right)$	$Fr_L$ , $\left(\frac{16Q_L^2}{\pi^2 g D^5}\right)$	$We_L$ , $\left(\frac{16\rho_L Q_L^2}{\pi^2 \gamma D^3}\right)$
Air-Canola Oil	105	1.0	0.0032	590	6331	21606
Air-Glycerine Solution	114	1.0	0.0032	840	7527	13959
Ratio (Canola-to-glycerine solution data)	0.9	1.0	1.0	0.7	0.8	1.5

Note that the surface tensions for the canola oil and glycerine-water liquids are 25 mN/m and 61 mN/m, respectively. The corresponding velocity profiles at  $x = 100, 202$  and 405 mm are presented in Figure 6.14. The figure also shows that the normalized velocity profiles also collapse on one another at all axial locations. This plot confirms that the self-similarity exists in the velocity profiles irrespective of the liquid surface tension in this study. The same observation is seen for a 2% *GLR* system as presented in Figure 6.15. The corresponding flow conditions for this *GLR* are presented in Table 6.6.

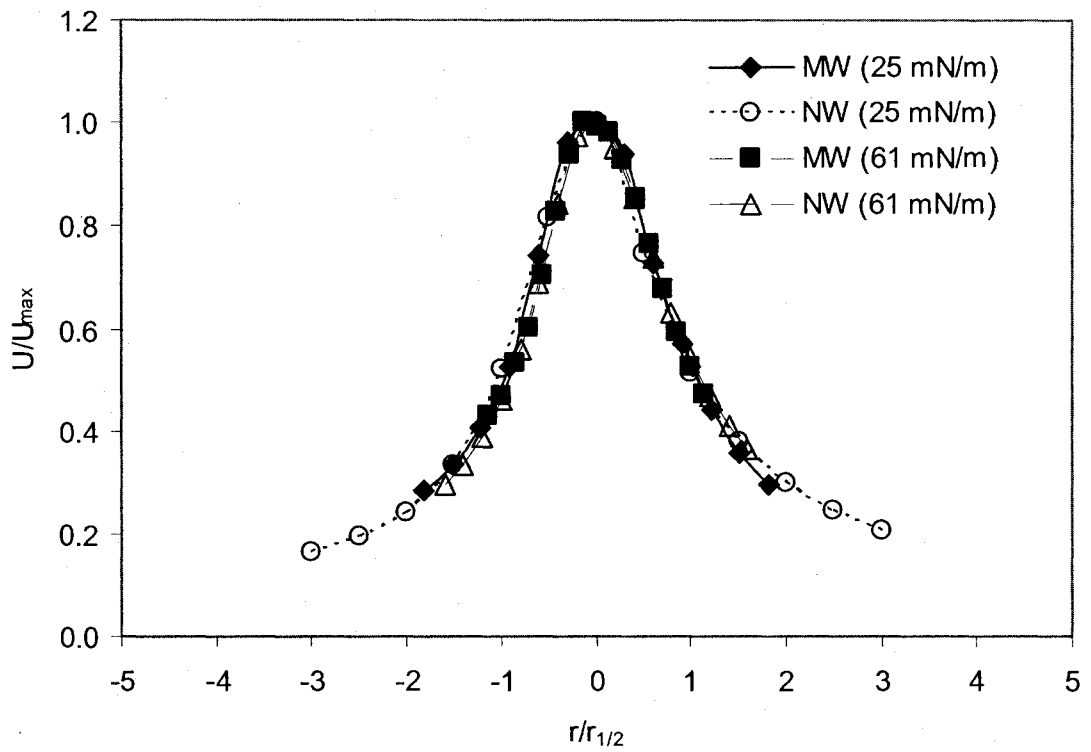


Figure 6.14 (a):  $x = 100$  mm

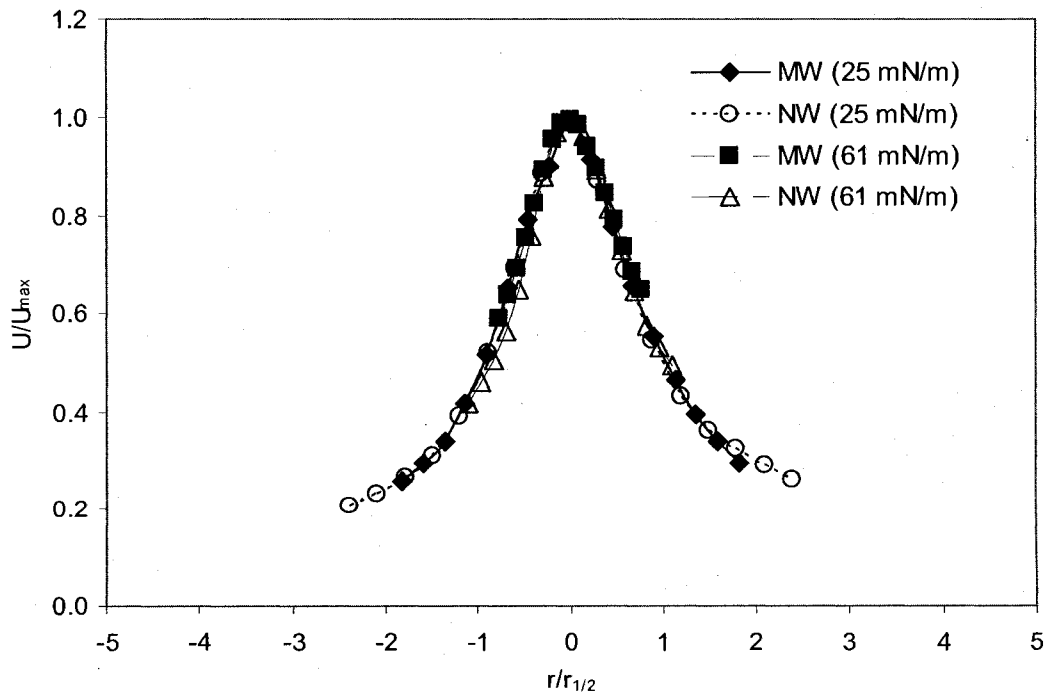


Figure 6.14 (b):  $x = 202$  mm

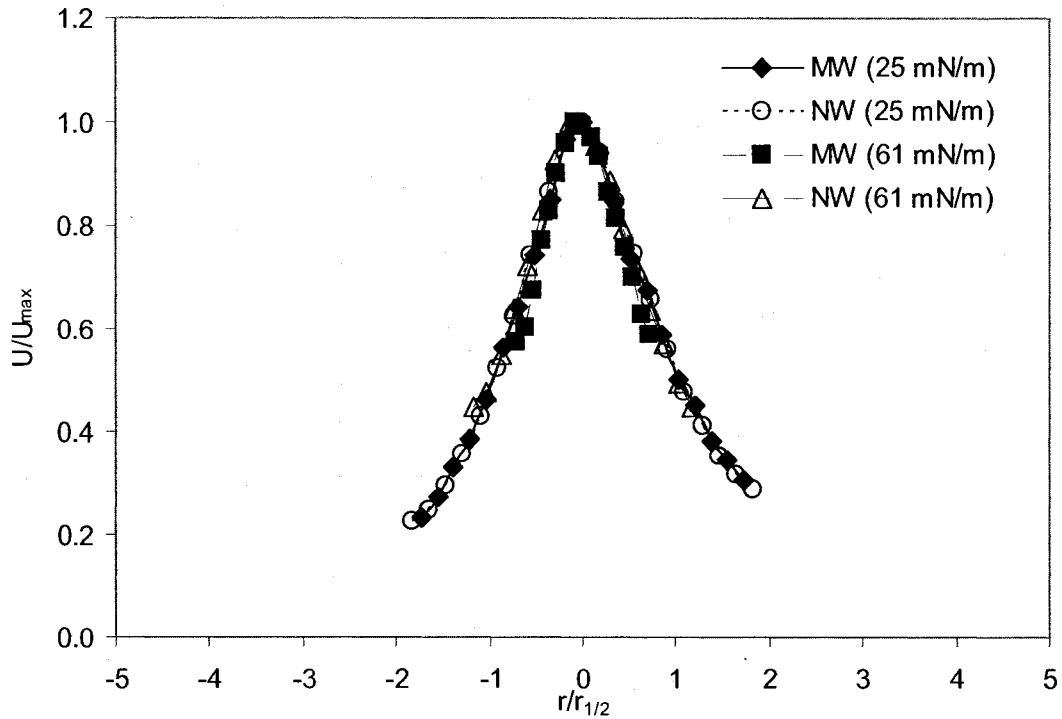


Figure 6.14 (c):  $x = 405\text{mm}$

Figure 6.14 – Comparison of normalized velocity profiles at axial positions (a) 100 mm, (b) 202 mm, and (c) 405 mm, for different liquid surface tensions at  $GLR = 1\%$  using SS-1.0 nozzle. Note that MW and NW denote mass-weighted and number-weighted velocity data.

Table 6.6 – Test conditions at 2%  $GLR$  to study the effect of surface tension on atomization using the SS-1.0 nozzle.

Fluid System	Liquid volume flow rate, $Q_L$ ( $\times 10^{-6} \text{ m}^3/\text{s}$ )	$GLR$ , $\left(\frac{m_G}{m_L}\right)$ (%)	$DR$ , $\left(\frac{\rho_G}{\rho_L}\right)$	$Re_L$ , $\left(\frac{4\rho_L Q_L}{\pi\mu_L D}\right)$	$Fr_L$ , $\left(\frac{16Q_L^2}{\pi^2 g D^5}\right)$	$We_L$ , $\left(\frac{16\rho_L Q_L^2}{\pi^2 \gamma D^3}\right)$
Air-Canola Oil	105	2.0	0.0043	590	6331	21606
Air-Glycerine Solution	105	2.0	0.0042	770	6331	11742
Ratio (Canola-to-glycerine solution data)	1.0	1.0	1.0	0.8	1.0	1.8

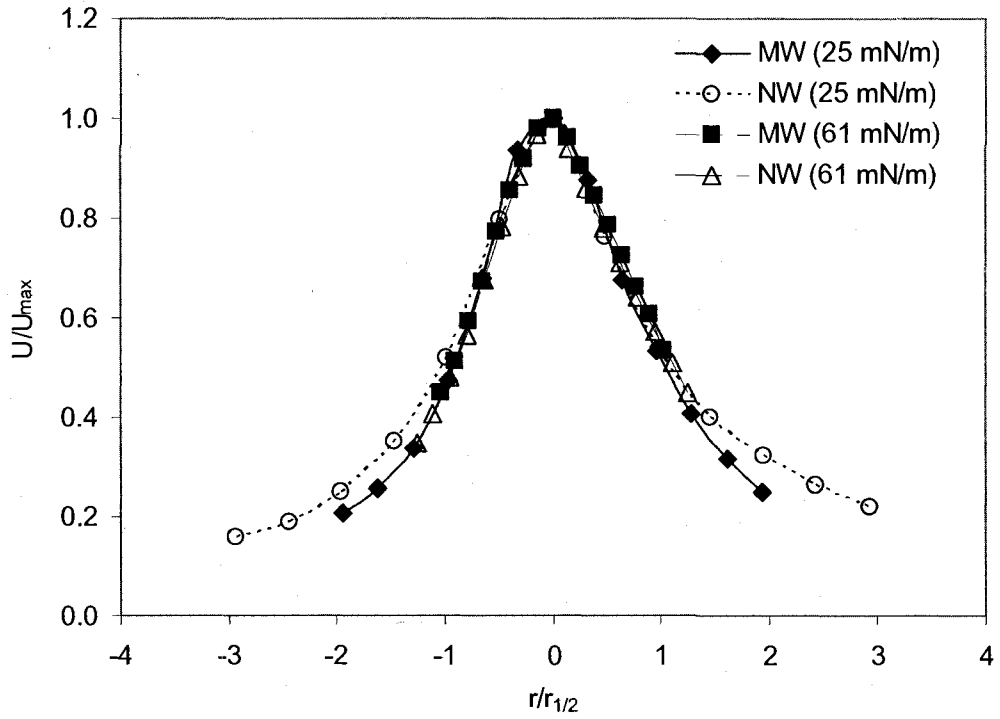


Figure 6.15 (a):  $x = 100$  mm

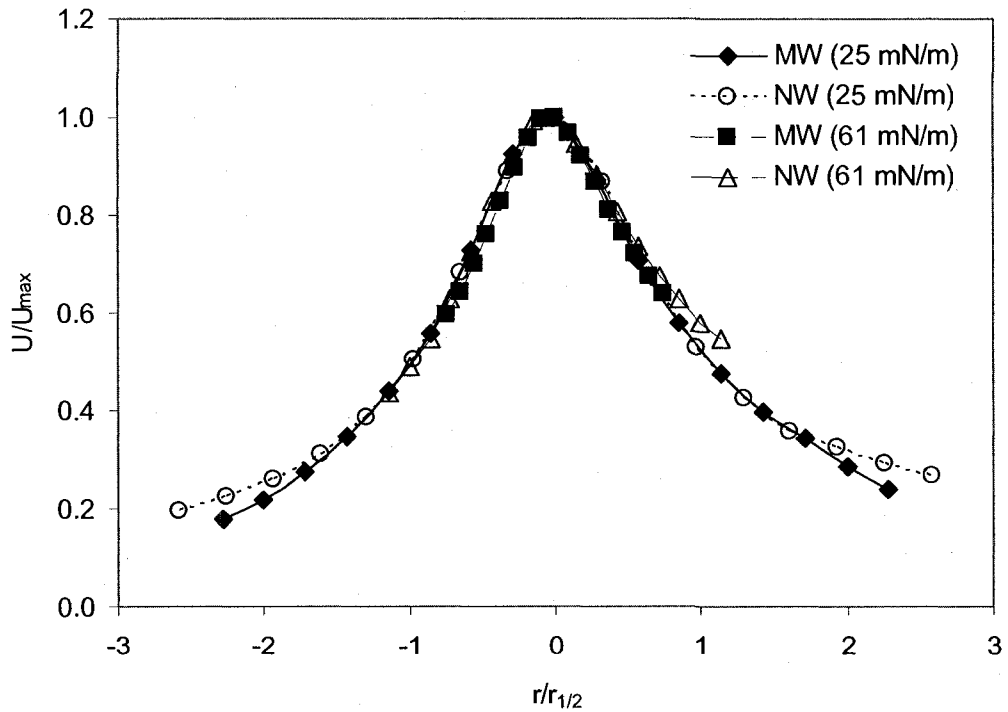


Figure 6.15 (b):  $x = 202$  mm

Figure 6.15 – Comparison of normalized velocity profiles at axial positions (a) 100 mm, and (b) 202 mm, for different liquid surface tensions at  $GLR = 2\%$ . Note that MW and NW denote mass-weighted and number-weighted velocity data.

### 6.4.3 Different nozzle sizes

In studying the effect of nozzle size on velocity profiles, using the SS-1.0 ( $D = 3.1$  mm) and SS-1.3 ( $D = 4.1$  mm) nozzles and same fluids, the most important dimensionless quantities that were conserved were the *GLR* and density ratio ( $\rho_G/\rho_L$ ). Similar tests were performed using both water and glycerine-water to check for data consistency. The air-glycerine solution and air-water flow conditions are presented in Tables 6.7 and 6.8, respectively. The corresponding plots are shown in Figures 6.16 and 6.17, respectively.

Table 6.7 – Test conditions at 1% *GLR* using air and glycerine solution to study the effect of nozzle size on atomization for SS-1.0 ( $D = 3.1$  mm) and SS-1.3 ( $D = 4.1$  mm) nozzles.

Nozzle name	Liquid volume flow rate, $Q_L$ ( $\times 10^{-6}$ m <sup>3</sup> /s)	<i>GLR</i> , $\left(\frac{m_G}{m_L}\right)$ (%)	<i>DR</i> , $\left(\frac{\rho_G}{\rho_L}\right)$	$Re_L$ , $\left(\frac{4\rho_L Q_L}{\pi\mu_L D}\right)$	$Fr_L$ , $\left(\frac{16Q_L^2}{\pi^2 g D^5}\right)$	$We_L$ , $\left(\frac{16\rho_L Q_L^2}{\pi^2 \gamma D^3}\right)$
SS-1.3	163	1.0	0.0022	902	3750	12165
SS-1.0	79	1.0	0.0022	580	3590	6658
Ratio (SS-1.3-to-SS-1.0 data)	2.1	1.0	1.0	1.6	1.0	1.8

Table 6.8 – Test conditions at 1% *GLR* using air and water to study the effect of nozzle size on atomization for SS-1.0 ( $D = 3.1$  mm) and SS-1.3 ( $D = 4.1$  mm) nozzles.

Nozzle name	Liquid volume flow rate, $Q_L$ ( $\times 10^{-6}$ m <sup>3</sup> /s)	<i>GLR</i> , $\left(\frac{m_G}{m_L}\right)$ (%)	<i>DR</i> , $\left(\frac{\rho_G}{\rho_L}\right)$	$Re_L$ , $\left(\frac{4\rho_L Q_L}{\pi\mu_L D}\right)$	$Fr_L$ , $\left(\frac{16Q_L^2}{\pi^2 g D^5}\right)$	$We_L$ , $\left(\frac{16\rho_L Q_L^2}{\pi^2 \gamma D^3}\right)$
SS-1.3	190	1.0	0.0034	58660	5110	12013
SS-1.0	95	1.0	0.0034	38791	5169	6948
Ratio (SS-1.3-to-SS-1.0 data)	2.0	1.0	1.0	1.5	1.0	1.7



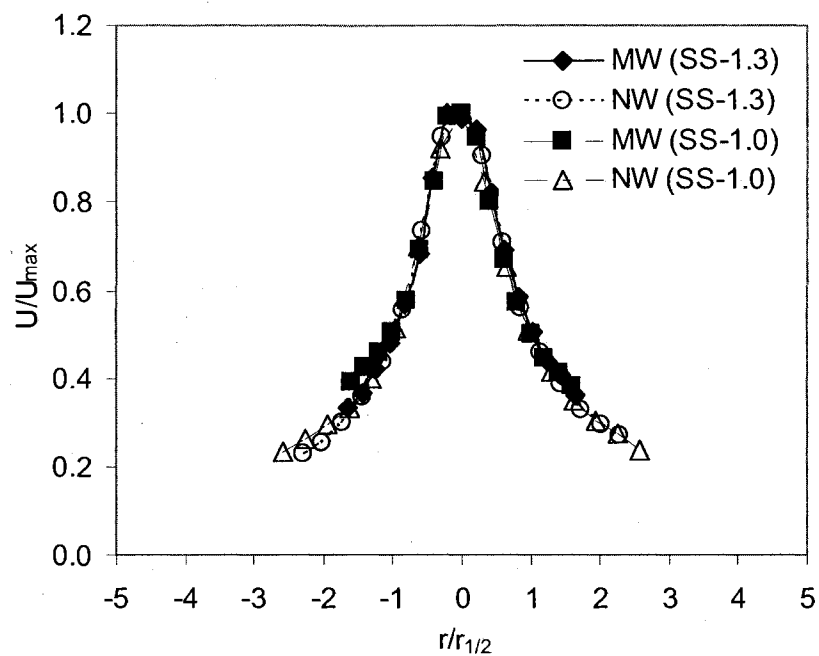


Figure 6.16 (a):  $x = 100$  mm

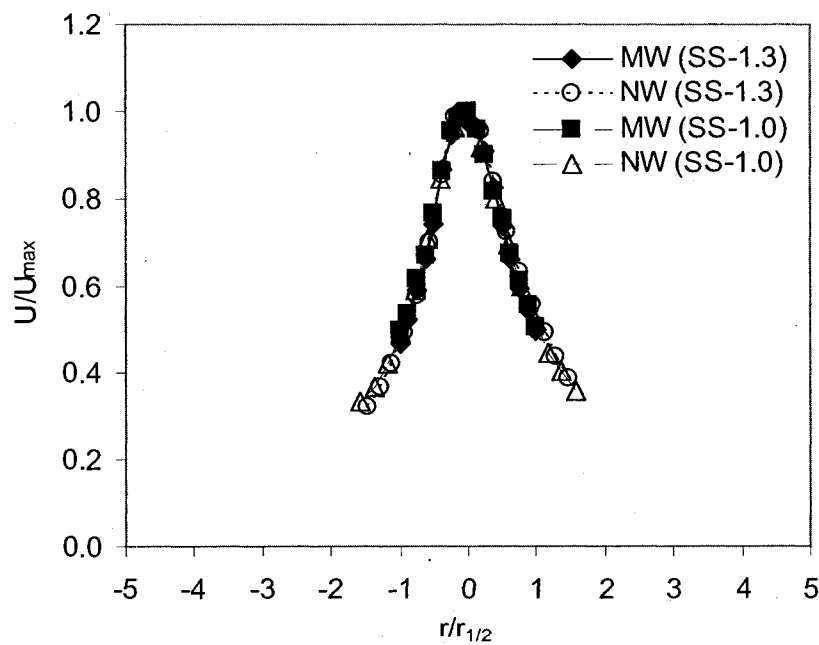


Figure 6.16 (b):  $x = 202$  mm

Figure 6.16 - Comparison of normalized velocity profiles for SS-1.0 and SS-1.3 nozzles at axial distances (a) 100 mm, and (b) 202 mm, for air and glycerine solution at  $GLR = 1\%$ . Note that MW and NW denote mass-weighted and number-weighted velocity data.

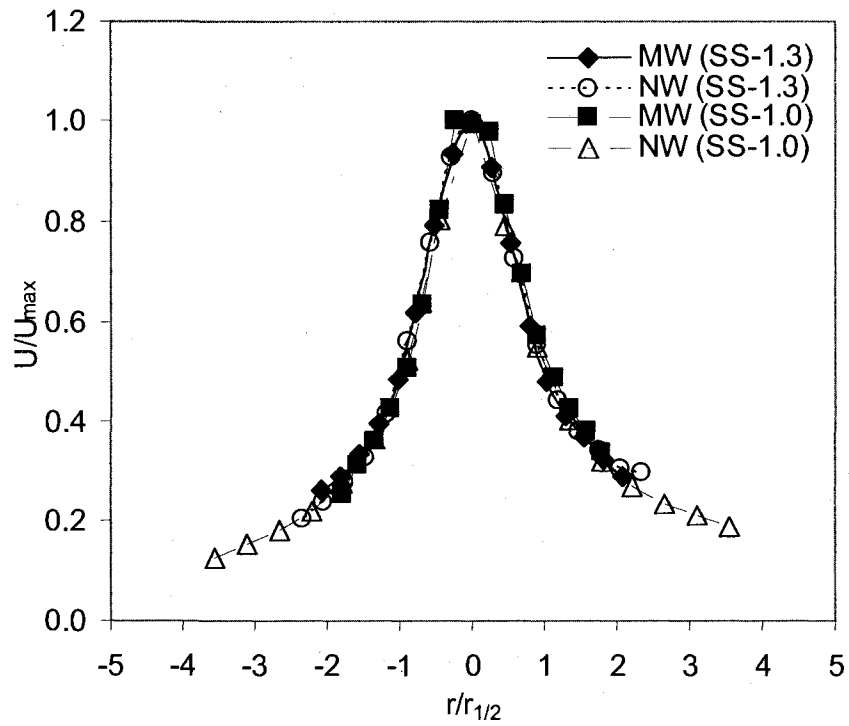


Figure 6.17 (a):  $x = 100$  mm

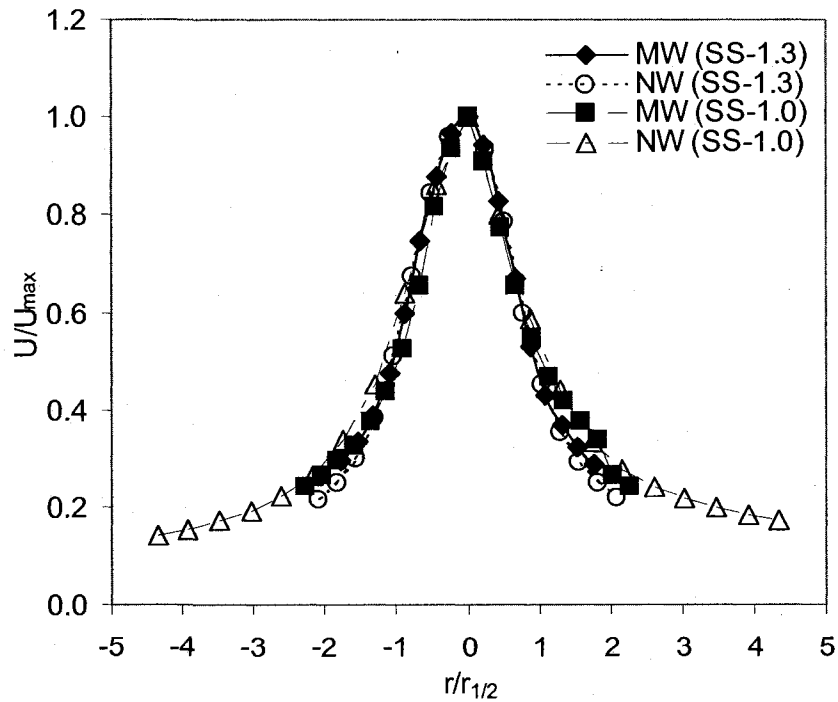


Figure 6.17 (b):  $x = 202$  mm

Figure 6.17 - Comparison of normalized velocity profiles for SS-1.0 and SS-1.3 nozzles at axial distances (a) 100 mm, and (b) 202 mm, for air and water at  $GLR = 1\%$ . Note that MW and NW denote mass-weighted and number-weighted velocity data.

The trends in Figures 6.16 and 6.17 are also similar to those in Figures 6.12 to 6.15. Therefore, self-similarity is present in sprays from both nozzle sizes. The general conclusion from the results in Figures 6.12 to 6.17, is that for the flow conditions in this test, velocity self-similarity was present and was independent of liquid viscosity, surface tension or nozzle size. In relation to the fluid coker, it implies that for similar flow conditions as in this study, self-similarity is also plausible for the axial distances studied. This means it may be possible to use a single velocity model from a small-scale study to characterize the spray velocity at entry to the fluid coker, before contact with the coke particles. Such models will help in nozzle design and operation optimization such as spray penetration.

# CHAPTER 7

## RESULTS AND DISCUSSION – DROP SIZE DATA

This chapter presents the drop size results for the same measurement positions as the velocity profiles presented in Chapter 6. Prior to presenting the drop size profiles, it is important to investigate the amount of liquid volume or mass in the spray. This can help to explain some of the drop size profiles obtained in the test. Additional plots related to drop size are shown in Appendix A5.

### 7.1. Liquid volume flux

#### 7.1.1 Air-water systems

Figure 7.1 shows a plot of the evaluated liquid (water) volume flux using Eqn. (5.5) at different axial positions downstream of the nozzle exit. The general trend at all axial positions is that there is a greater population of liquid drops at the centre of the spray, and decreases towards the spray periphery. This implies that the liquid flux is also high at the centre. Since flux is proportional to velocity, it means that velocity is highest at the centre of the spray, which is evident in the velocity profiles presented in Figure 6.7. Secondly, the population of drops at the centre of the spray decreases with axial distance, but this is compensated for by a subsequent increase of the radius at which the volume flux tends to zero. This trend is also evident in the decrease of velocity with axial distance presented in Figure 6.7. In Figure 7.1 this corresponds to approximately 45, 60 and 75 mm at 100, 202 and 405 mm, respectively. This increase in spray width is due to lower velocity for mass conservation within the spray. Such trend is also similar to the increase in jet half-width with axial distance for momentum conservation as presented in Figure 6.8.

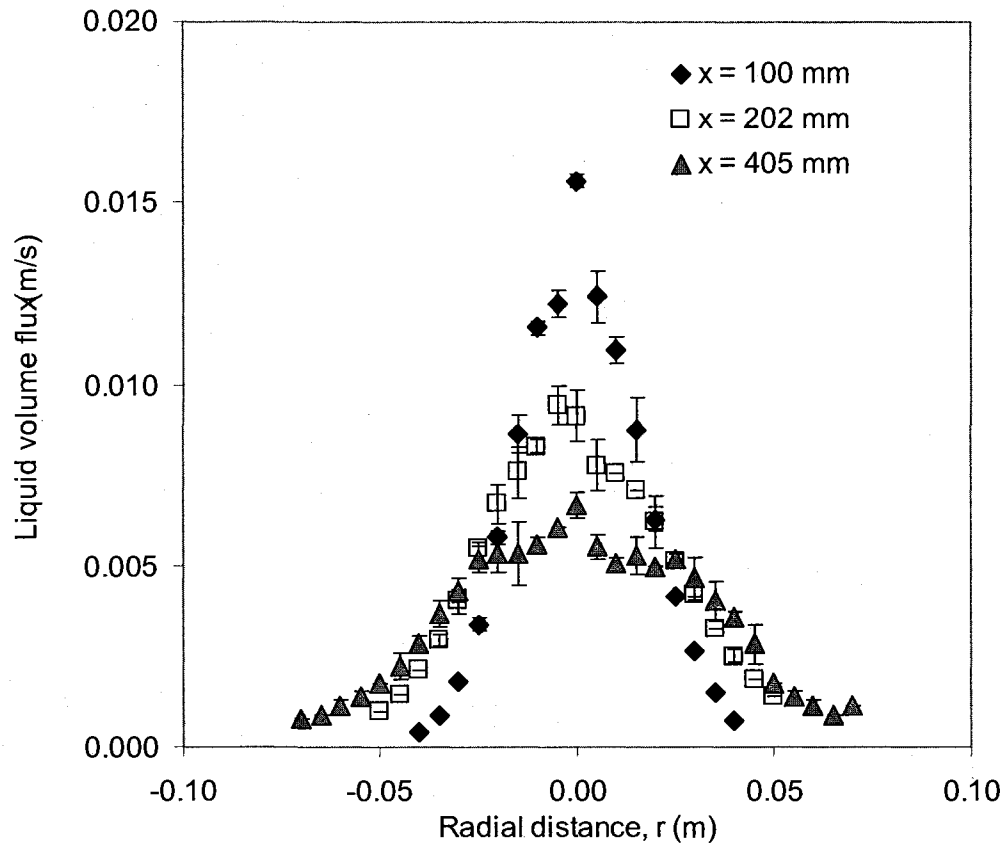


Figure 7.1: Plots of liquid volume flux across the spray at 3 axial distances using SS-1.0 nozzle. Data is for an air-water system with liquid flow rate of  $95 \times 10^{-6} \text{ m}^3/\text{s}$  and 1% *GLR*.

Based on the profiles in Figure 7.1, the average evaluated percentage of liquid volume (or mass) were 21, 31 and 41% at  $x = 100, 202$  and  $405 \text{ mm}$ , respectively using Eqn. (5.7). Note that although the entire spray cross-section was traversed, the low values as mentioned in Section 5.3.3, is affected mainly by simultaneous presence of two or more drops in the PDA probe volume in dense sprays [54].

A trend seen in Figure 7.1 is that the values of the liquid volume fluxes are not zero at the edge of the spray. Indeed, to get a good idea of the true spray edge, the plots can be

extrapolated to the horizontal axis. The area under this closed curve will give a higher value of the liquid volume (or mass) than that evaluated those quoted above. The increase in liquid volume gained by extrapolating to the horizontal axis in Figure 7.1 were 1%, 4% and 5% for  $x = 100, 202$  and  $405$  mm, respectively.

The above trends in Figures 7.1 were also similar to an air-water system with liquid flow rate of  $95 \times 10^{-6} \text{ m}^3/\text{s}$  at 2% *GLR*. The corresponding plots are shown in Figures 7.2.

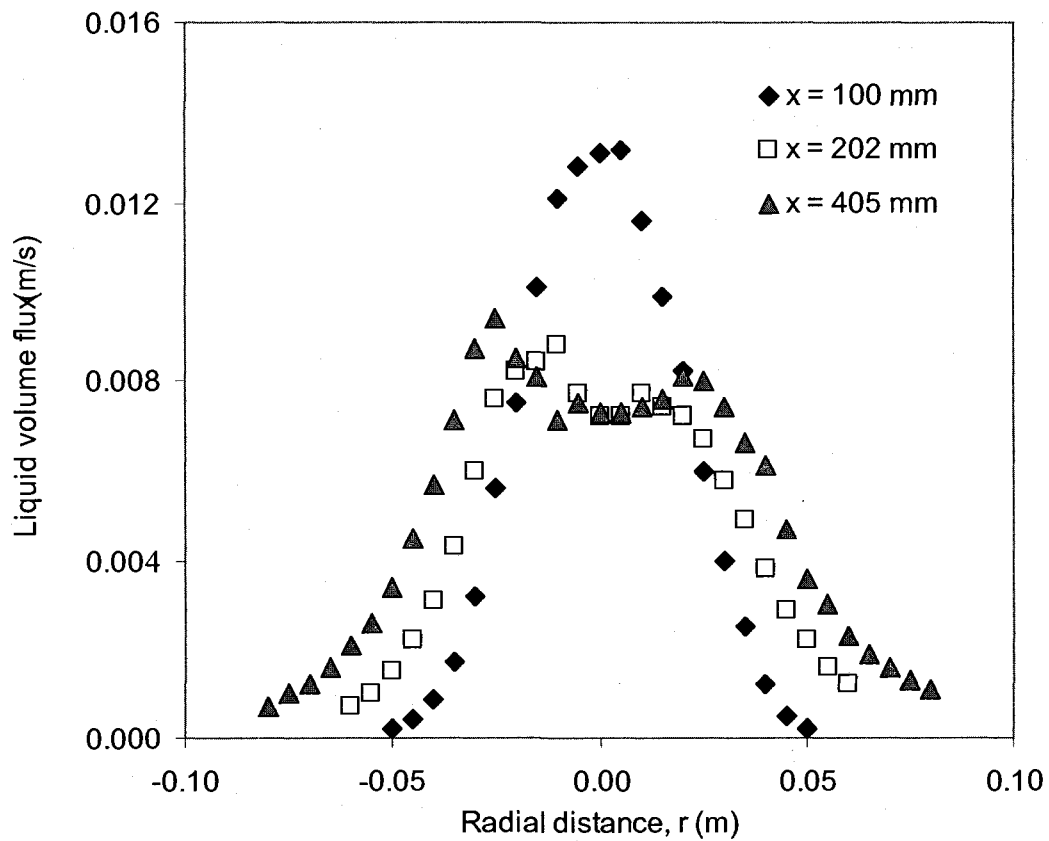


Figure 7.2 Plots of liquid volume flux at 3 axial distances within the spray using SS-1.0.

Data is for an air-water system with liquid flow rate of  $95 \times 10^{-6} \text{ m}^3/\text{s}$  and 2% *GLR*.

In this Figure, the spray edge is at a radius of 50, 70 and 90 mm at axial positions of 100, 202, and 405 mm, respectively. For the axial positions, the average amount of liquid in the spray was 28, 43 and 58%, respectively. The corresponding values obtained from extrapolating down to the horizontal axis were 28, 47 and 65%, respectively.

### **7.1.2 Air-glycerine solutions and air-canola oil systems**

A similar mass balance calculation was performed for the air-glycerine solution system with liquid flow rate of  $114 \times 10^{-6} \text{ m}^3/\text{s}$  and an air-canola oil system with liquid flow rate of  $105 \times 10^{-6} \text{ m}^3/\text{s}$ . Both systems were at 1% *GLR*. The corresponding values of the volume flux were about an order of magnitude lower than that of the air-water system at 1% *GLR* which had the same similar flow condition (plot in Figure 7.1). The very low volume flux values resulted in an average liquid mass fraction of 1% for the glycerine solution and about 10% for canola oil. A reason for the very low liquid volume flux values can be attributed to the differences in the liquid volume flow rates and associated data rates between water and the glycerine solution and canola oil. Recall that the liquid volume rate for the air-water spray was  $95 \times 10^{-6} \text{ m}^3/\text{s}$  to ensure dynamic similarity in density ratios at the nozzle exit. The higher liquid flow rates for the glycerine-water and canola sprays results in a much denser spray than that of the air-water system. The PDA data acquisition settings were kept constant to prevent bias from the measurement system. The consequence of having denser sprays is that the PDA system would not validate and count the drops passing through its control volume if they do not meet the fixed spherical criterion settings of the system. Furthermore, in denser sprays, the system may not be able to detect the smaller drops, which is one of the uncertainties associated

with the PDA [45, 46] as mentioned in Section 3.3. The combined effect of these two reasons results in a lower drop count per unit time (or data rate). This data rate is an important parameter in obtaining the liquid volume flux as shown in Eqn. (5.5). The lower data rates yield lower values of liquid volume flux and results in the more pronounced mass balance deficiency in the glycerine-water and canola sprays. Although the liquid volume fluxes were significantly underestimated in the glycerine solution and canola systems, the trend in the plots of liquid volume flux are similar to that of the air-water system. That is, regions near the centre of the spray have a high liquid volume flux compared to other radial locations. These plots are shown in Figures 7.3 and 7.4.

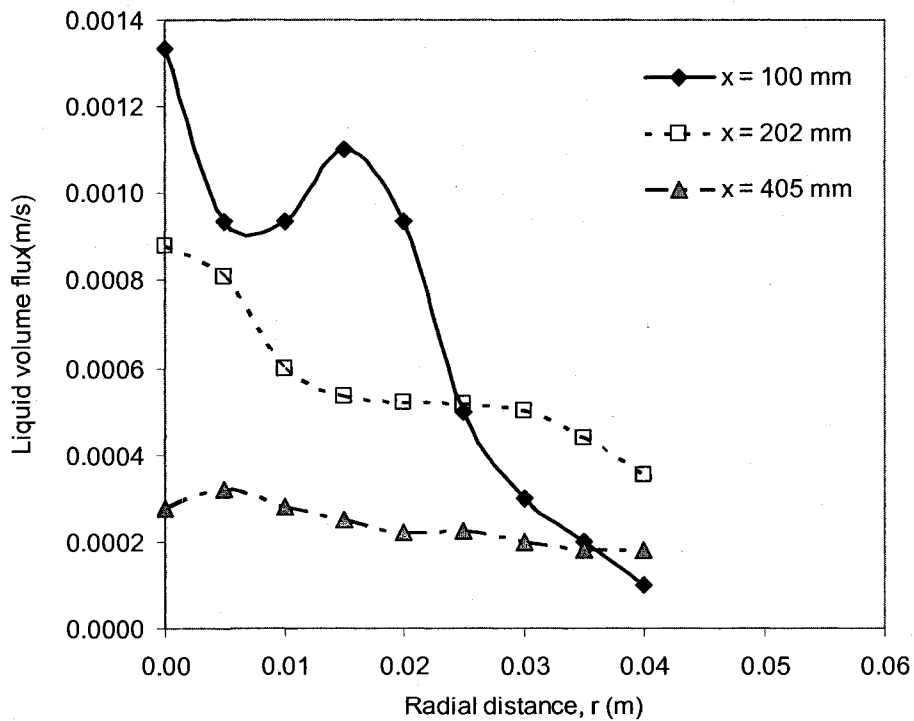


Figure 7.3 Radial plots of liquid volume flux within a spray at 3 axial distances using SS-1.0. Data is for an air-glycerine solution system with liquid flow rate of  $114 \times 10^{-6} \text{ m}^3/\text{s}$  and 1% GLR.



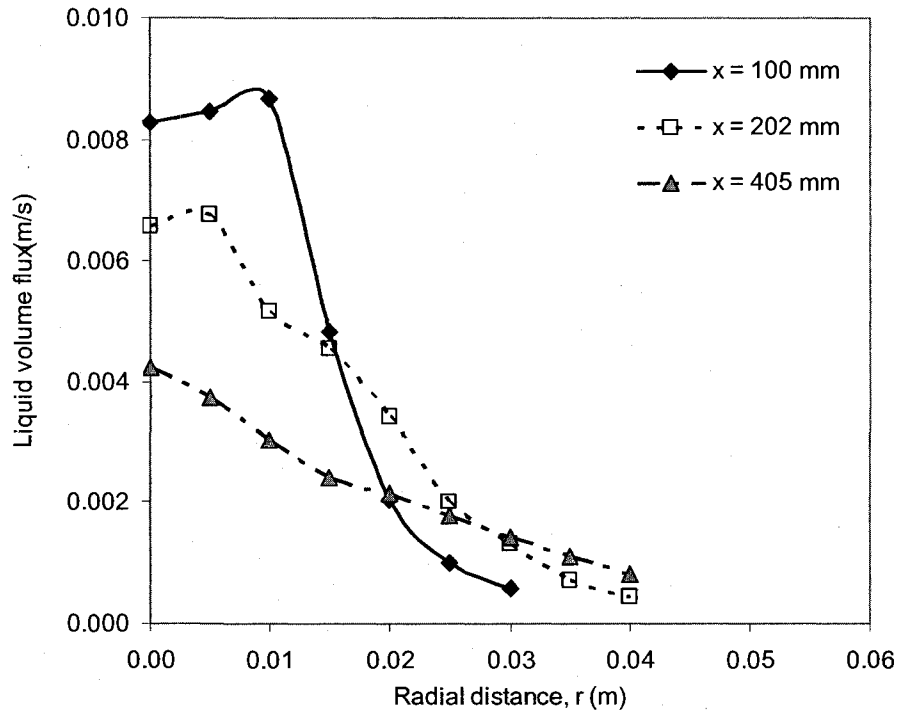


Figure 7.4 Radial plots of liquid volume flux within a spray at 3 axial distances using SS-1.0. Data is for an air-canola oil system with liquid flow rate of  $105 \times 10^{-6} \text{ m}^3/\text{s}$  and 1% GLR.

### 7.2 Effect of Liquid Viscosity on drop size at 1% GLR

The flow conditions required to study the effect of liquid viscosity on drop size for 1% GLR was presented in Table 6.3 of Section 6.4.1. The ratios of the superficial  $Re_L$ ,  $Fr_L$  and  $We_L$  in both sprays were 46, 0.7 and 0.5, respectively. The much higher ratios of  $Re_L$  ensured that viscosity effects were more dominant in one spray than the other.

The *SMD* profiles across the spray in the air- water ( $\mu_L = 1 \text{ mPa}\cdot\text{s}$ ) and glycerine-water systems ( $\mu_L = 67 \text{ mPa}\cdot\text{s}$ ) at an axial distance of 100 mm ( $x/D \cong 32$ ) downstream of the nozzle exit are presented in Figure 7.5. Recall from Section 5.3.4 that *SMD* comparison

for different drop size profiles in the spray will be made using the global  $SMD$  (i.e.  $SMD_{gb}$ ) from Eqn. (5.10). This is because,  $SMD_{gb}$  represents a liquid volume flux weighted average integrated over the spray cross-section compared to using a drop size at only a fixed radius in the spray.

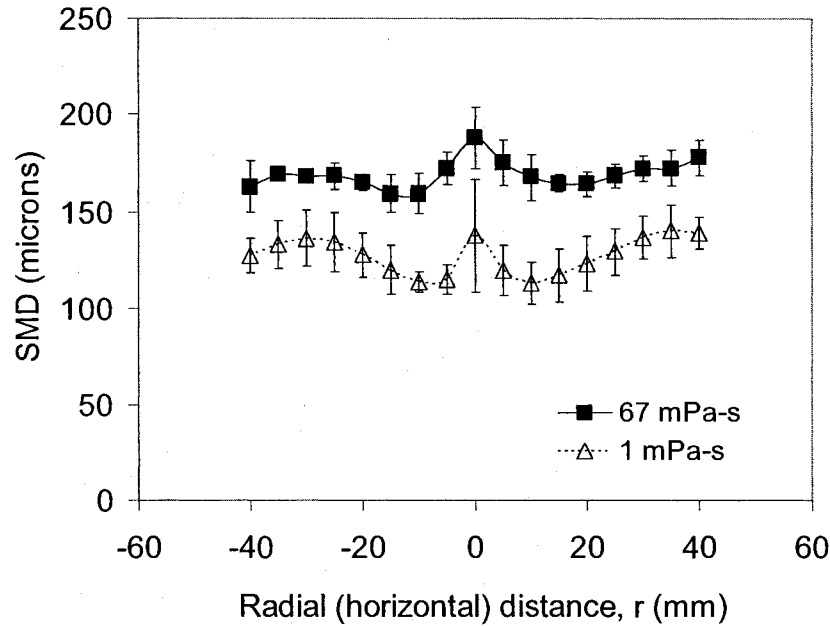


Figure 7.5 –  $SMD$  profiles for comparison of liquid viscosity at  $x = 100$  mm ( $GLR = 1\%$ ) using SS-1.0. Error bars denote a 95% confidence interval. Sampling time is 360 seconds.

From Figure 7.5, the corresponding  $SMD_{gb}$  for the 67 mPa-s (glycerine-water) and 1 mPa-s (water) sprays was 167  $\mu\text{m}$  and 125  $\mu\text{m}$ , respectively. This represents a 34% increase in drop size in the higher viscosity spray. A 5% test of significance suggests that this difference in  $SMD$  is significant. The presence of the large drops in the 67 mPa-s compared to the 1 mPa-s may seem to be attributed to the inhibition of the change in liquid geometry and delay in atomization due to the higher liquid viscosity.

Notice in both profiles the *SMD* increases at the centre resulting in a ‘W’ shaped. Recall from the drop size-velocity correlation coefficient that at this axial position (i.e. Figures 6.1 and 6.3), the small drops are accelerating whereas the large drops are decelerating due to momentum exchange with the gas-phase. The presence of the large drops at the centre of the spray significantly contributes to the increase in *SMD* in this region. This trend in *SMD* profile was also observed by Ariyapadi et al. [21] in their air-water tests using the same type of small-scale FC nozzle.

The *SMD* profiles at about 202 mm ( $x/D \cong 65$ ) and 405 mm ( $x/D \cong 131$ ) from the nozzle exit are shown in Figures 7.6 and 7.7, respectively.

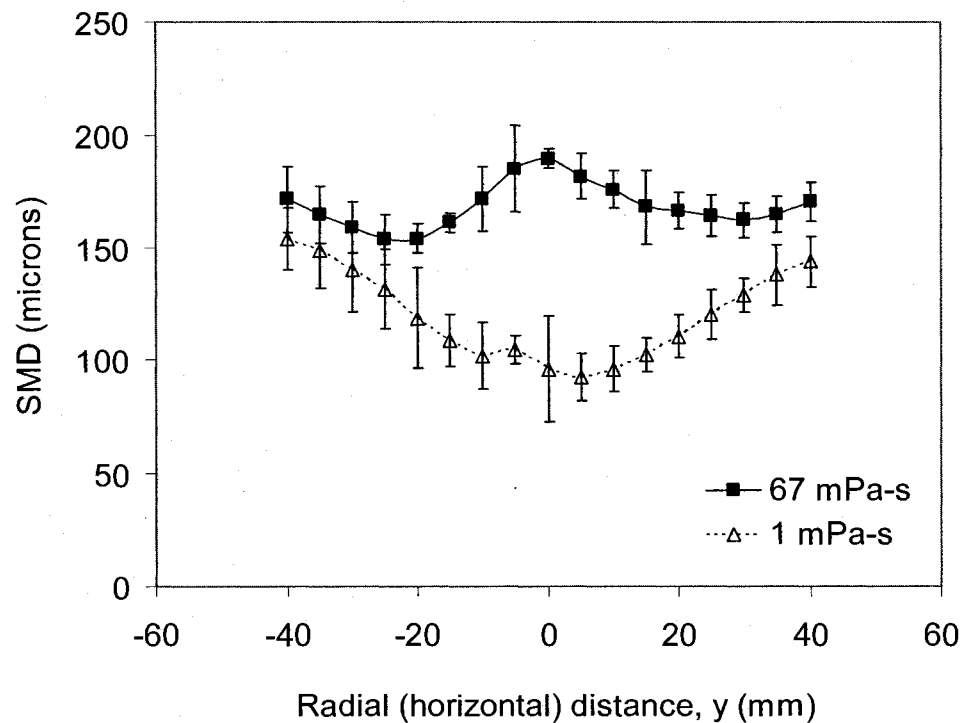


Figure 7.6 – *SMD* profiles for comparison of liquid viscosity at  $x = 202$  mm ( $GLR = 1\%$ ) using SS-1.0 nozzle. Error bars denote a 95% confidence interval. Sampling time is 360 seconds.

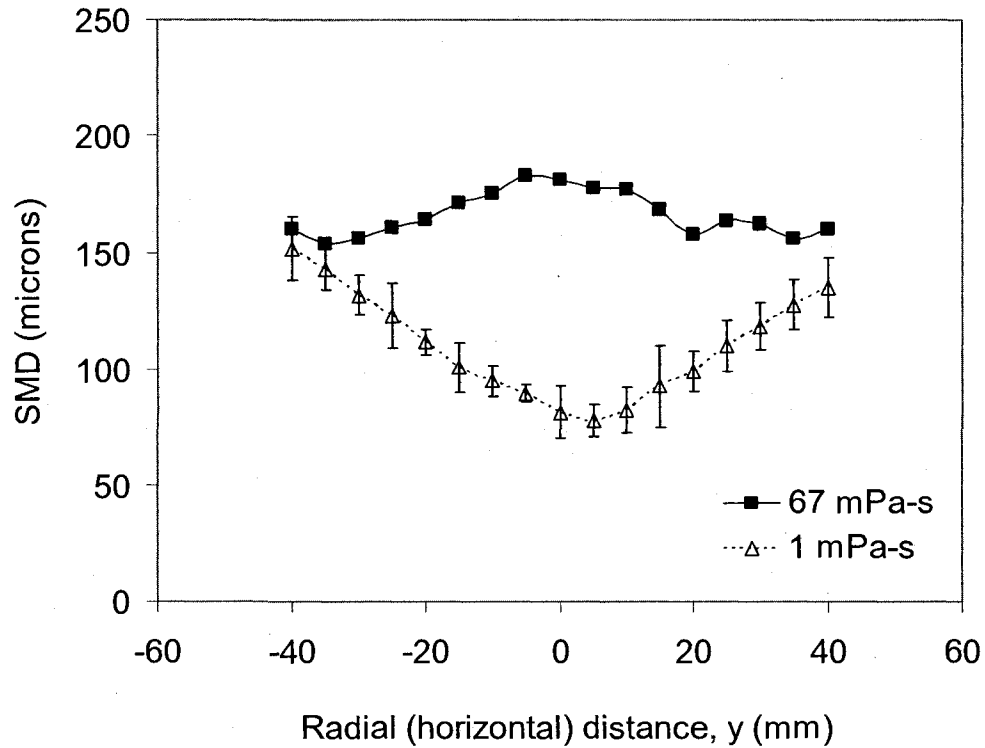


Figure 7.7 – *SMD* profiles for comparison of liquid viscosity at  $x = 405$  mm ( $GLR = 1\%$ ) using the SS-1.0 nozzle. Error bars denote a 95% confidence interval. Sampling time is 360 seconds.

At 202 mm, the corresponding  $SMD_{gb}$  are 165  $\mu\text{m}$  and 122  $\mu\text{m}$  for the glycerine solution and water systems, respectively. This implies that the spray with higher viscosity liquid produced 35% higher *SMD*. At  $x = 405\text{mm}$ ,  $SMD_{gb}$  was 163  $\mu\text{m}$  and 118  $\mu\text{m}$  in the glycerine-water and water sprays, respectively. This indicates an increase in drop size of 38% in the higher viscosity spray. Both increases in drop size with liquid viscosity were also found to be significant using a 5% test of significance.

From Figures 7.6 and 7.7, there is an evident difference in the *SMD* profiles with increasing axial distance. The increasing difference in *SMD* with increasing axial distance

in both sprays can be explained. For drops closer to the centre of the spray, comparing corresponding drop sizes from the glycerine solution spray at all three axial locations reveals that there is hardly a significant change in the *SMD* plot. This trend continues to show the influence of viscosity in delaying complete liquid atomization. The reverse is the case for the water spray close to the centre of the spray. Figures 7.5, 7.6 and 7.7 show that the *SMD* decreases with increasing axial distance. The different atomization mechanism for the high- and low-viscosity sprays therefore appears to be the main reason for the significant difference in drop size with increasing axial distance.

### **7.3 Effect of Liquid Viscosity on drop size at 2% *GLR***

The flow conditions required to study the effect of liquid viscosity on drop size for 2% *GLR* were presented in Table 6.4. The ratios of the superficial  $Re_L$ ,  $Fr_L$  and  $We_L$  between the two sprays were 50, 0.8 and 0.6, respectively. Similar to the case of 1% *GLR*, the much higher ratios of  $Re_L$  ensured that viscosity effects were more dominant in one spray than the other.

The corresponding profiles for the *SMD* at  $x = 100$  mm and 202 mm are presented in Figures 7.8 and 7.9. Note there is no data for  $x = 405$  mm, because the large axial distance causes deposition of a thin liquid coating on the PDA receiver, interfering with the measurements. At  $x = 100$  mm (from Figure 7.8), the  $SMD_{gb}$  was about 162  $\mu\text{m}$  for the glycerine solution and 116  $\mu\text{m}$  for the water system. This corresponds to an increase in drop size of 40% in the higher viscosity spray. At  $x = 202$  mm (from Figure 7.9), the  $SMD_{gb}$  for the glycerine solution is about 171  $\mu\text{m}$  and it is 104  $\mu\text{m}$  in the water spray.

This implies that there is a 64% increase in drop size due to the higher viscosity. These significantly larger drop size with higher viscosity is similar to observations in the 1% *GLR* spray. The same applies to the greater increase in drop size difference with axial distance between both sprays is also similar to those observed in the 1% *GLR* spray.

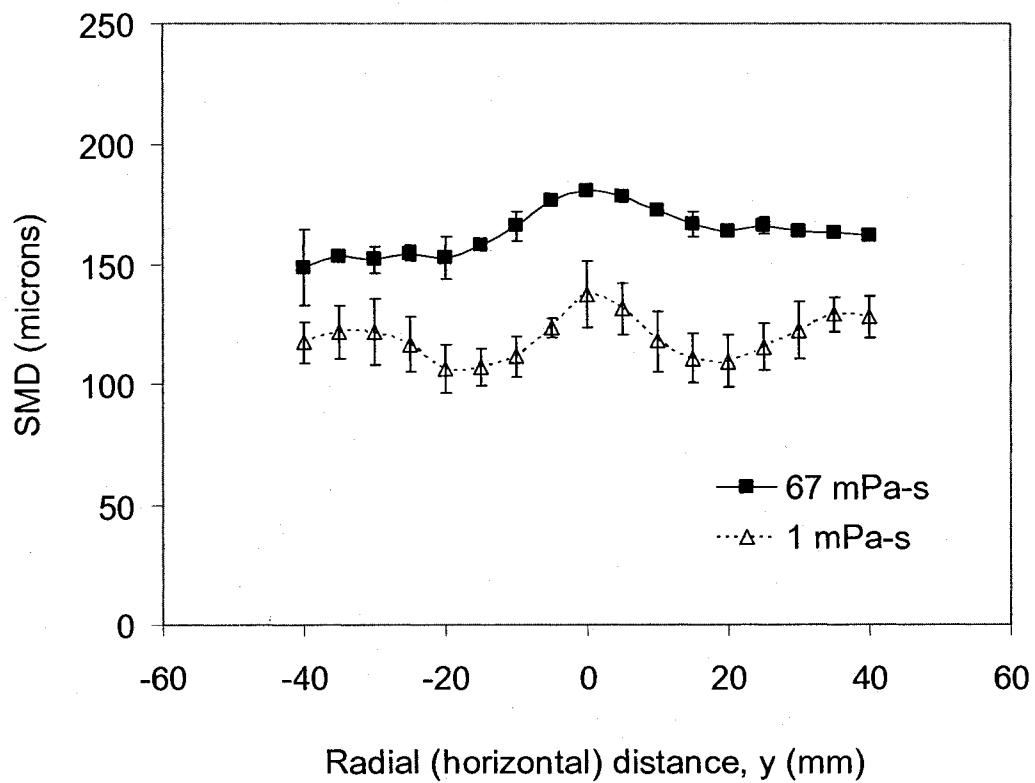


Figure 7.8 – *SMD* profiles for comparison of liquid viscosity at  $x = 100$  mm ( $GLR = 2\%$ ) using SS-1.0 nozzle. Error bars denote a 95% confidence interval. Sampling time is 360 seconds.

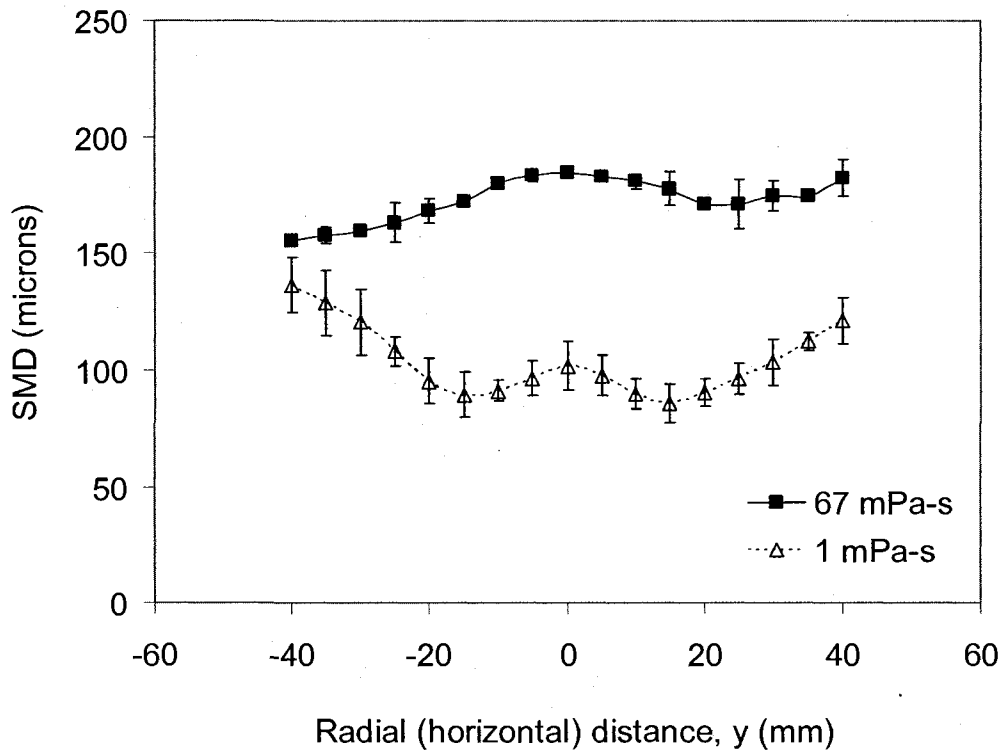


Figure 7.9 – *SMD* profiles for comparison of liquid viscosity at  $x = 202$  mm ( $GLR = 2\%$ ) using SS-1.0 nozzle. Error bars denote a 95% confidence interval. Sampling time is 360 seconds.

The increase in drop size with liquid viscosity observed in this study is similar to those made in twin-fluid atomizer studies by Elkotb et al. [8] and El Shanawany and Lefebvre [11], where *SMD* varies  $\sim \mu_L^{0.4}$  to  $1.0$ . The same observation was also observed in effervescent atomization studies Santangelo and Sojka [14], where *SMD* increased by about 115% and 75% at 2% and 10% *GLR*, respectively, for  $112 < \mu_L < 820$  mPa-s. However, results in this study differed from other effervescent atomizer studies by Buckner and Sojka [12] who observed a maximum 6% difference in *SMD* for  $400 < \mu_L < 968$  within  $5\% < GLR < 35\%$ . Also current test results differ from those by

Lund et al. [13] who observed 12% maximum difference in  $SMD$  for  $20 < \mu_L < 80$  mPa-s within  $1\% < GLR < 7\%$ . A final conclusion based on our data and those in literature shows that nozzle design and the magnitude of the viscosities tested can affect the observed change in  $SMD$ .

The results from this viscosity test can be used to infer the effect of liquid viscosity on operations in the fluid coker for similar flow conditions. Recall from Table 3.1 that the liquid bitumen viscosity injected into the fluid coker is of the same order as those in this study. The general observation is that the bitumen drop size will increase with its viscosity within the region prior to contact between the drop and coke particles.

#### **7.4 Effect of surface tension on drop size at 1% $GLR$**

The flow conditions required to study the effect of surface tension on drop size for 1%  $GLR$  was presented in Table 6.5. The ratios of the superficial  $We_L$ ,  $Fr_L$  and  $Re_L$ , between the two sprays were 1.5, 0.8 and 0.7, respectively. For these conditions, the ratio for  $We_L$  was highest in both sprays to ensure the effects of surface tension were more dominant in one spray than the other.

The corresponding profiles for the  $SMD$  at  $x = 100$  mm, 202 mm and 405 mm are presented in Figures 7.10, 7.11 and 7.12. At  $x = 100$  mm, the corresponding  $SMD_{gb}$  is about 167  $\mu\text{m}$  and 183  $\mu\text{m}$  for the glycerine solution and canola system, respectively. This corresponds to the lower surface tension liquid (canola) producing 10% higher  $SMD$



than the glycerine solution spray. A 5% test of significance showed that the difference in drop size is not significant at this distance from the nozzle exit.

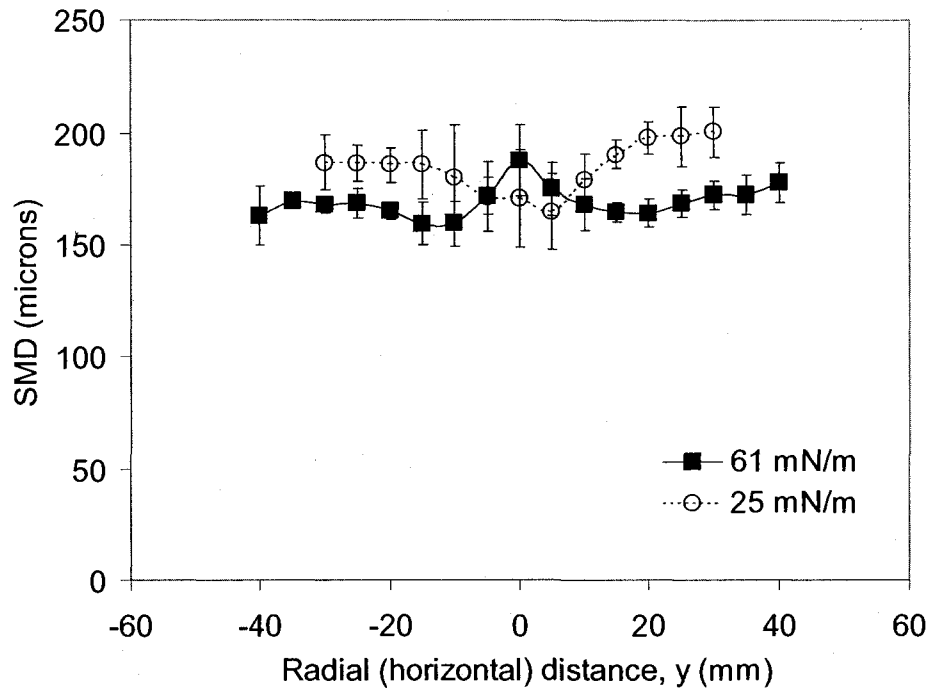


Figure 7.10 –  $SMD$  profiles for comparison of surface tension at  $x = 100$  mm ( $GLR = 1\%$ ) using SS-1.0 nozzle. Error bars denote a 95% confidence interval. Sampling time is 360 seconds.

At  $x = 202$  mm, the  $SMD_{gb}$  was  $165 \mu\text{m}$  in the glycerine solution spray, and  $190 \mu\text{m}$  in the canola oil spray. This indicates a 15% increase in drop size in the spray with the higher surface tension liquid. A similar comparison of the  $SMD_{gb}$  at  $x = 405$  mm, showed that the global  $SMD$  were  $195 \mu\text{m}$  and  $163 \mu\text{m}$ , in the canola and glycerine-water sprays, respectively. In this case, there is a drop size increase of 20% in the lower surface tension

spray. A 5% statistical test of significance showed that the 15% and 20% increase in drop size can be significant.

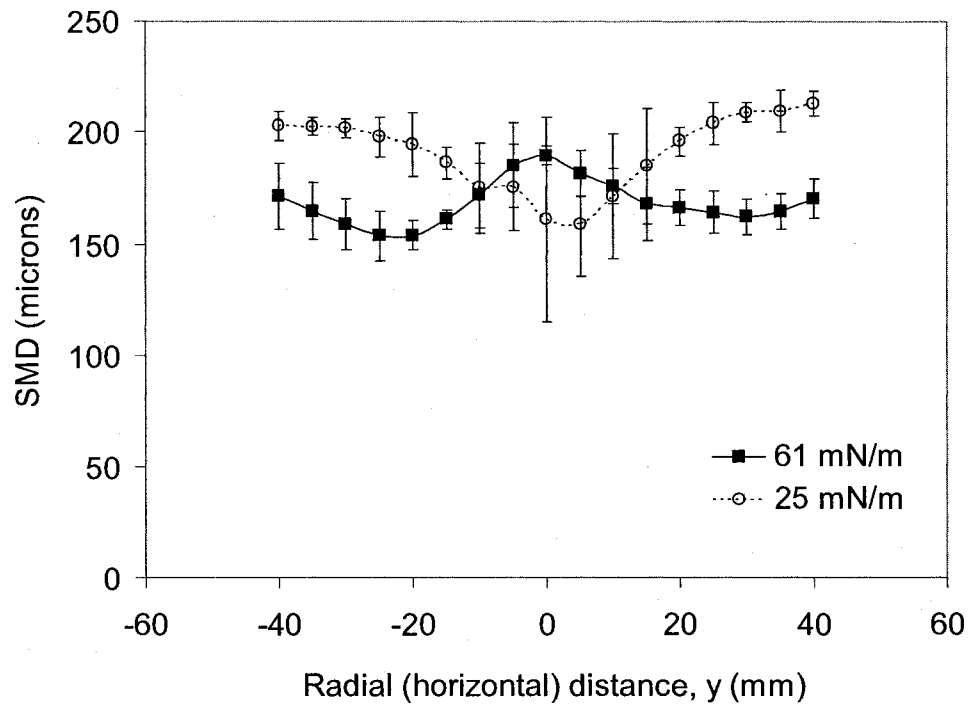


Figure 7.11 – *SMD* profiles for comparison of liquid viscosity at  $x = 202$  mm ( $GLR = 1\%$ ) using SS-1.0 nozzle. Error bars denote a 95% confidence interval. Sampling time is 360 seconds.

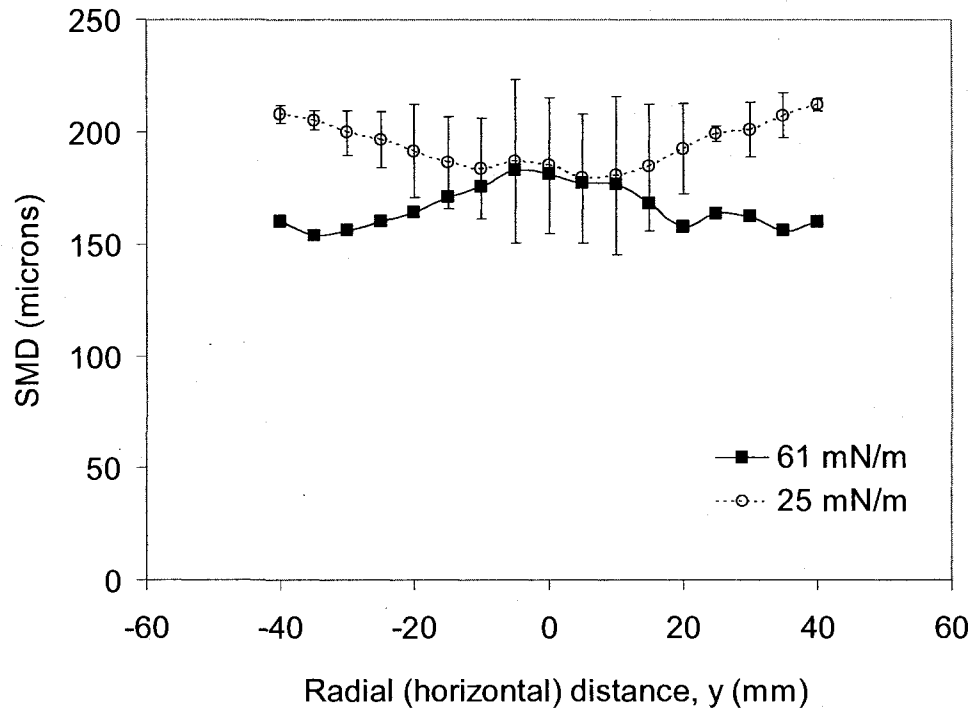


Figure 7.12 – *SMD* profiles for comparison of surface tension at  $x = 405$  mm ( $GLR = 1\%$ ) using SS-1.0 nozzle. Error bars denote a 95% confidence interval. Sampling time is 360 seconds.

Note that the *SMD* profiles at  $x = 405$  mm look much different from those at the other two axial locations, with an apparent inverse relation at the edges of the spray. This is so because a closer look at the profile for glycerine solution spray shows that there is hardly a significant change in drop size. However, drop sizes in the canola profile seem to increase with axial distance. This gives rise to the marked difference at the edges of the spray at this axial location.

### 7.5 Effect of surface tension on drop size at 2% GLR

The flow conditions required to study the effect of surface tension on drop size for 2% GLR were presented in Table 6.6. The ratios of the superficial  $We_L$ ,  $Fr_L$  and  $Re_L$ , between the two sprays were 1.8, 1.0 and 0.8, respectively. Again, for these conditions, the ratio for  $We_L$  was highest in both sprays to ensure the effects of surface tension were more dominant in one spray than the other.

Figures 7.13 and 7.14 show the *SMD* profiles for this system at 100 and 202 mm, respectively.

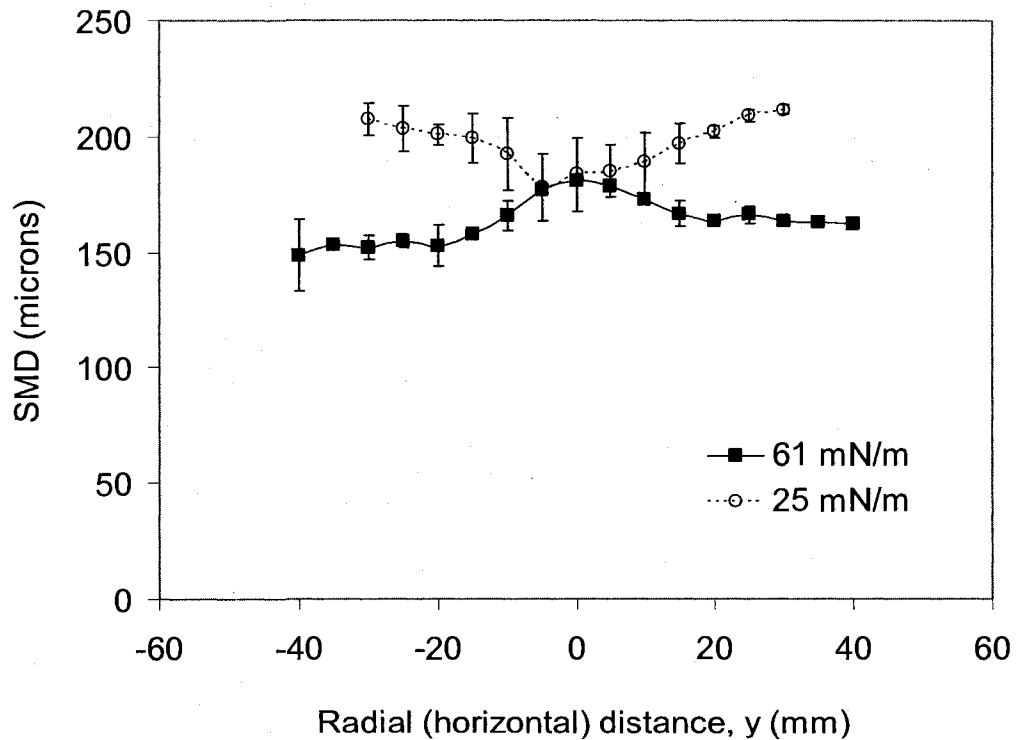


Figure 7.13 – *SMD* profiles for comparison of surface tension at  $x = 100$  mm ( $GLR = 2\%$ ) using SS-1.0 nozzle. Error bars denote a 95% confidence interval. Sampling time is 360 seconds.

At  $x = 100$  mm, the  $SMD_{gb}$  is  $196 \mu\text{m}$  and  $162 \mu\text{m}$  in the canola and glycerine solution sprays, respectively. This gives a 21% increase in drop size in the canola spray. At  $x = 202$  mm,  $SMD_{gb}$  is  $213 \mu\text{m}$  and  $171 \mu\text{m}$  in the canola and glycerine solution sprays, respectively. This corresponds to a 25% increase in drop size in the canola spray.

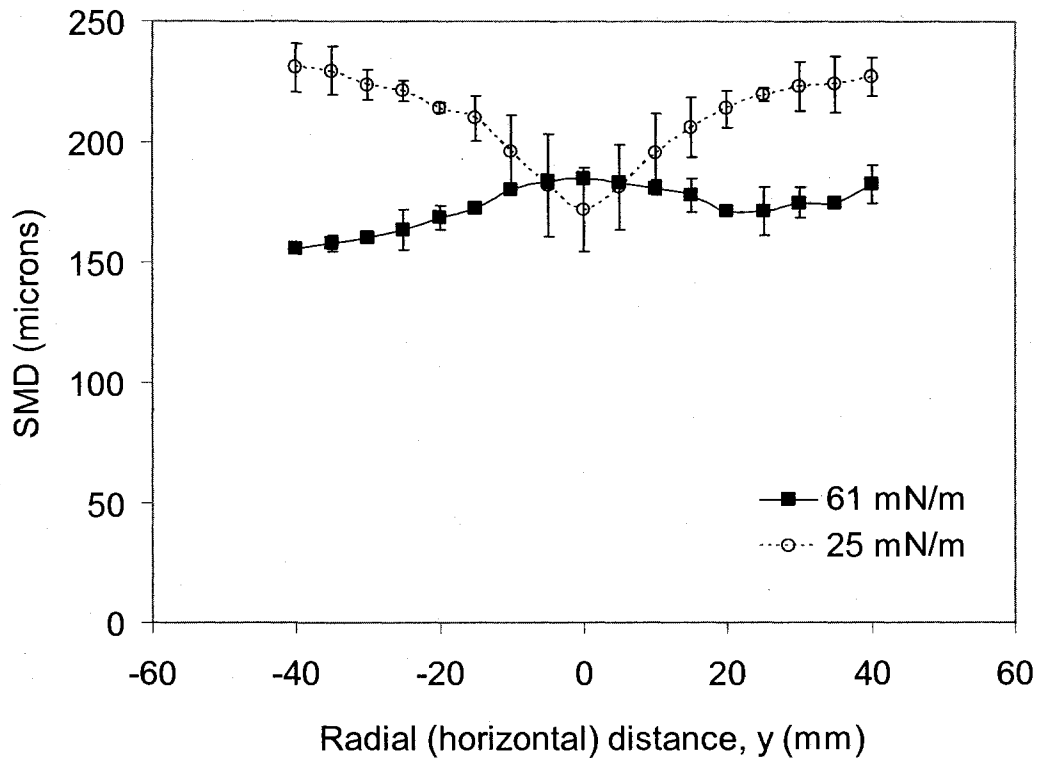


Figure 7.14 –  $SMD$  profiles for comparison of surface tension at  $x = 202$  mm ( $GLR = 2\%$ ) using SS-1.0 nozzle. Error bars denote a 95% confidence interval. Sampling time is 360 seconds.

The results for the effect of surface tension on drop size obtained above suggest that in the fluid coker, there will be a strong tendency for surface tension effects to be negligible for 1%  $GLR$  and within  $32D$  of the nozzle exit, prior to contact between the bitumen

drops and coke particles. For greater distances and  $GLR$ , surface tension effects become significant and tend to increase the drop size. The different effects of surface tension on drop size are evident in atomization literature. Lund et al. [13] observed that  $SMD$  decreased between 14% and 23% when surface tension increased from 30 to 67 mN/m, within  $1\% < GLR < 7\%$ . Another trend was observed by Santangelo and Sojka [14], who observed a maximum of 12% decrease in  $SMD$  when the surface tension was increased from 29 to 74 mN/m, for  $112 < \mu_L < 820$  mPa-s and  $2\% < GLR < 10\%$ . The observations in this study however, differ from those in twin-fluid atomizers [8, 11], where the  $SMD$  increases with liquid surface tension in the order  $\sim \gamma^{0.2}$ . Comparison of the results in this work shows the importance of obtaining radial profiles of  $SMD$  when studying the effect of a specific liquid property at given axial distance within a spray, which was generally absent in previous studies. Furthermore, it is also evident that the results observed for the effect of surface tension on  $SMD$  surface tension depends on nozzle design.

## **7.6 Effect of Nozzle size geometry**

### **7.6.1 Geometric effects at 1% $GLR$ using air and glycerine-water mixture**

The flow conditions required to study the effect of nozzle size on drop size in a glycerine-water spray at 1%  $GLR$  were presented in Table 6.7. The  $SMD$  profiles at  $x = 100$  and 202 mm for the test conditions above are presented in Figures 7.15 and 7.16. At  $x = 100$ mm, the evaluated  $SMD_{gb}$  were 176  $\mu\text{m}$  and 169  $\mu\text{m}$ , respectively for the SS-1.0 and SS-1.3 nozzles, respectively. At  $x = 202$  mm, the corresponding global  $SMD$ s were 179  $\mu\text{m}$  and 166  $\mu\text{m}$ , respectively. The difference in drop sizes produced from both

nozzles was 4% and 8%, respectively at 100 mm and 202 mm. A 5% test of significance showed that this difference was not significant.

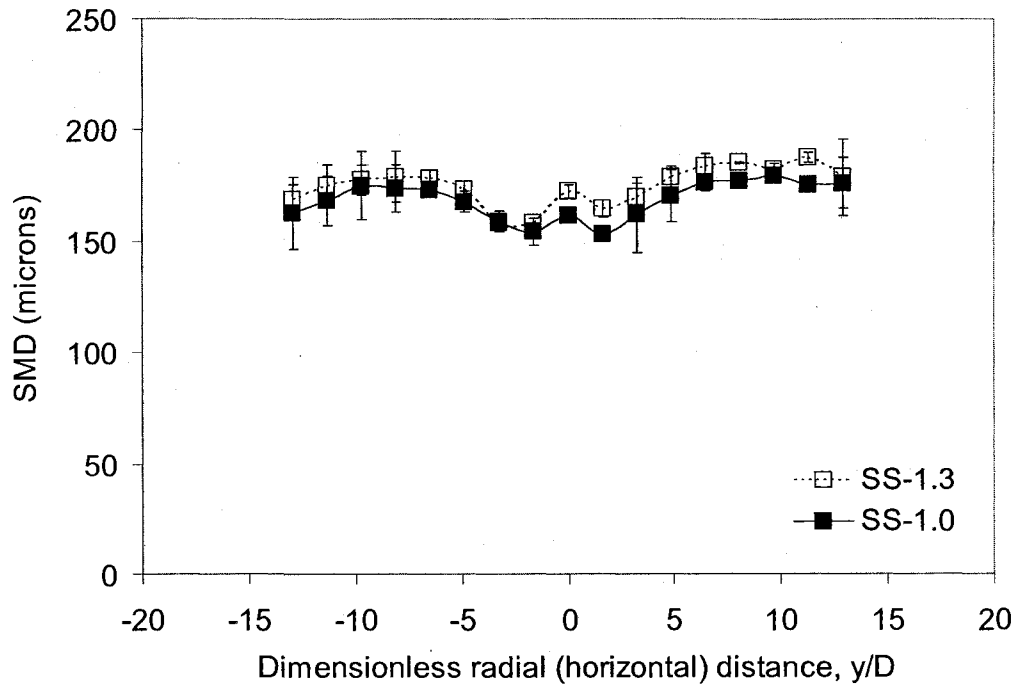


Figure 7.15: *SMD* profiles for comparison of nozzle size effects at  $x = 100$  mm ( $GLR = 1\%$ ) using SS-1.0 ( $D = 3.1$  mm) and SS-1.3 ( $D = 4.1$  mm). Data was produced using air and glycerine-water mixture. Sampling time is 360 seconds.

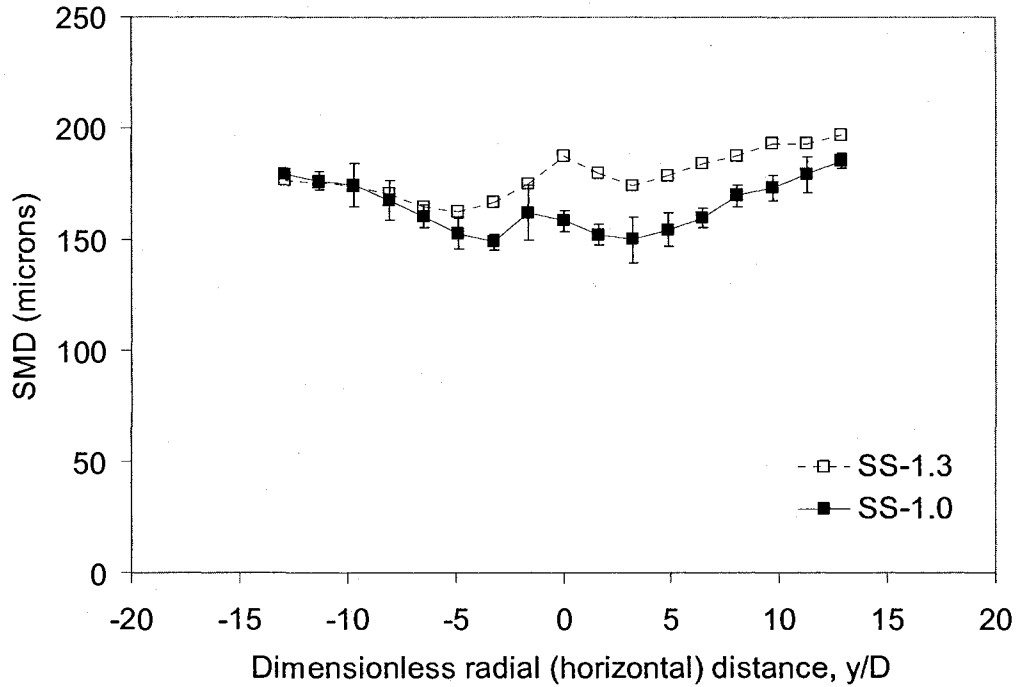


Figure 7.16: *SMD* profiles for comparison of nozzle size effects at  $x = 202$  mm ( $GLR = 1\%$ ) using SS-1.0 ( $D = 3.1$  mm) and SS-1.3 ( $D = 4.1$  mm). Data was produced using air and glycerine-water mixture. Sampling time is 360 seconds.

### 7.6.2 Geometric effects at 1% *GLR* using air and water

Similar tests as described in the previous section were also performed using air and water. The test conditions were presented in Table 6.8. The respective *SMD* profiles at  $x = 100$  and 202 mm are shown in Figures 7.17 and 7.18, respectively. At  $x = 100$  mm,  $SMD_{gb}$  for the SS-1.0 and SS-1.3 was 125 and 162  $\mu\text{m}$ , respectively. The corresponding  $SMD_{gb}$  at  $x = 202$  mm was 122  $\mu\text{m}$  and 160  $\mu\text{m}$ , for the small and large nozzle, respectively. The differences in drop size at 100 and 202 mm correspond to an increase of 30 and 31%, respectively. These difference were statistically significant based on a 5% test of significance level.



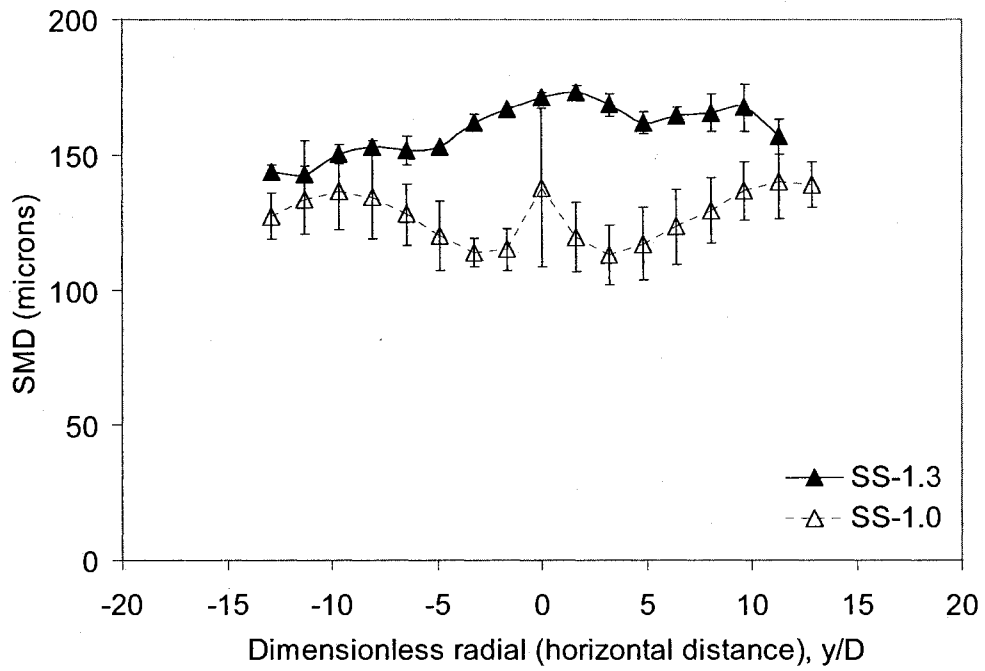


Figure 7.17: *SMD* profiles for comparison of nozzle size effects at  $x = 100\text{mm}$  ( $GLR = 1\%$ ) using SS-1.0 ( $D = 3.1\text{ mm}$ ) and SS-1.3 ( $D = 4.1\text{ mm}$ ). Data was produced using air and water. Sampling time is 360 seconds.

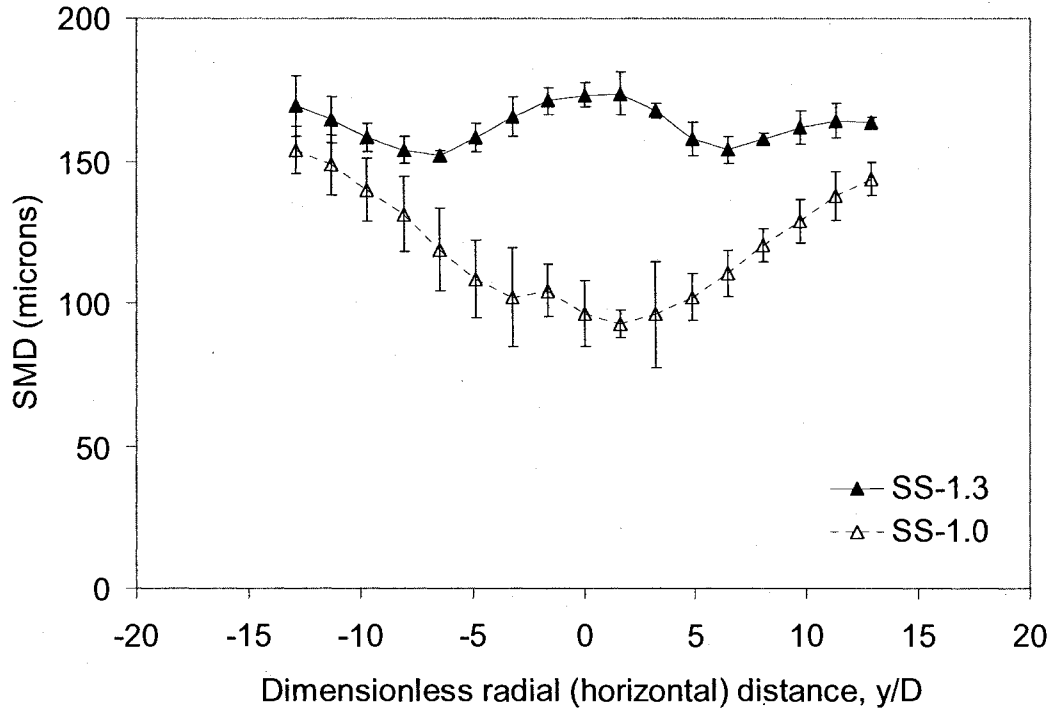


Figure 7.18: *SMD* profiles for comparison of nozzle size effects at  $x = 202\text{mm}$  ( $GLR = 1\%$ ) using SS-1.0 ( $D = 3.1\text{ mm}$ ) and SS-1.3 ( $D = 4.1\text{ mm}$ ). Data was produced using air and water. Sampling time is 360 seconds.

The general result from the influence of nozzle size on drop size showed that an increase in nozzle size geometry may increase the *SMD* produced in the respective sprays. The observed increase in *SMD* with nozzle size in these tests is similar to studies in twin-fluid atomizers [8, 11], where *SMD* varies according to  $\sim D^{0.5}$ . However, the insignificant change in *SMD* observed in the glycerine-water tests is also a similar trend in effervescent atomizers as documented by Sovani [17].

The results above can be related to the design of new geometrically similar nozzles used in fluid cokers and operating under similar flow conditions. It shows that the *SMD* is

likely to increase with nozzle (up to 31%), within the range of fluid physical properties and nozzle sizes used in this study. Knowledge of this trend in fluid coker nozzles will be valuable in nozzle development to allow for better designs. The combined results from Sections 7.2 to 7.6, which can be used in the nozzle design/development process to estimate  $SMD$  at axial regions within  $32D$  of the nozzle exit are presented in the next Section. Recall from Section 5.1 that axial positions within this range are of interest in the fluid coker, because a majority of the drops formed come in contact with the coke particles in this region.

### **7.7 Correlation for $SMD_{gb}$**

One of the thesis objectives is the development of a correlation for the  $SMD_{gb}$  in terms of nozzle operating conditions, fluid properties and nozzle sizes. The  $SMD_{gb}$  is a representative drop size in the spray at a given axial position downstream of the nozzle exit. Note that the radius from the spray centre that was used in this analysis corresponds to  $y/D = \pm 12.9$  for both nozzles. This radius was used since it contained most of the liquid flux across the spray for the fluid systems studied and both nozzle sizes.

As mentioned also in Section 5.3.5, a power law correlation may be used to fit the required data. The test data used in the curve-fit are presented in Table 7.1.

Table 7.1– Test data used in curve-fit for  $SMD_{gb}$  correlation. Data is for  $x = 100$  mm.

Fluid system	Nozzle Name	$\frac{SMD_{gb}}{D}$	GLR,	DR, (Density Ratio)	$Re_L$ ,	$Fr_L$ ,	$We_L$ ,
Air-Water	SS-1.0	0.0422	0.01	0.0034	38791	5169	6948
Air-Water	SS-1.0	0.0384	0.02	0.0046	38791	5169	6948
Air-Canola Oil	SS-1.0	0.0616	0.01	0.0032	590	6331	21606
Air-Canola Oil	SS-1.0	0.0660	0.02	0.0043	590	6331	21606
Air-Glycerine Solution	SS-1.0	0.0554	0.01	0.0022	580	3590	6658
Air-Glycerine Solution	SS-1.0	0.0543	0.01	0.0032	840	7527	13959
Air-Glycerine Solution	SS-1.0	0.0517	0.02	0.0042	770	6331	11742
Air-Glycerine Solution	SS-1.3	0.0435	0.01	0.0022	902	3750	12165
Air-Water	SS-1.3	0.0381	0.01	0.0034	58660	5110	12013

Note in Table 7.1 the exit diameter for SS-1.0 and SS-1.3 are 3.1 mm and 4.1 mm, respectively. From Eqn (5.11), the resulting correlation is given as:

$$\frac{SMD_{gb}}{D} = 1641 * (GLR)^{-0.55} (DR)^{1.20} (Re_L)^{-0.15} (Fr_L)^{-0.48} (We_L)^{-0.06} \quad (7.1)$$

The correlation in Eqn. (7.1) shows that the  $SMD_{gb}$  depends weakly on the  $We_L$ , and is negatively proportional to the  $Re_L$  and  $Fr_L$ . However, it increases with the density ratio ( $DR$ ) at the nozzle exit. From twin-fluid  $SMD$  correlations by Yamane et al. [7], Elkotb et al. [8], and El-Shanawany et al. [11], the variation  $GLR^{-0.29 \text{ to } -1.0}$ ,  $DR^{0.1 \text{ to } 0.26}$ ,  $Re_L^{-0.39 \text{ to } -0.5}$ ,

and  $We_L^{-0.18}$ . Except for the exponent of  $DR$  in Eqn. (7.1), that is greater than unity, the exponents in Eqn. (7.1) are quite comparable to the drop size correlation in twin-fluid systems.

Principle Component Analysis (PCA) was applied to the data in Table 7.1 using MATLAB and MAPLE softwares. The PCA was used to determine the eigenvector (or dimensionless quantity), with the highest order of significance. From the result, the order of decreasing significance was  $We_L$ ,  $Fr_L$  and  $Re_L$ . Note that from the PCA one may choose to ignore the components of lesser significance. However, knowledge of two-phase flows has shown that  $DR$  and  $GLR$  are very important parameters in spray atomization as they determine the flow pattern upstream of the nozzle in the conduit section. The PCA does not consider the variation in the flow regime that a change in  $GLR$  can cause, for example. Therefore, they were not discarded in the  $SMD_{gb}$  correlation.

To test the accuracy of the above correlation it was used to estimate the  $SMD_{gb}$  for four other test conditions and comparing it with actual  $SMD_{gb}$  obtained from measured data. The results are presented in Figure 7.19. The open squares denoted ‘correlation-fit data’ are the data used in obtaining the correlation in Eqn. (7.1). The figure shows that the maximum deviation from the actual data is about 15%. The  $SMD_{gb}$  corresponding to the closed triangles were estimated using Eqn. (7.1). From the data the maximum deviation between estimated and actual data is about 17%. This accuracy in the correlation is acceptable given the number of data used in obtaining Eqn. (7.1).

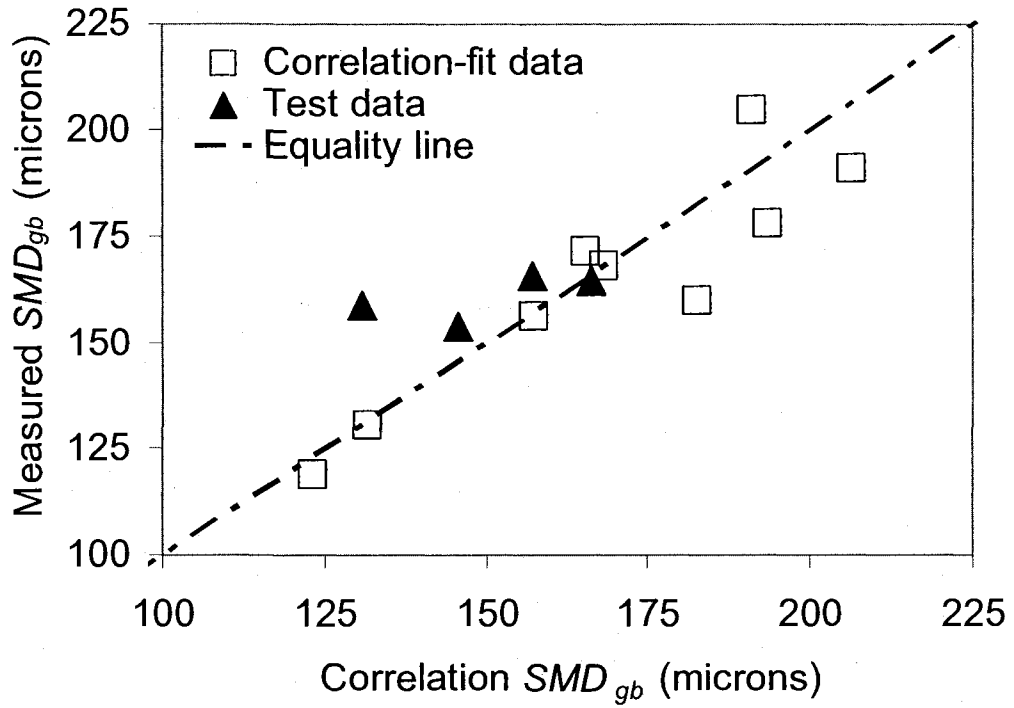


Figure 7.19: Comparison of correlation and measured  $SMD_{gb}$ .

More investigation should be performed to provide more data to further strengthen the validity of the correlation obtained. This ultimate goal will aid in the use of the above correlation as a tool to estimate representative drop sizes for flow conditions in the fluid coker.

# CHAPTER 8

## SUMMARY AND CONCLUSIONS

This Section summarizes the main objectives, salient results and conclusions based on experimental results. Recommendations for future tests and other atomization studies of interest are also presented in this Section.

The main objectives of this study were to compare the mean drop size (*SMD*) produced from sprays of different viscosities, surface tension and sizes of small-scale fluid coker (FC) nozzles. The comparisons were made by evaluating the differences between global *SMDs* (i.e.  $SMD_{gb}$ ), which is a representative drop size based on liquid volume flux within the spray cross section. The final objective was to establish an empirical relationship for the  $SMD_{gb}$  in the spray as a function of nozzle size, viscosity, surface tension and flow conditions. Small-scale laboratory tests provide inexpensive and easily accessible alternative to study the atomization behaviour of FC nozzles in situ. The overall goal in this study was to establish a fundamental means of understanding the performance of full-scale (or commercial) FC nozzles. This will aid in optimizing nozzle flow conditions in the FC for desired product yield, and serve as a major tool in nozzle design and development for future generations of FC nozzle.

Comparison of the  $SMD_{gb}$  for the different viscosity sprays showed that drop size has a significant increase between 34 to 64% for the *GLRs* studied. It can be concluded that in the fluid coker, the general tendency is that the bitumen drop size will increase with its viscosity within the region prior to contact between the drop and coke particles.

Surface tension effects on  $SMD_{gb}$  were negligible at 1%  $GLR$  and for an axial position within  $32D$  of the nozzle exit. The other results showed an increase (between 15 and 25%) in drop size with a decrease in surface tension. It can be concluded that in the fluid coker, the surface tension of the liquid bitumen may affect its drop size depending on the operating  $GLR$  and proximity of the drops from the nozzle exit.

An increase in nozzle size may increase the  $SMD_{gb}$  by up to 31% for the different gas-liquid systems studied. It can be concluded that for the full-scale fluid coker nozzle, the magnitude of increase in drop size associated with an increase in nozzle size depends on the properties of the fluid injected into the fluid coker.

Finally, the  $SMD_{gb}$  correlation developed is able to estimate the representative drop size within a maximum deviation of 17%. It can be concluded that this accuracy is fairly acceptable given the number of data used in developing the correlation.

Possible recommendations for future tests and studies, which should be of interest in the atomization experimental program are listed below:

- For flexibility in attaining a wider range of scattering angles, the PDA transmitter and receiver should be mounted in a vertical plane perpendicular to the plane of the nozzle exit orifice.



- In future atomization studies using the PDA, it is desirable to ensure that liquids have approximately equal refractive indices. This is because liquids with higher refractive index will tend to reduce the sensitivity of the PDA.
- Increasing the pressure capacity of the compressor is desired. This is because, there is currently a limit on the *GLR* that can be attained for a given liquid volume flow rate through the SS-1.0. As future needs arise, such as testing the SS-1.3 at higher *GLRs* or perhaps testing a full-size FC nozzle, it becomes very apparent that the current compressor capacity is insufficient. On the same note, the pump has to be changed to accommodate the higher liquid flow rates through the bigger nozzles
- It will be worthwhile to perform atomization studies similar to those in this study under different pressurized ambient conditions. This will be go a step further towards establishing a correlation, which incorporates varying ambient pressures in which nozzles in a fluid coker can discharge into.

In closing, it is important to note that based on the comparison of results of this test and those in literature, it is imperative to conduct in-house studies for specific nozzle characteristics to be investigated. This is evident since due to the differences in performance of different nozzle designs in literature, their spray behaviour may not specifically applicable to fluid coker nozzles.

## BIBLIOGRAPHY

1. Chan, E.W., Base, T.E., and McCracken, T, Design and development of Syncrude coker feed nozzles – A coker 2000 initiative, *Syncrude Report*, p. 26<sup>a</sup>, 175<sup>b</sup>, 228<sup>c</sup>, 205<sup>d</sup>, 210<sup>e</sup>, 66<sup>f</sup>, March 1999.
2. Knapper, B.A., Experimental studies on the hydrodynamics of fluid bed cokers, *Masters Thesis in Chemical Engineering, University of Saskatchewan*, p. 20, 2000.
3. Lefebvre, A.H., Atomization and Sprays, *Hemisphere Publishing Corporation*, New York, p. 202<sup>a</sup>, 27<sup>b</sup>, 238<sup>c</sup>, 260<sup>d</sup>, 1989.
4. Jermy, M.C., Hussain, M., and Greenhalgh, D.A., Operating liquid-fuel airblast injectors in low-pressure test rigs: strategies for scaling down the flow conditions, *Measurement Science and Technology*, vol. 14, pp. 1151-1158, 2003.
5. Hekestad, G., Scaling the interaction of water sprays and flames, *Fire Safety Journal*, vol. 37, pp. 535-548, 2002.
6. Elkotb, M.M. Fuel atomization for spray modeling, *Progress in Energy and Combustion Science* vol. 8, No. 1, pp. 61-91, 1982.
7. Yamane, Y., Yokota, H., and Kamimoto, T., Atomization and air-entrainment characteristics of unsteady dense sprays, *Japan Society of Mechanical Engineering* vol. 37, No. 3, pp. 604-610, 1994.
8. Elkotb, M.M, Mahdy, M.A., and Montaser, M.E. Investigation of external-mixing airblast atomizers, *Proceedings of the 2nd International Conference on Liquid Atomization and Sprays*, Madison, Wisconsin, U.S.A, pp. 107-115, 1982.

9. Rizkalla, A.A. and Lefebvre, A.H., The influence of air and liquid properties on airblast atomization, *Transactions of ASME Journal of Fluids Engineering*, vol. 97, No. 3, pp. 316-320, 1975.
10. Lefebvre, A.H., Airblast atomization, *Progress in Energy and Combustion Science*, Vol. 6, pp. 233-261, 1980.
11. El-Shanawany, M.S.M.R. and Lefebvre, A.H., Airblast atomization: The effect of linear scale on mean drop size, *Journal of Energy*, vol. 4, No. 4. pp. 184-189, 1980.
12. Buckner, H.N. and Sojka, P.E., Effervescent atomization of high-viscosity fluids: Part I, Newtonian liquids, *Atomization and Sprays*, vol. 1, pp. 239-252, 1991.
13. Lund, M.T., Sojka, P.E., Lefebvre, A.H., and Gosselin, P.G., Effervescent atomization at low mass flow rates. Part 1: the influence of surface tension, *Atomization and Sprays*, vol. 3, pp. 77-89, 1993.
14. Santangelo, P.J., and Sojka, P.E. A holographic investigation of the near nozzle structure of an effervescent atomizer produced spray, *Atomization and Sprays*, vol. 5, pp. 137-155, 1995.
15. Nasr, G.G., Yule, A.J., and Bendig, L., Industrial sprays and atomization: design, analysis and applications, *Springer-Verlag London Limited*, p. 10<sup>a</sup>, 17<sup>b</sup>, 23<sup>c</sup>, 12<sup>d</sup>, 2002.
16. Liu, H., Science and Engineering of droplets – Fundamentals and Applications, *William Andrew Publishing/Noyes*, p. 247<sup>a</sup>, 317<sup>b</sup>, 17<sup>c</sup>, 122<sup>d</sup>, 332<sup>e</sup>, 2000.
17. Sovani, S.D., Sojka, P.E. and Lefebvre, A.H., Effervescent atomization, *Progress in Energy and Combustion Science*, vol. 27, pp. 483-521, 2001.

18. Kirpalani, D.M. and McCracken, T.W., Performance diagnostics for nozzles fed with multiphase flow, *ILASS-Europe 2002, Zaragoza*, September 9 – 11, 2002.
19. Tafreshi, Z.M., Kirpalani, D.M., Bennett, A., and McCracken, T.W., Improving the efficiency of fluid cokers by altering two-phase feed characteristics, *Powder Technology*, vol. 125, No. 2, pp. 234-241, 2002.
20. Copan, J., Balachandar, R., and Berruti, F., Droplet size-velocity characteristics of sprays generated by two-phase feed nozzles, *Chemical Engineering Communications*, vol. 184, pp. 105-124, 2001.
21. Ariyapadi, S., Balachandar, R., and Berruti, F. Spray characteristics of two-phase feed nozzles, *Canadian Journal of Chemical Engineering*, vol. 81, pp. 923-939, 2003.
22. Shavit, U. and Chigier, N., Development and Evaluation of a new turbulence generator for atomization research, *Experiments in Fluids*, vol. 20, No. 4, pp. 291-301, 1996.
23. McCarthy, M.J. and Molloy, N.A. Review of stability of liquid jets and influence of nozzle design, *Chemical Engineering Journal*, vol. 7, pp. 1-20, 1974.
24. Pilch, M., and Erdman, C.A., Use of breakup time data and velocity history data to predict the maximum size of stable fragments for acceleration-induced breakup of a liquid drop, *International Journal of Multiphase Flow*, vol. 13, pp. 741-757, 1987.
25. Hsiang, L.-P., and Faeth, G.M., Drop deformation and breakup due to shock wave and steady disturbances, *International Journal of Multiphase Flow*, vol. 21, No. 4, pp. 545-560, 1995.
26. Rissio, F., The mechanisms of deformation and breakup of drops and bubbles, *Multiphase Science and Technology*, vol. 12, pp. 1-50, 2000.

27. Brodkey, R. S., The phenomena of fluid motions, *Addison-Wesley Publication Company*, Reading, Massachusetts, 1967.
28. Lefebvre, A.H., Wang, X.F., and Martin, C.A., Spray characteristics of aerated-liquid pressure atomizers, *AIAA Journal of Propulsion and Power*, vol. 4, No. 6, pp. 293-298, 1988.
29. Roesler, T.C. and Lefebvre, A.H., Studies on aerated-liquid atomization, *International Journal of Turbo Jet Engines*, vol. 6, pp.221-230, 1989.
30. Whalley, P. B., (1996), Two-Phase flow and heat transfer; *Oxford University Press*, New York, p. 5, 1996.
31. Chin, J.S. and Lefebvre, A.H., Flow regimes in effervescent atomization, *Atomization and Sprays*, vol. 3, pp. 463-475, 1993.
32. Semiao, V., Andrade, P., and Carvalho, M.G., Spray characterization: numerical prediction of Sauter mean diameter and droplet size distribution, *Fuel*, vol. 75, No. 15, pp. 1707-1714, 1996.
33. Squire, H.B., Investigation of the stability of a moving liquid film, *Journal of Applied Physics*, vol. 4, pp. 167-169, 1953.
34. Weber, G., Disintegration of liquid jets, *Z. Angew. Math. Mech.*, vol. 11, No. 2, pp. 136-154, 1931.
35. Chesters, A.K., The applicability of dynamic-similarity criteria to isothermal liquid-gas two-phase flows without mass transfer, *International Journal of Multiphase Flow*, vol. 2, pp. 191-212, 1975.
36. Geraets, J.J.M., Centrifugal scaling of isothermal gas-liquid flow in horizontal tubes, *International Journal of Multiphase Flow*, vol. 14, No. 3, pp. 287-303, 1988.

37. Hurlbert, K.M., Witte, L.C., Best, F.R, and Kurwitz, C., Scaling two-phase flows to Mars and Moon gravity conditions, *International Journal of Multiphase Flow*, vol. 30, pp. 351-368, 2004.
38. Douglas, J.F., Gasiorek, J.M, and Swaffield, J.A., Fluid Mechanics, Singapore, *Longman Scientific and Technical*, p. 268, 1995.
39. White, F.M., Fluid Mechanics, *McGraw-Hill Series*, U.S.A, p. 771, 1999.
40. Przybylski, R., Canola oil: physical and chemical properties, *Canola Council of Canada Publications*, p.1, 2001.
41. Parker, D.B., Positive displacement pumps - performance and application, *Proceedings of 11th International Pump Users Symposium*, 1994.
42. Cole-Parmer General Catalogue, Acrylic inline flow meters, p. 467, 2003/2004.
43. Dantec Dynamics A/S, *BSA Flow Software, Version 2.1: Installation and User's guide*, Skovlunde, 2003.
44. Durst, F., Brenn, G., and Xu, T.H., A review of the development and characteristics of planar phase-Doppler anemometry, *Measurement Science Technology*, vol. 8, pp. 1203-1221, 1997.
45. Widmann, J.F. Presser, C., and Leigh, S.D., Improving phase Doppler volume flux measurements in low data rate applications, *Measurement Science Technology*, vol. 12, pp. 1180-1190, 2001.
46. Dullenkopf, K., Willmann, M., Wittig, S., Schöne, F., Stieglmeier, M., Tropea, C., and Mundo, C.), Comparative mass flux measurements in sprays using a patternator and the phase-doppler technique, *Part. Part. Syst. Charact.*, vol. 15, pp. 81-89, 1998.

47. Taitel, Y. and Dukler, A. E., A model for predicting flow regime transitions in horizontal and near horizontal gas-liquid flow, *AIChE Journal*, vol. 22, No. 1, pp. 47-55, 1976.
48. Baker, O., Simultaneous flow of oil and gas, *Oil and Gas Journal*, vol. 53, p. 185, 1954.
49. Scott, D. S., Properties of co-current gas-liquid flow, *AIChE*, vol. 4, pp. 199-277, 1963.
50. Maldonado, S., Improving the stability of gas-liquid sprays by modifying the two-phase flow entering the nozzle, *Master of Science Thesis*, Department of Mechanical Engineering, University of Alberta, Appendix A1, pp.113 – 114.
51. Baron, P.A. and Willeke, K., ed., Aerosol Measurement - Principles, Techniques, and Applications, 2nd Edition, *John Wiley and Sons*, p. 89, 2001.
52. Shahidi, F., ed., Bailey's Industrial Oil and Fat Products, vol. 1-6, 6th Edition, *John Wiley and Sons*, p. 63, 2005.
53. Perry, R.H. and Green, D.W., *Perry's Chemical Engineer's Handbook, Sixth Edition*, p. 5-22, 1984.
54. Ricou, F. P., and Spalding, D. B., Measurements of entrainment by axisymmetrical turbulent jets, *Journal of Fluid Mechanics*, vol. 11, pp. 21-32, 1961.
55. Bush, S.G. and Sojka, P.E., Entrainment by effervescent sprays at low mass flow rates, *Proceedings of the Sixth International Conference on Liquid Atomization and Spray Systems*, Rouen, France, pp. 609-615, 1994.

56. McQuiston, F.C., Parker, J.D., and Spitler, J.D., Heating, ventilation and air conditioning: Analysis and Design, John Wiley and Sons Inc., 6<sup>th</sup> Edition, pp. 407 – 413, 2005.
57. Scheaffer, R.L. and McClave, J.T., Probability and Statistics for Engineers, 4<sup>th</sup> Edition, California, Wadsworth Publishing Company, p. 496, 1995.
58. Pope, S.B., Turbulent Flows, 1<sup>st</sup> Edition, Cambridge, Cambridge University Press, p.97<sup>a</sup>, 100<sup>b</sup>, 98<sup>c</sup>, 115<sup>d</sup>, 116<sup>e</sup>, 119<sup>f</sup>, 2000.
59. Coleman, H.W. and Steele (Jr), W.G., Experimentation and uncertainty analysis for engineers, New York: *John Wiley and Sons*, p. 28, 42, 1989.



## **APPENDICES**

# APPENDIX A1 – CALIBRATION PLOTS

This Appendix presents all the plots obtained during the calibration of the measuring instruments used during the study.

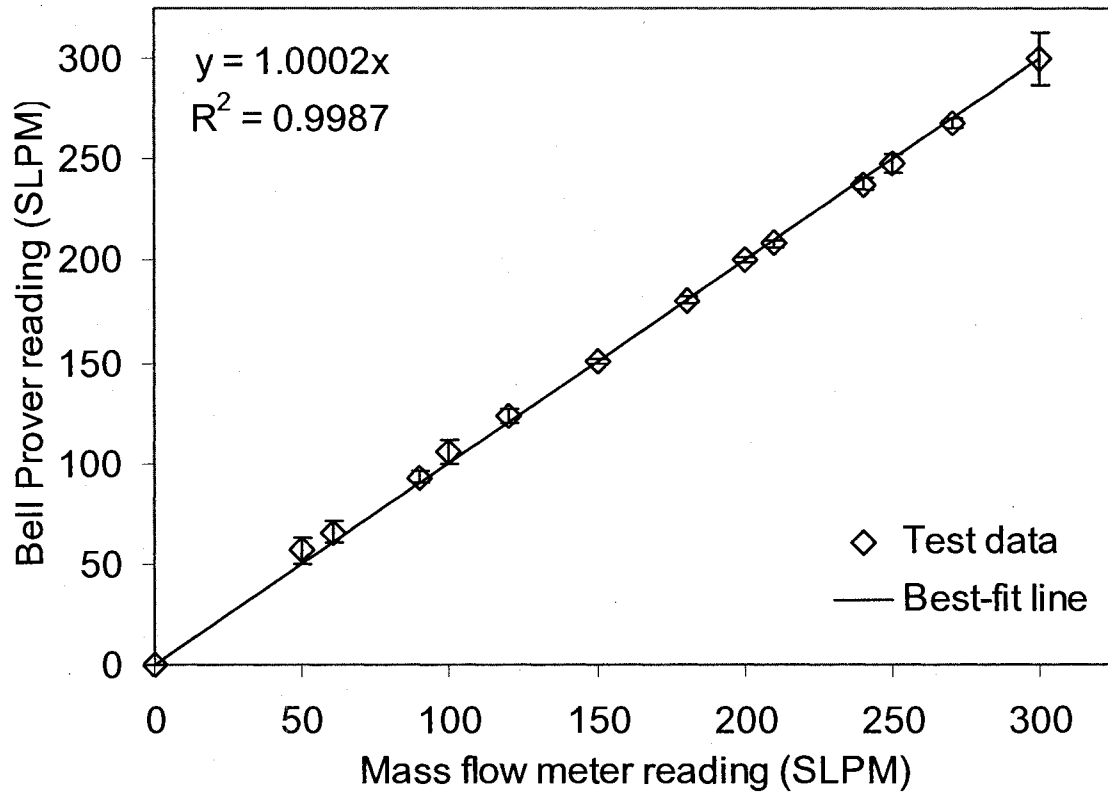


Figure A1-1: Calibration plot for air mass flow meter

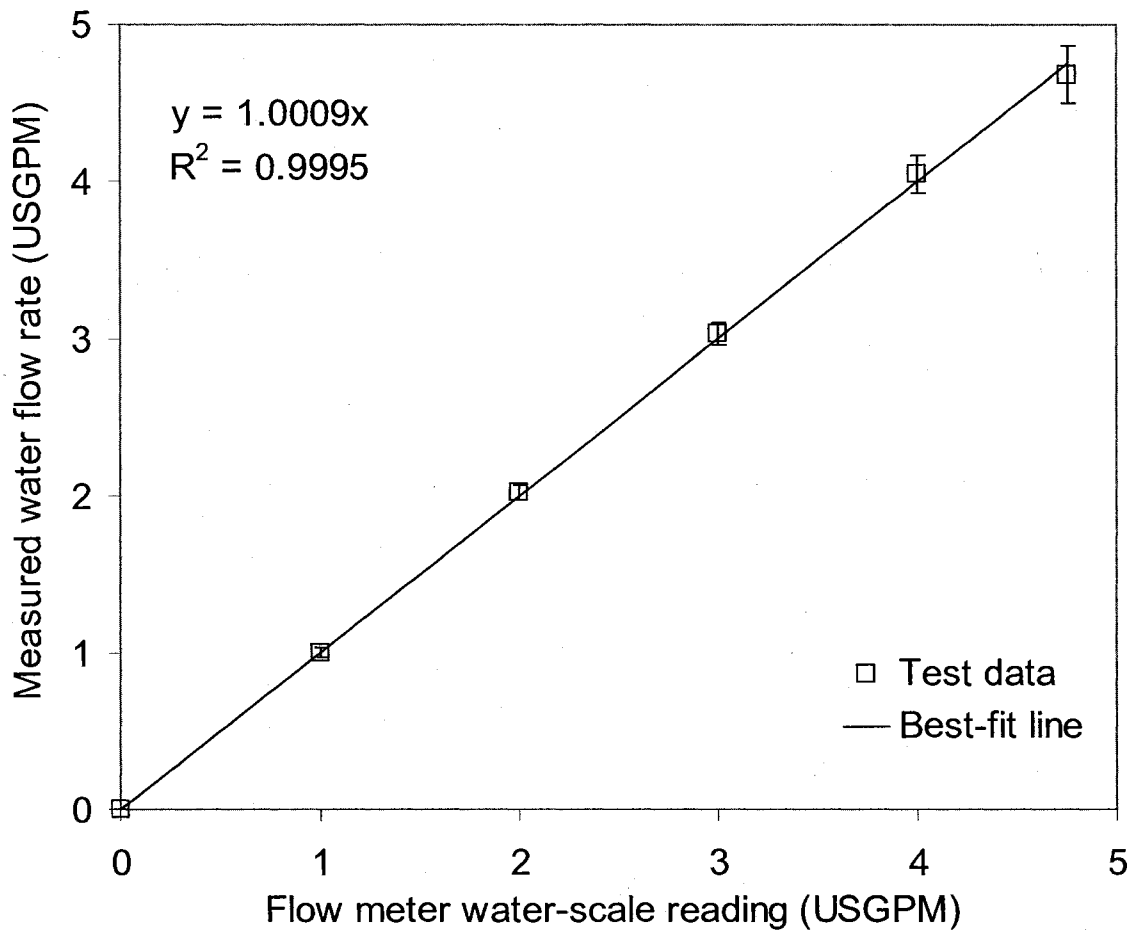


Figure A1-2: Calibration plot for liquid flow meter using water

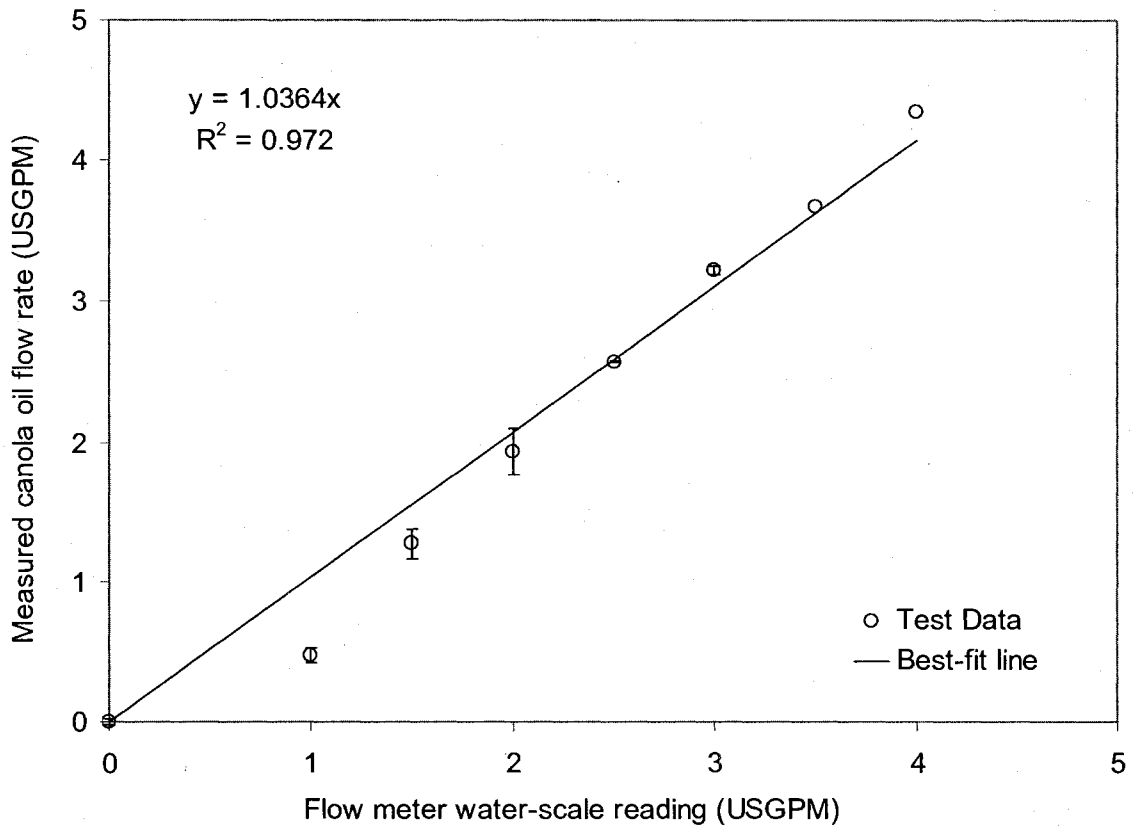


Figure A1-3: Calibration plot for liquid flow meter using canola oil

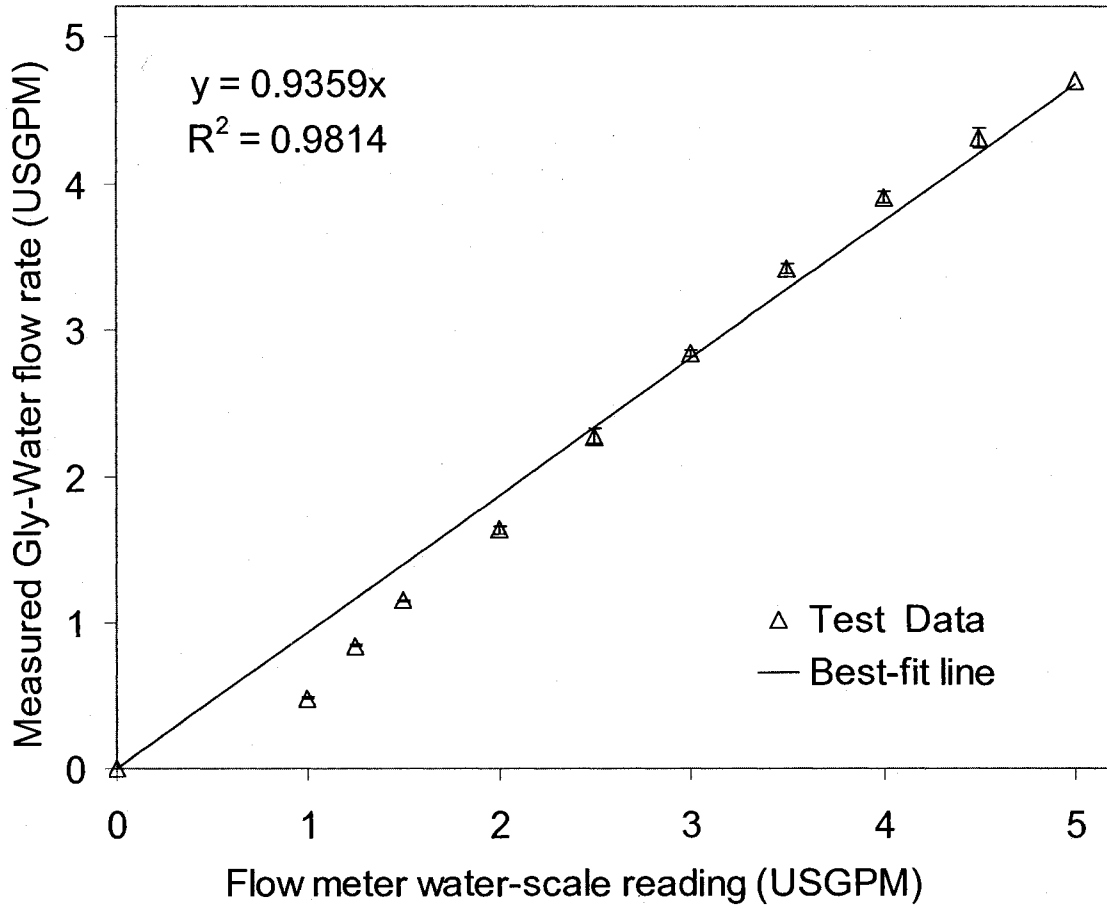


Figure A1-4: Calibration plot for liquid flow meter using glycerine-water mixture

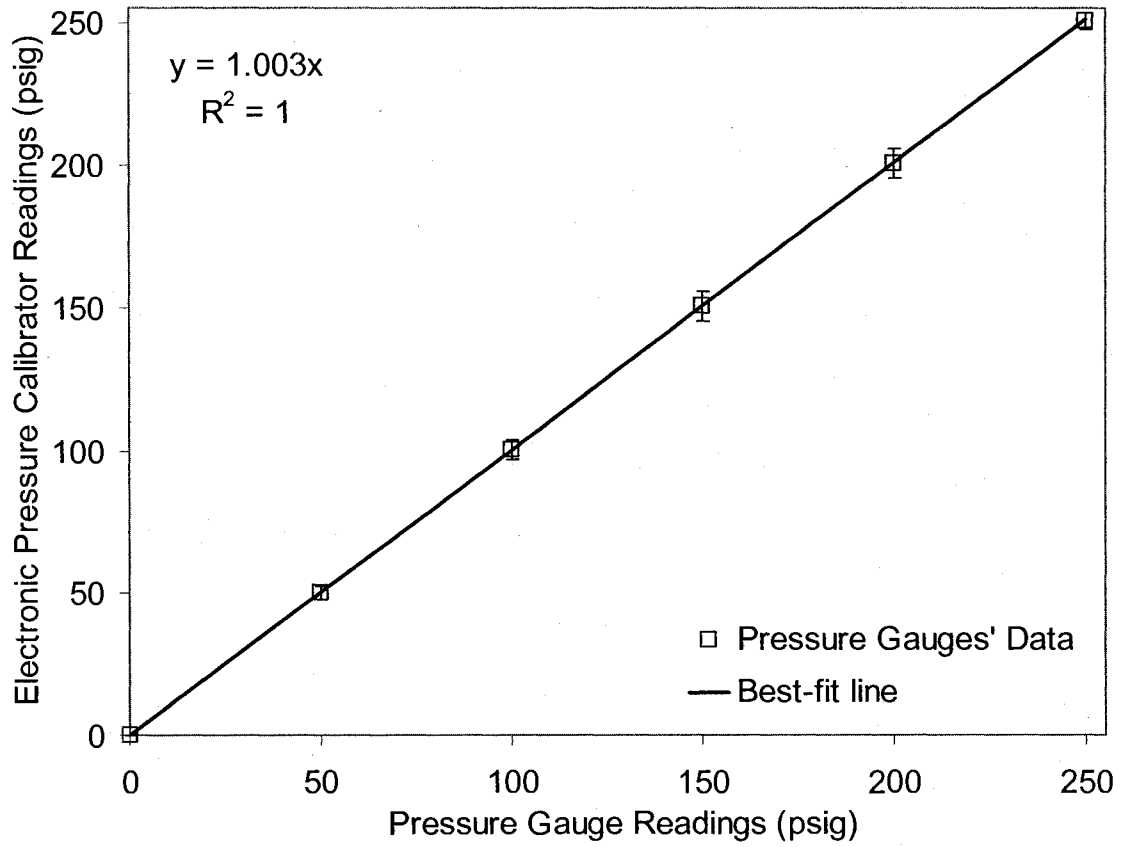


Figure A1-5: Calibration plot for static pressure gauges

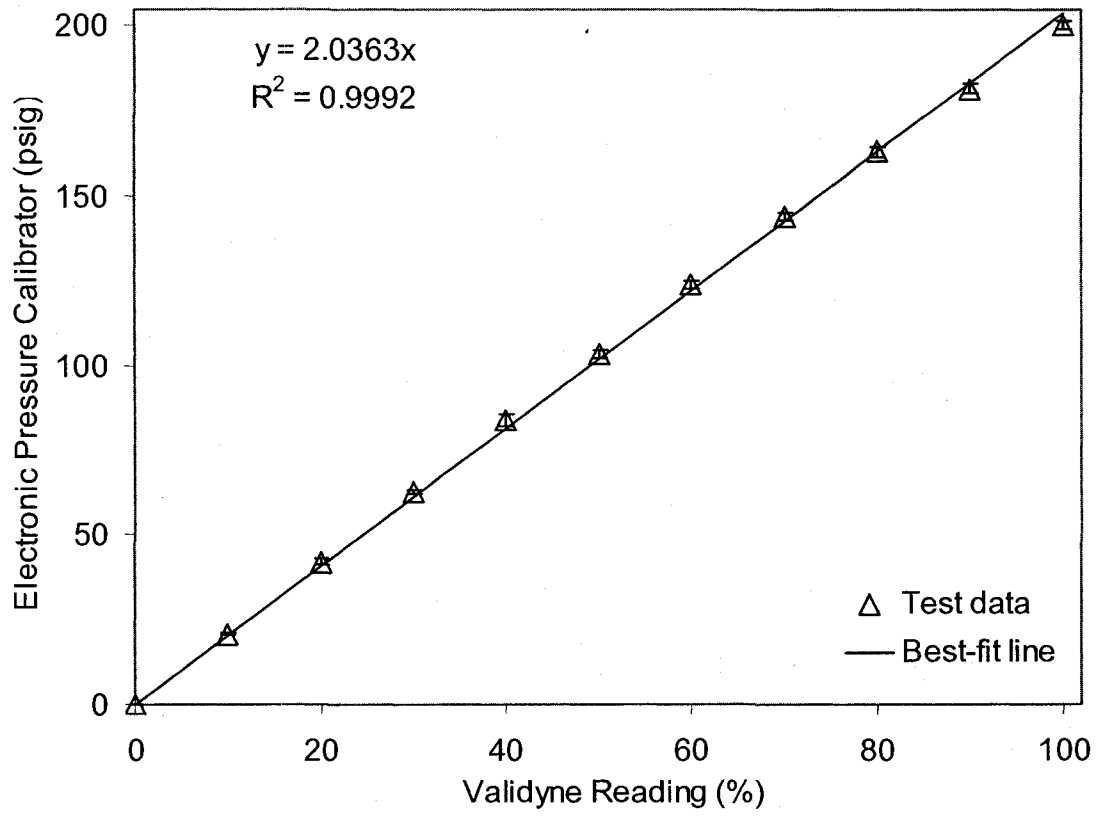


Figure A1-6: Calibration plot for Validyne transducer





1.8861, -1.8861, -1.8861, -1.8861, -1.8861, -1.8861, -  
 1.8861, -1.8861, -1.8861, -1.8861, -1.8861, -1.8861, -  
 1.8861, -1.8861, -1.8861, -1.8861, -1.8861, -1.8861, -  
 1.8861, -1.8861, -1.7100, -1.7100, -1.7100, -1.7100, -  
 1.7100, -1.7100, -1.7100, -1.7100, -1.7100, -1.7100, -  
 1.7100, -2.5086, -2.5086, -2.5086, -2.5086, -2.5086, -  
 2.5086], [1.7977, 1.7715, 1.7380, 1.7026, 1.6767, 1.6562, 1.5  
 922, 1.5229, 1.8315, 1.7994, 1.7820, 1.7632, 1.7418, 1.7206, 1  
 .6632, 1.5998, 1.8635, 1.8501, 1.8329, 1.8151, 1.7951, 1.7737  
 , 1.7166, 1.6543, 1.8774, 1.8608, 1.8418, 1.8175, 1.7700, 1.70  
 77, 1.8883, 1.8741, 1.8557, 1.8056, 1.7515, 1.5913, 1.5604, 1.  
 5250, 1.5027, 1.4805, 1.4543, 1.4249, 1.3580, 1.2551, 1.6869,  
 1.4109, 1.4909, 1.5256, 1.5417, 1.3424, 1.7685, 1.5151, 1.614  
 8, 1.5952, 1.5868, 1.4232, 1.6094, 1.8096, 1.6251, 1.8040, 1.8  
 65911)];



$$P = -0.1675823064 + 0.5962696963 M + 0.4896412551 Q - 2.145706200 D$$

The result implies:  $\text{LOG}_{10}P_{\text{gauge}} = -0.17 + 0.60\text{LOG}_{10}M + 0.49\text{LOG}_{10}Q - 2.15\text{LOG}_{10}D$

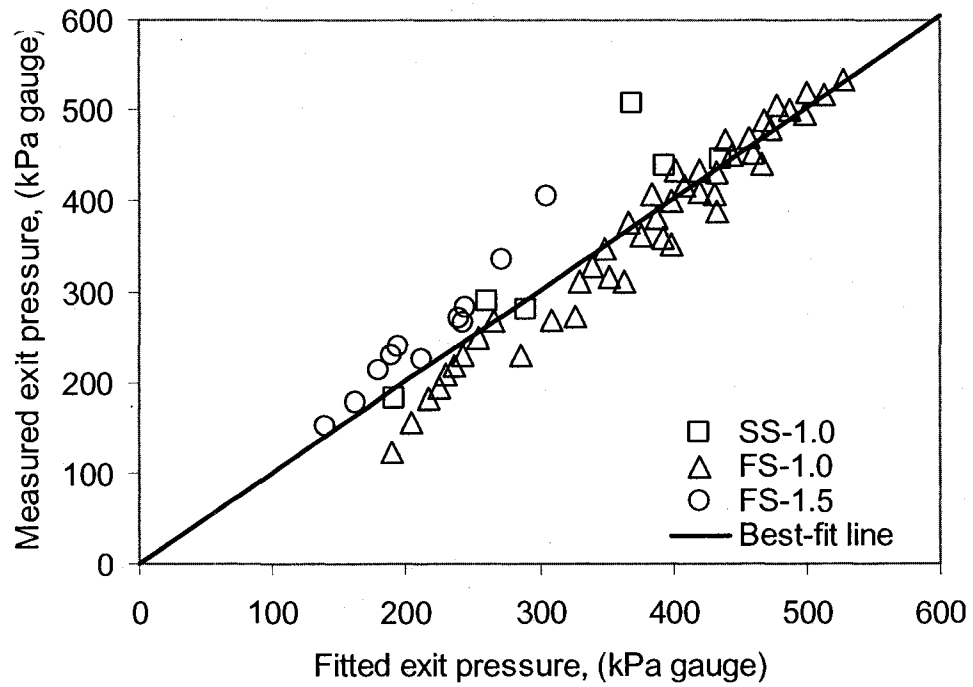


Figure A2-1 – Comparison of measured and fitted exit pressures from the SS-1.0, FS-1.0 and FS-1.5 nozzles. The best-fit line has a Pearson correlation coefficient of 0.8986.

### Section A2-2

In Eqn. (4.14), for air-canola oil tests at 1.66 USGPM and 4% GLR, the relevant data substituted were:

Entrainment number,  $E = 0.15$

Liquid mass flow rate,  $m_L = 0.095 \text{ kg/s}$ ;

Entrained gas density,  $\rho_e = 1.11 \text{ kg/m}^3$ ;

Atomizing gas density at the nozzle exit,  $\rho_G = 5.68 \text{ kg/m}^3$ ;

Liquid density,  $\rho_L = 905 \text{ kg/m}^3$ ;

Gas-to-liquid ratio (by mass),  $GLR$  (i.e.  $ALR$ ) = 0.04

Slip ratio,  $SR = 1$  (i.e. assuming a homogeneous flow)

**The corresponding entrained gas mass flow rate,  $m_e = 548 \text{ SCFM}$ .**

**Section A2-3**

Table A2-1 – Excel spreadsheet of ventilation system design for the U of A spray facility

	D duct (inches)	Q (SCFM)	Q (Std m <sup>3</sup> /s)
	16	1100	0.519142188
Point of minor(or separation) loss	Leq/D	Leq	Minor loss in terms of Q <sup>2</sup>
		(m)	(m of air)
Abrupt 90 deg entrance	50.00	20.32	3.03
Filter pressure drop near duct entry (assume C = 3.0, for perforation area ratio = 0.40)	150.00	60.96	9.09
Round butterfly damper (C = 0.52)	26.00	10.57	1.58
Through converging 45 deg. Wye (with other branch shut-off)	2.50	1.02	0.15
90 deg elbow	21.00	8.53	1.27
Round-to-round converging transition from 16" duct to fan inlet	15.47	6.29	0.94
System effect factor b4 blower inlet	48.41	19.67	2.93
System effect factor after blower exit	0.00	0.00	0.00
Rectangular-to-round diverging transition to 16" duct at roof top	63.77	25.92	3.86
130 deg. Elbow at exit and abrupt expansion at exit	90.00	36.58	5.45
<b>Sum of minor (or separation) losses</b>			<b>28.30</b>

Point of friction loss	L	L	Friction loss in terms of Q <sup>2</sup>
	(inches)	(m)	(m of air)
16" circular duct run from fume hood to blower inlet	72.0	1.83	0.27
8" by 12" rectangular duct from blower exit to diverging transition (D <sub>hyd</sub> = 9.372")	48.0	1.22	2.64
16" square duct run from diverging transition to exit	36.0	0.91	0.14
<b>Sum of friction losses</b>			<b>3.04</b>

**Total sum of (minor (or separation) and friction) losses**

Elevation head (z <sub>2</sub> - z <sub>1</sub> )	Z <sub>2</sub> - Z <sub>1</sub>	Z <sub>2</sub> - Z <sub>1</sub>	Elevation Head
	(inches)	(m)	(m of air)
Height between exhaust point and inlet from fume hood	116	2.95	2.95

Static head = $(P_2 - P_1)/(\rho \cdot 9.81)$	P2 (Pa)	P1 (Pa)	Static Head (m of air)
Static (atm) pressure difference between room and outside air	93000	93000	0.00

**Total sum of (elevation and static) losses 2.95**

	Total Head (m of air)	Total Head (inches of water)
Sum of static and elevation heads	2.95	0.14
Sum of minor and friction head losses	8.45	0.40
<b>Total head to be developed by the blower at Q above</b>	<b>11.39</b>	<b>0.54</b>

The main equation used for the design was the steady flow energy equation given by (from the ASHRAE handbook):

$$\frac{\Delta p_{fan}}{\rho g} = \frac{\Delta p_{system}}{\rho g} = \frac{(P_2 - P_1)}{\rho g} + (Z_2 - Z_1) + \frac{(V_2^2 - V_1^2)}{2g} + \sum h_{friction\ losses} + \sum h_{minor\ losses} \quad (A)$$

In Eqn. (A), subscript 1 denotes air inlet point into the duct system and 2 denotes air exit point from the duct system. Other parameters above are defined thus:

$\Delta p_{fan}$  = Pressure difference developed across the blower (Pa)

$\Delta p_{system}$  = Pressure loss through the entire duct system (Pa)

$\rho$  = Air density ( $\text{kg/m}^3$ )

P = Air static pressure (Pa)

Z = Elevation (m)

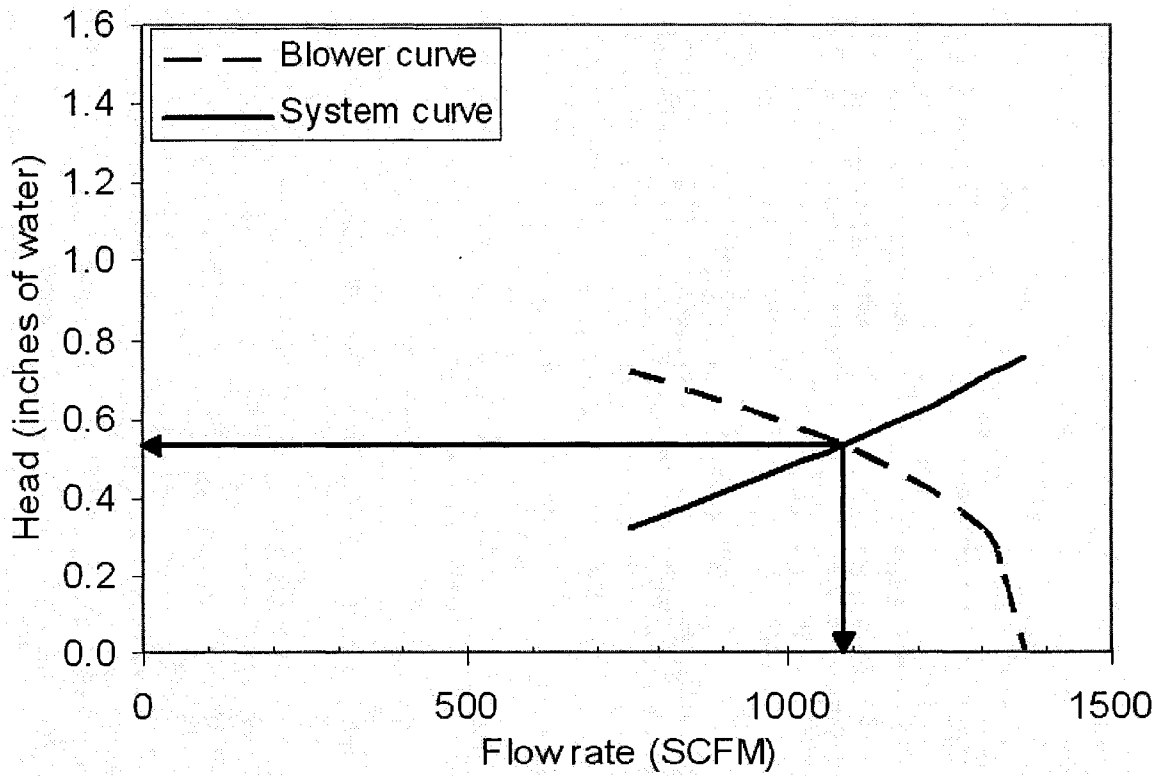
V = Air velocity (m/s)

$h_{friction\ losses}$  = Frictional head losses in the duct system (metre of air)

$h_{\text{friction losses}}$  = Minor head losses in the duct system (metre of air)

**NOTE:** The units of each term in Eqn. (A) are in 'metres of air',  $H_{\text{air}}$ . To convert to inches of water  $H_{\text{water}}$ , the equation below was used:

$$H_{\text{water}} = \left( \frac{\rho_{\text{air}}}{\rho_{\text{water}}} \right) \frac{H_{\text{air}}}{0.0254} \quad (\text{B})$$



FigureA2-2 – Blower-system curves for the 16" duct ventilation system showing operation point of about 1100 SCFM and 0.54".

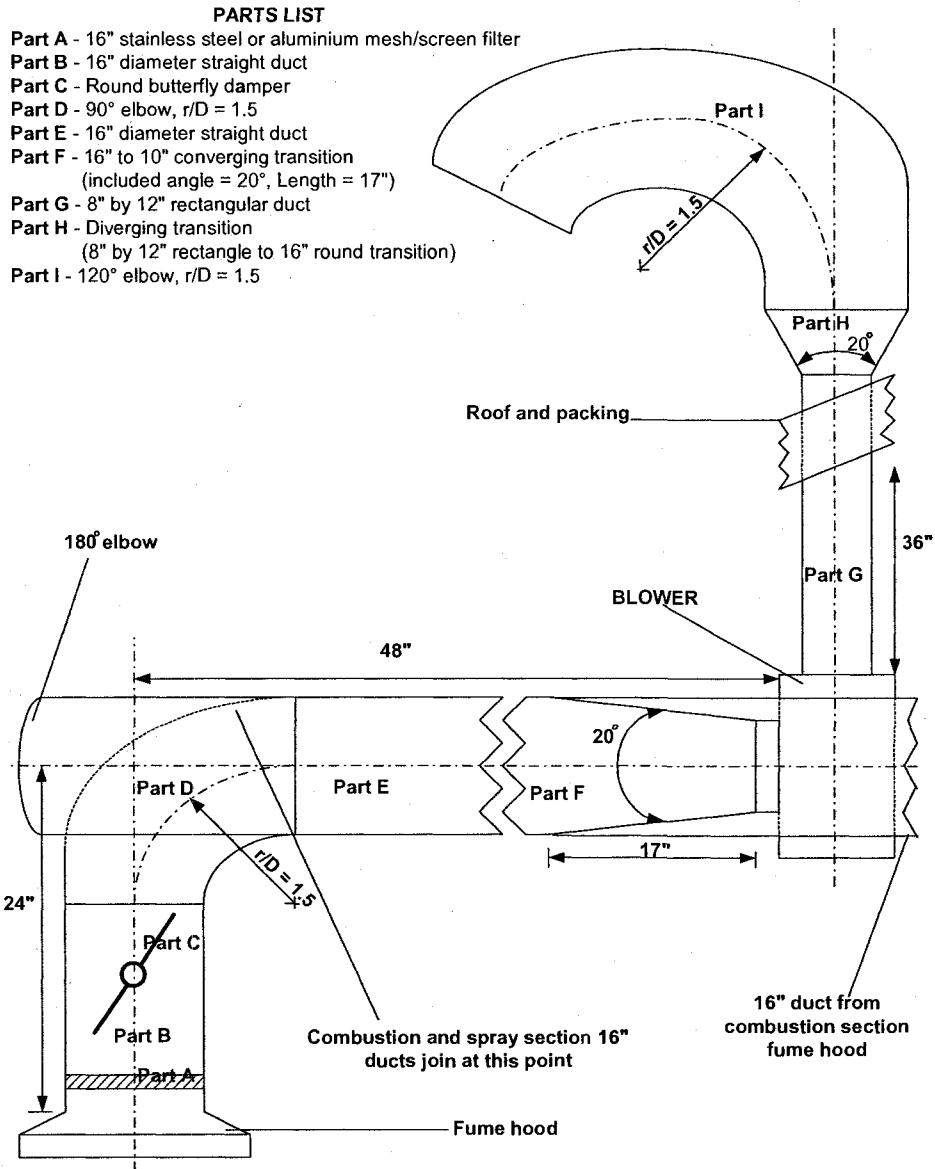


Figure A2-3 – Proposed ventilation duct layout for the spray facility.



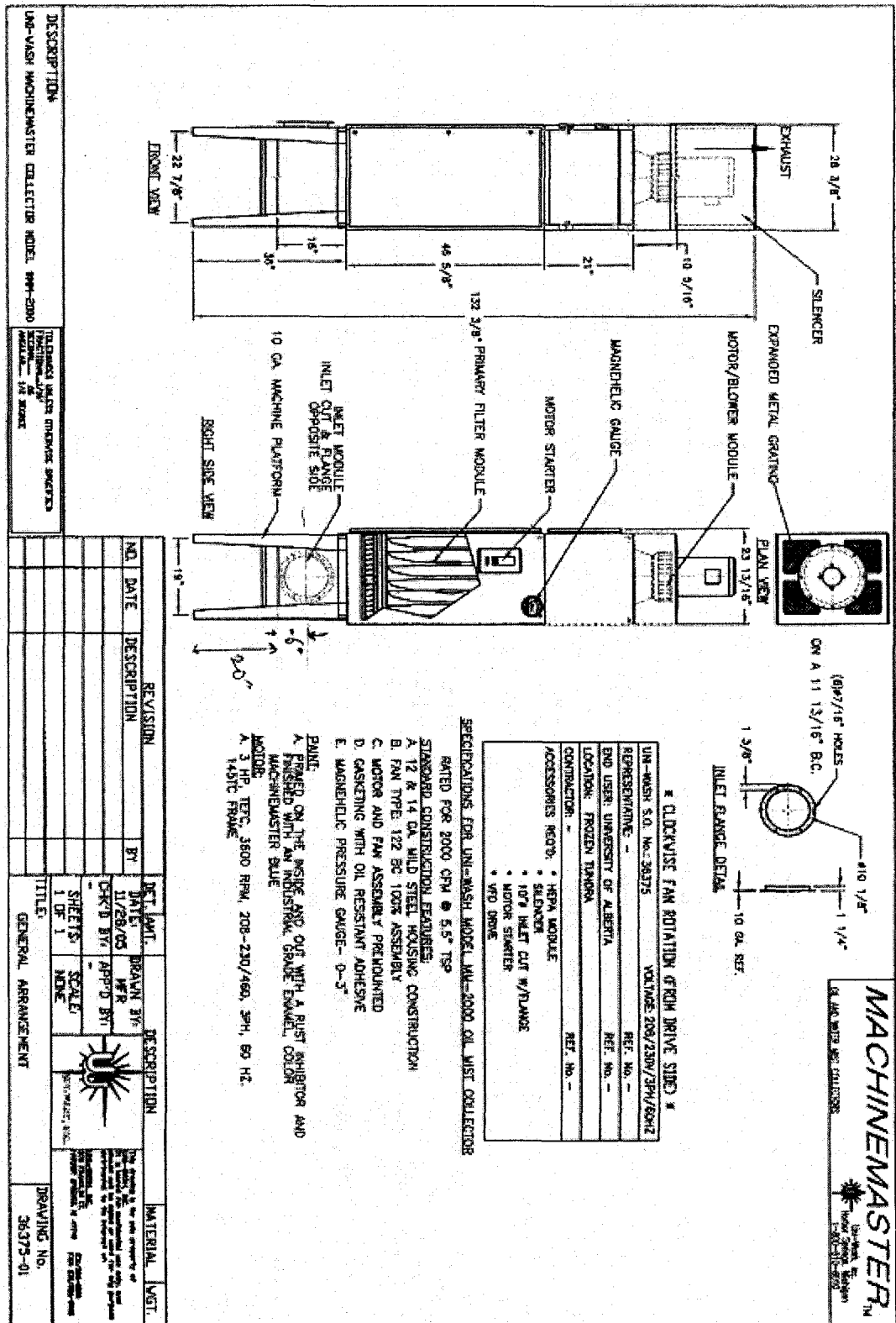


Figure A2-4 –Drawing showing the different sections of the mist extraction system.

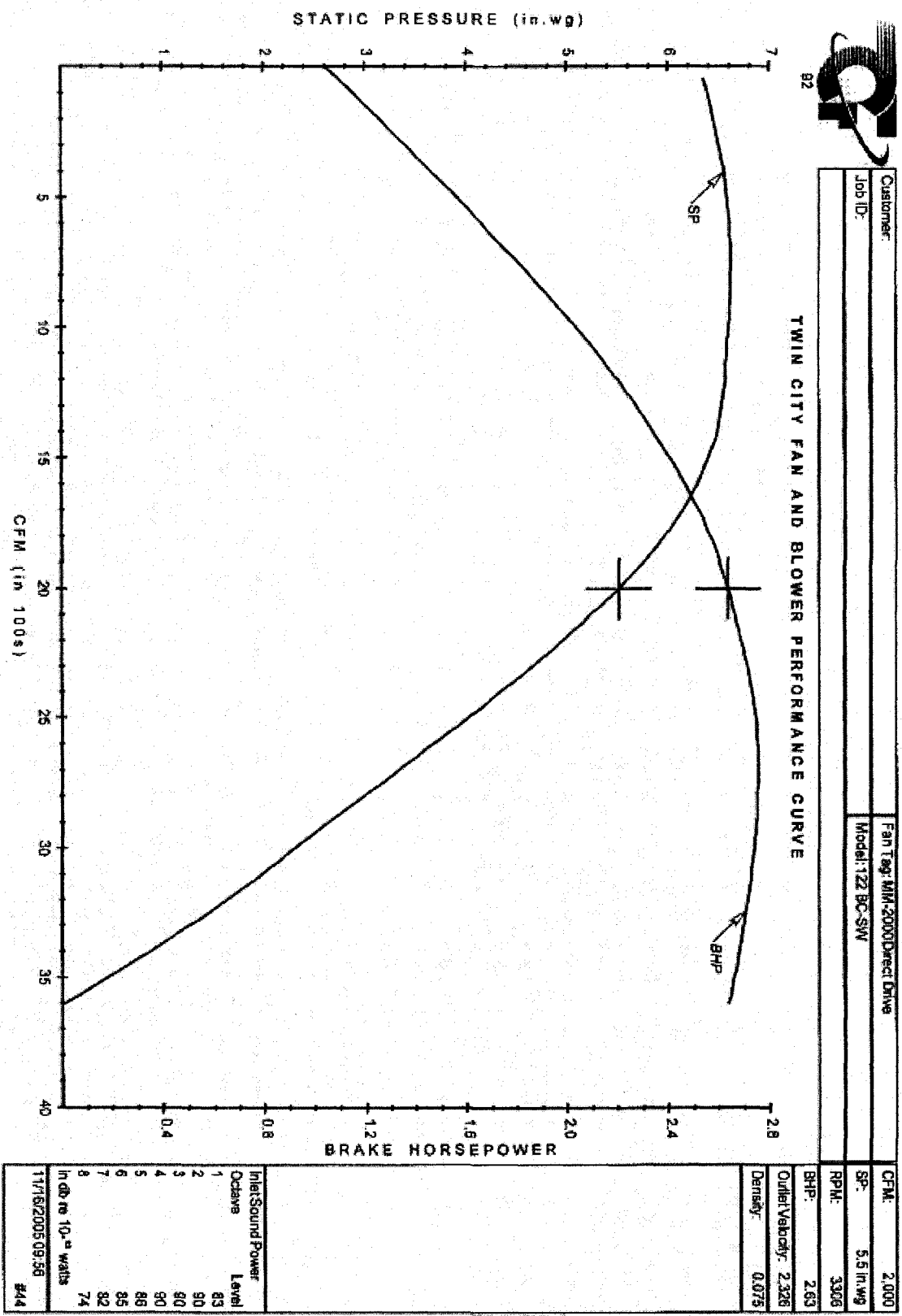


Figure A2-5: Blower performance curves for the extraction system.

# APPENDIX A3 – MATLAB PROGRAM FOR CALCULATING LIQUID VOLUME FLUX

This Appendix presents the MATLAB program used to calculate the liquid volume flux from text files containing experimental data.

```
%*****%  
%function volume_flux          %  
%Calculates volume flux of spray    %  
%*****%  
function volume_flux  
global dataset  
volfluxmat=[];  
for n=1:1:size(dataset,1)  
    datafilename=dataset{n,1}; %Use CURLY brackets  
    fid=fopen(datafilename,'r');  
    junk=fgets(fid);  
    junk=fgets(fid);  
    junk=fgets(fid);  
    junk=fgets(fid);  
    junk=fgets(fid);  
    diametermatrix=fscanf(fid,'%f',[7,inf]);  
    %Calculate di^3
```

```

diameters=[];

diameters=diametermatrix(:,7);

di3=sum((diameters(:,1)).^3);           %Sum cubed diameters (um^3)

%Calculate area

area=0.000000042;                       % Measurement area (in m^2)

%Calculate time

times=[];

times=diametermatrix(:,1);

tfixed=times(end,1)-times(1,1);         %Subtract last time value with first time
value (ms)

%Calculate dq/dA

volflux=(pi./(6*area*tfixed*10^15))*di3; %dq/dA (m/s)

%Assign matrices named volflux1, volflux2, ... for each file

eval(['volflux' num2str(n) '=volflux;']);

%Collect all dq/dA into array "volfluxmat"

volfluxmat=cat(1,volfluxmat,volflux)

end

%Output volume flux results to file

volfluxfilename='C:\Documents and Settings\OWNER\Desktop\volumefluxresults.txt';

fidd=fopen(volfluxfilename,'W');

fprintf(fidd,'VOLUME FLUX (m/s)\n');

fprintf(fidd,'%11.5fn',transpose(volfluxmat));

fclose(fidd);

```

## APPENDIX A4 – VELOCITY RESULTS

This Appendix presents plots related to velocity measurements in the different sprays studied. These include the following:

- velocity-drop size correlation coefficient ( $CC$ ) across the spray
- drop velocity variation across the spray
- jet half-width variation with axial distance
- variation of centerline velocity with axial distance
- dimensionless velocity profiles across the spray and at different axial positions
- curve-fit of single-phase velocity profile to compare with experimental data

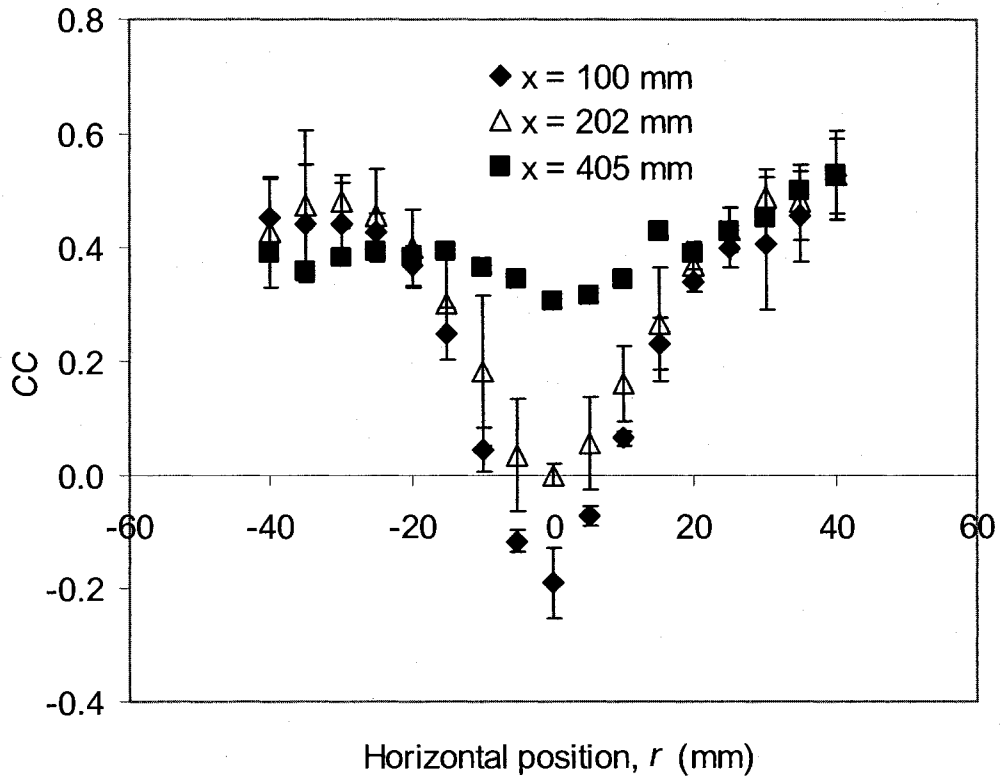


Figure A4-1: Profiles of  $CC$  across the spray and at axial positions,  $x = 100, 202,$  and  $405$  mm for the SS-1.0 nozzle ( $D = 3.1$ mm). Data is for air-glycerine solution spray ( $\mu_L = 67$  mPa-s,  $\gamma = 61$  mN/m) with liquid flow rate of  $79 \times 10^{-6}$  m<sup>3</sup>/s and 1.0% GLR. The error bars show the 95% confidence limits for the  $CC$  values.

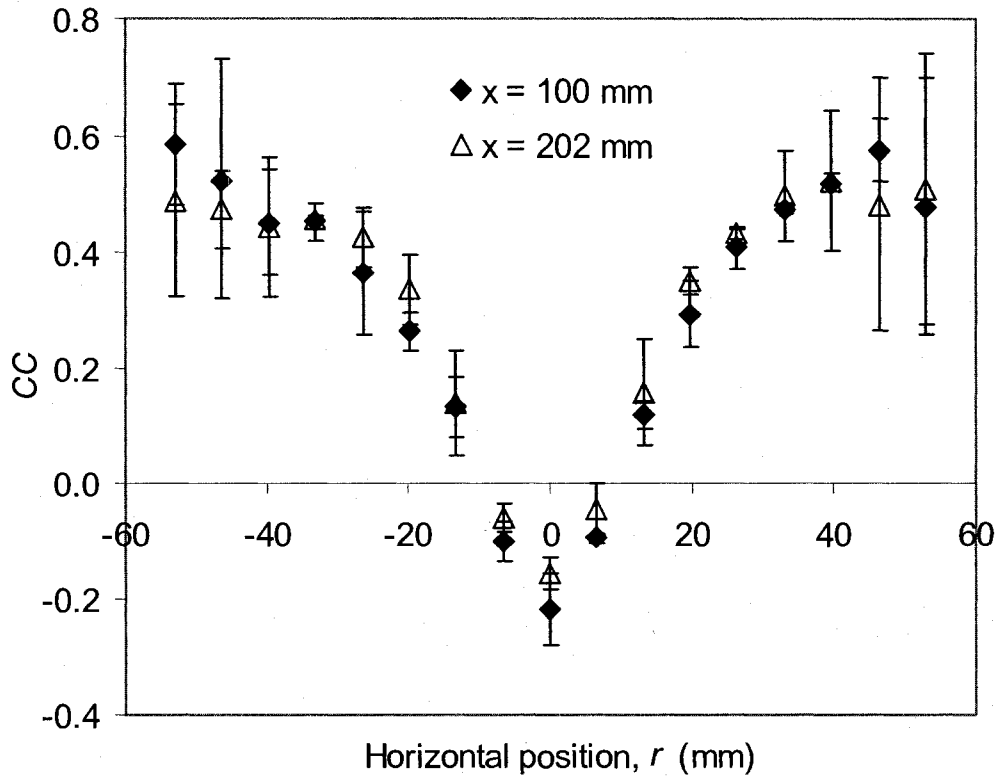


Figure A4-2: Profiles of  $CC$  across the spray and at axial positions,  $x = 100$  and  $202$  mm for the SS-1.3 nozzle ( $D = 4.1$ mm). Data is for air-glycerine solution spray ( $\mu_L = 67$  mPas,  $\gamma = 61$  mN/m) with liquid flow rate of  $163 \times 10^{-6}$  m<sup>3</sup>/s and 1.0%  $GLR$ . The error bars show the 95% confidence limits for the  $CC$  values.

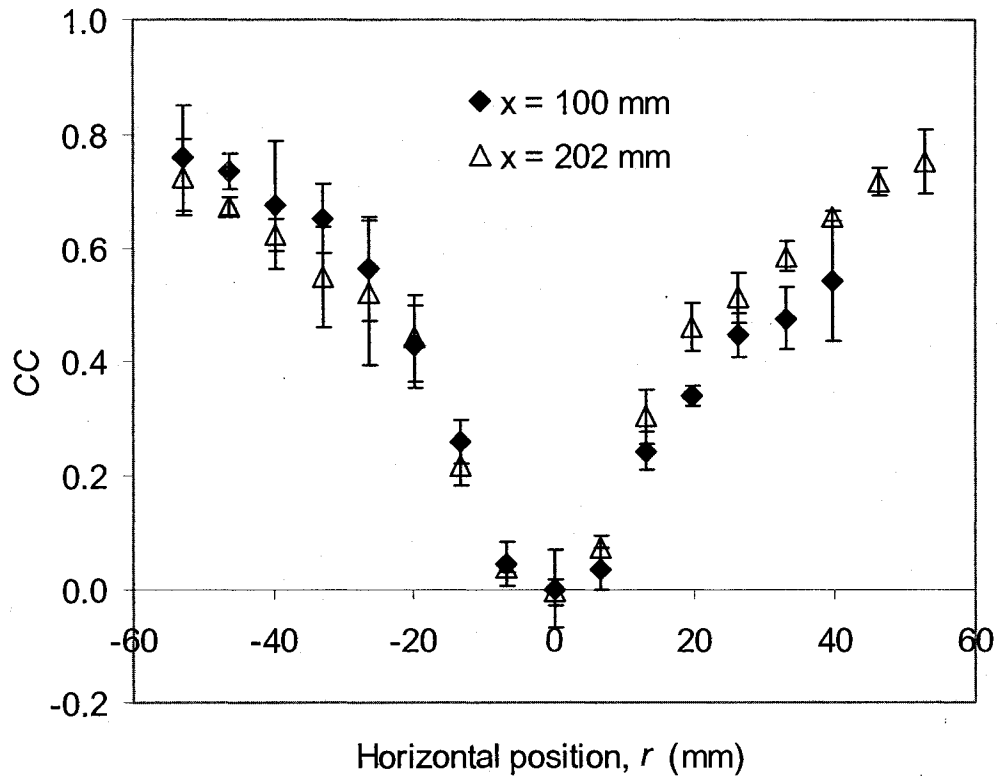


Figure A4-3: Profiles of  $CC$  across the spray and at axial positions,  $x = 100$  and  $202$  mm for the SS-1.3 nozzle ( $D = 4.1$ mm). Data is for air-water spray ( $\mu_L = 1$  mPas,  $\gamma = 70$  mN/m) with liquid flow rate of  $190 \times 10^{-6}$  m<sup>3</sup>/s and 1.0%  $GLR$ . The error bars show the 95% confidence limits for the  $CC$  values.



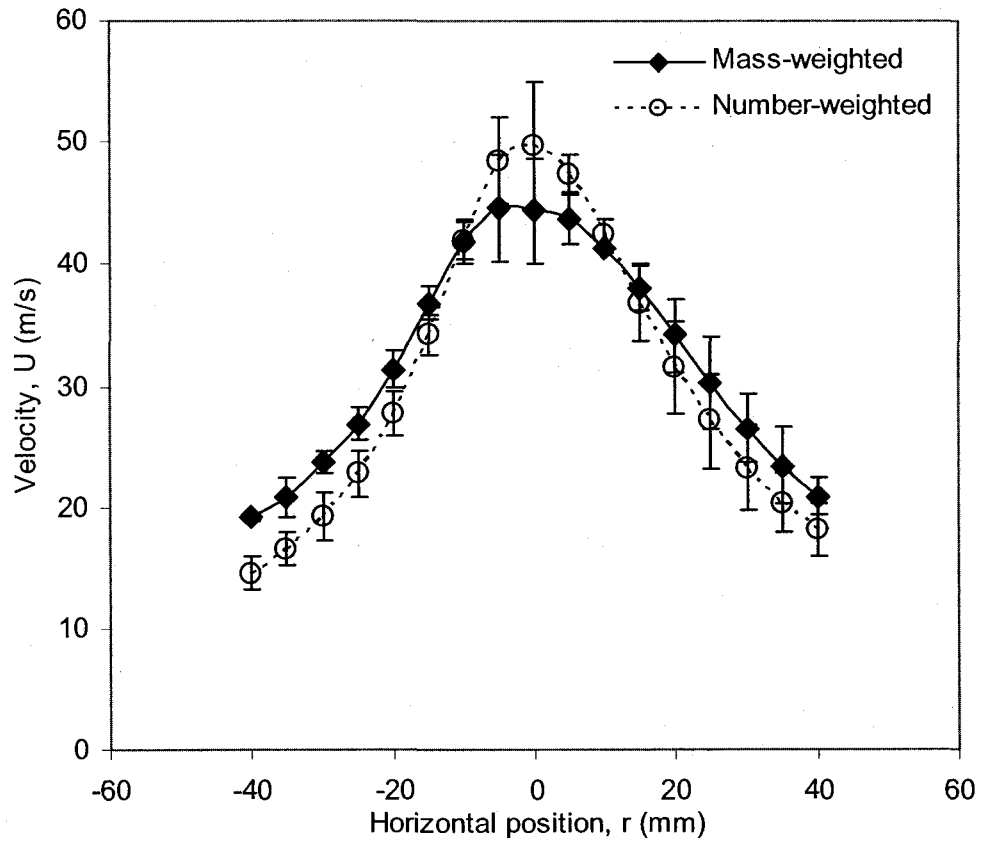


Figure A4-4: Number and mass-weighted velocity profiles at axial position,  $x = 100$  mm for SS-1.0 nozzle ( $D = 3.1$ mm). Data is for air-glycerine solution spray ( $\mu_L = 67$  mPa-s,  $\gamma = 61$  mN/m) with liquid flow rate of  $114 \times 10^{-6}$  m<sup>3</sup>/s and 1.0% GLR. The error bars show the 95% confidence limits for the velocity measurements.

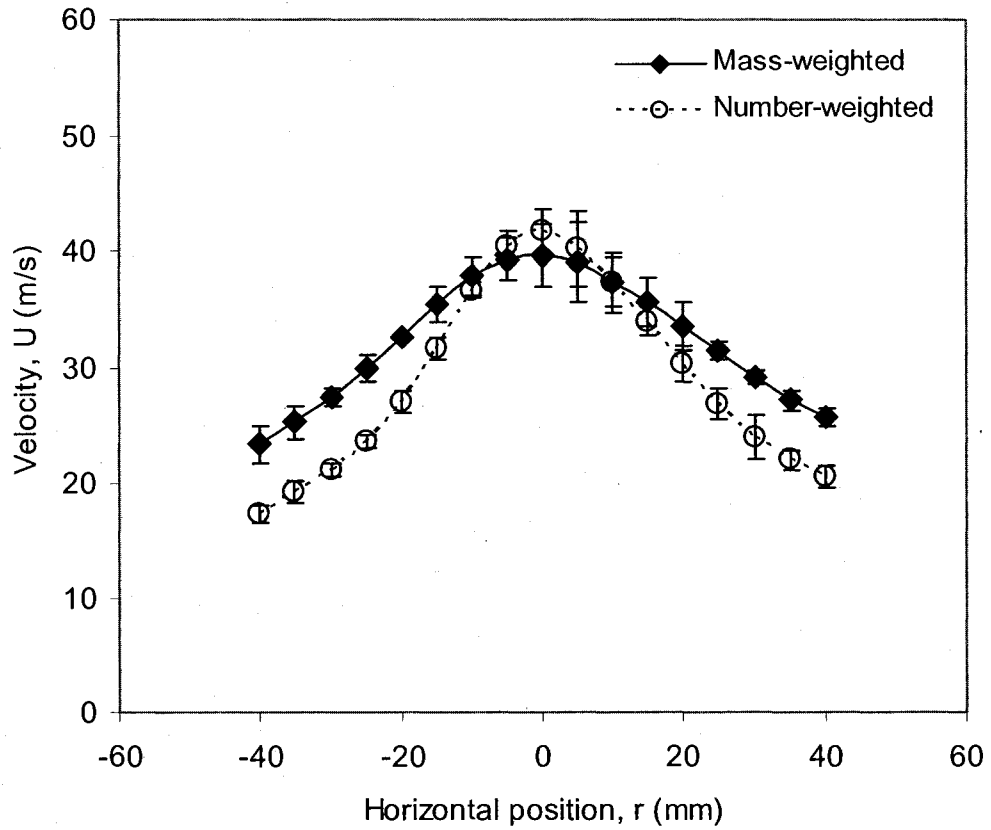


Figure A4-5: Number and mass-weighted velocity profiles at axial position,  $x = 202$  mm for SS-1.0 nozzle ( $D = 3.1$ mm). Data is for air-glycerine solution spray ( $\mu_L = 67$  mPa-s,  $\gamma = 61$  mN/m) with liquid flow rate of  $114 \times 10^{-6}$  m<sup>3</sup>/s and 1.0% GLR. The error bars show the 95% confidence limits for the velocity measurements.

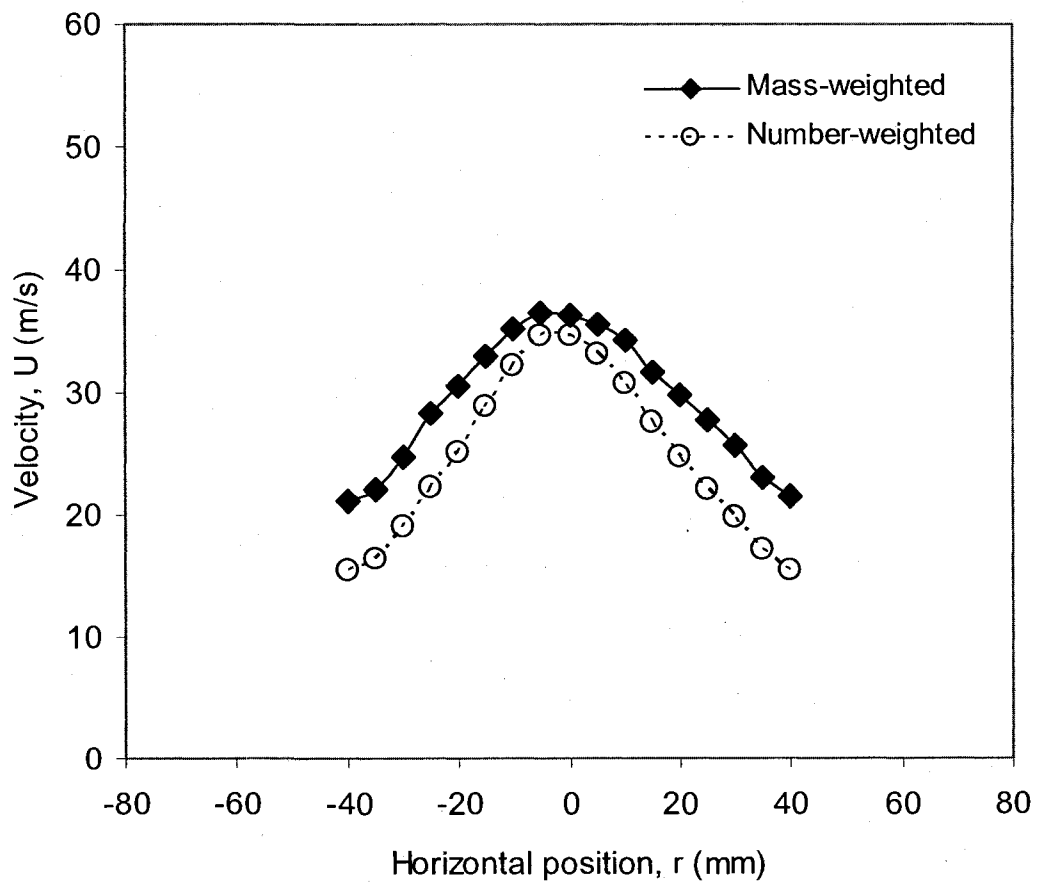


Figure A4-6: Number and mass-weighted velocity profiles at axial position,  $x = 405$  mm for SS-1.0 nozzle ( $D = 3.1$ mm). Data is for air-glycerine solution spray ( $\mu_L = 67$  mPa-s,  $\gamma = 61$  mN/m) with liquid flow rate of  $114 \times 10^{-6}$  m<sup>3</sup>/s and 1.0% GLR.

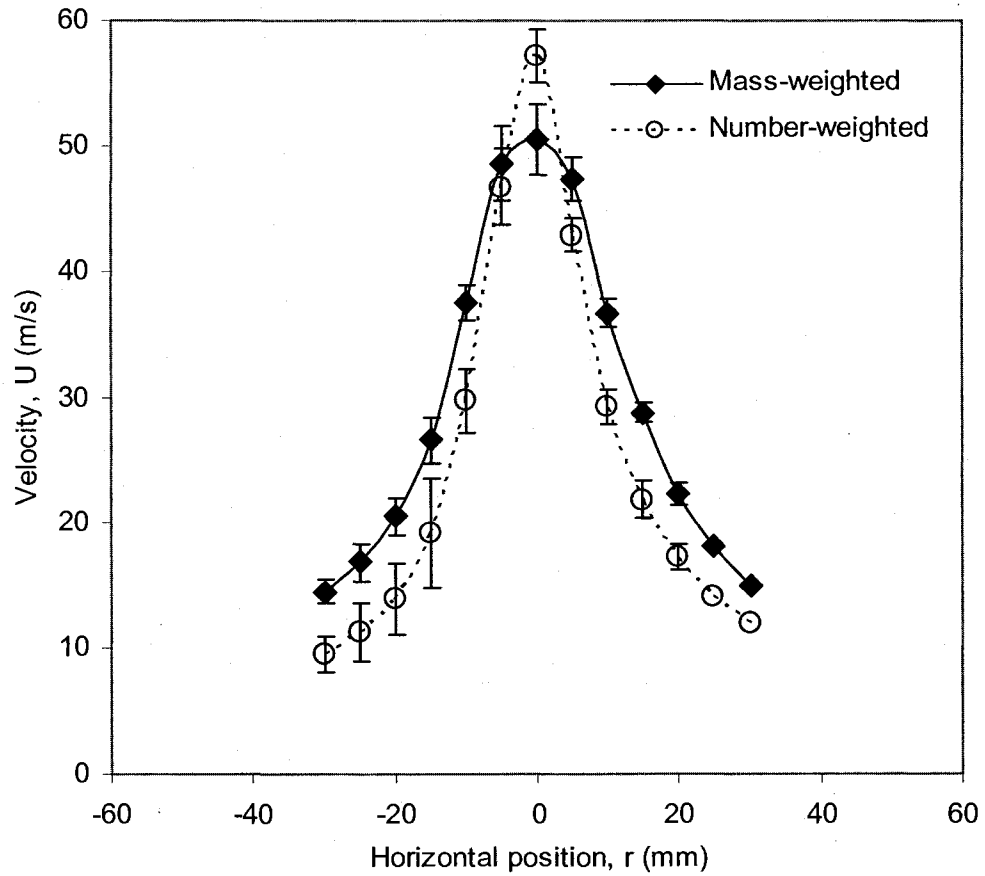


Figure A4-7: Number and mass-weighted velocity profiles at axial position,  $x = 100$  mm for SS-1.0 nozzle ( $D = 3.1$ mm). Data is for air-canola oil spray ( $\mu_L = 66$  mPa-s,  $\gamma = 25$  mN/m) with liquid flow rate of  $105 \times 10^{-6}$  m<sup>3</sup>/s and 1.0% GLR. The error bars show the 95% confidence limits for the velocity measurements.

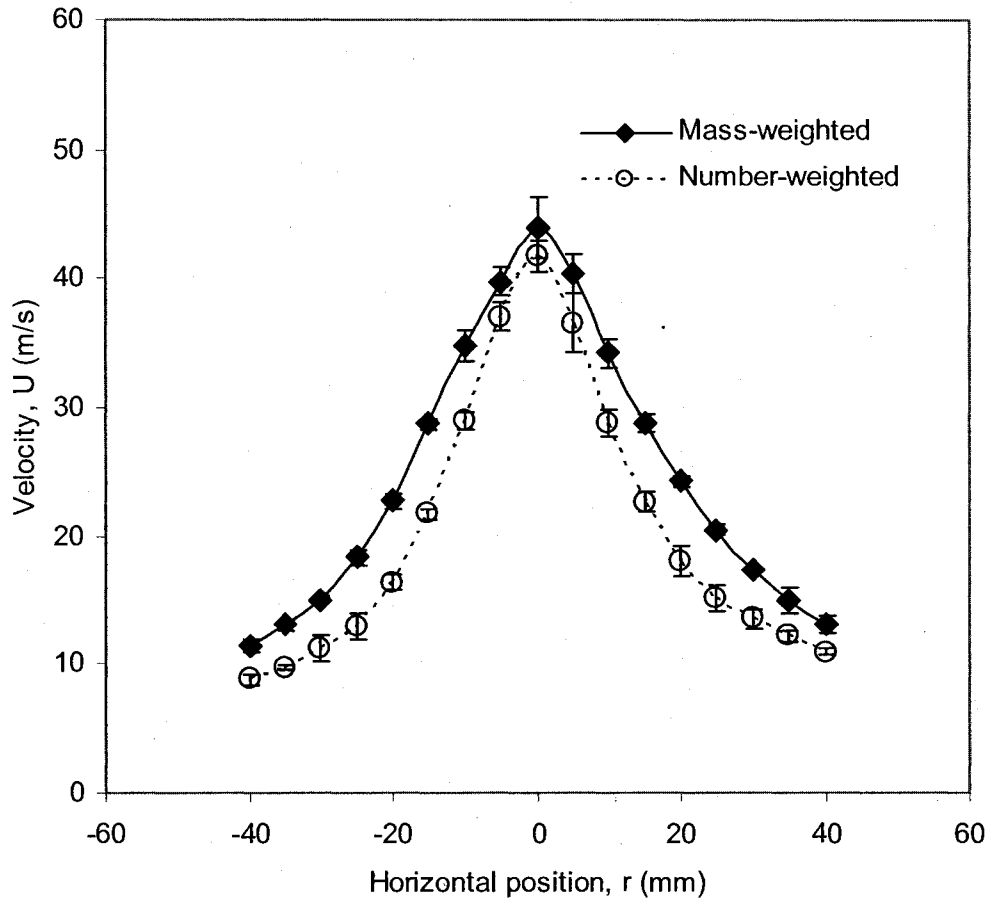


Figure A4-8: Number and mass-weighted velocity profiles at axial position,  $x = 202$  mm for SS-1.0 nozzle ( $D = 3.1$ mm). Data is for air-canola oil spray ( $\mu_L = 66$  mPa-s,  $\gamma = 25$  mN/m) with liquid flow rate of  $105 \times 10^{-6}$  m<sup>3</sup>/s and 1.0% GLR. The error bars show the 95% confidence limits for the velocity measurements.

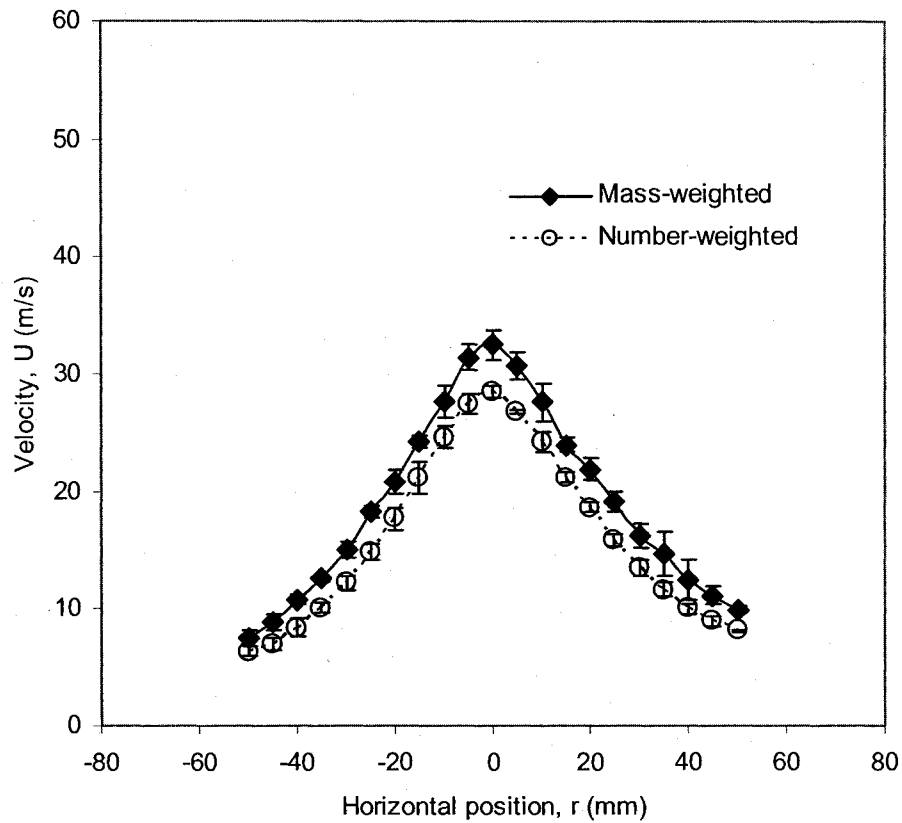


Figure A4-9: Number and mass-weighted velocity profiles at axial position,  $x = 405$  mm for SS-1.0 nozzle ( $D = 3.1$ mm). Data is for air-canola oil spray ( $\mu_L = 66$  mPa-s,  $\gamma = 25$  mN/m) with liquid flow rate of  $105 \times 10^{-6}$  m<sup>3</sup>/s and 1.0% GLR. The error bars show the 95% confidence limits for the velocity measurements.

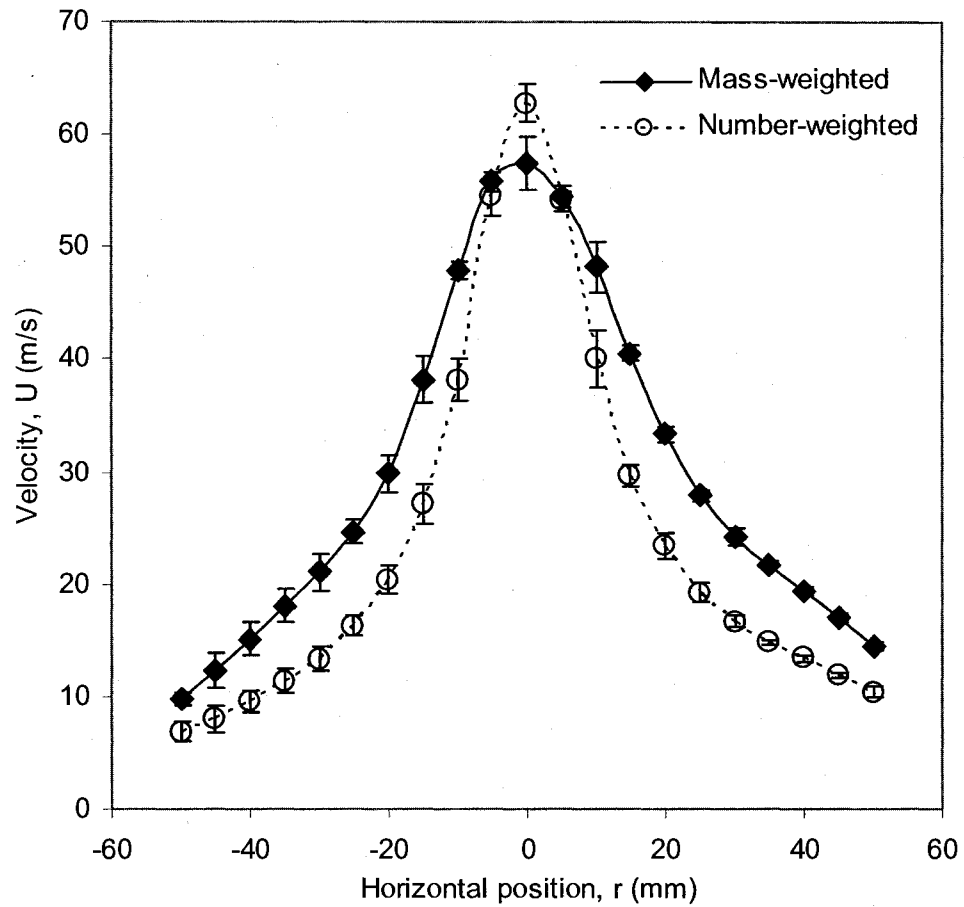


Figure A4-10: Number and mass-weighted velocity profiles at axial position,  $x = 100$  mm for SS-1.0 nozzle ( $D = 3.1$ mm). Data is for air-water spray ( $\mu_L = 1$  mPa-s,  $\gamma = 70$  mN/m) with liquid flow rate of  $95 \times 10^{-6}$  m<sup>3</sup>/s and 2.0% GLR. The error bars show the 95% confidence limits for the velocity measurements.

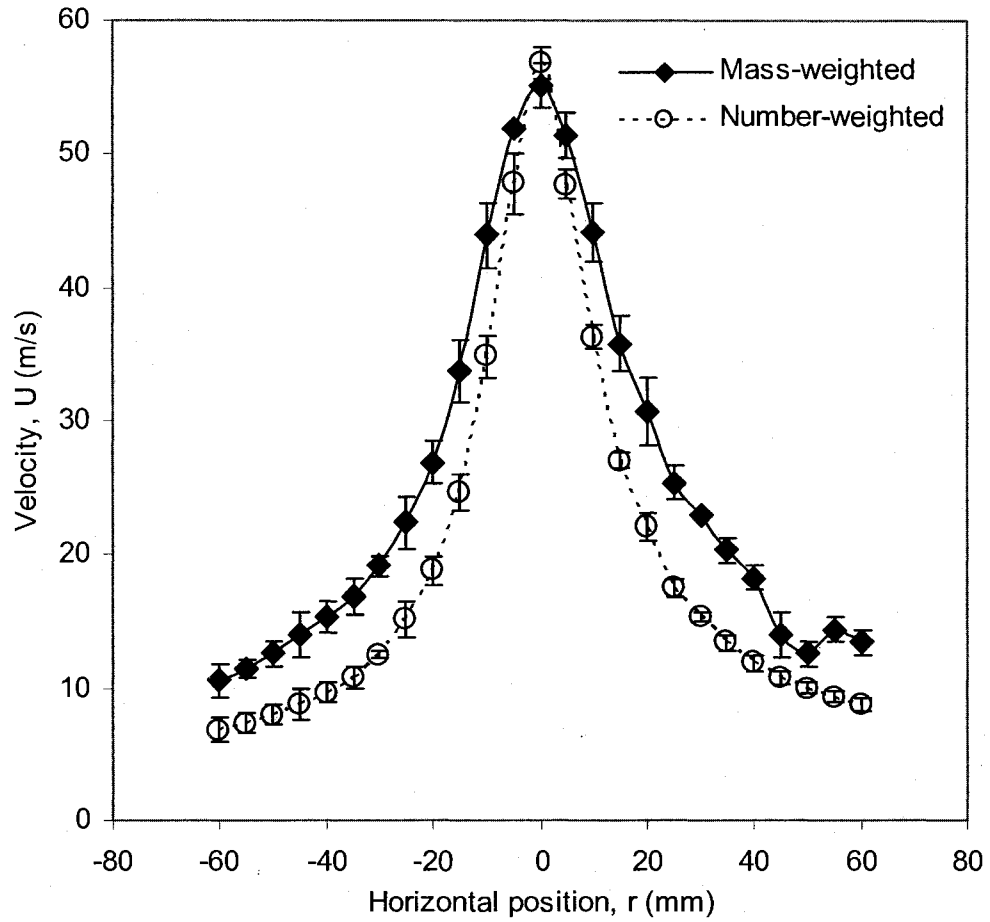


Figure A4-11: Number and mass-weighted velocity profiles at axial position,  $x = 202$  mm for SS-1.0 nozzle ( $D = 3.1$  mm). Data is for air-water spray ( $\mu_L = 1$  mPa-s,  $\gamma = 70$  mN/m) with liquid flow rate of  $95 \times 10^{-6}$  m<sup>3</sup>/s and 2.0% GLR. The error bars show the 95% confidence limits for the velocity measurements.



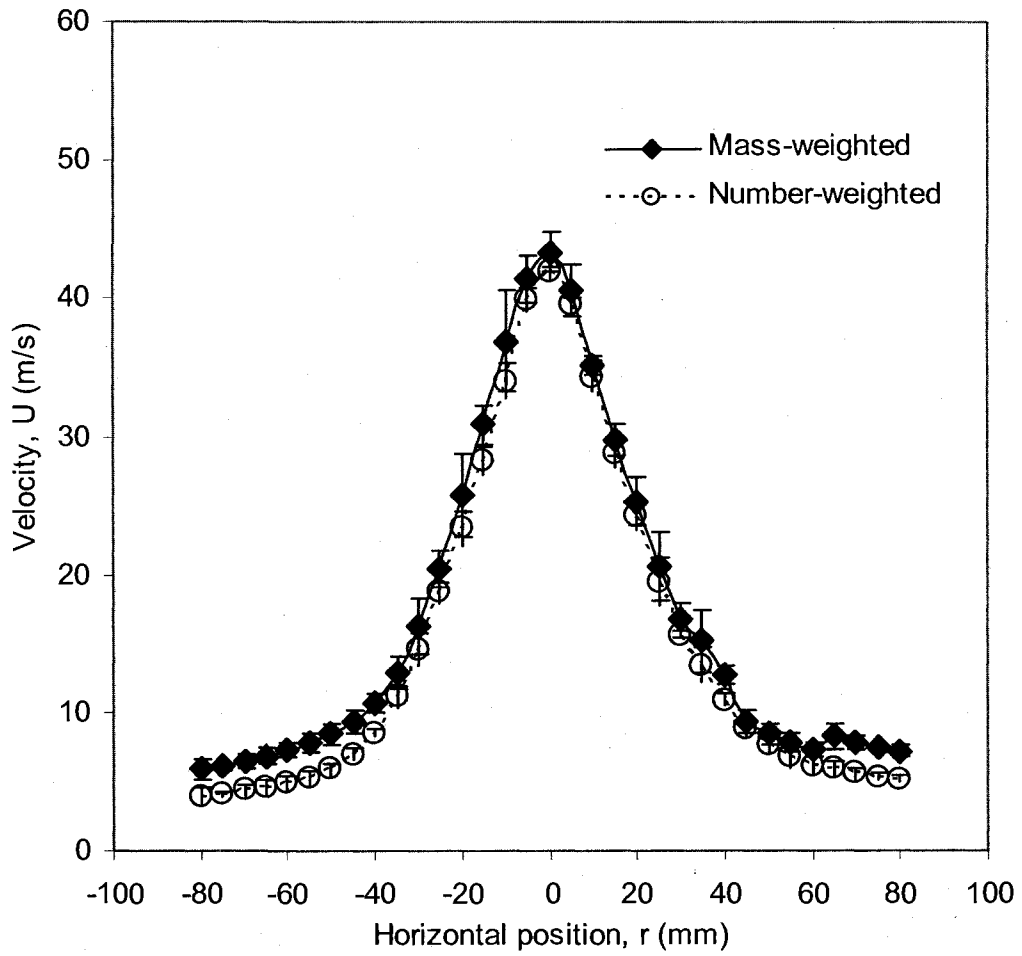


Figure A4-12: Number and mass-weighted velocity profiles at axial position,  $x = 405$  mm for SS-1.0 nozzle ( $D = 3.1$ mm). Data is for air-water spray ( $\mu_L = 1$  mPa-s,  $\gamma = 70$  mN/m) with liquid flow rate of  $95 \times 10^{-6}$  m<sup>3</sup>/s and 2.0% GLR. The error bars show the 95% confidence limits for the velocity measurements.

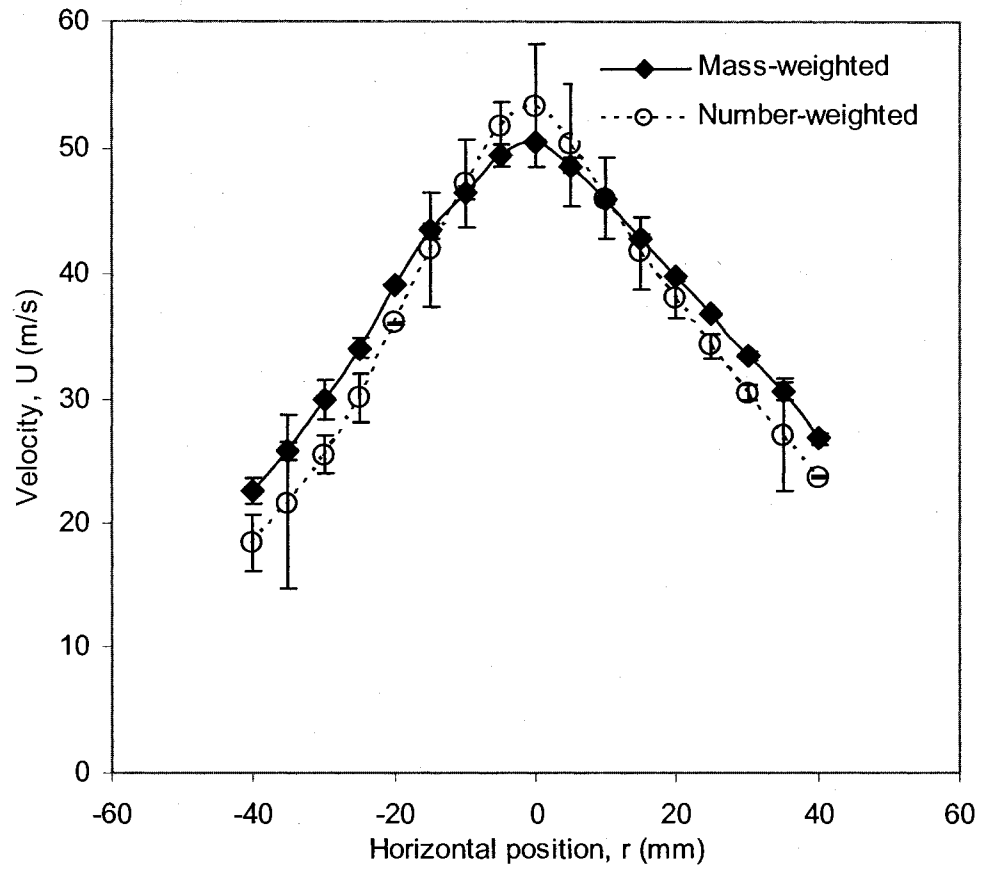


Figure A4-13: Number and mass-weighted velocity profiles at axial position,  $x = 100$  mm for SS-1.0 nozzle ( $D = 3.1$ mm). Data is for air-glycerine solution spray ( $\mu_L = 67$  mPa-s,  $\gamma = 61$  mN/m) with liquid flow rate of  $105 \times 10^{-6}$  m<sup>3</sup>/s and 2.0% GLR. The error bars show the 95% confidence limits for the velocity measurements.

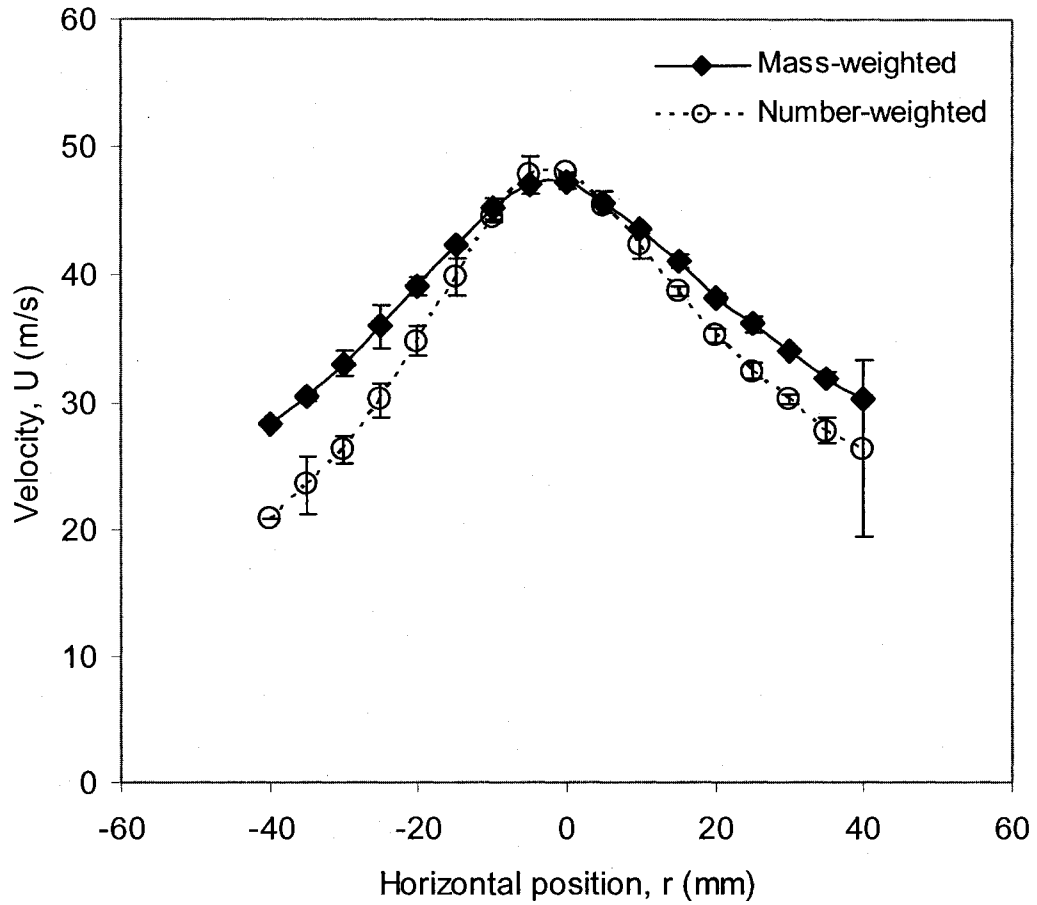


Figure A4-14: Number and mass-weighted velocity profiles at axial position,  $x = 202$  mm for SS-1.0 nozzle ( $D = 3.1$ mm). Data is for air-glycerine solution spray ( $\mu_L = 67$  mPa-s,  $\gamma = 61$  mN/m) with liquid flow rate of  $105 \times 10^{-6}$  m<sup>3</sup>/s and 2.0% GLR. The error bars show the 95% confidence limits for the velocity measurements.

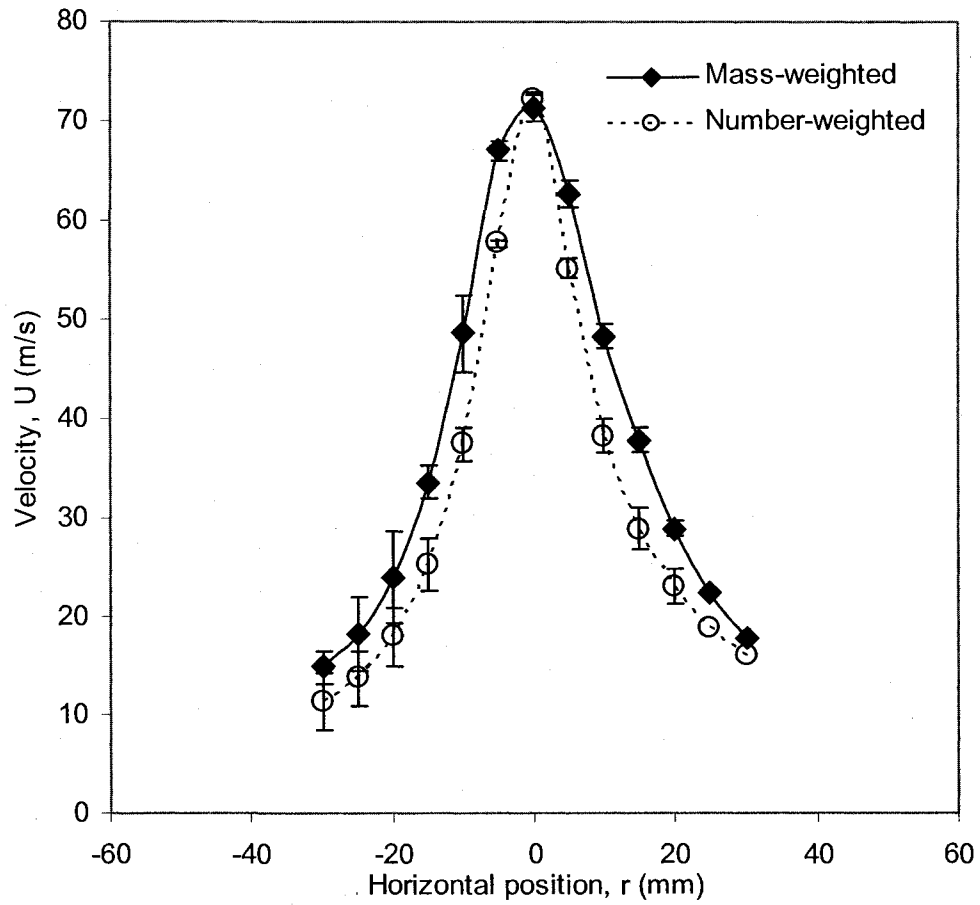


Figure A4-15: Number and mass-weighted velocity profiles at axial position,  $x = 100$  mm for SS-1.0 nozzle ( $D = 3.1$ mm). Data is for air-canola oil spray ( $\mu_L = 66$  mPa-s,  $\gamma = 25$  mN/m) with liquid flow rate of  $105 \times 10^{-6}$  m<sup>3</sup>/s and 2.0% GLR. The error bars show the 95% confidence limits for the velocity measurements.

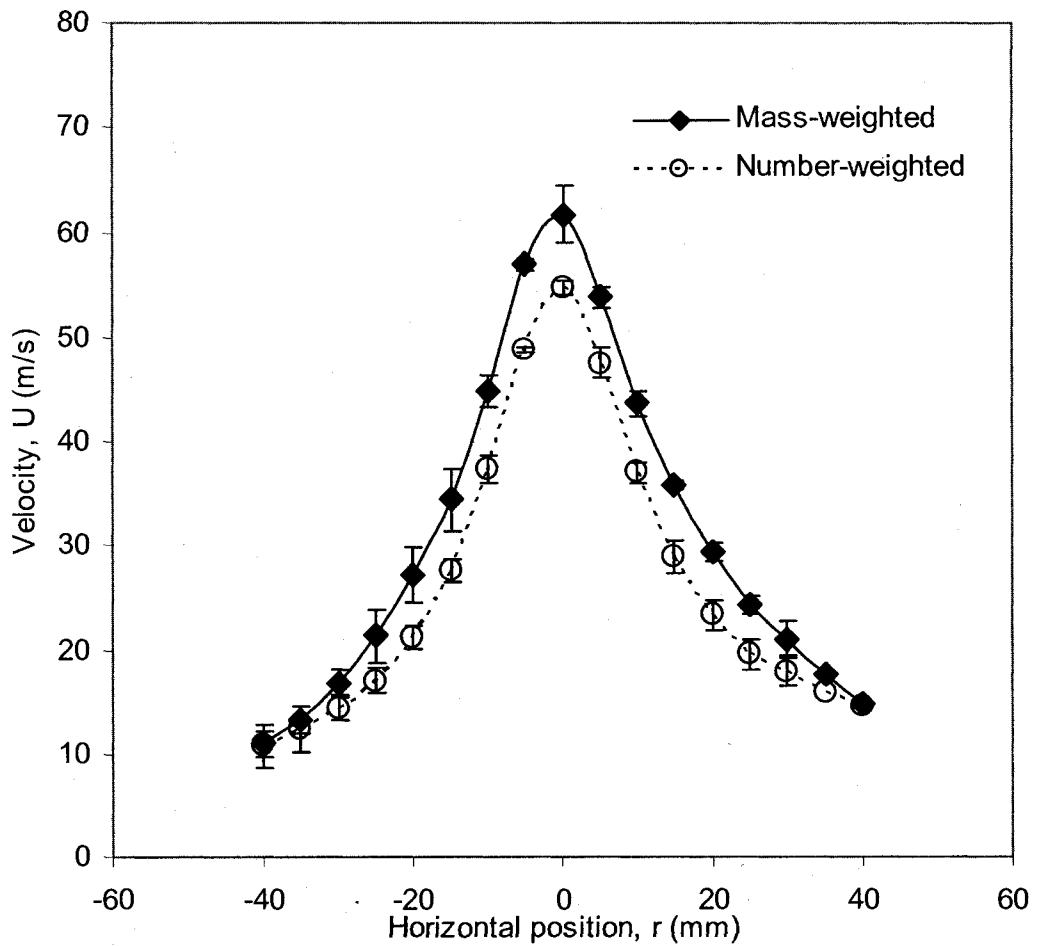


Figure A4-16: Number and mass-weighted velocity profiles at axial position,  $x = 202$  mm for SS-1.0 nozzle ( $D = 3.1$ mm). Data is for air-canola oil spray ( $\mu_L = 66$  mPa-s,  $\gamma = 25$  mN/m) with liquid flow rate of  $105 \times 10^{-6}$  m<sup>3</sup>/s and 2.0% GLR. The error bars show the 95% confidence limits for the velocity measurements.

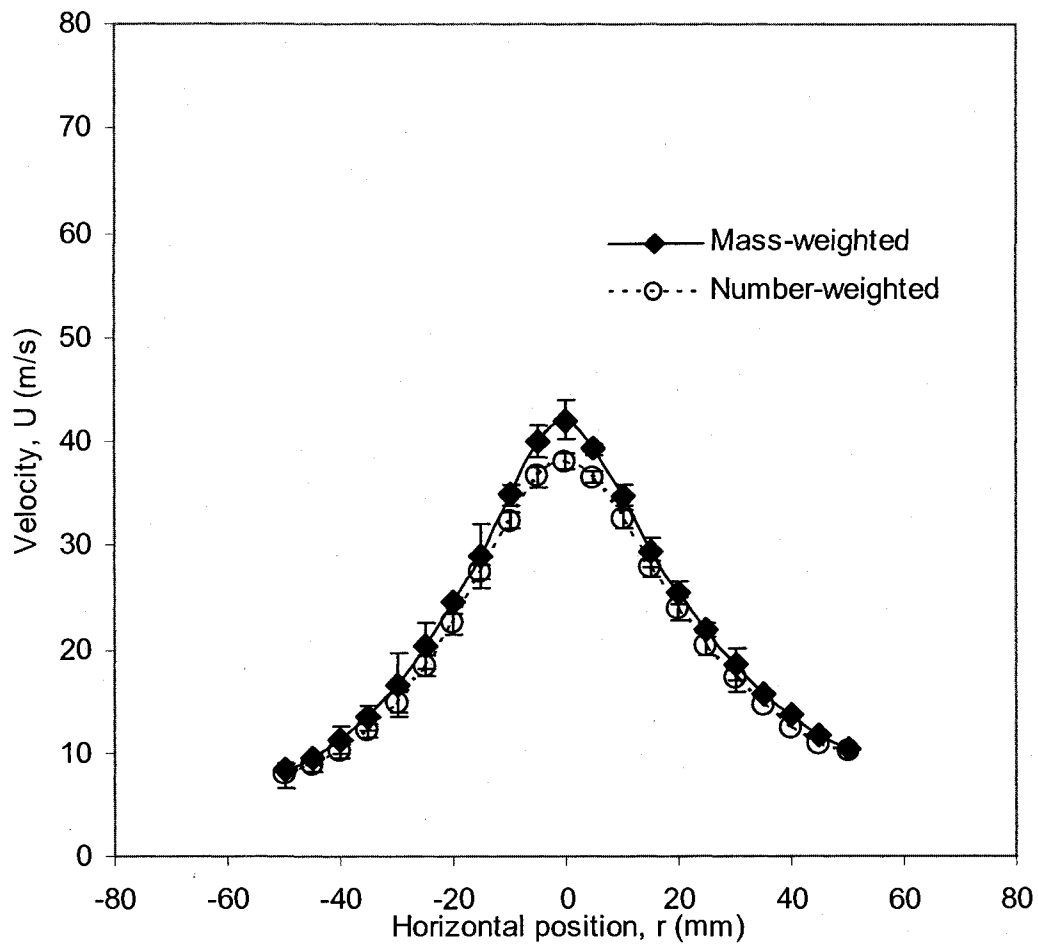


Figure A4-17: Number and mass-weighted velocity profiles at axial position,  $x = 405$  mm for SS-1.0 nozzle ( $D = 3.1$ mm). Data is for air-canola oil spray ( $\mu_L = 66$  mPa-s,  $\gamma = 25$  mN/m) with liquid flow rate of  $105 \times 10^{-6}$  m<sup>3</sup>/s and 2.0% GLR. The error bars show the 95% confidence limits for the velocity measurements.

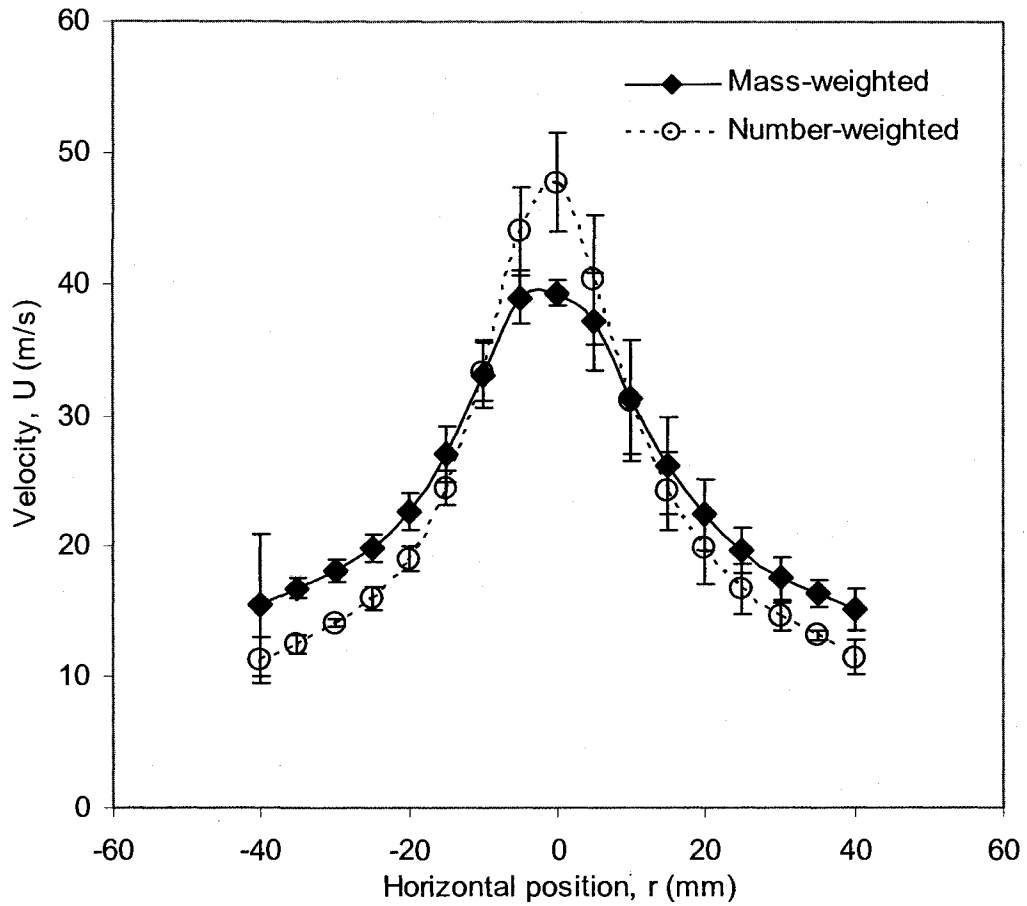


Figure A4-18: Number and mass-weighted velocity profiles at axial position,  $x = 100$  mm for SS-1.0 nozzle ( $D = 3.1$ mm). Data is for air-glycerine solution spray ( $\mu_L = 67$  mPa-s,  $\gamma = 61$  mN/m) with liquid flow rate of  $79 \times 10^{-6}$  m<sup>3</sup>/s and 1.0% GLR. The error bars show the 95% confidence limits for the velocity measurements.

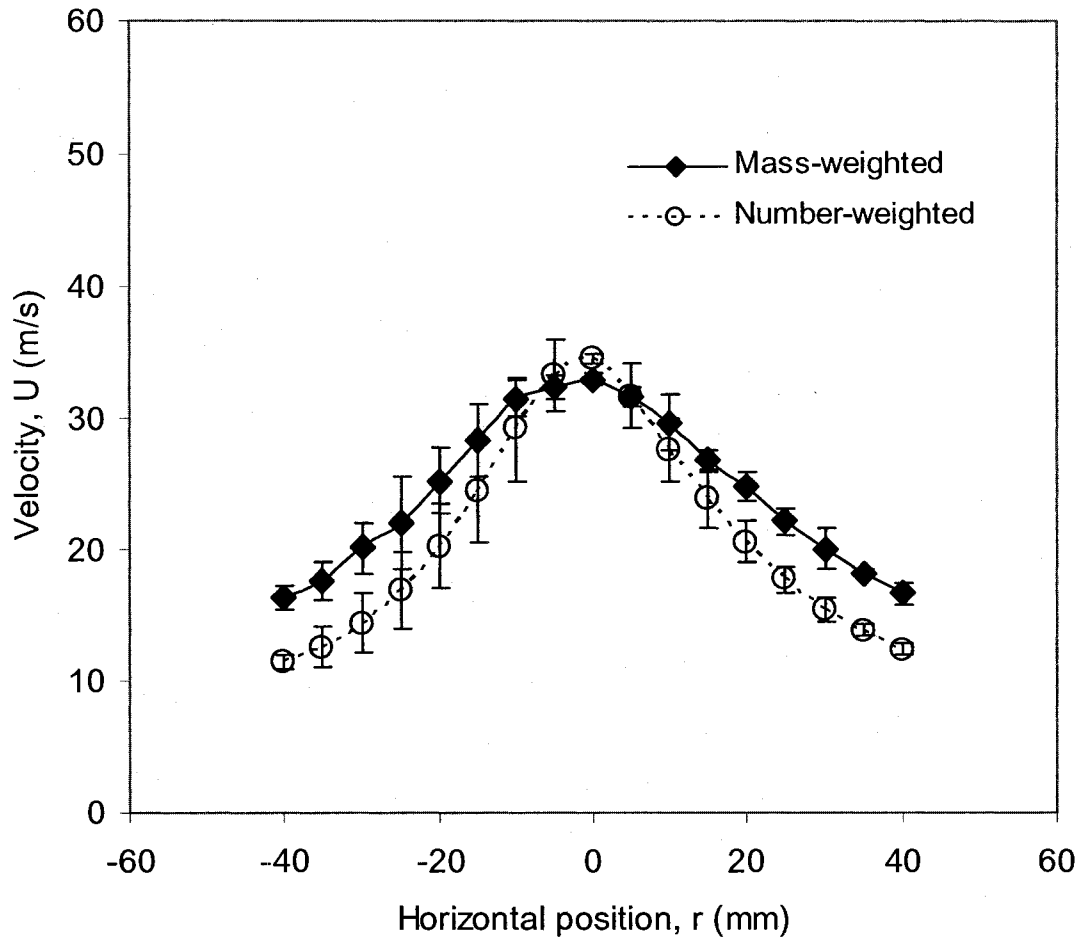


Figure A4-19: Number and mass-weighted velocity profiles at axial position,  $x = 202$  mm for SS-1.0 nozzle ( $D = 3.1$  mm). Data is for air-glycerine solution spray ( $\mu_L = 67$  mPa-s,  $\gamma = 61$  mN/m) with liquid flow rate of  $79 \times 10^{-6}$  m<sup>3</sup>/s and 1.0% GLR. The error bars show the 95% confidence limits for the velocity measurements.



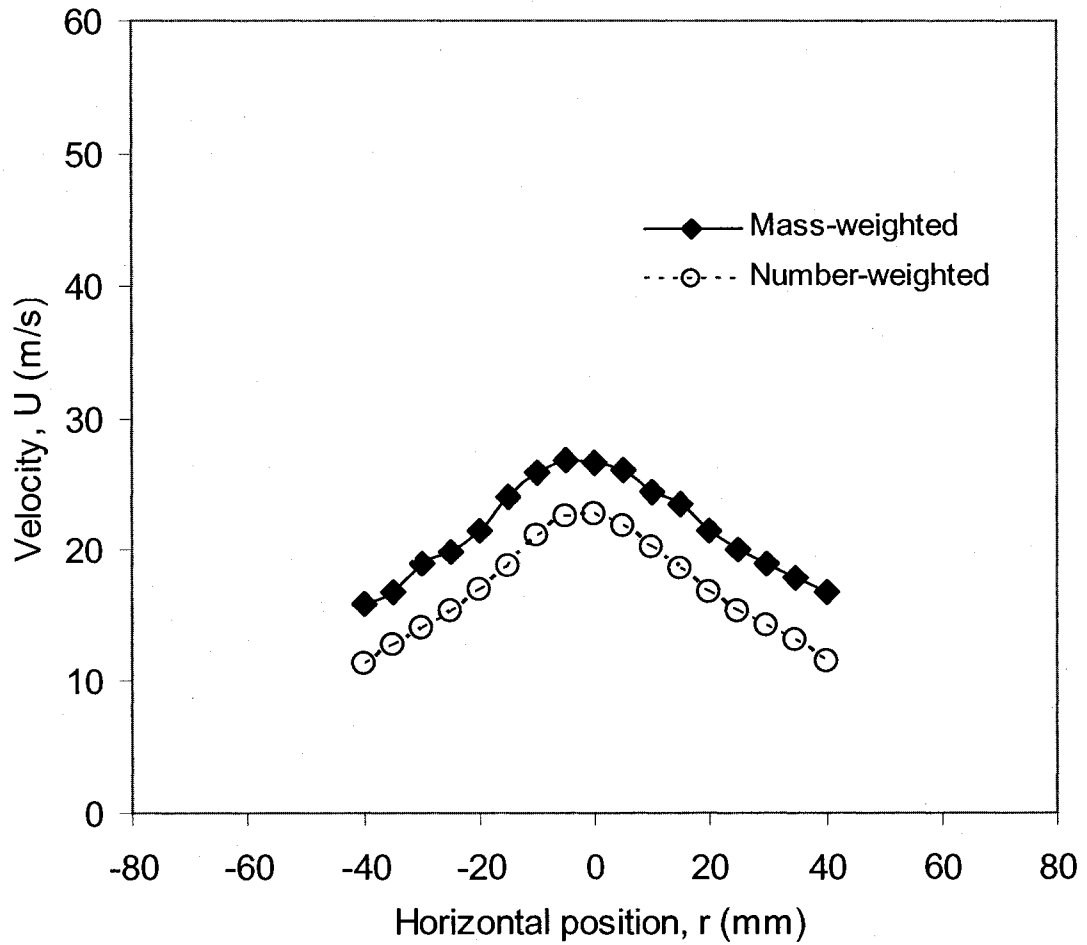


Figure A4-20: Number and mass-weighted velocity profiles at axial position,  $x = 405$  mm for SS-1.0 nozzle ( $D = 3.1$ mm). Data is for air-glycerine solution spray ( $\mu_L = 67$  mPa-s,  $\gamma = 61$  mN/m) with liquid flow rate of  $79 \times 10^{-6}$  m<sup>3</sup>/s and 1.0% GLR. The error bars show the 95% confidence limits for the velocity measurements.

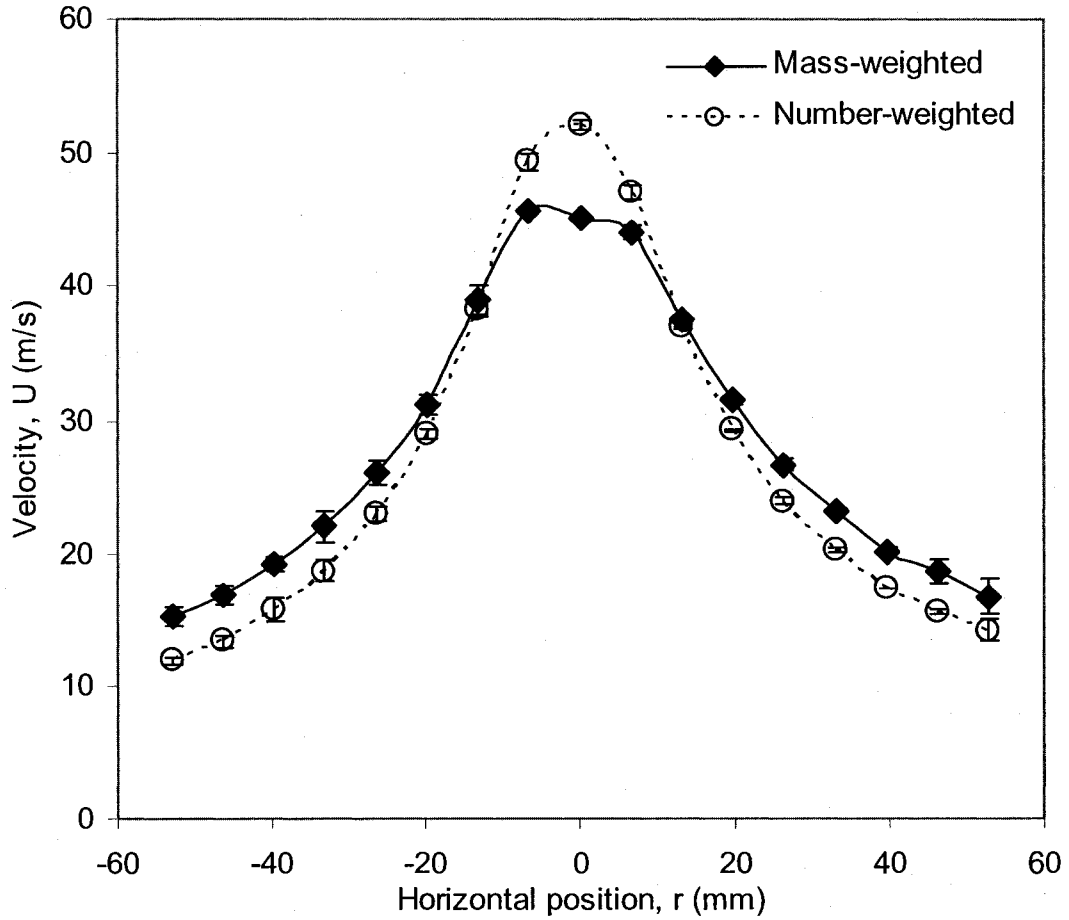


Figure A4-21: Number and mass-weighted velocity profiles at axial position,  $x = 100$  mm for SS-1.3 nozzle ( $D = 4.1$ mm). Data is for air-glycerine solution spray ( $\mu_L = 67$  mPa-s,  $\gamma = 61$  mN/m) with liquid flow rate of  $163 \times 10^{-6}$  m<sup>3</sup>/s and 1.0% GLR. The error bars show the 95% confidence limits for the velocity measurements.

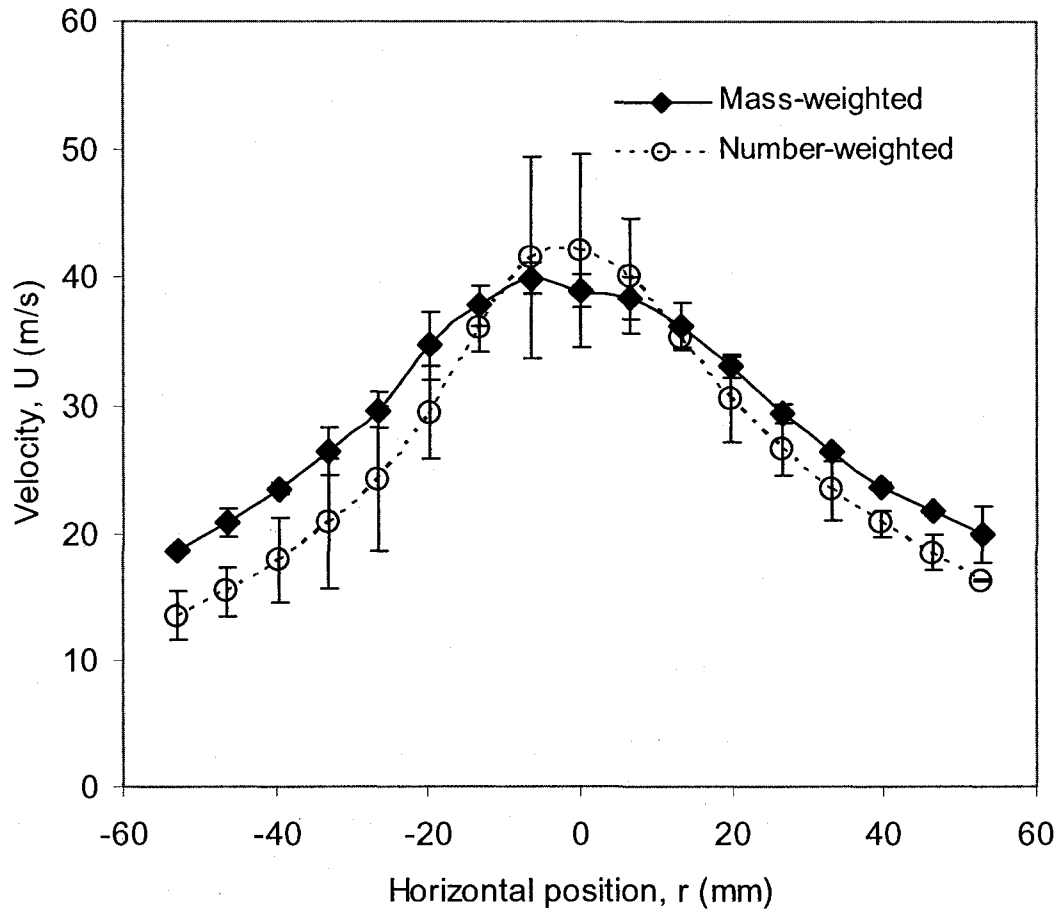


Figure A4-22: Number and mass-weighted velocity profiles at axial position,  $x = 202$  mm for SS-1.3 nozzle ( $D = 4.1$ mm). Data is for air-glycerine solution spray ( $\mu_L = 67$  mPa-s,  $\gamma = 61$  mN/m) with liquid flow rate of  $163 \times 10^{-6}$  m<sup>3</sup>/s and 1.0% GLR. The error bars show the 95% confidence limits for the velocity measurements.

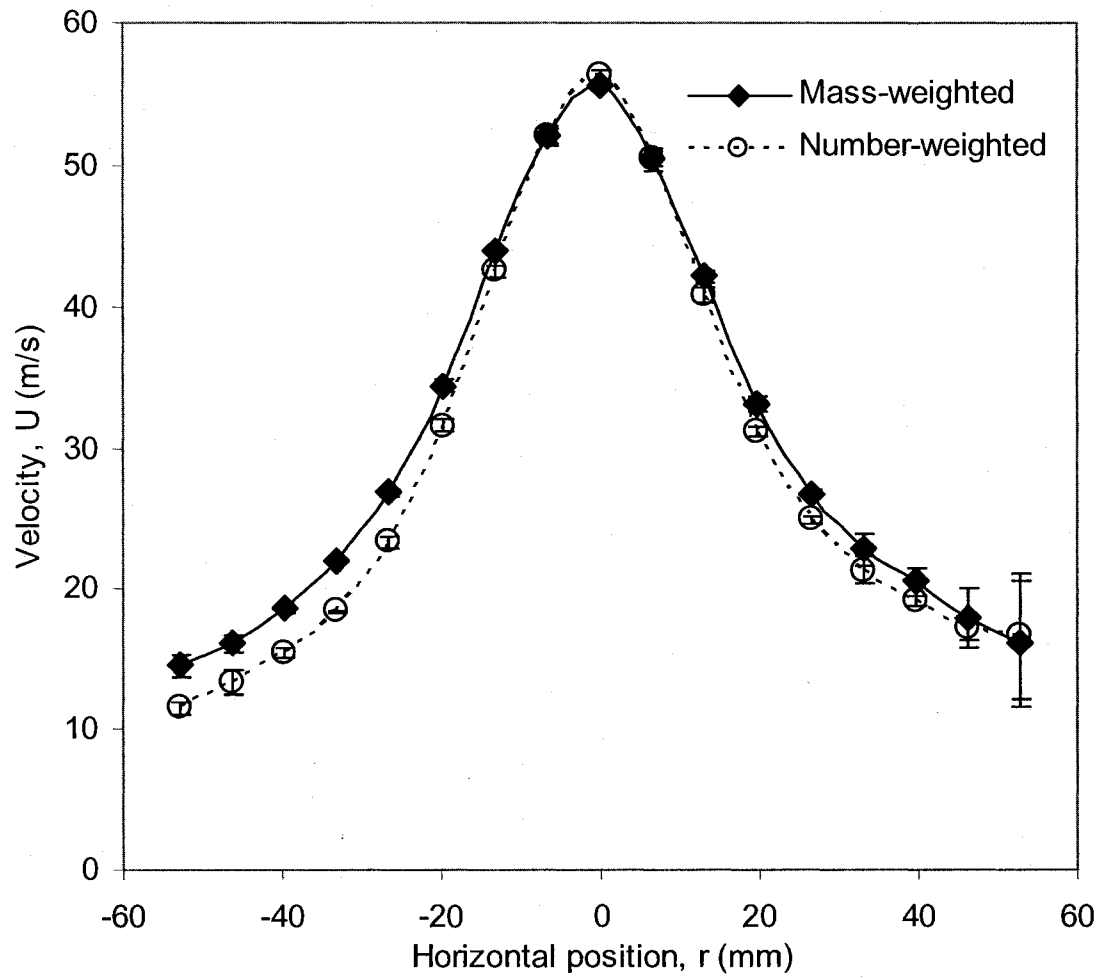


Figure A4-23: Number and mass-weighted velocity profiles at axial position,  $x = 100$  mm for SS-1.3 nozzle ( $D = 4.1$  mm). Data is for air-water spray ( $\mu_L = 1$  mPa-s,  $\gamma = 70$  mN/m) with liquid flow rate of  $190 \times 10^{-6}$  m<sup>3</sup>/s and 1.0% GLR. The error bars show the 95% confidence limits for the velocity measurements.

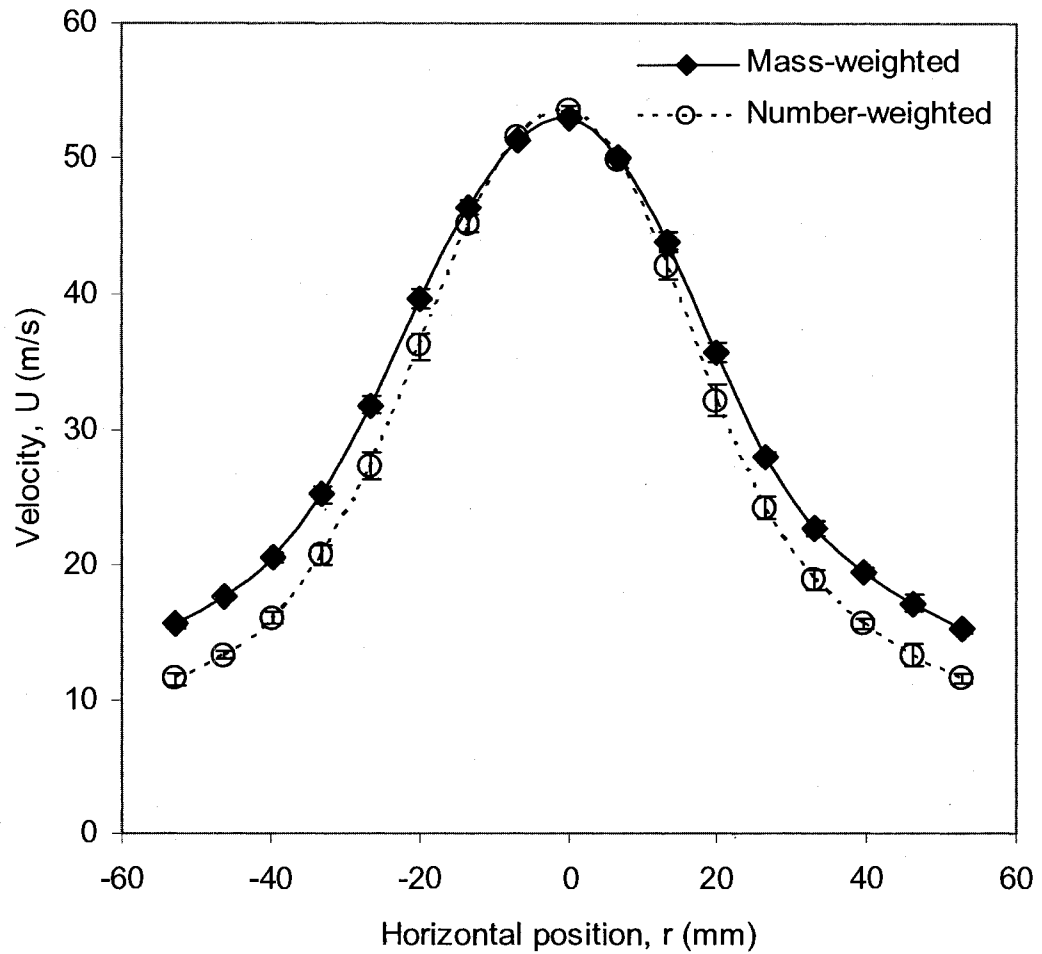


Figure A4-24: Number and mass-weighted velocity profiles at axial position,  $x = 202$  mm for SS-1.3 nozzle ( $D = 4.1$ mm). Data is for air-water spray ( $\mu_L = 1$  mPa-s,  $\gamma = 70$  mN/m) with liquid flow rate of  $190 \times 10^{-6}$  m<sup>3</sup>/s and 1.0% GLR. The error bars show the 95% confidence limits for the velocity measurements.

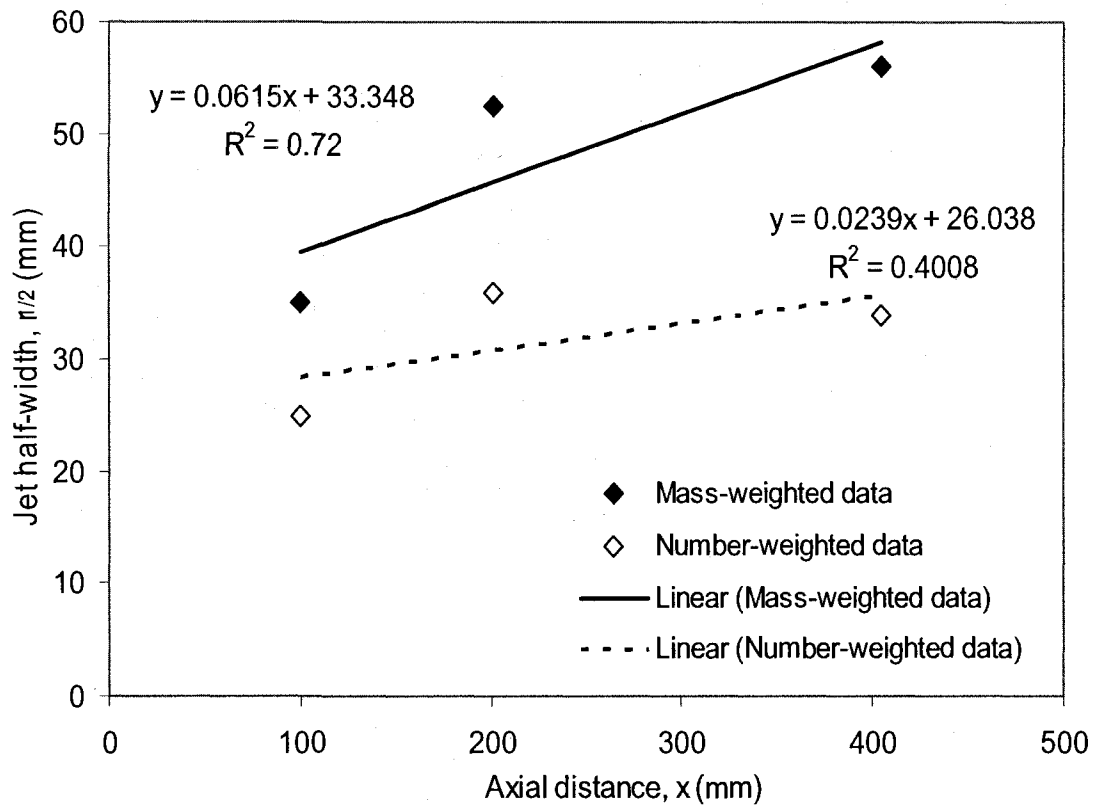


Figure A4-25: Variation of jet-half-width (from number and mass-weighted velocity profiles) at axial positions 100, 202, and 405 mm for SS-1.0. Data is for air-glycerine solution spray ( $\mu_L = 67$  mPa-s,  $\gamma = 61$  mN/m) with liquid flow rate of  $114 \times 10^{-6}$  m<sup>3</sup>/s and 1.0% GLR. Virtual origin ( $x_0$ ) is 542 mm and 1090 mm for the mass-weighted and number-weighted velocity data, respectively.

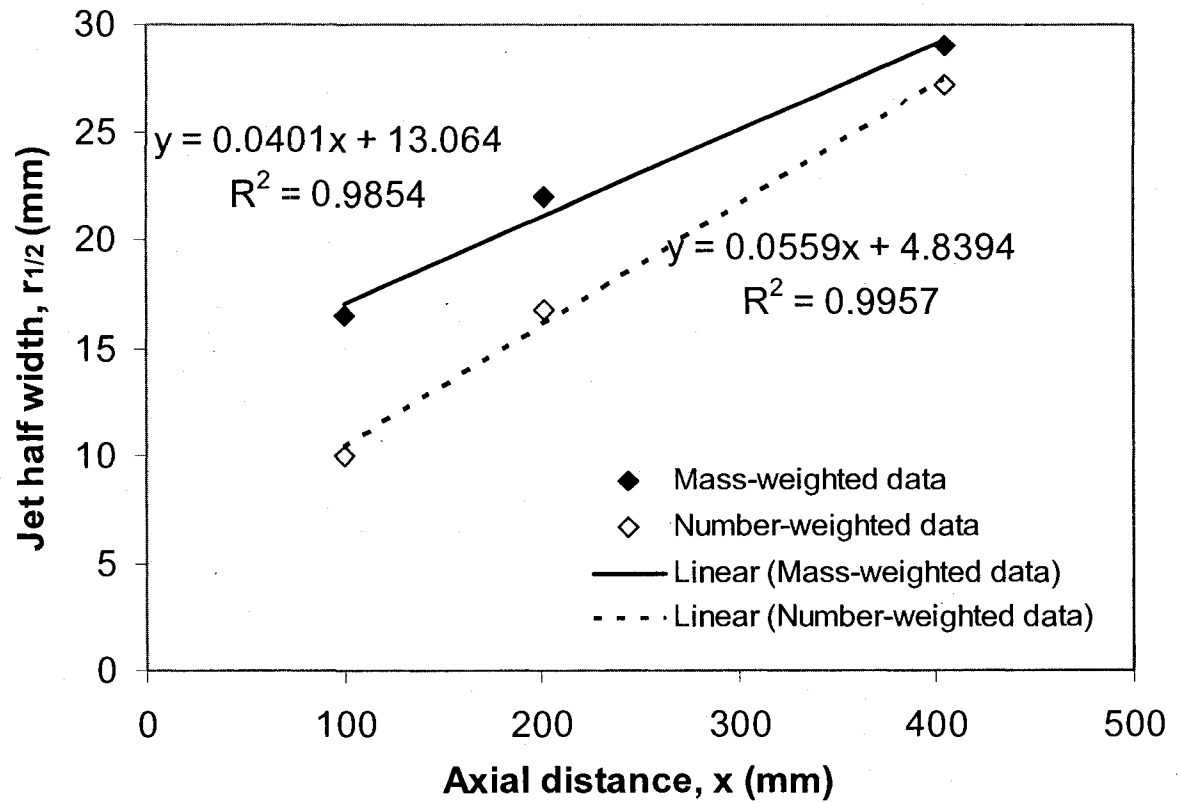


Figure A4-26: Variation of jet-half-width (from number and mass-weighted velocity profiles) at axial positions 100, 202, and 405 mm for SS-1.0. Data is for air-canola oil spray ( $\mu_L = 66$  mPa-s,  $\gamma = 25$  mN/m) with liquid flow rate of  $105 \times 10^{-6}$  m<sup>3</sup>/s and 1.0% GLR. Virtual origin( $x_0$ ) is 326 mm and 87 mm for the mass-weighted and number-weighted velocity data, respectively.

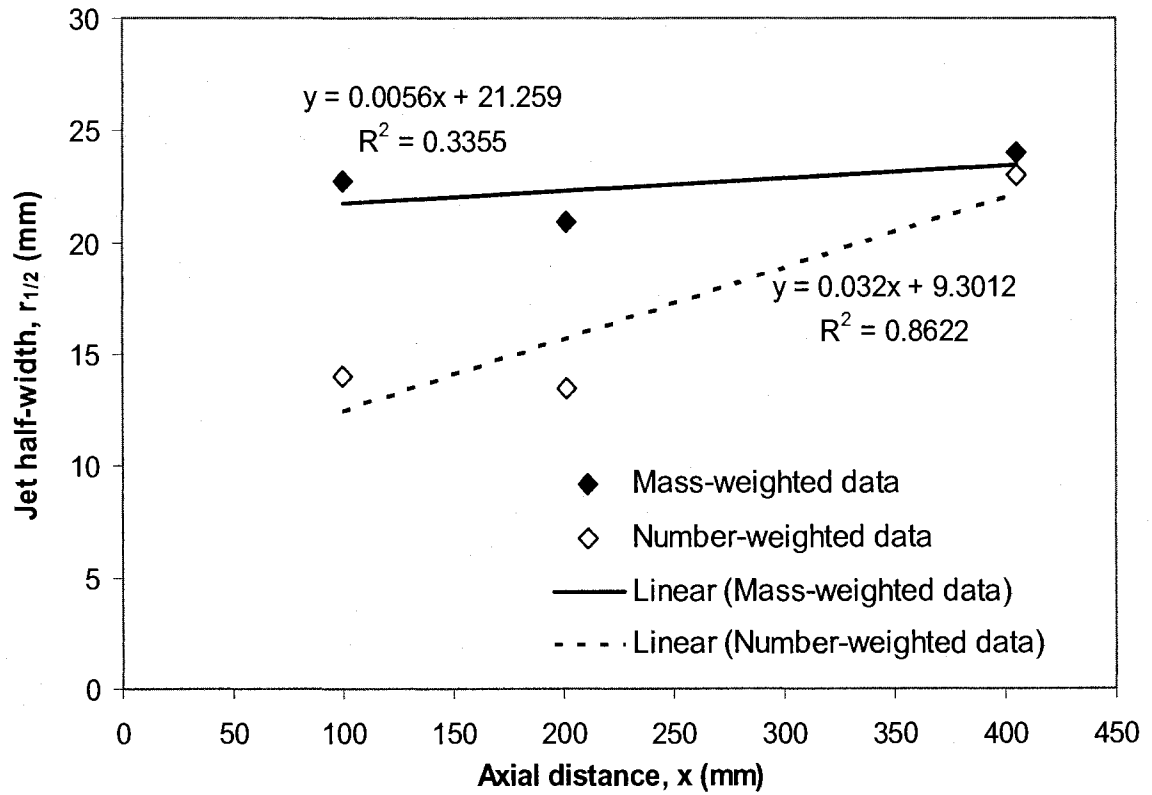


Figure A4-27: Variation of jet-half-width (from number and mass-weighted velocity profiles) at axial positions 100, 202, and 405 mm for SS-1.0. Data is for air-water spray ( $\mu_L = 1 \text{ mPa}\cdot\text{s}$ ,  $\gamma = 70 \text{ mN/m}$ ) with liquid flow rate of  $95 \times 10^{-6} \text{ m}^3/\text{s}$  and 2.0% *GLR*. Virtual origin( $x_0$ ) is 3796 mm and 291 mm for the mass-weighted and number-weighted velocity data, respectively.



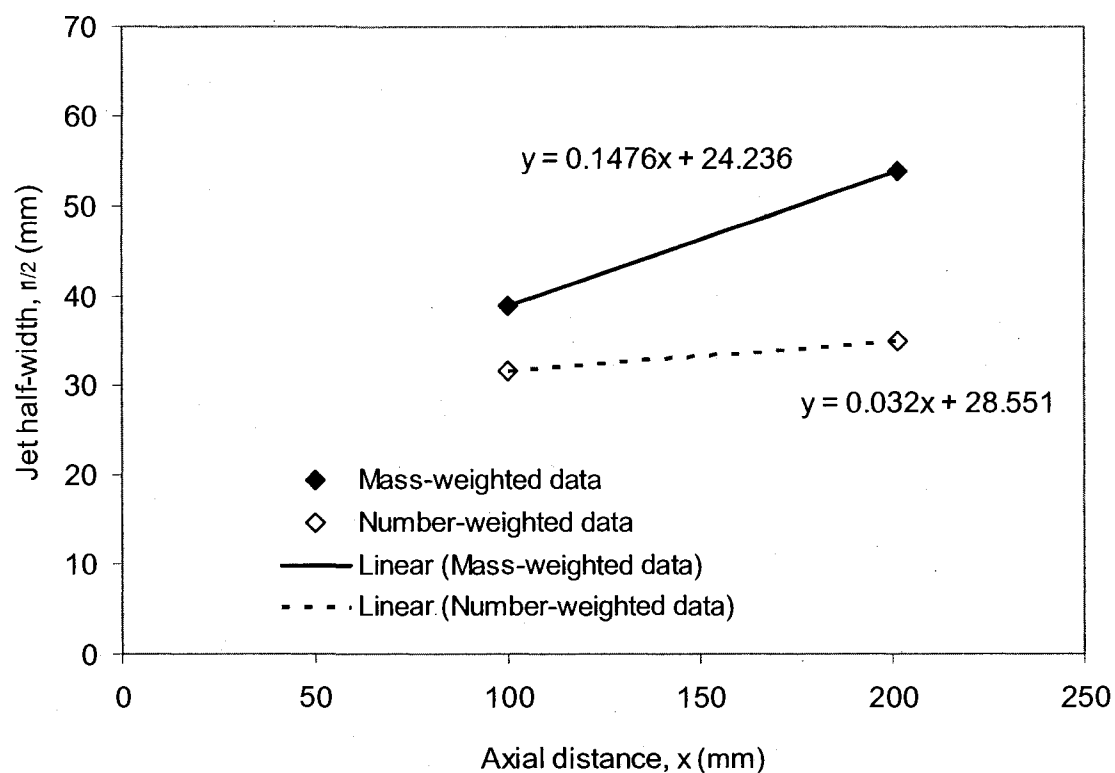


Figure A4-28: Variation of jet-half-width (from number and mass-weighted velocity profiles) at axial positions 100 and 202 mm for SS-1.0. Data is for air-glycerine solution spray ( $\mu_L = 67$  mPa-s,  $\gamma = 61$  mN/m) with liquid flow rate of  $105 \times 10^{-6}$  m<sup>3</sup>/s and 2.0% GLR. Virtual origin( $x_0$ ) is 164 mm and 892 mm for the mass-weighted and number-weighted velocity data, respectively. Note that the linear relationship for the 2-data point above is for consistency of analysis compared to plots with 3 data-points.

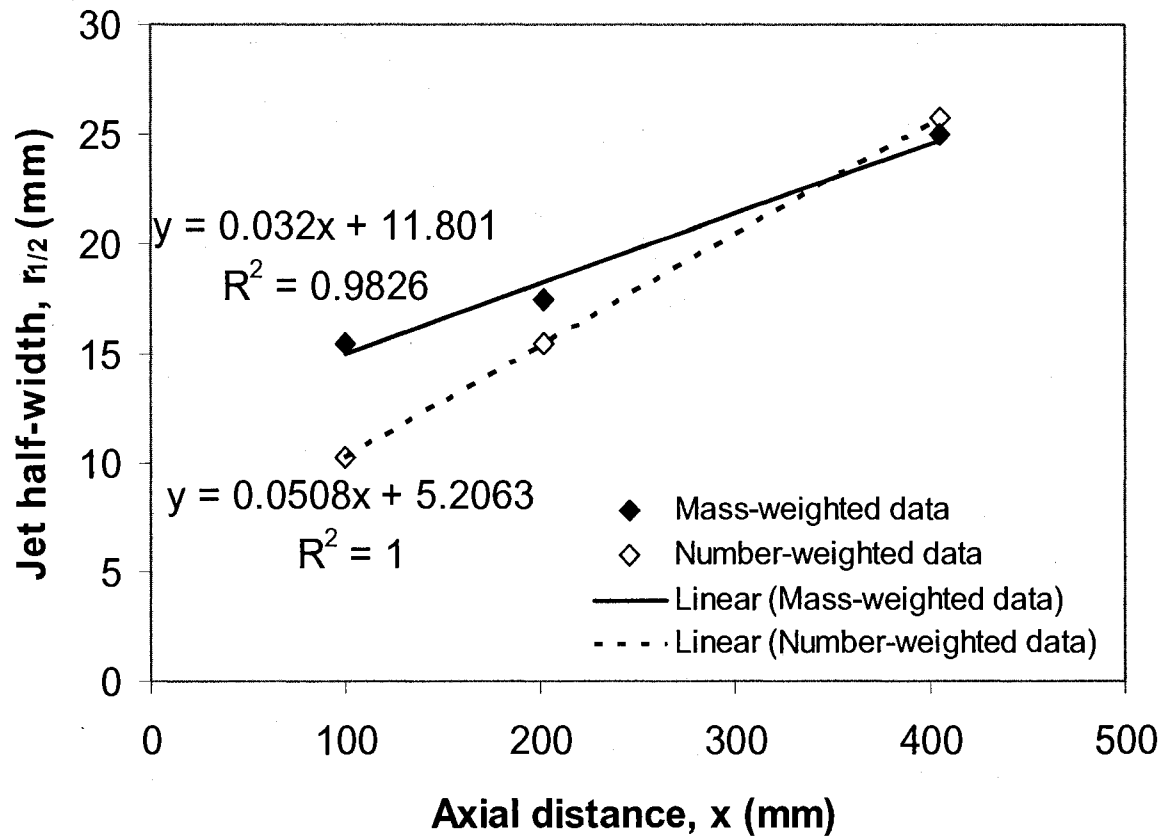


Figure A4-29: Variation of jet-half-width (from number and mass-weighted velocity profiles) at axial positions 100, 202, and 405 mm for SS-1.0. Data is for air-canola oil spray ( $\mu_L = 66$  mPa-s,  $\gamma = 25$  mN/m) with liquid flow rate of  $105 \times 10^{-6}$  m<sup>3</sup>/s and 2.0% GLR. Virtual origin( $x_0$ ) is 369 mm and 103 mm for the mass-weighted and number-weighted velocity data, respectively.

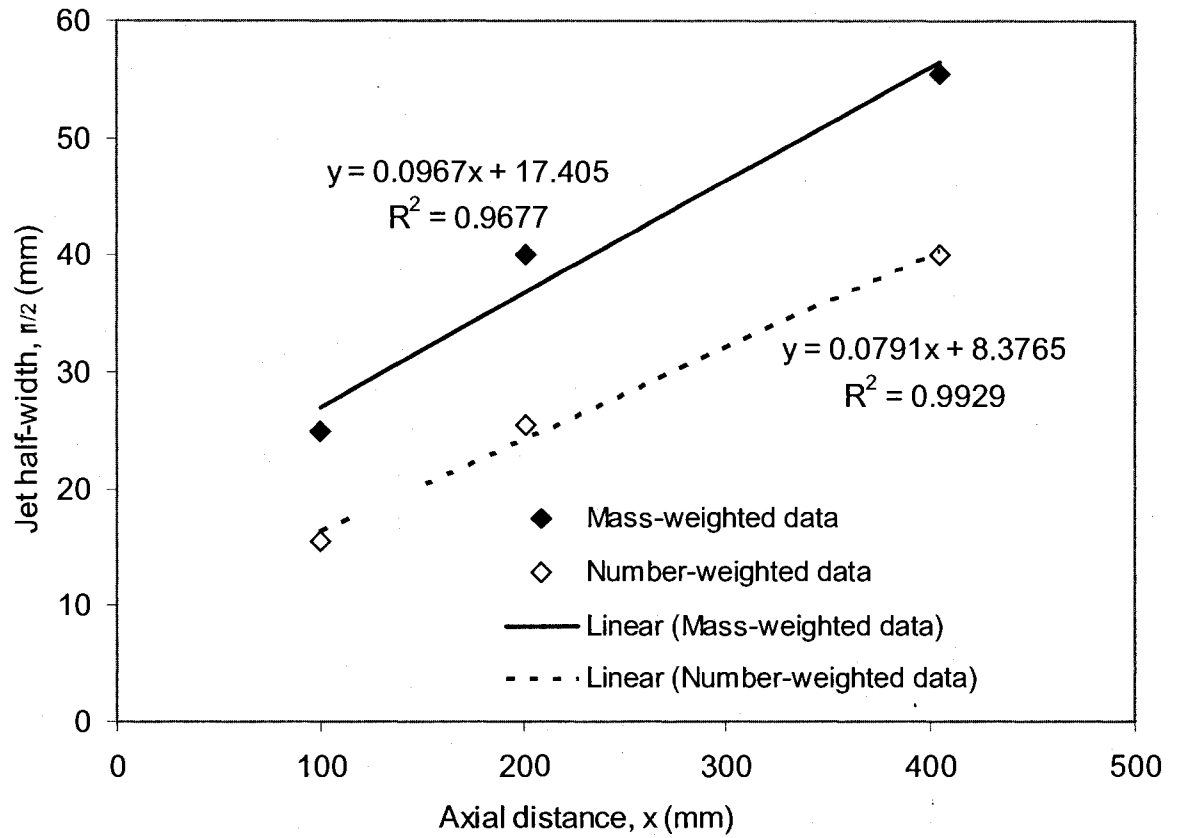


Figure A4-30: Variation of jet-half-width (from number and mass-weighted velocity profiles) at axial positions 100, 202, and 405 mm for SS-1.0. Data is for air-glycerine solution spray ( $\mu_L = 67$  mPa-s,  $\gamma = 61$  mN/m) with liquid flow rate of  $79 \times 10^{-6}$  m<sup>3</sup>/s and 1.0% GLR. Virtual origin( $x_0$ ) is 180 mm and 106 mm for the mass-weighted and number-weighted velocity data, respectively.

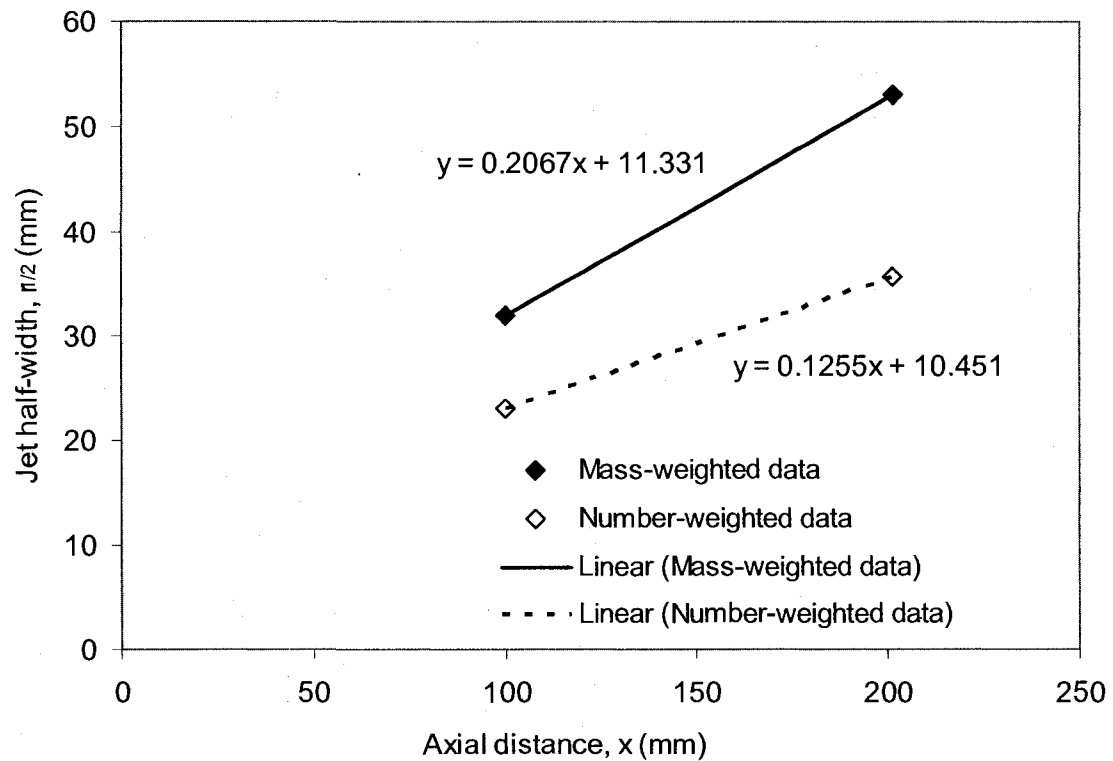


Figure A4-31: Variation of jet-half-width (from number and mass-weighted velocity profiles) at axial positions 100 and 202 mm for SS-1.3. Data is for air-glycerine solution spray ( $\mu_L = 67$  mPa-s,  $\gamma = 61$  mN/m) with liquid flow rate of  $163 \times 10^{-6}$  m<sup>3</sup>/s and 1.0% GLR. Virtual origin( $x_0$ ) is 55 mm and 83 mm for the mass-weighted and number-weighted velocity data, respectively. Note that the linear relationship for the 2-data point above is for consistency of analysis compared to plots with 3 data-points.

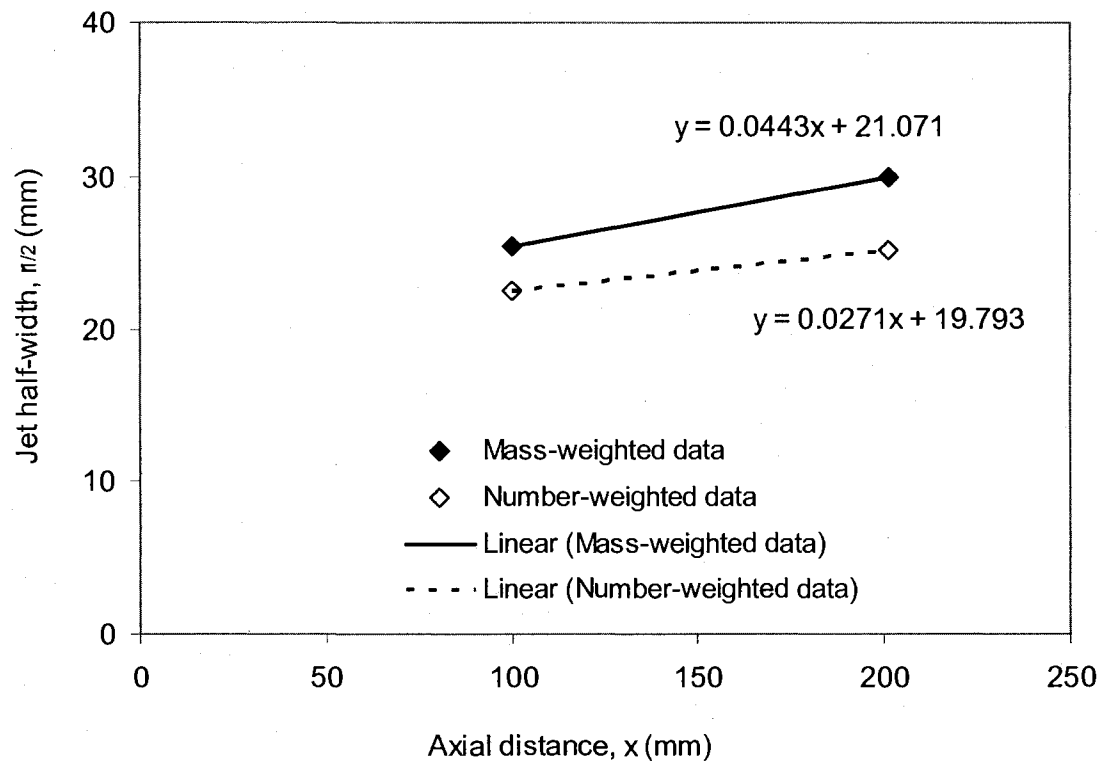


Figure A4-32: Variation of jet-half-width (from number and mass-weighted velocity profiles) at axial positions 100 and 202 mm for SS-1.3. Data is for air-water spray ( $\mu_L = 1$  mPa-s,  $\gamma = 70$  mN/m) with liquid flow rate of  $190 \times 10^{-6}$  m<sup>3</sup>/s and 1.0% GLR. Virtual origin( $x_0$ ) is 476 mm and 730 mm for the mass-weighted and number-weighted velocity data, respectively. Note that the linear relationship for the 2-data point above is for consistency of analysis compared to plots with 3 data-points.

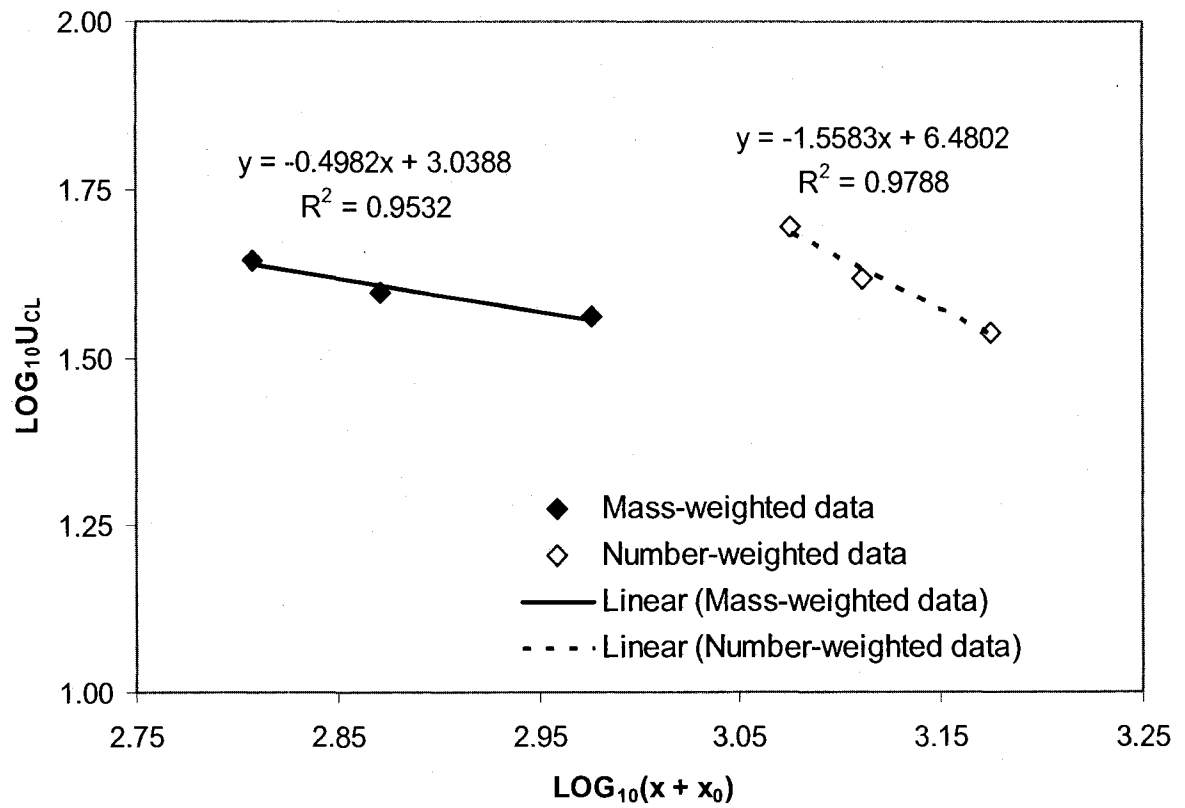


Figure A4-33: Variation of centreline velocity (from number and mass-weighted velocity profiles) at axial positions 100, 202, and 405 mm for SS-1.0. The slopes for the mass and number-weighted data are -0.5 and -1.6, respectively. Data is for air-glycerine solution spray ( $\mu_L = 1 \text{ mPa}\cdot\text{s}$ ,  $\gamma = 70 \text{ mN/m}$ ) with liquid flow rate of  $114 \times 10^{-6} \text{ m}^3/\text{s}$  and 1.0% GLR.

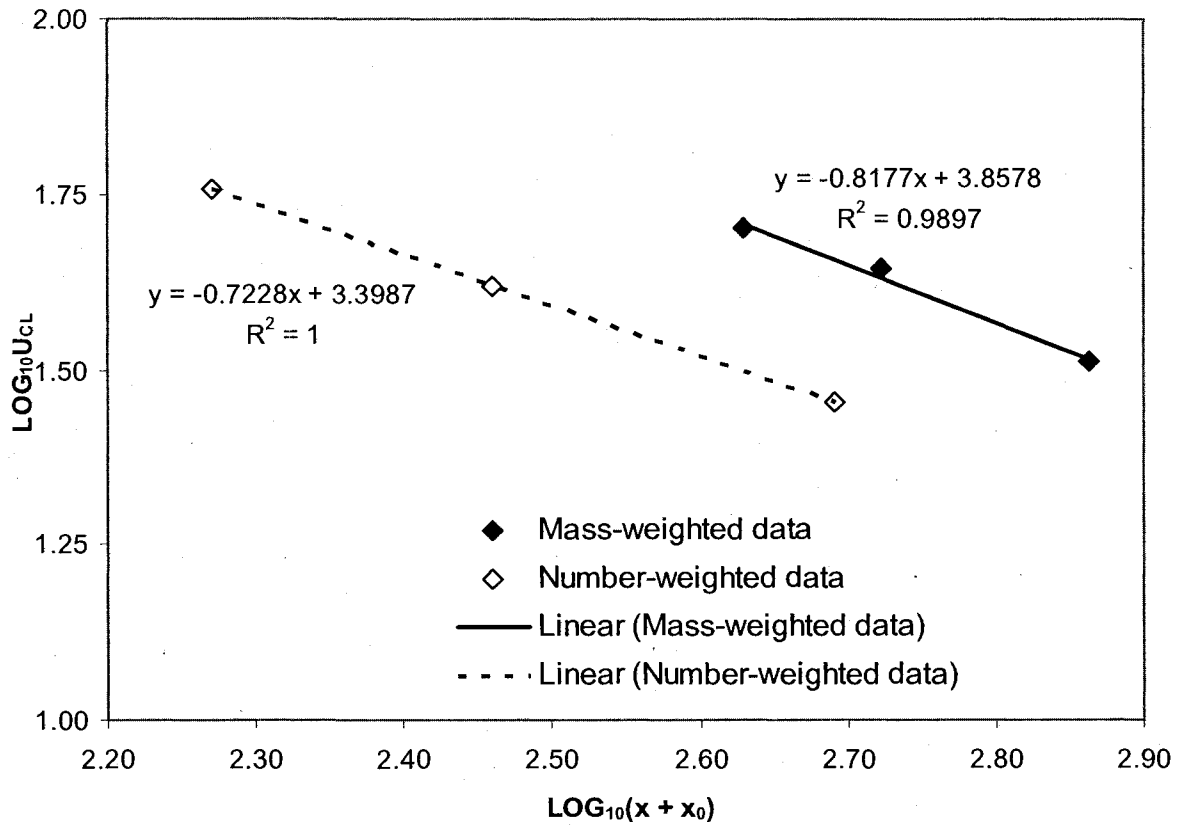


Figure A4-34: Variation of centreline velocity (from number and mass-weighted velocity profiles) at axial positions 100, 202, and 405 mm for SS-1.0. The slopes for the mass and number-weighted data are -0.8 and -0.7, respectively. Data is for air-canola oil spray ( $\mu_L = 66$  mPa-s,  $\gamma = 25$  mN/m) with liquid flow rate of  $105 \times 10^{-6}$  m<sup>3</sup>/s and 1.0% GLR.

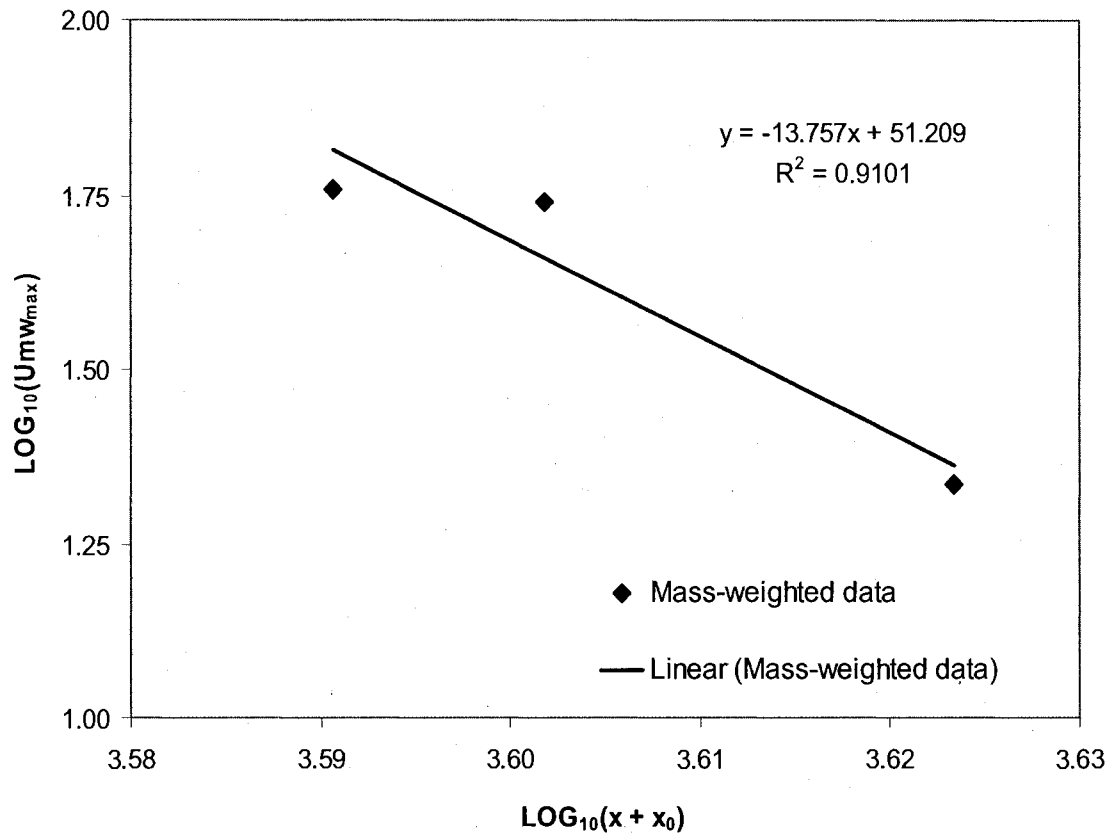


Figure A4-35: Variation of centreline velocity (from mass-weighted velocity profiles) at axial positions 100, 202, and 405 mm for SS-1.0. The slope of the graph is -13.757 (This value is an outlier). Data is for air-water spray ( $\mu_L = 1$  mPas,  $\gamma = 70$  mN/m) with liquid flow rate of  $95 \times 10^{-6} \text{ m}^3/\text{s}$  and 2.0% GLR.



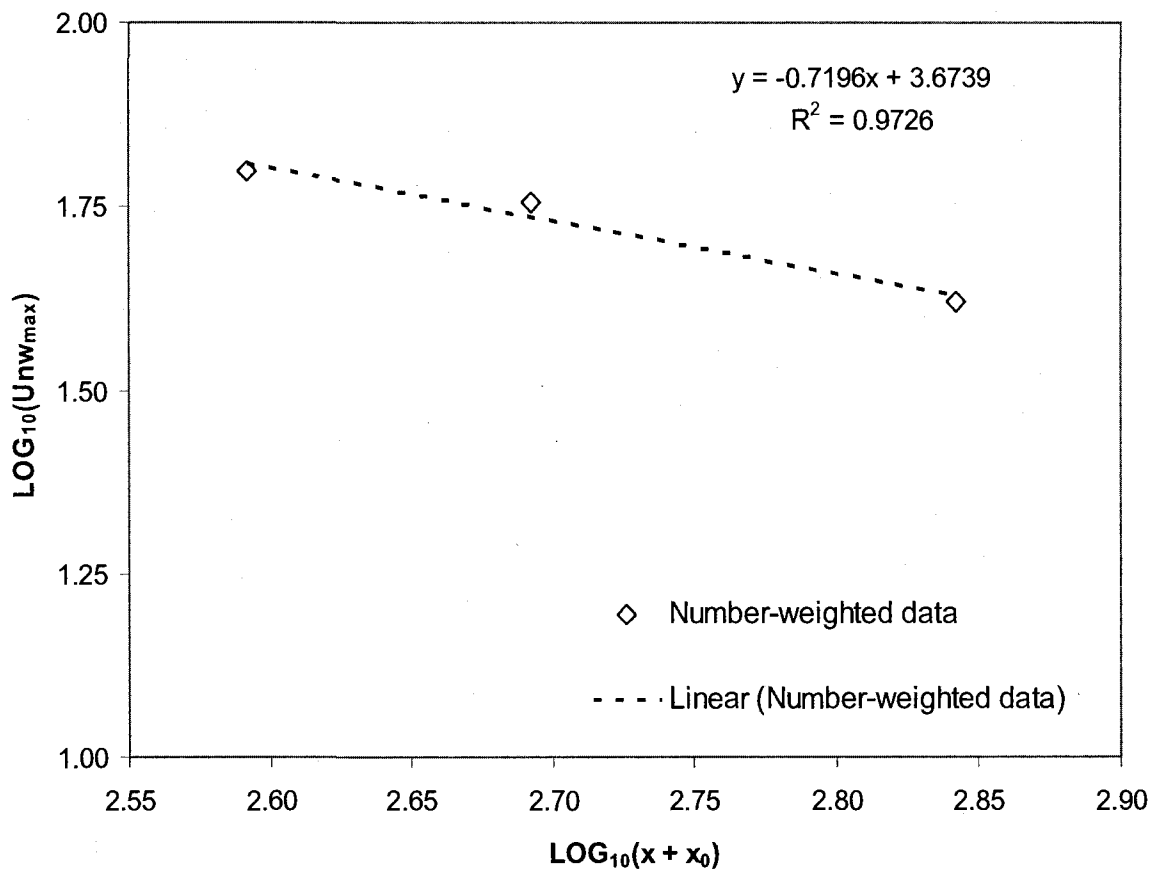


Figure A4-36: Variation of centreline velocity (from number-weighted velocity profiles) at axial positions 100, 202, and 405 mm for SS-1.0. The slope of the graph is -0.7. Data is for air-water spray ( $\mu_L = 1$  mPas,  $\gamma = 70$  mN/m) with liquid flow rate of  $95 \times 10^{-6}$  m<sup>3</sup>/s and 2.0% GLR.

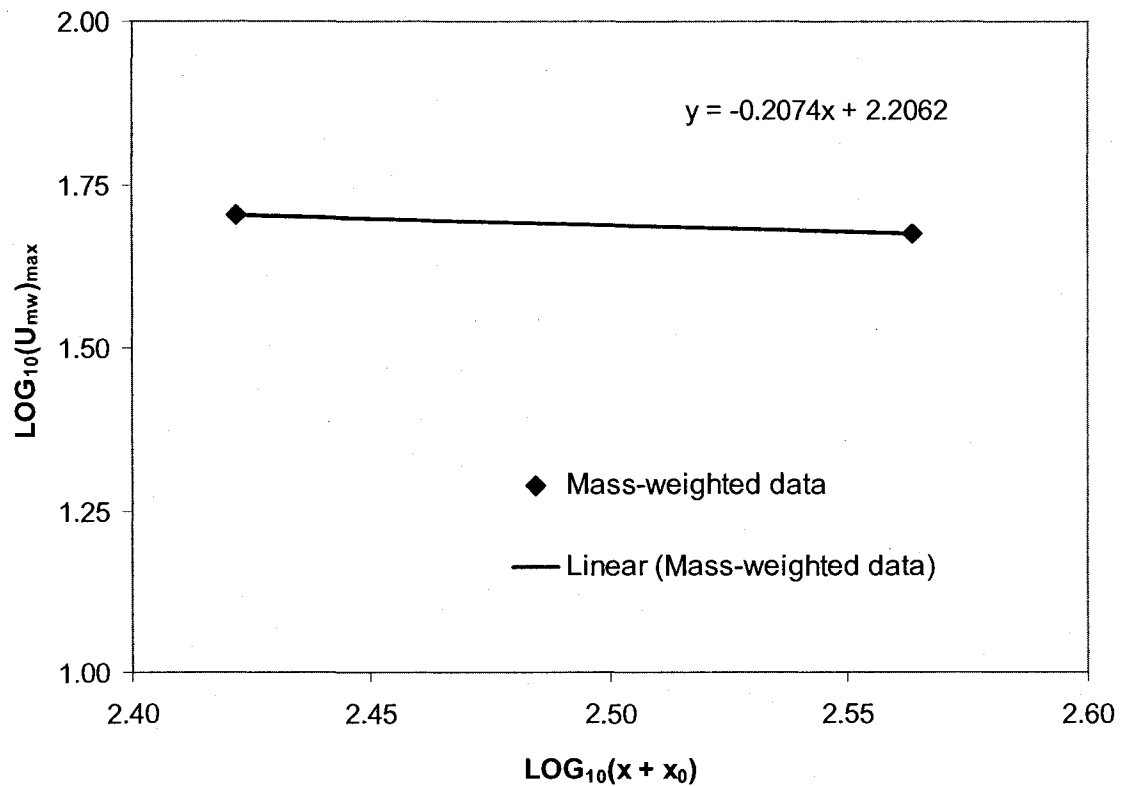


Figure A4-37: Variation of centreline velocity (from mass-weighted velocity profiles) at axial positions 100 and 202 mm for SS-1.0. The slope of the graph is -0.2. Data is for air-glycerine solution spray ( $\mu_L = 67$  mPa-s,  $\gamma = 61$  mN/m) with liquid flow rate of  $105 \times 10^{-6}$  m<sup>3</sup>/s and 2.0% GLR. Note that the linear relationship for the 2-data point above is for consistency of analysis compared to plots with 3 data-points.

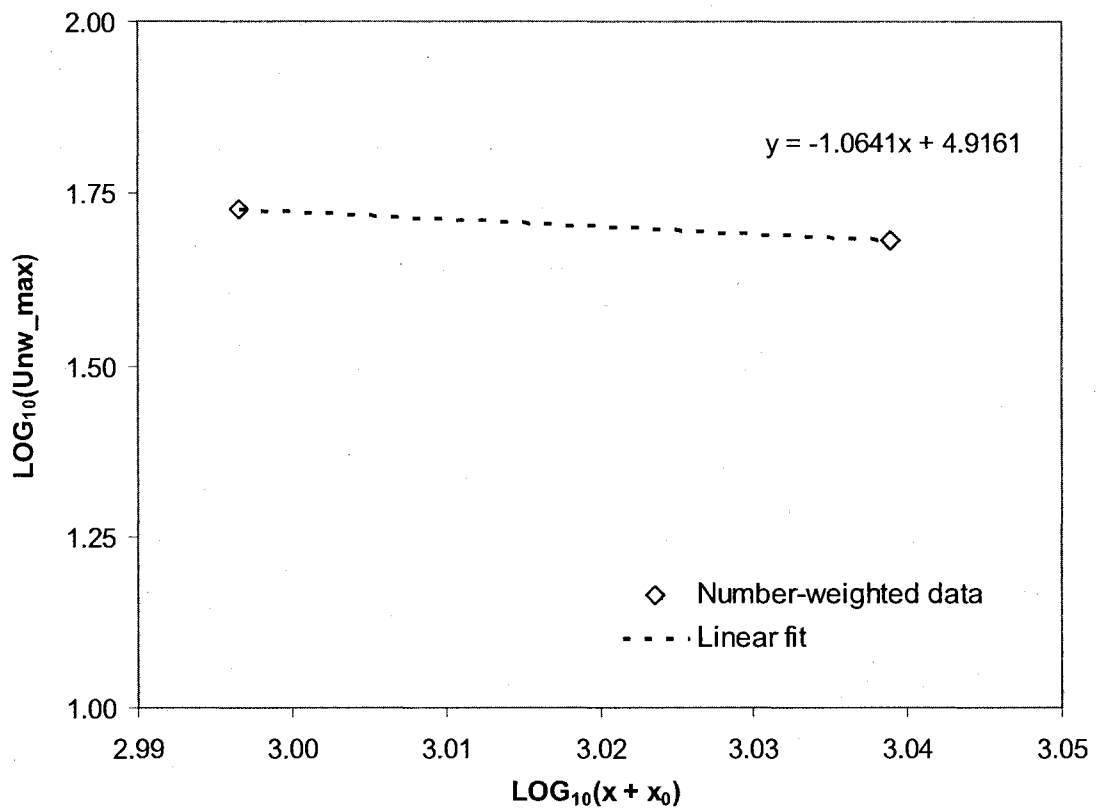


Figure A4-38: Variation of centreline velocity (from number-weighted velocity profiles) at axial positions 100 and 202 mm for SS-1.0. The slope of the graph is -1.1. Data is for air-glycerine solution spray ( $\mu_L = 67$  mPa-s,  $\gamma = 61$  mN/m) with liquid flow rate of  $105 \times 10^{-6}$  m<sup>3</sup>/s and 2.0% GLR. Note that the linear relationship for the 2-data point above is for consistency of analysis compared to plots with 3 data-points.

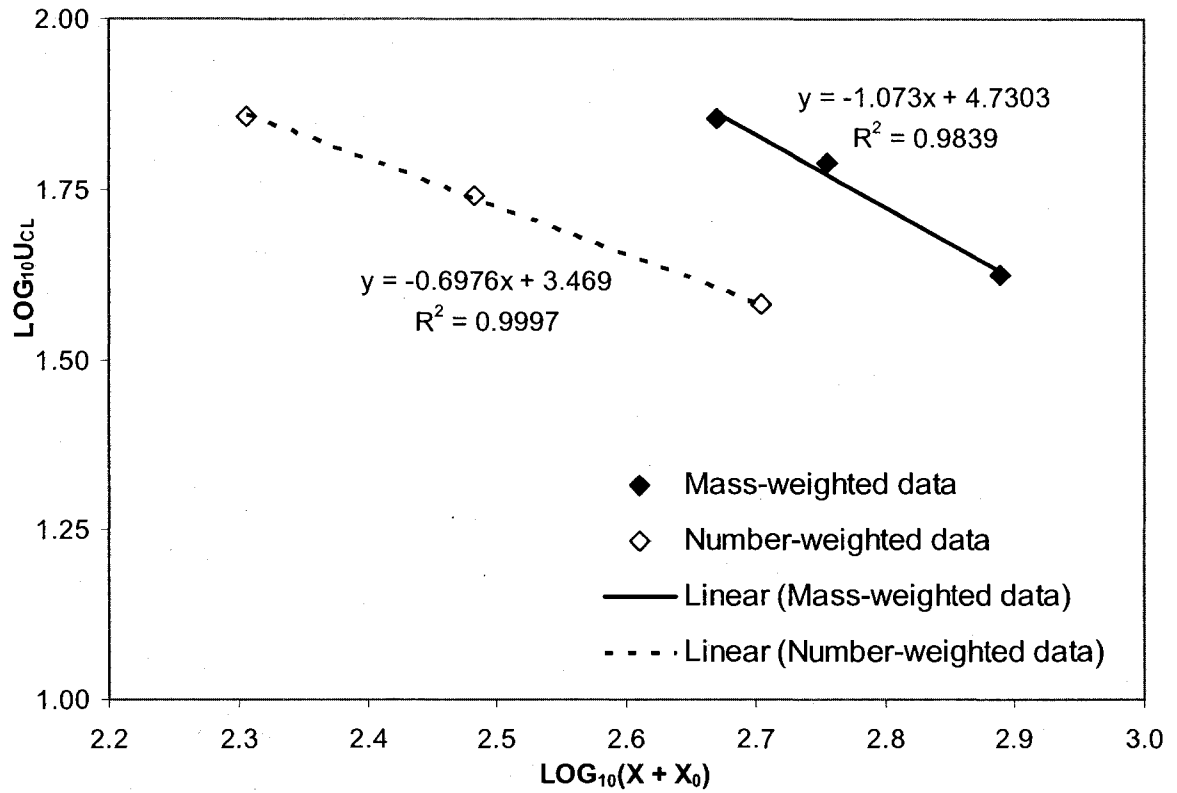


Figure A4-39: Variation of centreline velocity (from number-weighted velocity profiles) at axial positions 100, 202, and 405 mm for SS-1.0. The slopes for the mass and number-weighted data are -1.1 and -0.7, respectively. Data is for air-canola oil spray ( $\mu_L = 66$  mPas,  $\gamma = 25$  mN/m) with liquid flow rate of  $105 \times 10^{-6}$  m<sup>3</sup>/s and 2.0% GLR.

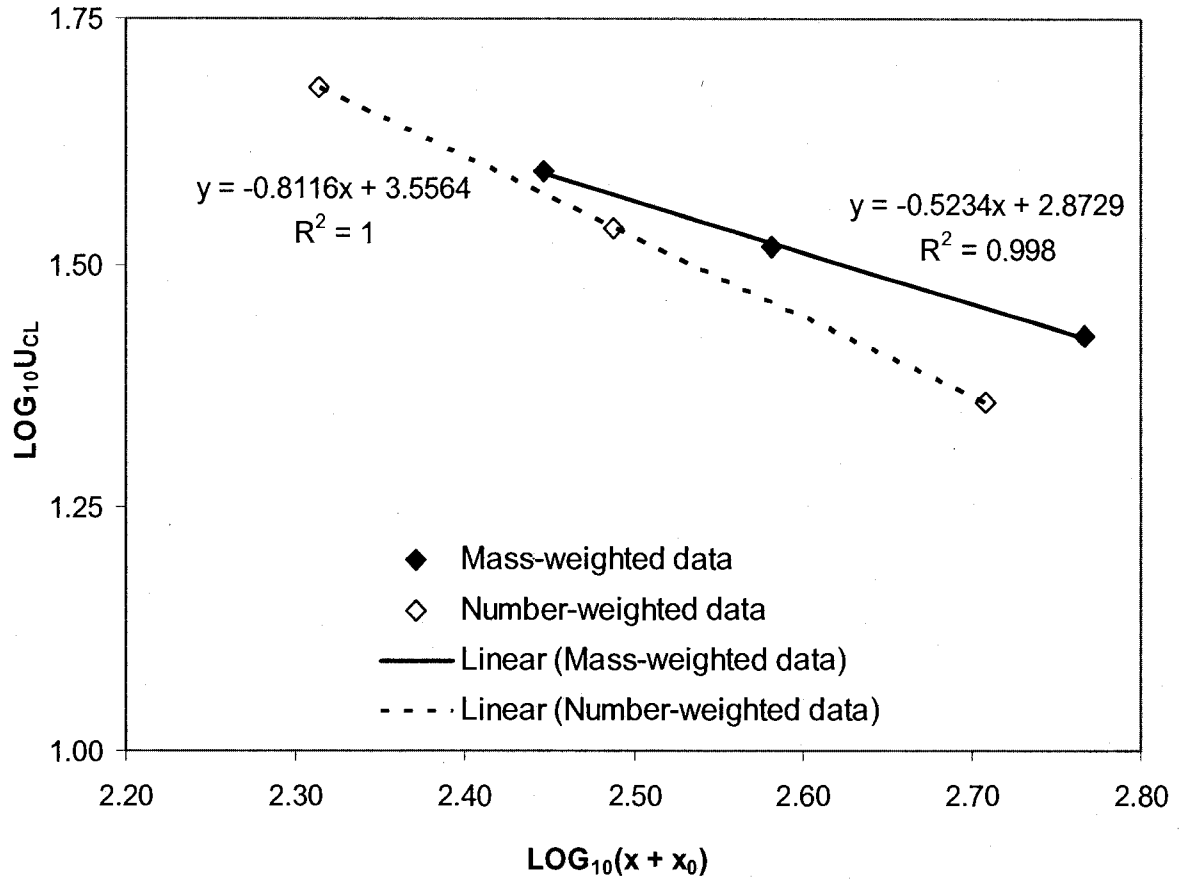


Figure A4-40: Variation of centreline velocity (from number-weighted velocity profiles) at axial positions 100, 202, and 405 mm for SS-1.0. The slopes for the mass and number-weighted data are -0.5 and -0.8, respectively. Data is for air-glycerine solution spray ( $\mu_L = 67$  mPas,  $\gamma = 61$  mN/m) with liquid flow rate of  $79 \times 10^{-6}$  m<sup>3</sup>/s and 1.0% GLR.

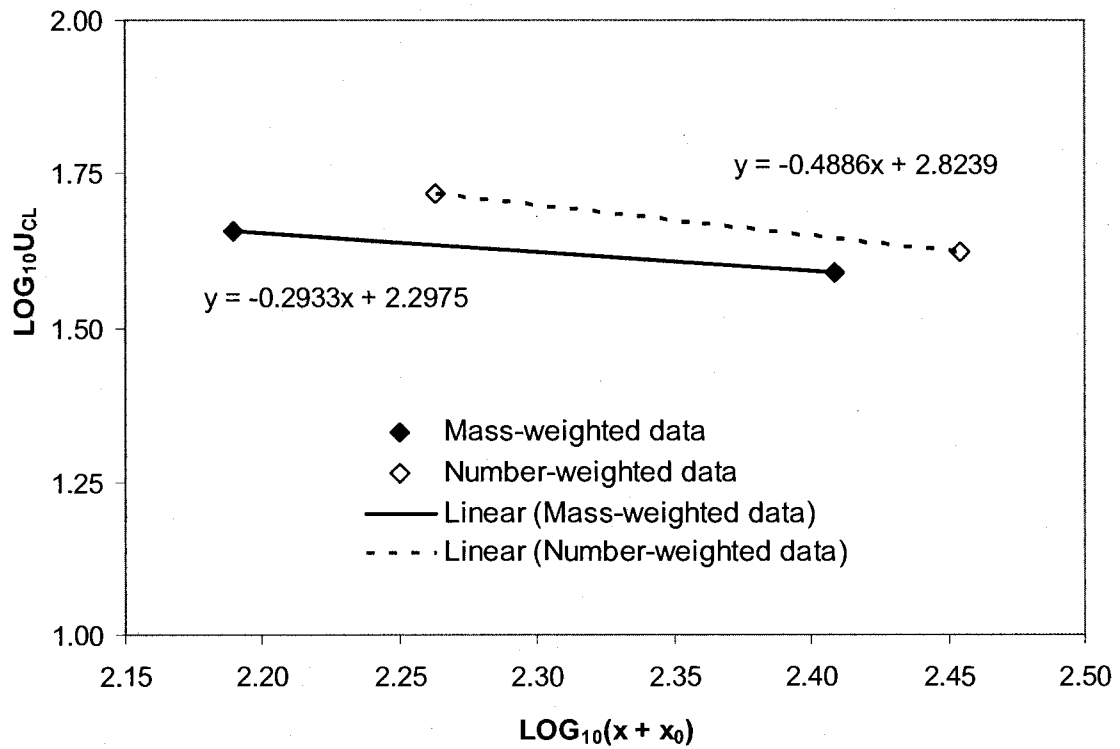


Figure A4-41: Variation of centreline velocity (from number-weighted velocity profiles) at axial positions 100 and 202 mm for SS-1.3. The slopes for the mass and number-weighted data are -0.3 and -0.5, respectively. Data is for air-glycerine solution spray ( $\mu_L = 67$  mPas,  $\gamma = 61$  mN/m) with liquid flow rate of  $163 \times 10^{-6}$  m<sup>3</sup>/s and 1.0% *GLR*. Note that the linear relationship for the 2-data point above is for consistency of analysis compared to plots with 3 data-points.

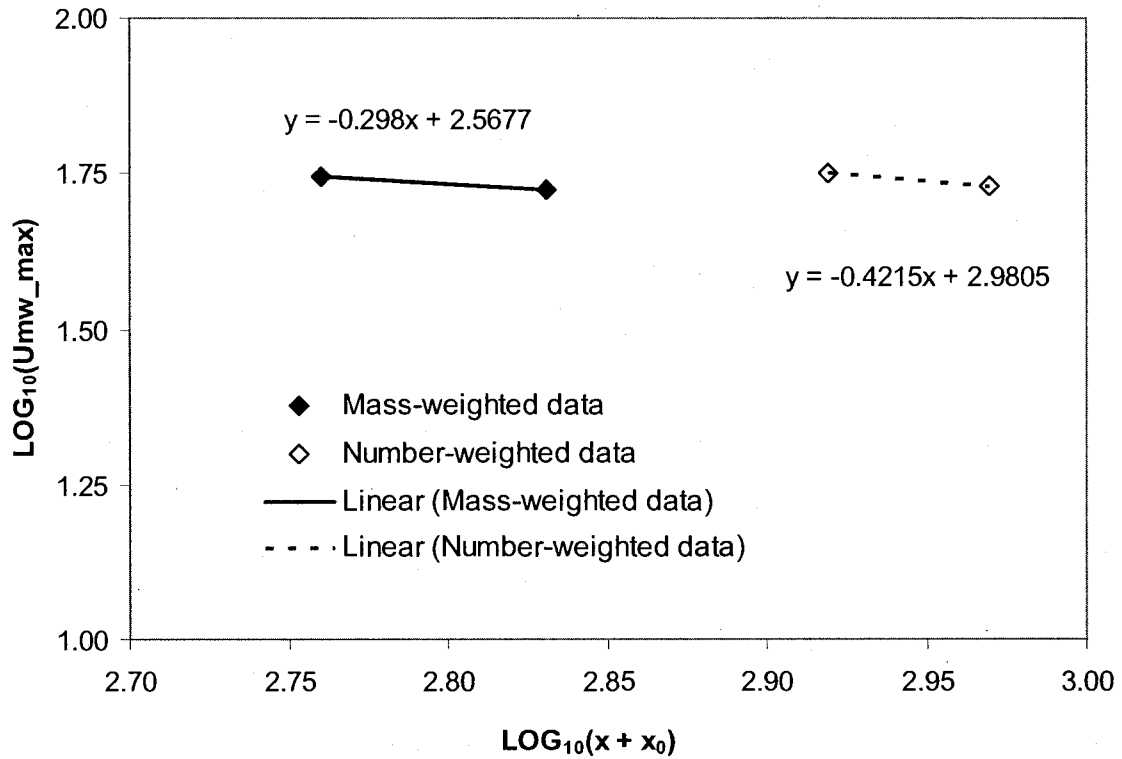


Figure A4-42: Variation of centreline velocity (from number-weighted velocity profiles) at axial positions 100 and 202 mm for SS-1.3. The slopes for the mass and number-weighted data are -0.3 and -0.4, respectively. Data is for air-water spray ( $\mu_L = 1$  mPas,  $\gamma = 70$  mN/m) with liquid flow rate of  $190 \times 10^{-6}$  m<sup>3</sup>/s and 1.0% *G**L**R*. Note that the linear relationship for the 2-data point above is for consistency of analysis compared to plots with 3 data-points.

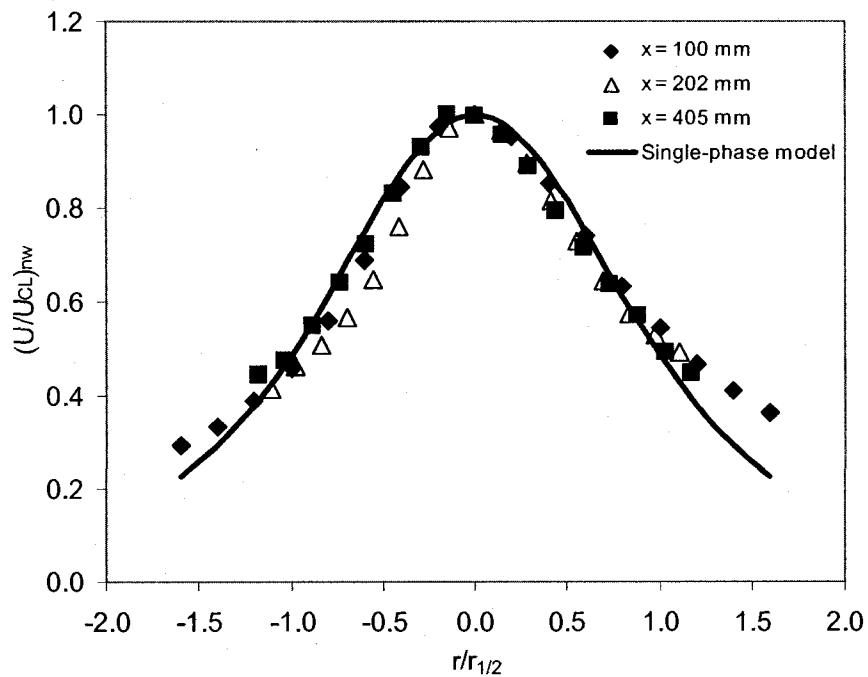
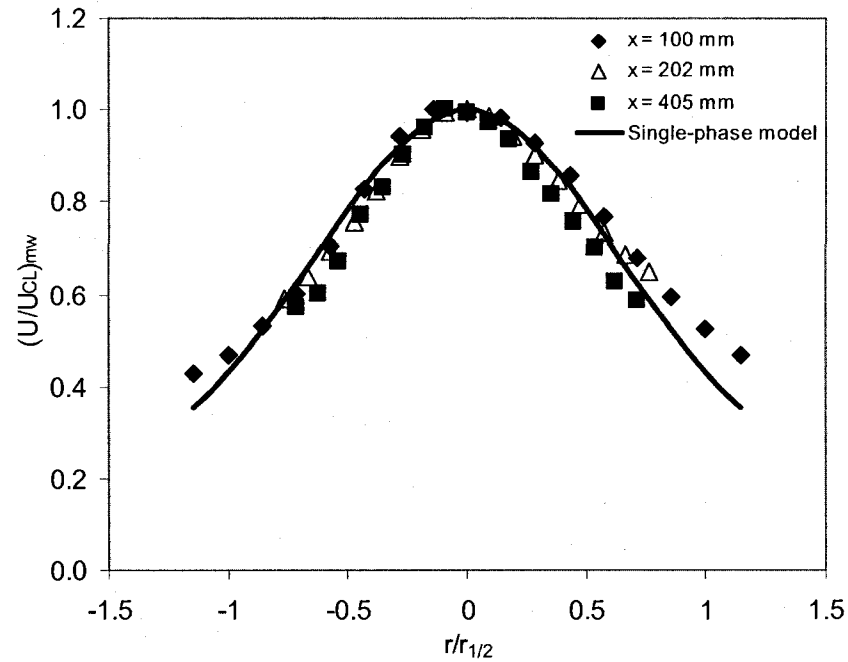


Figure A4-43: Curve-fit of single-phase velocity model on normalized mass-weighted (top) and number-weighted (bottom) velocity profiles at different axial distances. Data is for air-glycerine solution spray with liquid flow rate of  $114 \times 10^{-6} \text{ m}^3/\text{s}$  and 1.0% *GLR* through nozzle SS-1.0. The curve-fit coefficients of  $(r/r_{1/2})^2$  were 0.5204 and 0.4342, for the mass and number weighted data, respectively.



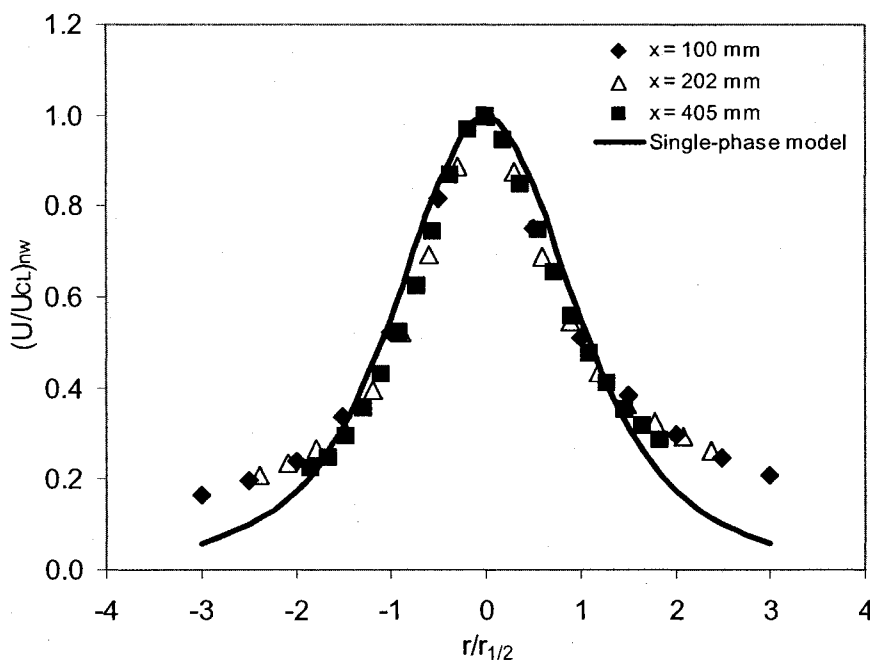
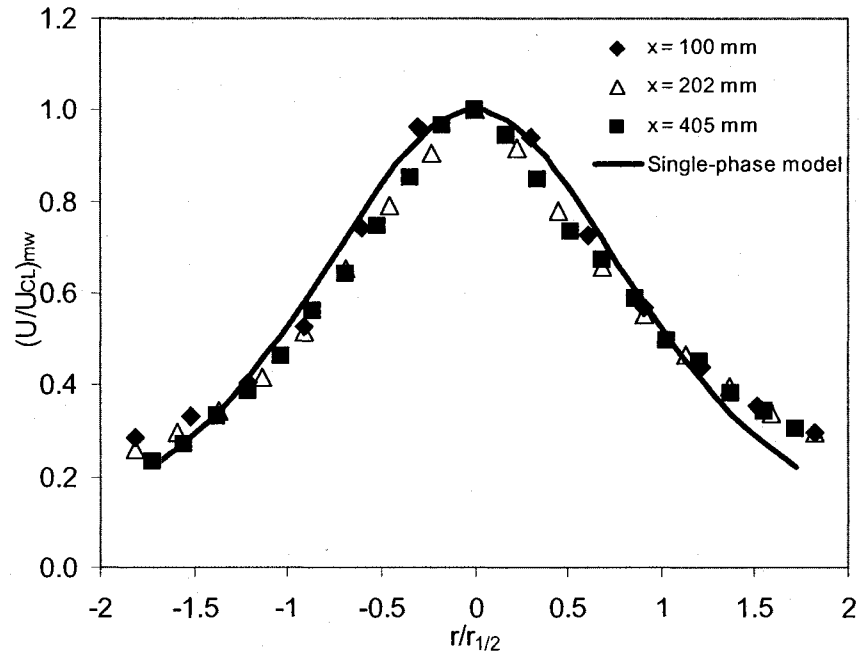


Figure A4-44: Curve-fit of single-phase velocity model on normalized mass-weighted (top) and number-weighted (bottom) velocity profiles at different axial distances. Data is for air-canola oil spray with liquid flow rate of  $105 \times 10^{-6} \text{ m}^3/\text{s}$  and 1.0% *GLR* through nozzle SS-1.0. The curve-fit coefficients of  $(r/r_{1/2})^2$  were 0.3783 and 0.3485, for the mass and number weighted data, respectively.

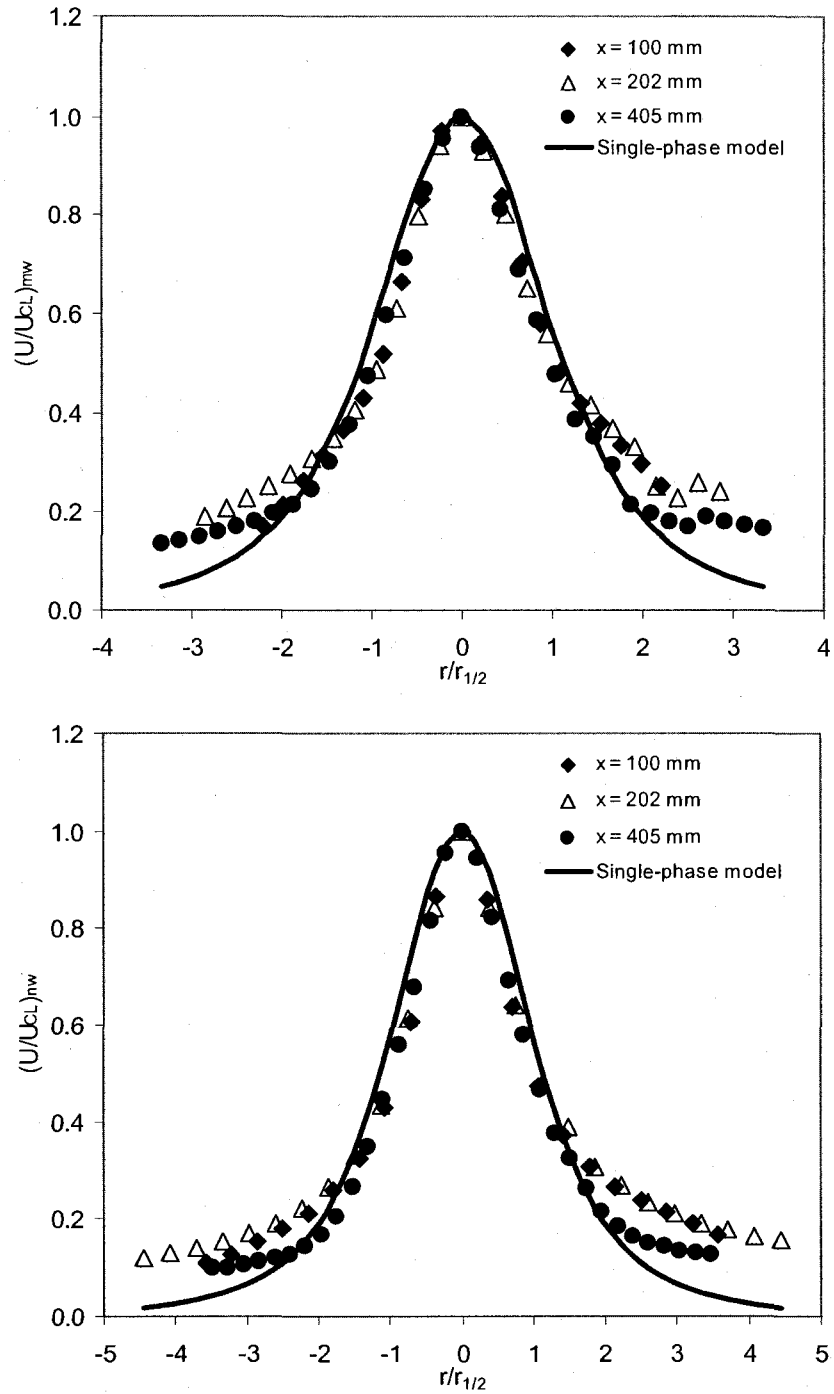


Figure A4-45: Curve-fit of single-phase velocity model on normalized mass-weighted (top) and number-weighted (bottom) velocity profiles at different axial distances. Data is for air-water spray with liquid flow rate of  $95 \times 10^{-6} \text{ m}^3/\text{s}$  and 2.0% GLR through nozzle SS-1.0. The curve-fit coefficients of  $(r/r_{1/2})^2$  were 0.3251 and 0.3256, for the mass and number weighted data, respectively.

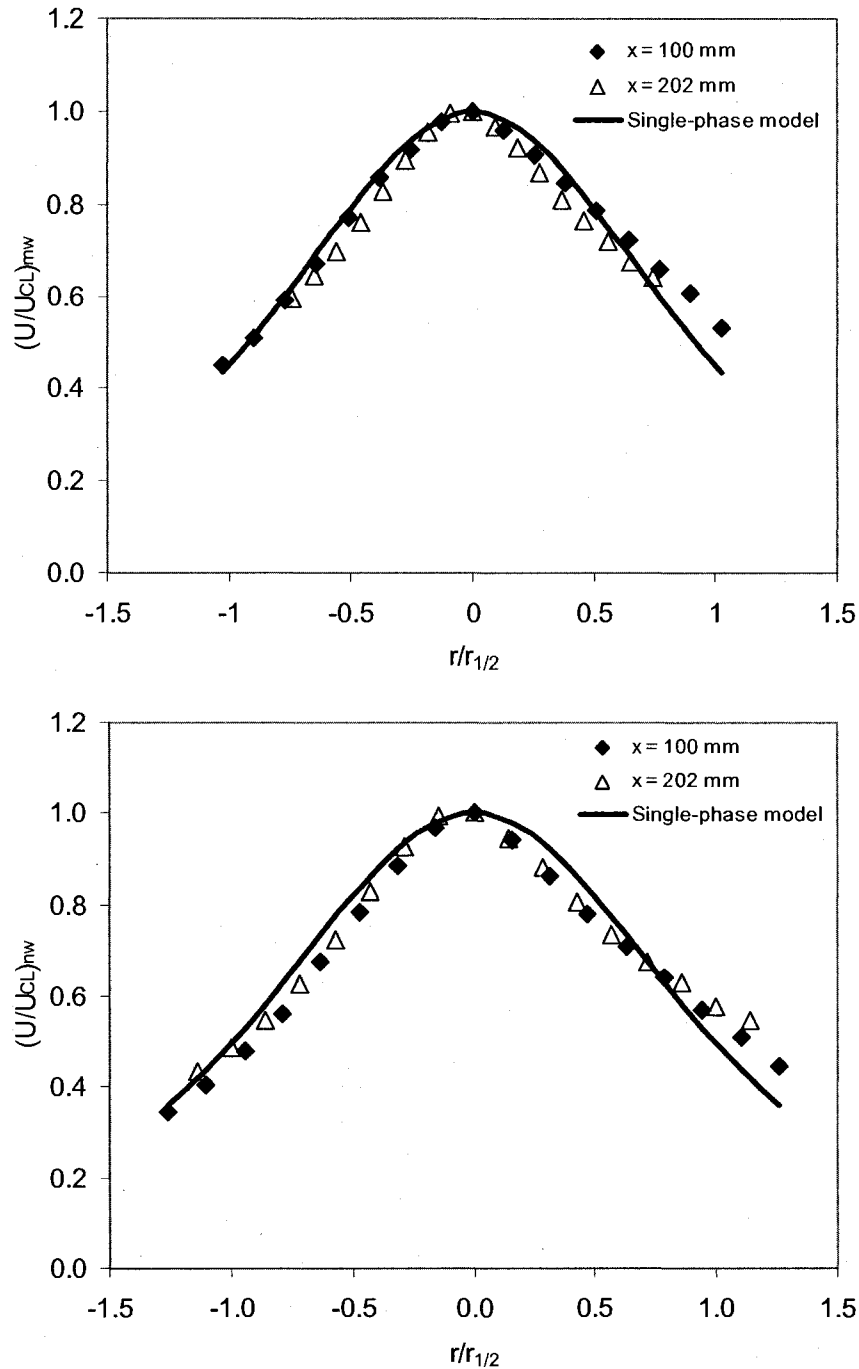


Figure A4-46: Curve-fit of single-phase velocity model on normalized mass-weighted (top) and number-weighted (bottom) velocity profiles at different axial distances. Data is for air-glycerine solution spray with liquid flow rate of  $105 \times 10^{-6} \text{ m}^3/\text{s}$  and 2.0% GLR through nozzle SS-1.0. The curve-fit coefficients of  $(r/r_{1/2})^2$  were 0.4920 and 0.4205, for the mass and number weighted data, respectively.

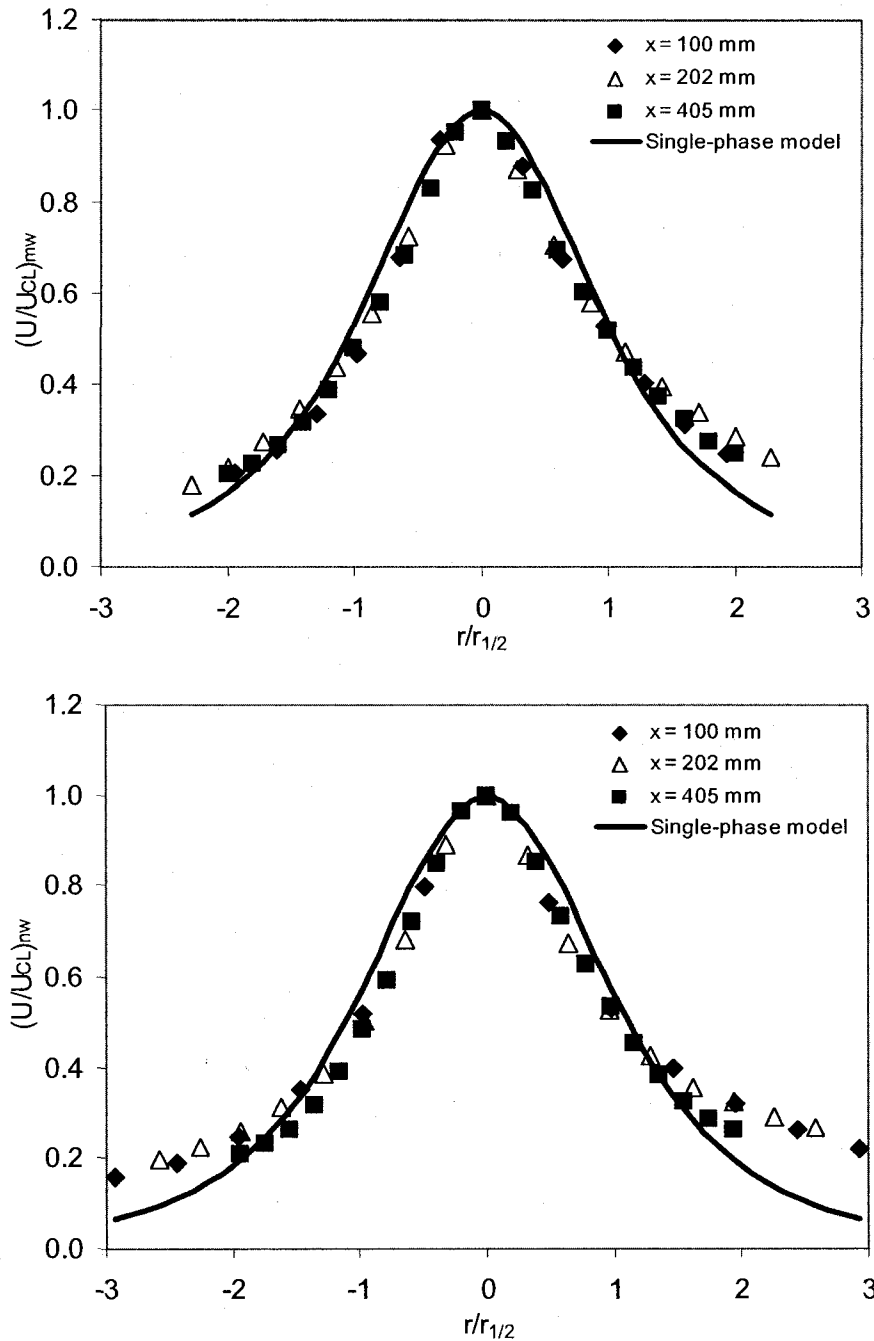


Figure A4-47: Curve-fit of single-phase velocity model on normalized mass-weighted (top) and number-weighted (bottom) velocity profiles at different axial distances. Data is for air-canola oil spray with liquid flow rate of  $105 \times 10^{-6} \text{ m}^3/\text{s}$  and 2.0% *GLR* through nozzle SS-1.0. The curve-fit coefficients of  $(r/r_{1/2})^2$  were 0.3698 and 0.3364, for the mass and number weighted data, respectively.

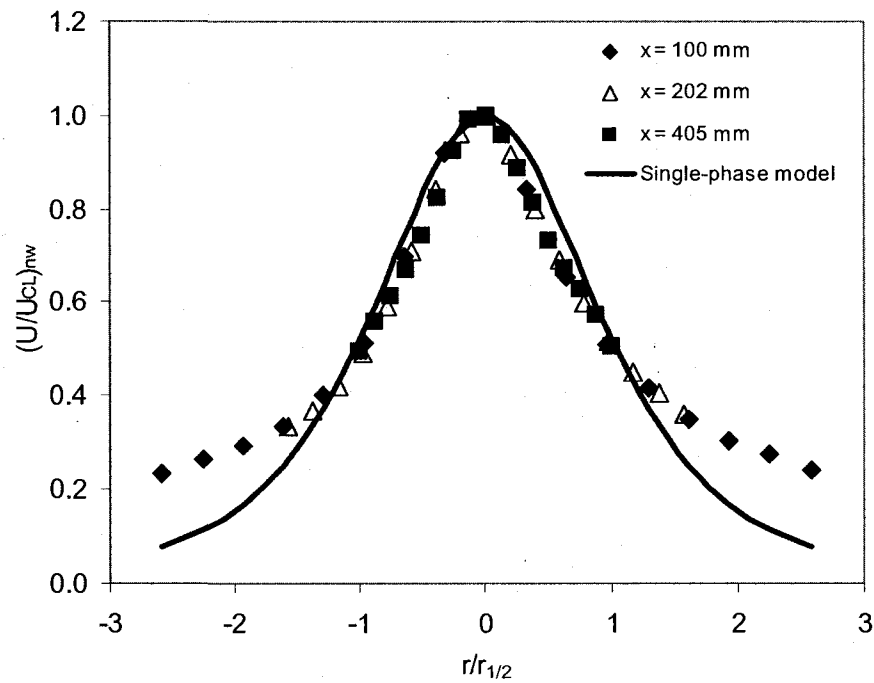
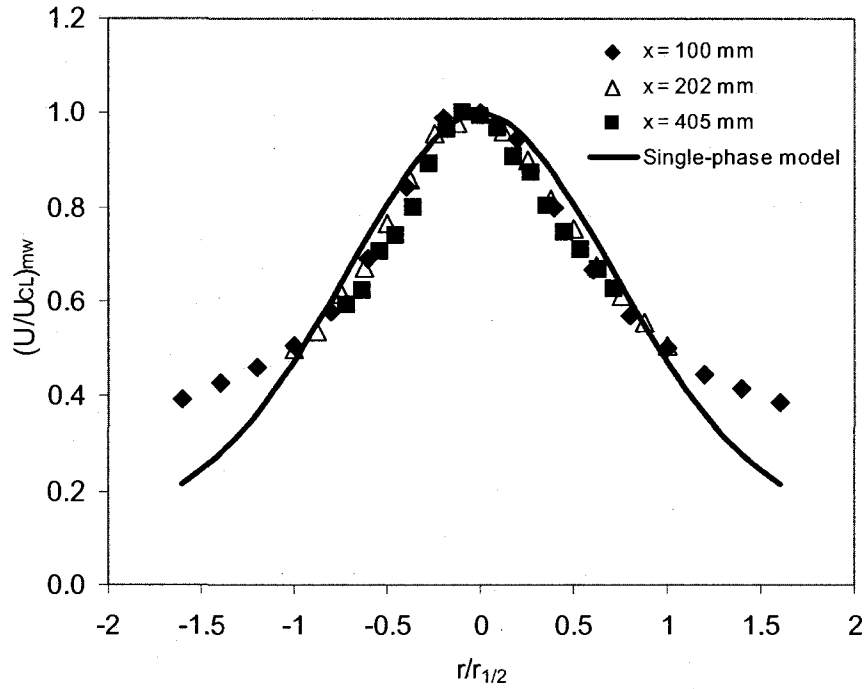


Figure A4-48: Curve-fit of single-phase velocity model on normalized mass-weighted (top) and number-weighted (bottom) velocity profiles at different axial distances. Data is for air-glycerine solution spray with liquid flow rate of  $79 \times 10^{-6} \text{ m}^3/\text{s}$  and 1.0% *GLR* through nozzle SS-1.0. The curve-fit coefficients of  $(r/r_{1/2})^2$  were 0.4560 and 0.3844, for the mass and number weighted data, respectively.

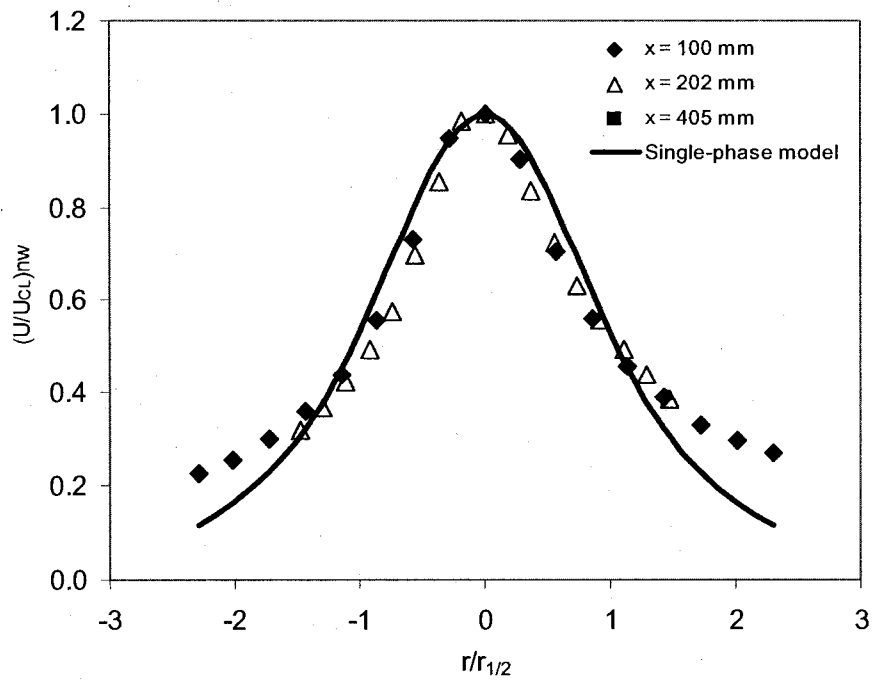
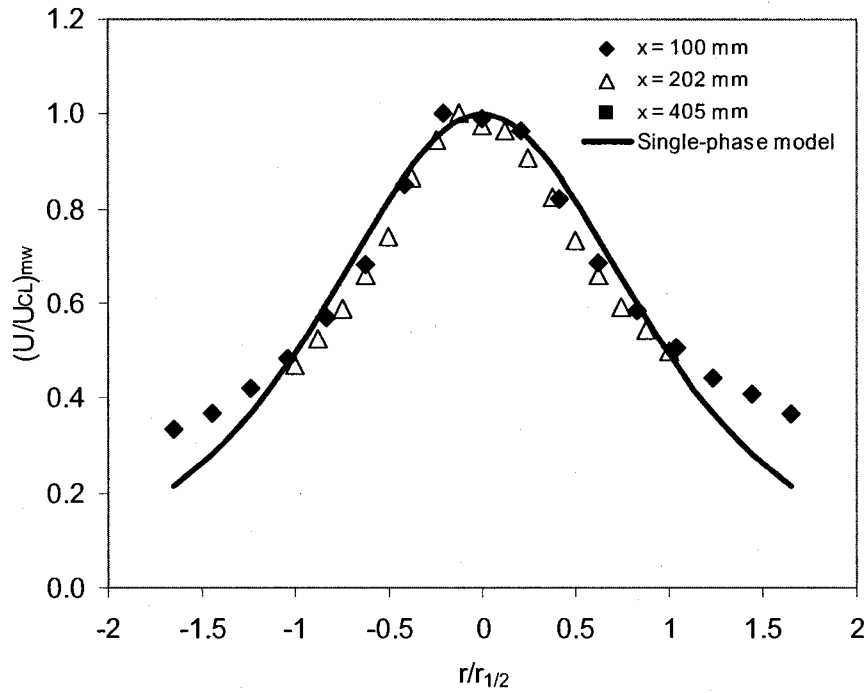


Figure A4-49: Curve-fit of single-phase velocity model on normalized mass-weighted (top) and number-weighted (bottom) velocity profiles at different axial distances. Data is for air-glycerine solution spray with liquid flow rate of  $163 \times 10^{-6} \text{ m}^3/\text{s}$  and 1.0% *GLR* through nozzle SS-1.3. The curve-fit coefficients of  $(r/r_{1/2})^2$  were 0.4237 and 0.3650, for the mass and number weighted data, respectively.

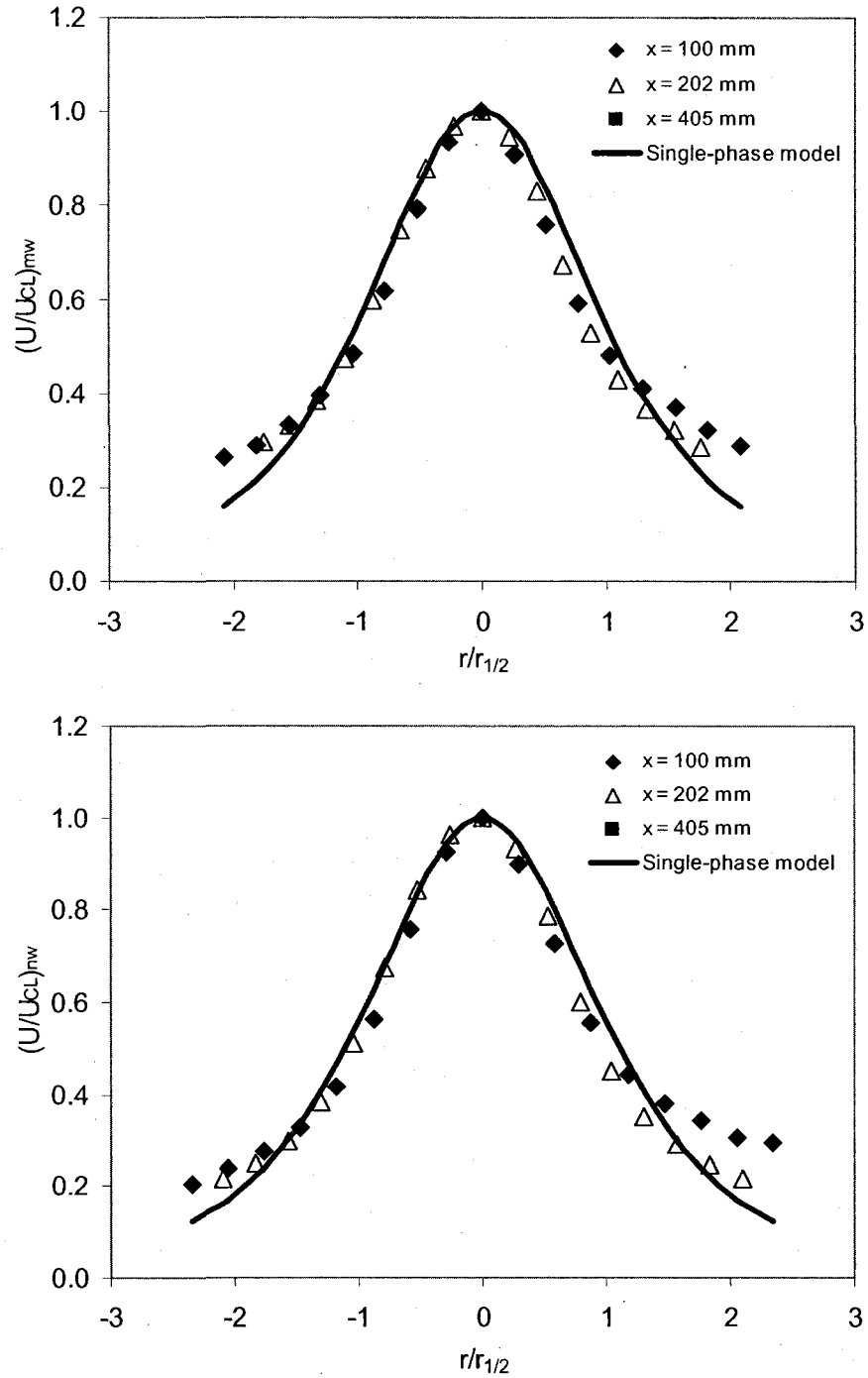


Figure A4-50: Curve-fit of single-phase velocity model on normalized mass-weighted (top) and number-weighted (bottom) velocity profiles at different axial distances. Data is for air-water spray with liquid flow rate of  $190 \times 10^{-6} \text{ m}^3/\text{s}$  and 1.0% GLR through nozzle SS-1.3. The curve-fit coefficients of  $(r/r_{1/2})^2$  were 0.3491 and 0.3375, for the mass and number weighted data, respectively.

## APPENDIX A5 – DROP SIZE RESULTS

This Appendix mainly presents the remaining plots of liquid volume flux per unit radius and PDFs for different sprays not presented in the main body of the thesis.

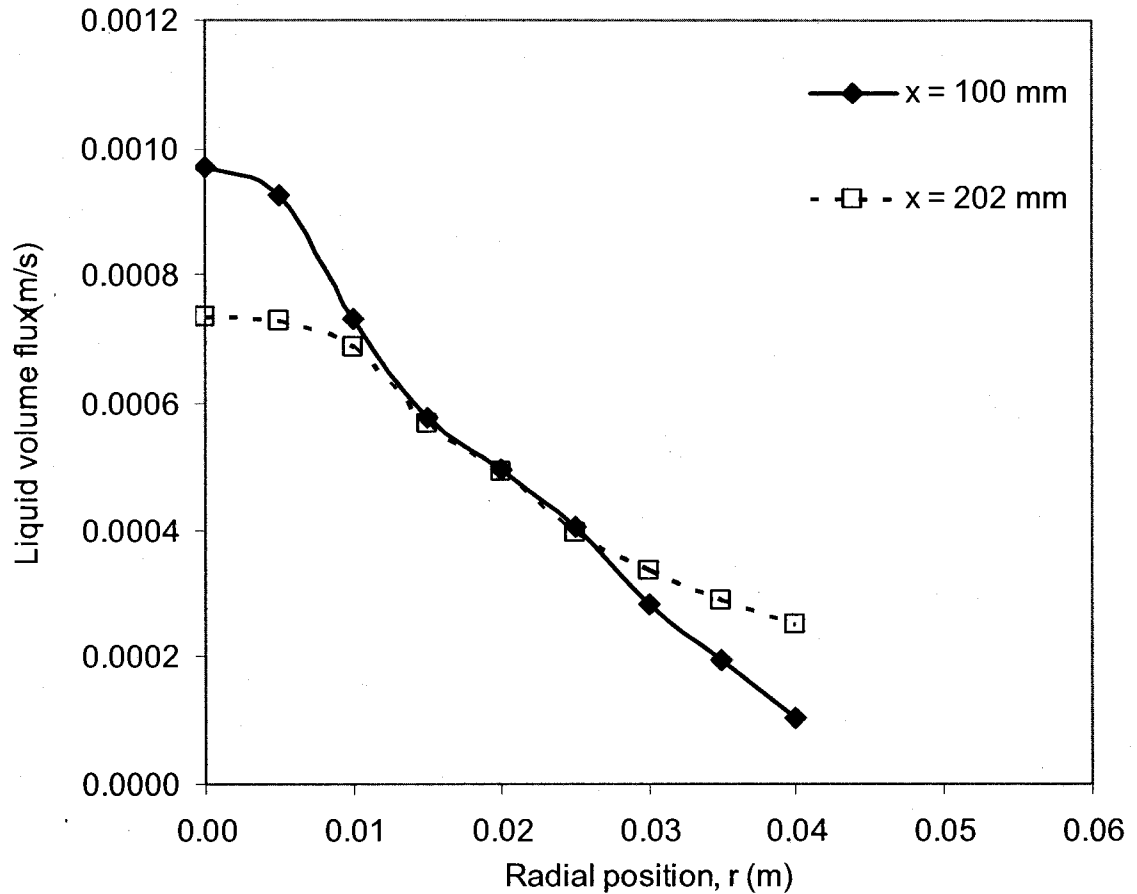


Figure A5-1: Plots of liquid volume flux at different axial distances. Data is for air-glycerine solution spray with liquid flow rate of  $105 \times 10^{-6} \text{ m}^3/\text{s}$  and 2% *GLR* through nozzle SS-1.0 ( $D = 3.1 \text{ mm}$ ). The representative spray radius is 25 and 35 mm, at  $x = 100 \text{ mm}$  and 202 mm, respectively.



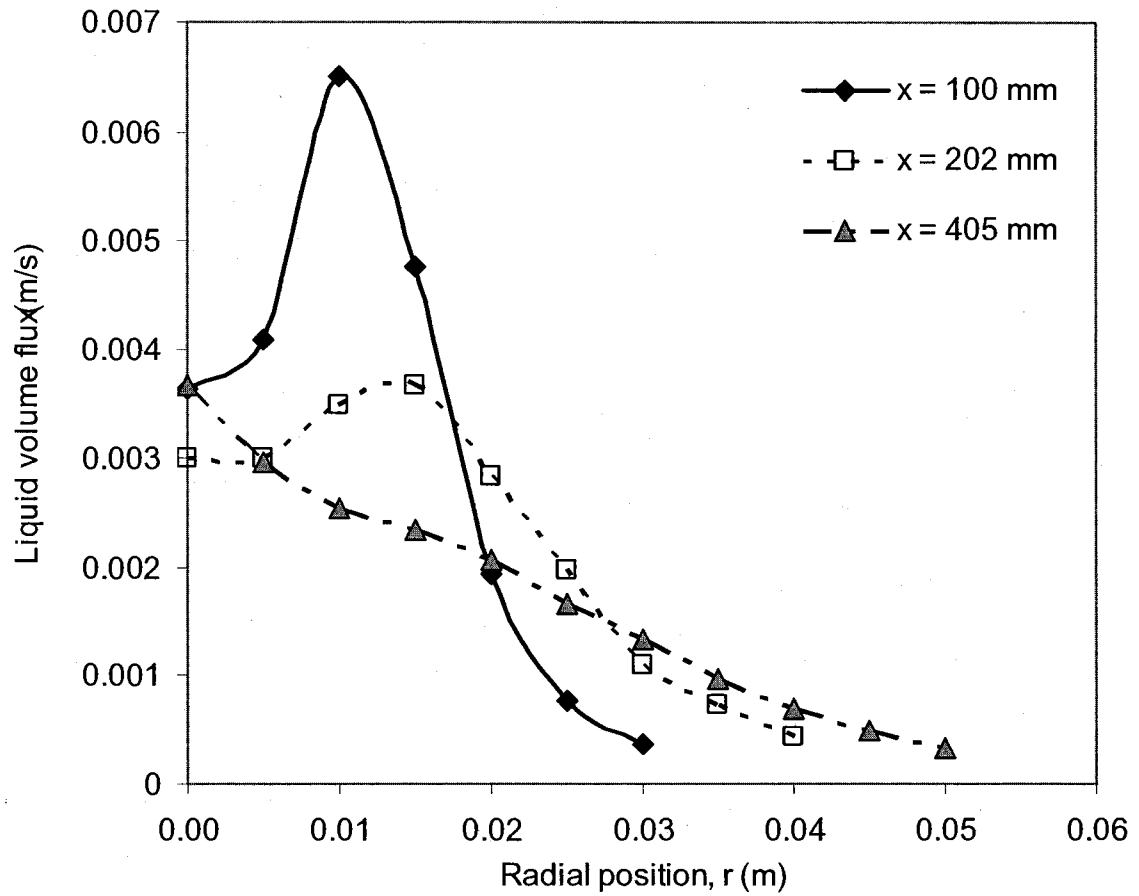


Figure A5-2: Plots of liquid volume flux at different axial distances. Data is for air-canola oil spray with liquid flow rate of  $105 \times 10^{-6} \text{ m}^3/\text{s}$  and 2% *GLR* through nozzle SS-1.0 ( $D = 3.1 \text{ mm}$ ). The representative spray radius is 15, 20, and 25 mm, at  $x/D = 100 \text{ mm}$ , 202 mm, and 405 mm, respectively.

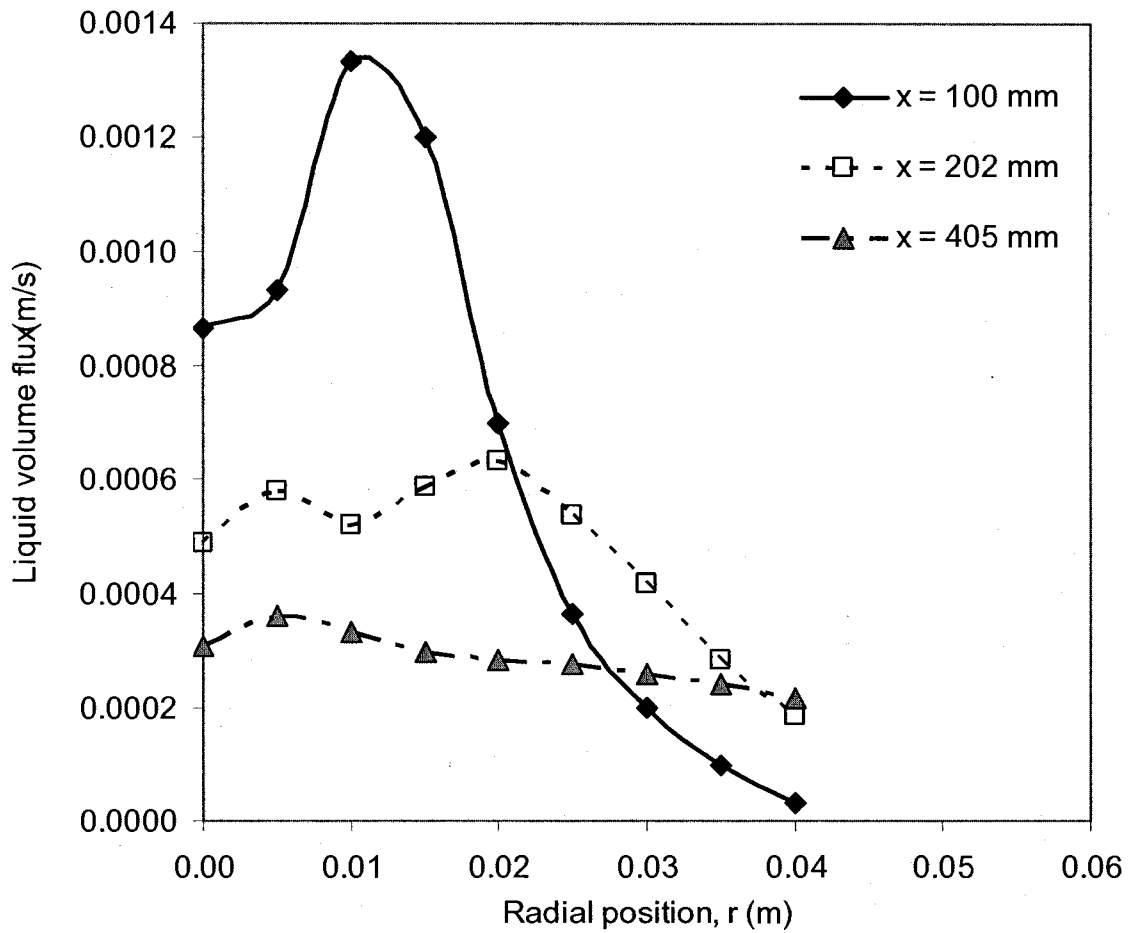


Figure A5-3: Plots of liquid volume flux at different axial distances. Data is for air-glycerine solution spray with liquid flow rate of  $79 \times 10^{-6} \text{ m}^3/\text{s}$  and 1% *GLR* through nozzle SS-1.0 ( $D = 3.1 \text{ mm}$ ). The representative spray radius is 15 and 25 mm, at  $x/D = 100 \text{ mm}$  and  $202 \text{ mm}$ , respectively.

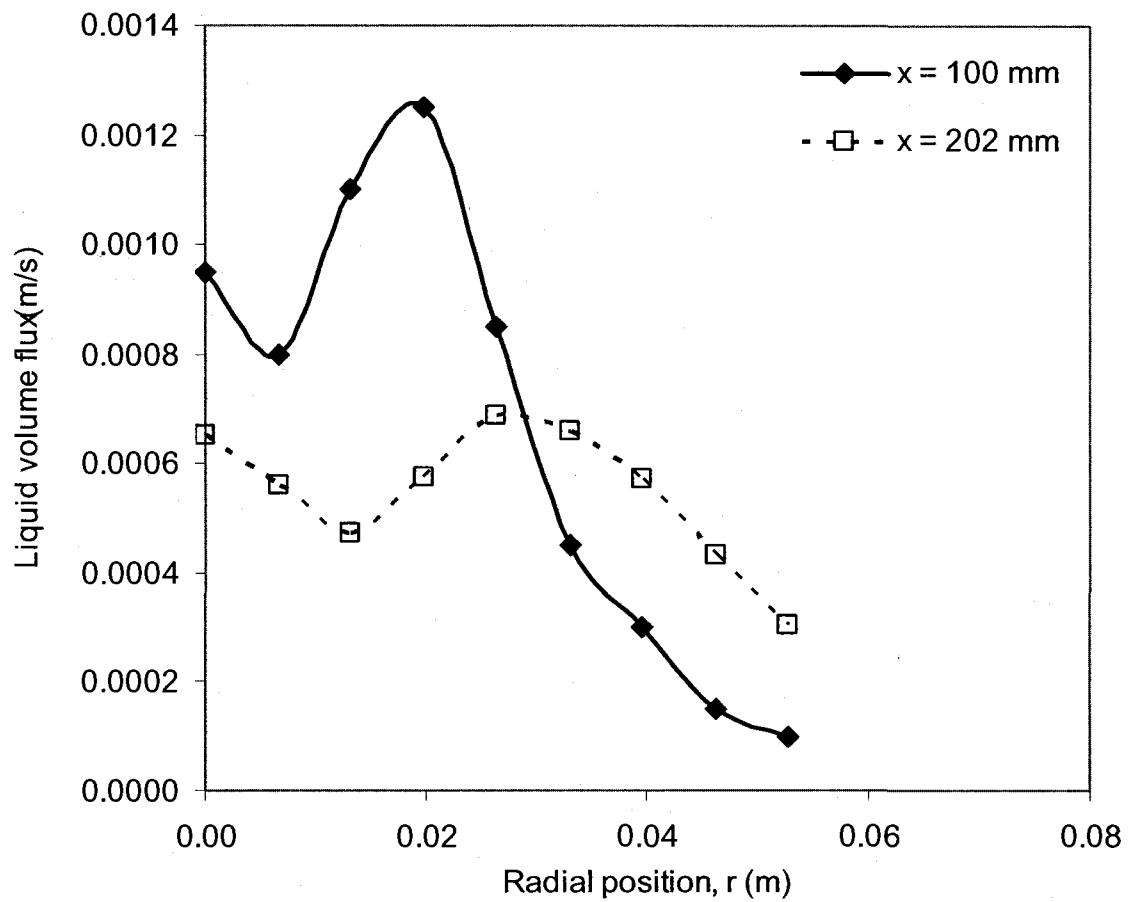


Figure A5-4: Plots of liquid volume flux at different axial distances. Data is for air-glycerine solution spray with liquid flow rate of  $163 \times 10^{-6} \text{ m}^3/\text{s}$  and 1% *GLR* through nozzle SS-1.3 ( $D = 4.1 \text{ mm}$ ). The representative spray radius is 20 and 40 mm, at  $x = 100$  and 202 mm, respectively.

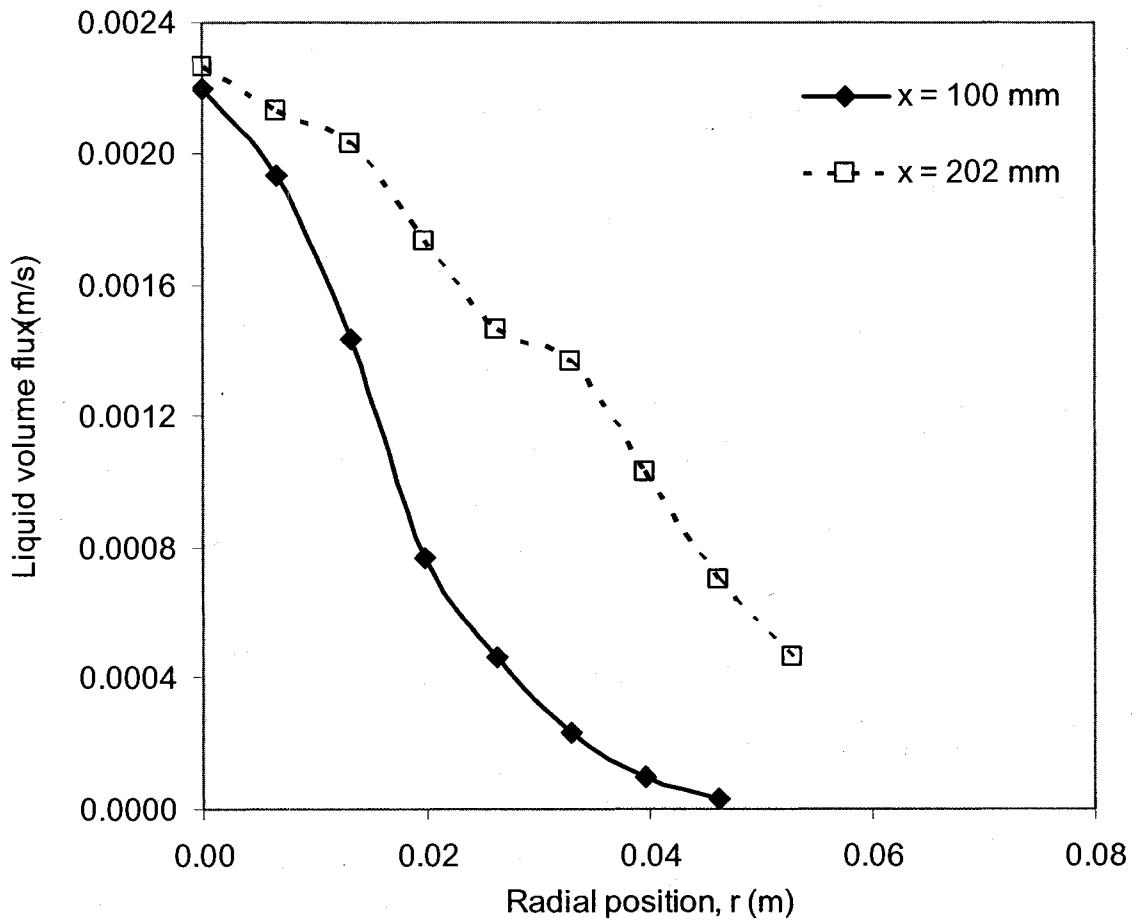


Figure A5-5: Plots of liquid volume flux at different axial distances. Data is for air-water spray with liquid flow rate of  $190 \times 10^{-6} \text{ m}^3/\text{s}$  and 1% GLR through nozzle SS-1.3 ( $D = 4.1 \text{ mm}$ ). The representative spray radius is 13 and 33 mm, at  $x = 100$  and 202 mm, respectively.